Making connectivity work reliably in harsh electromagnetic environments

Narrowband interference removal algorithms for OFDM-based communication

Aleksandr Ovechkin

Supervisors:
Prof. dr. ir. D. Pissoort
Prof. ir. ir. G. Vandenbosch
Dr. ing. D. Vanoost

Dissertation presented in partial fulfillment of the requirements for the degree of Doctor of Engineering Technology (PhD)

June 2023

Making connectivity work reliably in harsh electromagnetic environments
Narrowband interference removal algorithms for OFDM-based communication

Aleksandr OVECHKIN

Examination committee:
Em. prof. dr. ir. B. Meesschaert, chair
Prof. dr. ir. D. Pissoort, supervisor
Prof. ir. ir. G. Vandenbosch, supervisor
Dr. ing. D. Vanoost, supervisor
Prof. dr. ir. S. Pollin
Prof. dr. ir. H. Hallez
Dr. ing. T. Claeys
Dr. J. F. Dawson CEng, MIET, MIEEE
  (The University of York)
MSc. E. El Amam
  (RH Marine)

June 2023

Preface

"Aut consilio.
Aut ense"

— A common Latin expression translated from Ancient Greek

"Never retreat.
Never surrender.
Prepare for glory"

— Presumably Ancient Greek quote

The first expression was originally used by Spartan mothers who would ask their sons to come back from a battle either with a shield or on a shield. If you come back with a shield, then you survived and you are hailed upon the return. Being returned on a shield means that you could not make it. Nevertheless, the honour will be also given to you since you were holding the shield until the end and you were also protecting your battle brothers since a shield during the Spartan era was cumbersome to protect phalanx formations.

The second quote also originates from Ancient Greek and serves as a battle cry.

Although the mentioned quotes may seem dramatic both of them apply to me. Four years ago I ventured into the unknown fields, electromagnetic fields. The knowledge and support of my supervisors and peers were my armour and shield, while my sword was my determination. Today is a very important day to me because a lot has been put at stake. After these years spent at KU Leuven, a revelation came to me that the biggest enemy and challenge was not the subject

I was investigating but me. Irrespective of the outcome of this day, I can say that I was trying to not let down my battle brothers (my fellow colleagues, Safer Autonomous Systems (SAS) participants) and generals (my supervisors), and I am glad that I could make it until the end and did not flee from the battlefield. My parents have already told me that they were proud of me and this warms my heart and fills it with vehement elation.

My path to science started a long time before I was even thinking about a PhD. My parents were the ones who, first, noticed my acute attitude of planning the budget of my pocket money and regulating my sweets stocks. Then my mathematics and physics teachers proved the initial thoughts of my parents. Still, at that time I did not even think and care about my future professional path. This is how with a slight push from my parents I ended up in a technical lyceum in my home city, Tula. I owe this school my initial technical knowledge and due to the teaching style of Ludmila Ivanovna Baryshnikova and Elena Nikolaevna Rudneva, teachers of mathematics and physics, I started liking these subjects and became inclined to electrical engineering. This resulted in my first scientific quest when I left my home place and embarked upon an arduous Russian capital life full of temptations and distractions. However, I maintained determination and during the hardships of life, I knew that I could not give in. The originally mentioned warrior/knight principles helped me at that time and have been serving me well up until now. Unlike my fellow students who during the third year of our Bachelor's in electrical engineering mostly chose a professor, I chose an interesting topic related to overvoltages and current surges in electrical power stations and substations. My supervisor was Aleksandr Dmitrievich Kupchinov, a PhD student at that time. He was very enthusiastic about the topic and he sparked my interest in proceeding with my research during my Master's with him again.

After successfully defending my Bachelor's and Master's titles in Russia, I aspired to expand my knowledge and scientific skills by applying to PhD programmes. Albeit I knew that I could get a PhD position overseas, I was vacillating between the Russian PhD programme and a foreign one. As I mentioned before, I and, especially my doubts, were the main obstacles on the way to success. As a result, I decided to proceed with part-time research activities in Moscow and ventured into a position as a design engineer. However, very soon I came to a realisation that I had not finished my started scientific quest and I should not be led astray. This is how I resumed my research apprenticeship search in overseas universities. At the same time, my doubts, my arch-enemy, came back from hibernation. At a difficult period, when my strength and vigour were withering away, I stumbled upon Davy Pissoort. That person could see the inner potential in me for I am deeply thankful.

This is how I ended up in the Kingdom of Belgium, in a medieval city full of

history, Bruges, where a KU Leuven Campus is situated. There I started as a page under the command of Dries Vanoost, Guy A. E. Vandenbosch and Davy Pissoort. Each of them had a different personality with unique traits and a strong background in different fields. For example, Mr Vanoost was always eager to help not just me but many pages and squires under his guidance. He was very meticulous and attentive to details and this helped to produce mathematical derivations of the algorithms presented in this work. Mr Pissoort was like a senator always having a bird's eye view on the things in which he was barely involved allowing him to be always up-to-date. His valuable advice and immense support were helping me at the brink of breakdown. He had an innate ability to inspire me to go further. Although the talks with Mr Vandenbosch were not as frequent as with Mr Pissoort and Mr Vanoost, every time I discussed my work with Mr Vandenbosch, I received a valuable remark. Despite the fact that my supervisors made a gigantic input to my work and invested a lot of time and effort to put me on the science path, the work would not have the needed scientific merit without my assessors and members of the examination committee: Tim Claeys, John Frederick Dawson, Ehab El Amam, Hans Hallez, and Sofie Pollin.

Tim Claeys was the assessor who taught me how to work independently. He improved my determination and ability to grind further until results are reached. He was telling me that 95 % of my actions would lead to nothing whereas the remaining 5 % would yield to the results I look for. This helped me during countless code debugging and laboratory tests in which Mr Claeys was involved. He also appreciated my attempt to learn Dutch and from time to time he taught me Flemish in a humorous way. John Dawson's steadfast support for my laboratory measurements and research tremendously helped me during my stay in the other Kingdom at the University of York. His critical thinking, questions and quips also contributed to the quality of this work. Mr Emam was always looking at my work from an industrial point of view and made my work not to become purely scientific. Mr Hallez and Ms Pollin carefully read my work and gave their feedback improving the overall quality and giving the food for thought regarding further improvements of my technical solutions.

Chapter 5 would not be possible without the industrial help from Case New Holland industrial (CNHi) and Analog Devices. The former was represented by Marcel Verhoeven who guided me into the needs of the agricultural field and also piqued my curiosity by showing the innards of a combined harvester and the agricultural vehicle production process. Analog Devices was represented by Paul Hartanto-Doeser who helped me crack the mystery of SmartMesh IP and its applicability in the agricultural sector.

When doing research and a PhD, the atmosphere tremendously matters. Therefore, I would like to mention other people who contributed to my work

both directly and indirectly. Jonas Lannoo introduced me to the art of coding and eased my first steps in research. Hassan Tirmizi inspired me to be better than I am. His penchant for linguistics motivated me and I cherish the moments when I could read his texts written in excellent English. While Hassan was my guide in English, Brent De Blaere, Laure Buysse, and Brian Leeman were the ones who helped me with my Dutch quest and also reviewed the Dutch parts of the thesis. Brian was also a critical eye on some of my works and I enjoyed having technical discussions with him. Hasan Habib and Pejman Memar were always available for me if I was down and they introduced me to the delicious Pakistani and Iranian cuisine. Dejana Ugrenovic was a Slavic sister to me during the first half of my PhD, while Gregory De Ruyter became a Slavic brother during the second half. Bozheng Pang was responsible for good vibes in the office, while Niel Rillaerts and Nico De Smet were helping when I had issues with my computer or network. To ease my head from administrative and bureaucratic affairs Stephane Stroobant, Joke Margodt, and An Roose were eager to assist me. If I had any questions related to the laboratory equipment, then Filip Vanhee and Klaas Pluvier were of service to me. The assistance with correspondence and meetings was provided by the Campus Service. I am also grateful to the colleagues who were enthusiastic about joining sports sessions with me: Vikas Ashok Ghatge, Lirim Koraqi, Chandu Kancharla, Calvin Hubbard and others. I also enjoyed spending these four years with peers, pages and squires on their way to the title of ~~Knight~~ Doctor. Special gratitude is for the SAS participants who participated in the project creation and made a strong community through these years.

Outside the university, I also met a number of people who contributed to my well-being and at times were listening ears: B/kot neighbours, Dutch classmates, and the Josan family, thank you for that. The latter became the second family to me overseas. Of course, it goes without saying that the unwavering support of my close people and friends from Russia represented by Arthur Fomin, Sergej Scheck, Artyom Vodeniktov, Denis Popov, Anastasia Muravyova, Olga Finaeva, Elena Gorina and others kept my batteries charged, especially, during COVID times.

Finally, I would like to thank my family and parents who raised me the way I am now. My parents pushed my boundaries, motivated me to study further and dismissed me from worrying about the means during my Bachelor's and Master's periods for they wanted me to focus on my studies. I shall never forget that and I shall use a similar approach with my kids in future. I would like to express gratitude in Russian, so even my grandmother would understand me.

Дорогие родители, члены семьи и родственники. Данная работа не была бы возможна без вашей поддержки! Я искренне благодарен вам за то, что вы взрастили меня таким, какой я есть. На протяжении всей моей

жизни вы давали мне ценные советы и продолжаете их давать до сих пор. Некоторые из них, например, приоритет в образовании, я определённо буду использовать при воспитании своих детей. Спасибо, что мотивируете меня на новые подвиги! Уверен, что это не последнее событие, эмоции которого мы разделим вместе. Искренне ваш сын, брат, внук и племянник.

After every quest, a warrior brings something: trophies, experience or honour. In my case, I brought a different version of myself that could overcome my inside enemy of fear and doubts. Defeating this enemy does not mean that he will not come again. However, the epiphany that I should always rather try than feel sorry will remain with me until my last day.

<div align="right">

Aleksandr Ovechkin

Bruges, the 23$^{\text{rd}}$ of October, 2023

</div>

Acknowledgement

Figure 1: The European flag.

Abstract

With the advent of technology, more and more technological novelties come into human life. While 30 years ago self-driving vehicles or co-bots were bordering on science fiction, now they have become a reality. For example, a lot of countries are actively investing in Autonomous Vehicles (AVs) and Unmanned Aerial Vehicles (UAVs) since they are not only able to facilitate and improve our lives but also increase safety while decreasing casualties. As a result, these systems are categorised into the safety-critical group in which safety requirements are very high to provide the needed reliability levels. Safety-critical systems will possess communication modules using which a communication session can be established with other systems and devices. This challenges the reliability of safety-critical systems because they have to operate in an environment electromagnetically "polluted" by numerous and constantly growing communication devices. At the same time, the decreasing rated voltage and increasing operating frequency (also within safety-critical systems) compound the already existing harsh ElectroMagnetic (EM) environment. Consequently, to keep up with high reliability requirements, one has to provide protection against ElectroMagnetic Disturbances (EMDs) to prevent them from turning into ElectroMagnetic Interferences (EMIs) and disrupting safety. Therefore, this thesis focuses on making connectivity work reliably in the presence of EMDs by creating and simulating harsh EM environments in order to work out techniques, methods and guidelines.

After investigating safety-critical systems, especially Autonomous Systems (ASs), the founding technology serving as a communication basis was identified. This is Orthogonal Frequency Division Multiplexing (OFDM) and it is used because it can transmit large amounts of data without having an InterCarrier Interference (ICI) and deals with the multipath fading effects of the transmission channel.

However, despite evident advantages, OFDM may have a large Peak-to-Average Power Ratio (PAPR) leading to more complex receiver designs and a careful choice of coding techniques. OFDM is vulnerable to NarrowBand Interferences (NBIs). In most cases, NBIs are not aligned in the period with the transmitted signal and as a result, the resulting received signal is not coherently sampled. When feeding this signal to the Fast Fourier Transform (FFT) block, the output creates the spectral leakage phenomenon. This causes the NBI energy to be spread along different subcarriers affecting most of the ones spectrally close to the NBI's frequency. Therefore, the main focus of this work was to find ways of reducing the influence of the spectral leakage phenomenon in OFDM systems to a bare minimum.

This work provides two solutions to the spectral leakage phenomenon issue due to NBIs. They are "Mod-remod" and "Differential" algorithms. Both of them exploit the spectral leakage pattern inherent to NBIs in the received OFDM signal. The "Mod-remod" algorithm performs re-modulation procedure to identify the NBI parameters, while the "Differential" algorithm sacrifices half of the bandwidth to be able to transmit the mirrored copy of the signal. This helps to locate an NBI after folding the received spectrum by performing manipulations with two halves of the signal. The initial results of the two algorithms were achieved in simulations and later validated through laboratory tests. The algorithms are able to improve the performance of OFDM systems in the presence of NBI and white noise. The "Differential" algorithm has an option of iteratively locating multiple NBIs and also has a built-in refinement procedure.

In addition, this manuscript also investigated the potential Wireless Sensor Networks (WSNs) in the agricultural sector. After investigating sector needs, WSNs were limited to two technologies: SmartMesh IP and IO-link Wireless (IOLW). Since an Agricultural Vehicle (AgV) possesses a lot of metal parts its worst EM environment was replicated in a Reverberation Chamber (RC). After conducting a series of tests in the RC, the SmartMesh IP technology was chosen to further proceed with tests on a real harvester due to mainly energy benefits compared to IOLW. The experimental results helped to make recommendations for the use of WSN in the agricultural sector. In addition, it also gave insights into recreating an AgV's EM environment in a laboratory setting.

Finally, the NBI removal algorithms were proposed to be valorised. For that, the work proposes the brand name "NoEMI" and offers NBI removal algorithms as the main NoEMI product realised as Software-As-A-Service (SAAS) and ElectroMagnetic Compatibility (EMC) consultancy services as a side product. The algorithms were estimated for their societal benefit in the automotive market which was chosen as the initial market. The latter was estimated for potential customers and competitors and the market penetration strategy was chosen

through the already established companies in the automotive product value chain. The initial investments and cash flow for 10 years were also predicted and shown in the manuscript.

Beknopte samenvatting

Met de technologische vooruitgang komen er steeds meer technologische uitvindingen in het leven van de mens. Terwijl dertig jaar geleden zelfrijdende voertuigen en co-bots nog sciencefiction waren, zijn die nu ondertussen werkelijkheid geworden. Veel landen investeren bijvoorbeeld actief in autonome voertuigen en onbemande luchtvaartuigen, omdat ze niet alleen ons leven kunnen vergemakkelijken en verbeteren, maar ook de veiligheid verhogen en het aantal slachtoffers verminderen. Als gevolg hiervan worden deze systemen gecategoriseerd in de veiligheidskritieke groep waarin de veiligheidseisen zeer hoog zijn om de nodige betrouwbaarheidsniveaus te garanderen. Veiligheidskritieke systemen beschikken over communicatiemodules waarmee een verbinding met andere systemen en apparaten kan worden gemaakt. Dit stelt de betrouwbaarheid van veiligheidskritieke systemen in vraag, omdat ze moeten werken in een omgeving die elektromagnetisch "vervuild" is door talrijke en voortdurend evoluerende communicatieapparaten. Tegelijkertijd verergert de bestaande elektromagnetische (EM) omgeving door de afnemende elektrische spanning en toenemende werkfrequentie. Om aan de hoge betrouwbaarheidseisen te kunnen blijven voldoen, moet er dus bescherming worden geboden tegen elektromagnetische verstoringen (EMV's) zodat deze niet resulteren in elektromagnetische interferenties (EMI's) en de veiligheid in gedrang brengen. Daarom richt deze scriptie zich op de betrouwbaarheid van draadloze communicatie in aanwezigheid van EMV's. Gebaseerd op simulaties van zware EM-omgevingen worden nieuwe methoden en richtlijnen uitgewerkt.

Bij het bestuderen van van veiligheidskritieke systemen, met name autonome systemen, werd orthogonal frequency division multiplexing (OFDM) als fundamentele techniek geïdentificeerd. OFDM kan grote hoeveelheden gegevens verzenden zonder intercarrier interference en kan goed om met multipad fading

effecten van het transmissiekanaal. Ondanks de duidelijke voordelen kan OFDM echter een grote peak-to-average power ratio hebben, waardoor er nood is aan meer complexe ontwerpen van ontvangers en resistente coderingstechnieken. Bovendien OFDM is kwetsbaar voor narrowband interferences (NBI's). In de meeste gevallen zijn NBI's niet uitgelijnd met de periode van het uitgezonden signaal en wordt als gevolg daarvan het ontvangen signaal niet coherent bemonsterd. Wanneer dit signaal wordt getransformeerd naar het frequentiespectrum met het Fast Fourier Transform blok, ontstaat het fenomeen van spectrale verliezen. Hierdoor wordt de NBI-energie verspreid over verschillende subcarriers. Dit beïnvloedt vooral de subcarriers die spectraal dicht bij de frequentie van de NBI liggen. De belangrijkste focus in dit werk was daarom om een methode te vinden om spectrale verliezen in OFDM-systemen tot een minimum te beperken.

Dit werk biedt twee oplossingen: het "Mod-remod" algoritme en het "Differentiële" algoritme. Beide maken gebruik van het spectraal verliespatroon dat inherent is aan NBI's in het ontvangen OFDM-signaal. Het "Mod-remod" algoritme voert een hermodulatieprocedure uit om de NBI-parameters te identificeren, terwijl het "Differentiële" algoritme de helft van de bandbreedte opoffert om de gespiegelde kopie van het signaal te kunnen verzenden. Dit helpt bij het lokaliseren van een NBI na het opvouwen van het ontvangen spectrum door manipulaties uit te voeren met de twee helften van het signaal. De eerste resultaten van de twee algoritmen werden behaald in simulaties en zijn later gevalideerd door middel van testen in een laboratorium. De bovengenoemde technieken zijn in staat om de prestaties van OFDM-systemen in de aanwezigheid van NBI en witte ruis te verbeteren. Het "Differentiële" algoritme heeft bovendien een optie om meerdere NBI's iteratief te lokaliseren en een ingebouwde verfijningsprocedure.

Daarnaast wordt in dit manuscript het potentieel van draadloze sensornetwerken (DSN) in de landbouwsector bestudeerd. Na onderzoek van de behoeften van de sector, werden DSN's beperkt tot twee technologieën: SmartMesh IP en IO-link wireless (IOLW). Aangezien een landbouwvoertuig (LbV) veel metalen onderdelen bevatten, werd de worst-case EM-omgeving nagebootst in een reverberatie kamer. Na een reeks experimenten werd besloten om verder te gaan met SmartMesh IP en de technologie te testen op een echte maaidorser, dit voornamelijk door de energievoordelen ten opzichte van IOLW. De experimentele resultaten hebben bijgedragen aan aanbevelingen voor het gebruik van DSN in de landbouwsector. Daarnaast gaf het ook inzicht in het nabootsen van de EM-omgeving van een LbV in een laboratoriumomgeving.

Tot slot werd voorgesteld om de kennis die is verkregen tijdens de jaren van onderzoek en de NBI-verwijderingsalgoritmen te valoriseren. Het werk stelt daarvoor de merknaam "NoEMI" voor. Het belangrijkste product

hierbij zijn de NBI-verwijderingsalgoritmen die als software-as-a-service werden gerealiseerd. Daarnaast biedt "NoEMI" adviesdiensten over elektromagnetische compatibiliteit (EMC) als nevenproduct aan. De algoritmen werden geschat op hun maatschappelijke voordelen in de automobielmarkt, die als initiële markt werd gekozen. Deze markt werd geschat op potentiële klanten en concurrenten. De markpenetratiestrategie werd gekozen via de reeds gevestigde bedrijven in de waardeketen van autoproducten. Tenslotte worden de initiële investeringen en de voorspelde cashflow voor 10 jaar besproken in het manuscript.

List of Abbreviations

3GPP 3rd Generation Partnership Project

5G NR 5G New Radio

5G-ACIA 5G Alliance for Connected Industries and Automation

5GAA 5G Automotive Association

A/D Analog-to-Digital

AGC Automatic Gain Control

AgV Agricultural Vehicle

AS Autonomous System

AV Autonomous Vehicle

AWGN Additive White Gaussian Noise

BER Bit Error Rate

BPSK Binary Phase-Shift Keying

BT Bluetooth

C-V2X Cellular-V2X

CFO Coarse Frequency Offset

CN Convergence Number

CNHi Case New Holland industrial

CP Cyclic Prefix

CTO Coarse Timing Offset

CW Continuous Wave

DC Direct Current

DFT Discrete Fourier Transform

DPM Distance Preserving Mapping

EM ElectroMagnetic

EMC ElectroMagnetic Compatibility

EMD ElectroMagnetic Disturbance

EMI ElectroMagnetic Interference

ET Elapsed Time

ETN European Training Network

ETSI European Telecommunications Standards Institute

FDMA Frequency Division Multiple Access

FFO Fine Frequency Offset

FFT Fast Fourier Transform

FTO Fine Timing Offset

GSMA Global System for Mobile Communications Association

HD Hop Depth

ICI InterCarrier Interference

IDFT Inverse Discrete Fourier Transform

IEEE Institute of Electrical and Electronics Engineers

IFFT Inverse Fourier Transform

IOLW IO-link Wireless

IoT Internet-of-Things

ISM Instrumental, Scientific and Medical

ITS Intelligent Transportation Systems

LDPC Low-Density Parity Check

LLR Log-Likelihood Ratio

LLTF Legacy Long Training Field

LO Local Oscillator

LoS Line-of-Sight

LSTF Legacy Short Training Field

LTE Long Term Evolution

M2M Machine-to-Machine

MER Modulation Error Rate

NBI NarrowBand Interference

Non-LoS Non-Line-of-Sight

NRTx Number of ReTransmissions

OBU On-Board Unit

OEM Original Equipment Manufacturer

OFDM Orthogonal Frequency Division Multiplexing

PAPR Peak-to-Average Power Ratio

PDP Power Delay Profile

PER Packet Error Rate

PR Publish Rate

PSD Power Spectral Density

PSK Phase-Shift Keying

QAM Quadrature Amplitude Modulation

QoS Quality of Service

QPSK Quadrature Phase-Shift Keying

R&S Rohde & Schwarz

RAT Radio Access Technology

RC Reverberation Chamber

RF Radio Frequency

RFP Residual Failure Probability

RSSI Received Signal Strength Indication

RSt Refinement Step

RSU Road-Side Unit

SAAS Software-As-A-Service

SAS Safer Autonomous Systems

SDN Software-Defined Network

SDR Software-Defined Radio

SF Smart Farming

SIR Signal-to-Interference Ratio

SNR Signal-to-Noise Ratio

TDMA Time Division Multiple Access

TP Troublesome Place

TSCH Time-Slotted Channel Hopping

TxP Transmission Power

UAV Unmanned Aerial Vehicle

UDP User Datagram Protocol

V2X Vehicle-to-Everything

WLAN Wireless Local Area Network

WP Work Package

WSN Wireless Sensor Network

List of Symbols

Frequency domain expressions are with capital letters small letters represent time domain expressions. Time domain expressions are with small letters. Variable notation uses both capital and small letters.

S_m Quadrature Amplitude Modulation (QAM)-modulated data

m current subcarrier number

S_m^{est} the data component estimation of QAM-modulated data in the frequency domain

I_m QAM-modulated in-phase data component

Q_m QAM-modulated quadrature data component

K the total number of subcarriers

n the current time domain sample

x_n the current Orthogonal Frequency Division Multiplexing (OFDM) sample

a_n the current in-phase sample

b_n the current quadrature sample

t time variable

f_c carrier frequency

s_n transmitted time domain signal

b_n the current quadrature sample

d_{NBI} the NarrowBand Interference (NBI) component of the disturbance variable

d_{AWGN} the Additive White Gaussian Noise (AWGN) component of the disturbance variable

A_{NBI} the amplitude of an NBI

f_{NBI} the NBI frequency

$f_{\mathrm{NBI}}^{\mathrm{est}}$ the estimated NBI frequency

θ_{NBI} the NBI phase

f_{diff} the difference frequency between f_{NBI} and f_c

p the nearest subcarrier to the f_{NBI}

α the position of the NBI with relation to the subcarriers p and $p+1$ surrounding it

H subcarrier spacing

B_{d} symbol or baud rate

z_n the current received sample

r_n the current received sample after performing conversion to the baseband frequency

w_c angular carrier frequency

w_{diff} angular NBI frequency

R_m the current received sample in the frequency domain

m the current subcarrier number

K the current quadrature sample

γ amplification coefficient for the Automatic Gain Control (AGC)

E_m the NBI component in the received signal in the frequency domain

E_m^{est} the NBI component estimation in the received signal in the frequency domain

a the spectral position of the NBI with regard to a neighbouring subcarrier as follows $d + \alpha = -a$

q new summation limits for Maths simplification having the relation with n such as $n = 2q$

X_m the received signal after performing the summation of the first half with the second half: $X_m = R_m + R_{m+\frac{K}{2}}$

E_m^{numer} the numerator part of (3.6)

E_m^{denom} the denominator part of (3.6)

X_m^{upd} the updated X_m value after subtracting from it the reconstructed E_m values

X_m^{ref} the reference X_m values before the refinement procedure

v the threshold parameter equal to a percentage value of the minimum Euclidean distance between neighbouring points on the I-Q constellation of the chosen modulation scheme

D_{min} the minimum Euclidean distance between neighbouring points on the I-Q constellation of the chosen modulation scheme

T_{FFT} duration of data within one OFDM symbol

S_1 the first (out of 10) short Legacy Short Training Field (LSTF) training symbol

L_1 the first (out of 2) Legacy Long Training Field (LLTF) long training symbol

T_{CP} duration of Cyclic Prefix (CP)

T_{sym} OFDM symbol duration

N_{syms} the number of OFDM symbols

A, B, C, P sliding windows

g_n the energy within the sliding window A

g_n the energy within the sliding window A

y_n the energy within the sliding window B

r_n the received signal in the time domain at sample n

u a sample number within the sliding window A

M the sliding window size

l a sample number within the sliding window A

m_n packet detection metric depending on the sample number n

D the length of an LSTF's short training symbol

c_n the energy value of the sliding window C

p_n the energy value of the sliding window P

T_s duration of the total OFDM symbol

T_u duration of the useful data portion of an OFDM symbol

t_Δ the sampling period offset

T_{Tx} the sampling period of the transmitter

T_{Rx} the sampling period of the receiver

s_n the transmitted signal

z an intermediate value for the maximum-likelihood frequency estimator

f_Δ the carrier frequency offset

L the length in samples of the training symbol

$\hat{f}_\Delta$ carrier frequency offset estimation

ϕ_z phase offset

$\hat{t}_s$ timing detection estimation

H_m the influence of the transmission channel resulting in the signal's attenuation or amplification

W_m the equalisation factor for the subcarrier m

$e(y)$ phase rotation correction using pilots

y the current OFDM symbol

N_p the total number of pilots

p_{num} the original pilot

$\hat{p}_{\mathrm{num}}$ the pilot estimation

num the current pilot number

S_{RMS} the root mean square value of the signal in the time domain

$V_{\mathrm{out}}^{\mathrm{thr}}$ the threshold output voltage value of a power amplifier

$V_{\text{in}}^{\text{thr}}$ the threshold input voltage value of a power amplifier

V_{avg} the average voltage value of the linear response region of a power amplifier

V_{peak} the peak voltage value of the linear response region of a power amplifier

R_m^{impr} the improved received R_m values

$E_m^{\text{max\_est}}$ the maximum value of the estimated E_m^{est} array

$f_{\text{diff\_}m}^{\text{est}}$ a set of possible $f_{\text{diff}}^{\text{est}}$ estimations

Y the number of bits

A_s the amplitude of the signal

E_m^{NBI} the NBI error component in the frequency domain

E_m^{AWGN} the AWGN error component in the frequency domain

E_m^{Total} the total error in the frequency domain

δ_m^{AWGN} the AWGN's error fraction in the NBI error

P_s the power value of the signal

P_{NBI} the power value of the NBI

Contents

List of Figures

List of Tables

Chapter 1

Introduction

In 2000 there were approximately 0.7 billion wirelessly connected devices [3]; by the beginning of 2023 this number had risen to more than 8 billion [4]. All these wireless connections allow people everywhere to stay in touch, but there are many other applications—like remote surgical procedures, aircraft flight control and nuclear systems—that have potentially life-threatening impacts, environmental harm or severe damage to property, and which we must classify as safety-critical.

The carrier frequencies of these safety-critical systems and their associated devices have been increasing over time, making them increasingly susceptible to ElectroMagnetic Disturbances (EMDs). This is compounded by the reduced operating voltages of microprocessors and the increased levels of noise in the environment. For these reasons, we must ensure that Autonomous Systems (ASs) are immune to external interference so that we can guarantee a person's safety. The single largest factor to consider is the ElectroMagnetic (EM) environment in which the AS has to operate. In other words, for an AS to obtain the necessary trust from the persons who interact with it, the system must have ensured resilience against EMDs. However, to be able to improve the resiliency and dependability of ASs in the presence of EMDs we must first determine the weak points in the ASs that are the most susceptible to EMDs.

The research described in this thesis is designed to identify these weak spots and research techniques to improve the dependability (being reliable in terms of wireless communication and, thus trusted by people) of wireless communication protocols that are capable of receiving and transmitting information in a noisy environment. The work involves creating such an EM environment in which wireless communication protocols can be exposed to very harsh EMDs so as to

locate the weak spots and then eliminate them by nullifying the impact of the EM environment.

1.1 Wireless communication in ASs

The results in this Section were already published in [5], which includes a literature review of wireless communication protocols for ASs.

An AS is an independently digitised electromechanical system that is capable of learning, adapting and reacting to an environment. Although ASs have demonstrated their abilities to perform routine tasks as well as carry out risky procedures, they have not yet demonstrated their trust credentials. There have been many improvements in the safety of ASs, but they are not flawless, people still get injured and this undermines the public's trust in such systems [6].

ASs will soon see widespread deployment, taking over important tasks in sectors such as:

- Automotive;

- Marine;

- Aerial;

- Agricultural;

- Medical.

ASs will be complex in terms of wireless communication. They will connect with each other as well as with non-AS objects and systems. This wireless communication must first be reliable, with the user's convenience being a secondary consideration. In the automotive sector, for example, there is a division between safety and non-safety applications, which can be realised using Vehicle-to-Everything (V2X) communications to share information about obstacles, pedestrians, up-coming manoeuvres, etc. In the agricultural sector, M2M or tractor platooning, allows a group of tractors to move simultaneously in formation. Table 1.1 lists the various wireless-communication protocols together with the functions and latencies the protocols will provide in the ASs.

From Table 1.1, one may notice that for the agricultural sector, 6LoWPAN operating over the IEEE 802.15.4 networks can also be used. 6LoWPAN allows utilising low-power radio communication with relatively low data rates. This can be predominantly used for sensor communication within an Agricultural

Table 1.1: Summary table of wireless-communication protocols of ASs in various sectors

Sector	Parameters		
	Communication protocol	Designated functions	Maximum allowed latency,[a] ms
Automotive	IEEE 802.11p/ITS G5; 4G/5G	Active road-safety applications	<100 (<50 ms for a pre-crash sensing warning)[7]
		Cooperative traffic efficiency	< 200 [7]
		Infotainment	< 500 [7]
Marine	IEEE 802.11p/ITS G5; 4G/5G; HAP; satellite systems [8]	Connection with a remote shore-control centre	N/A[b]
		Remote sensing	N/A
Aerial	IEEE 802.11p/ITS G5; 4G/5G	Aeroplanes (urban taxis and long-distance aeroplanes) [9]	N/A
		Unmanned Aerial Vehicles (UAVs)	N/A
Agricultural	4G/5G	Cloud connection	< 1000
	IEEE 802.11p/ITS G5; 4G/5G; IEEE 802.15.4 (6LoWPAN)	Machine-to-Machine (M2M) (platooning while ploughing and sowing, "Shepherd and herd" communication)	< 100 [10]
Medical	IEEE 802.11b/g/n	System-information exchange for fault diagnosis and updates; making incisions and suturing	< 50 [11]

[a] stipulates the maximum allowed latency for the field or designated function and not for the algorithm.
[b] N/A — not available.

Vehicle (AgV) or between AgVs. In most cases, the latency requirements are not stringent (< 100 ms, see Table 1.1), as a result, one may keep the sensors

in a sleeping mode or even turn them for a while. A more detailed overview of the wireless connectivity of AgVs is given in Chapter 5.

However, the agricultural sector as well as others will perform operations that are safety-related. As a result, the dominant protocols are high throughput 4G/5G and Wi-Fi-based IEEE 802.11. Despite being safety- or non-safety-related, most of the protocols in Table 1.1 share one particular technique. This technique is called Orthogonal Frequency Division Multiplexing (OFDM).

1.2 OFDM
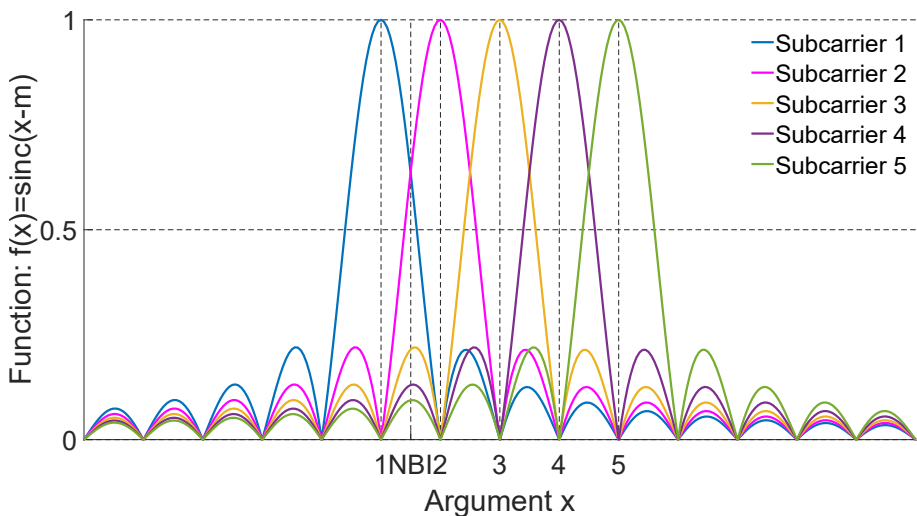
Figure 1.1: An example of orthogonality in OFDM.

OFDM has already proved its efficiency [12]. The multicarrier system and support of different modulation schemes allow for achieving higher throughputs. Due to the orthogonality property, OFDM introduces better bandwidth usage. This property also solves the problem of InterCarrier Interference (ICI). Fig. 1.1 shows the spectrum of an OFDM system. For simplicity, only five OFDM subcarriers are shown. The subcarriers are represented as sinusoids shifted from each other by a subcarrier width. Since no windowing is implemented, the Fast Fourier Transform (FFT) acts as a rectangular window over the input sinusoidal data. Consequently, the resulting frequency spectrum has sinc features (see the vertical axis represented as $f(x) = \text{sinc}(x - m)$, where x is the argument and m

is the current subcarrier number). Nevertheless, the subcarriers are distanced from each other in such a way that the FFT always has an integer number of periods of any subcarrier. Therefore, when any subcarrier reaches its maximum value, the others have a value of zero.

OFDM also introduces a Cyclic Prefix (CP) that boosts the OFDM's performance in multipath-fading environments [12]. Figure 1.2 shows the CP's realisation in an OFDM symbol. This involves appending a number of samples from the tail of an OFDM frame. In this way, OFDM starts having a guard interval at the beginning of its symbol. This prevents aliasing from the delayed copies of the previous symbol.
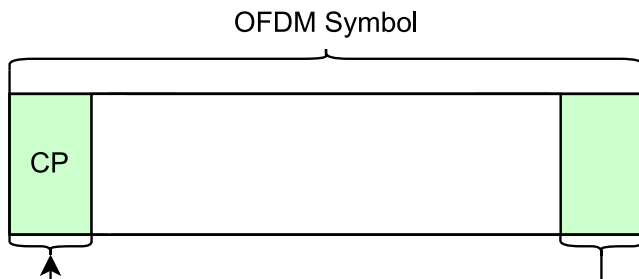
Figure 1.2: CP representation in an OFDM symbol.

OFDM also has disadvantages. One of them is a large Peak-to-Average Power Ratio (PAPR) that limits the efficiency of a system's power amplifier and, as a result, sets higher requirements for it. Let us turn to Fig. 1.3, which shows a power amplifier's transfer function that models the system's output voltage for a given input voltage. The amplifier has two regions that are split by a vertical dashed line at the threshold input voltage ($V_{\text{in}}^{\text{thr}}$): a linear and a non-linear one. To provide a constant output value, the amplifier has to deliver a linear amplification of a signal (the threshold output value is $V_{\text{out}}^{\text{thr}}$) whenever the power of the signal changes. Therefore, the most effective range for regulating the power is the linear region. When the power amplifier is not properly set for potential OFDM high peaks, the latter can cause the amplifier to work in the non-linear region. Operating in the non-linear region not only reduces the efficiency, but can lead to distortion of the signal. In addition, a higher PAPR demands a higher resolution for the Analog-to-Digital (A/D) converter, which leads to extra complexity on the receiver side.

The other disadvantage of OFDM-based systems is their vulnerability to EMD, in particular to NarrowBand Interference (NBI), which is a type of EMD that introduces an interference over a narrow frequency range. NBIs can be
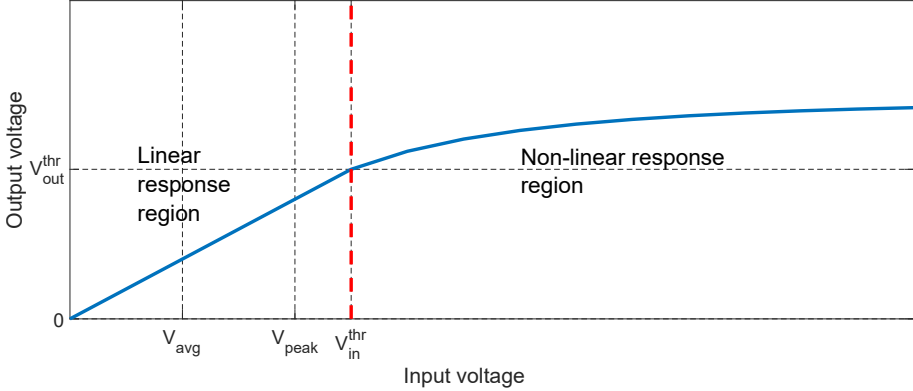
Figure 1.3: Power-amplifier transfer function.

intentional and unintentional. The former can be freely bought [13] and used for useful purposes (signal jamming during state exams) or malicious ones. Unintentional NBIs can happen due to different protocols working in the same frequency bands, hence their frequencies overlap. This thesis focuses on NBIs in general and considers an NBI frequency range to be limited to the OFDM's subcarrier width. The particular case of an NBI considered here is a Continuous Wave (CW) EMD.

If we insert an NBI with the same power level as the signal, i.e., the Signal-to-Interference Ratio (SIR) is equal to 0 dB, exactly between the first and second subcarriers (see Fig. 1.4), the red curve representing the NBI breaks the orthogonality, i.e., at the moment when the subcarrier is at its maximum value with all the other subcarrier values being zero (as in Fig. 1.1). This happens because the periods of the NBI are not aligned with the signal's sinusoids (NBI$_{pos}$ standing for the spectral position of the NBI is not equal to any integer subcarrier m). As a result, the power from the disturbance affects all the subcarriers, especially those that are spectrally close to it, i.e., subcarriers 1 and 2 in Fig. 1.4. This is known as spectral leakage.

1.3 Spectral leakage

Spectral leakage occurs when a non-integer number of signal periods undergo the Fourier transform and, as a result, the non-coherently sampled signal is truncated. This causes the signal's energy to leak to frequency components
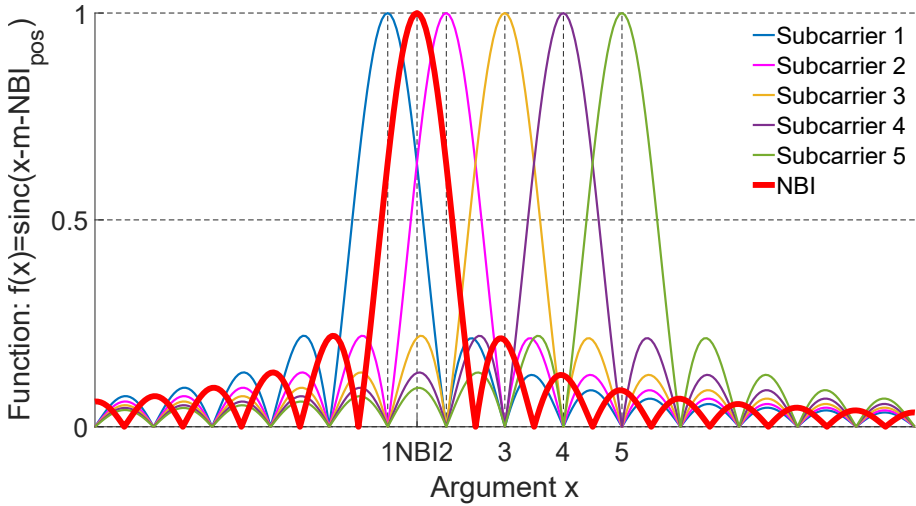
Figure 1.4: An example of orthogonality breakdown when an NBI is injected into an OFDM system.

that do not exist in the original signal. In OFDM systems, spectral leakage occurs on the receiver's side as part of the Fourier transform. Figure 1.5 shows a simplified version of an OFDM communication system, the transmitter, the receiver and a transmission channel in between, to which an NBI is added.
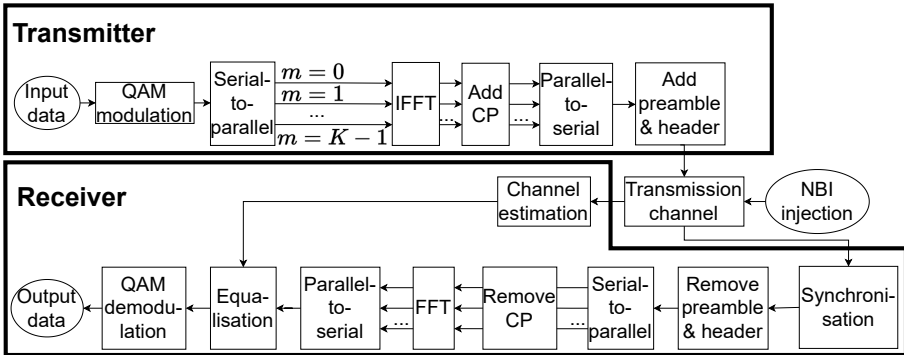
Figure 1.5: A simplified OFDM communication system.

The input binary data are subjected to digital modulation. There is a variety

of digital modulation schemes, however, the one used in Fig. 1.5 depicts the most commonly used scheme for data modulation - Quadrature Amplitude Modulation (QAM). For the presented case, QAM uses two digital bit streams, otherwise two analog signals are used. Using the amplitude shift keying, the amplitude of two carrier waves is changed. At the same time, these carriers have identical frequencies which are out of phase by 90°. This introduces the orthogonality property that is also called quadrature, hence, the name - QAM. The QAM output has, therefore, two components: in-phase and quadrature which are represented in Fig. 1.6. This figure presents a constellation diagram for the case when four bits represent one QAM symbol. Hence, the name is QAM16. The number of bits in one QAM symbol represents the modulation order. As a rule of thumb, the lower the modulation order of the QAM digital modulation, the harsher, in terms of noise, the environment in which the communication system is used.

After the digital modulation block, data are parallelised to be fed into the Inverse Fourier Transform (IFFT). It allows converting the data from the frequency domain to the time domain using the inverse Fourier transform. Then, the last bits of the IFFT output are taken and pre-pended, therefore, CP addition happens. To be able to transmit the signal using a single antenna, the signal is converted back to a serial version and the preamble along with the header are pre-pended. Both the preamble and the header serve for synchronisation purposes. Their composition differs depending on the application and synchronisation method. For example, the header may contain the rate information or the number of symbols, while the preamble can be split in training sequences allowing to detect the beginning of an OFDM frame and perform both time and frequency synchronisation.

Going back to Fig. 1.5, after the preamble and header block the signal leaves the transmitter and enters the transmission channel in which an NBI is present. The receiver processes the captured signal from the transmission channel by estimating it for subsequent equalisation. Normally, it happens by comparing the already known sequence that is transmitted in the preamble part with the one obtained at the receiver's side. By taking a ratio between the received and transmitted known sequences, one may estimate the channel and, consequently adjust it. Then, synchronisation happens. The essence of it is to identify the start of the signal as well as correct its frequency and phase offsets. The remaining operations of the receiver are the opposite of those performed at the transmitter side: removing the preamble, header and CP, performing an FFT and demodulating the resulting data. More details about the OFDM frame transmission and the mathematical operations involved can be found in Chapter 2, whereas the details of the OFDM frame composition, equalisation and synchronisation are in Chapter 4.
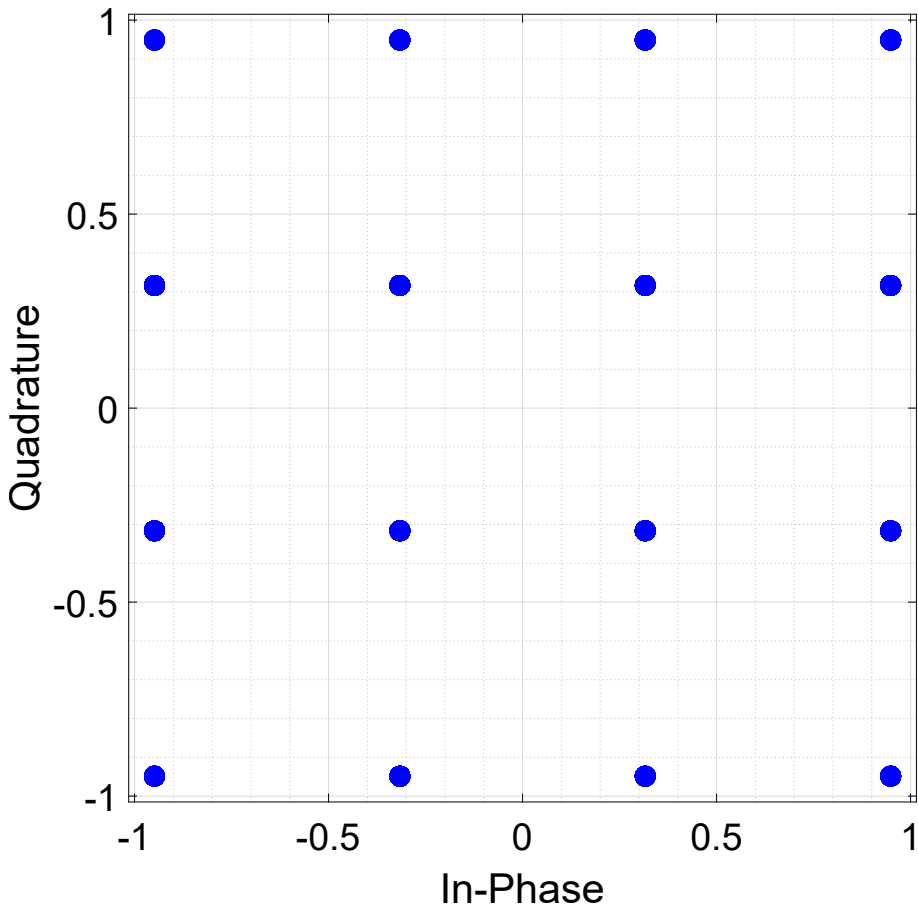
Figure 1.6: QAM16 constellation.

When an NBI is added to the transmission channel, a non-spectral leakage case can occur. Figure 1.7a highlights this case and has the NBI shown as blue crosses, and the original data shown as orange circles. Of the 64 OFDM subcarriers only one is disturbed by an NBI. This happens when the disturbance frequency coincides with one of the signal's subcarrier frequencies. In this case, the NBI can be treated as a burst disturbance (the disturbance having its power confined within one subcarrier) that can be further negated by implementing coding techniques, e.g., row-column interleaving [14].
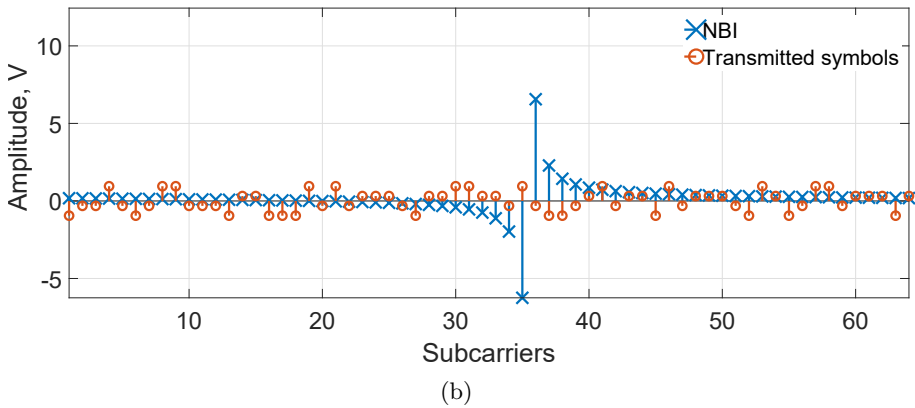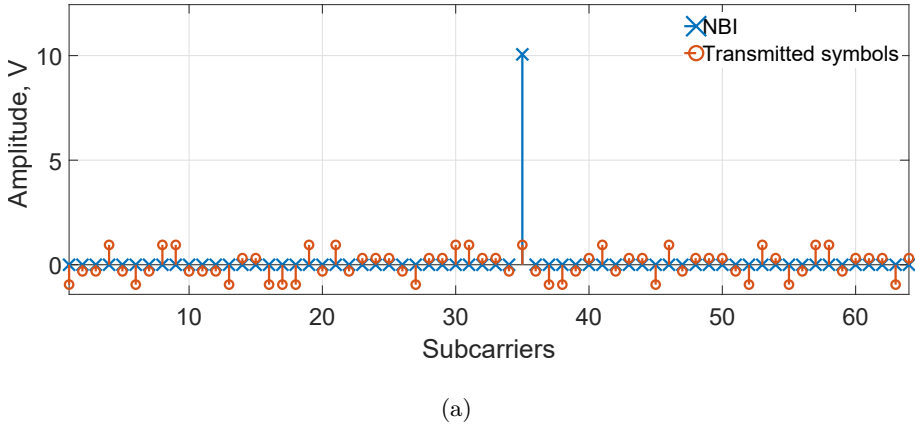
Figure 1.7: The non-spectral leakage (a) and spectral leakage (b) cases after FFT when an NBI is injected into the transmission channel. Only real spectra values are shown.

Figure 1.7b shows the opposite case to that in Fig. 1.7a when spectral leakage occurs between two subcarriers and has the maximum detrimental effect. Due to the truncation during the Fourier transform of the non-coherently sampled signal, the NBI's energy leaks to adjacent subcarriers, spreading almost uniformly to the left- and right-hand sides from the peak values. Such an equal distribution of energy across the subcarriers can only happen when the NBI frequency is within the bandwidth of the signal and its value is equal to any subcarrier plus half of the subcarrier spacing. In other words, the disturbance happens between any two adjacent subcarriers.
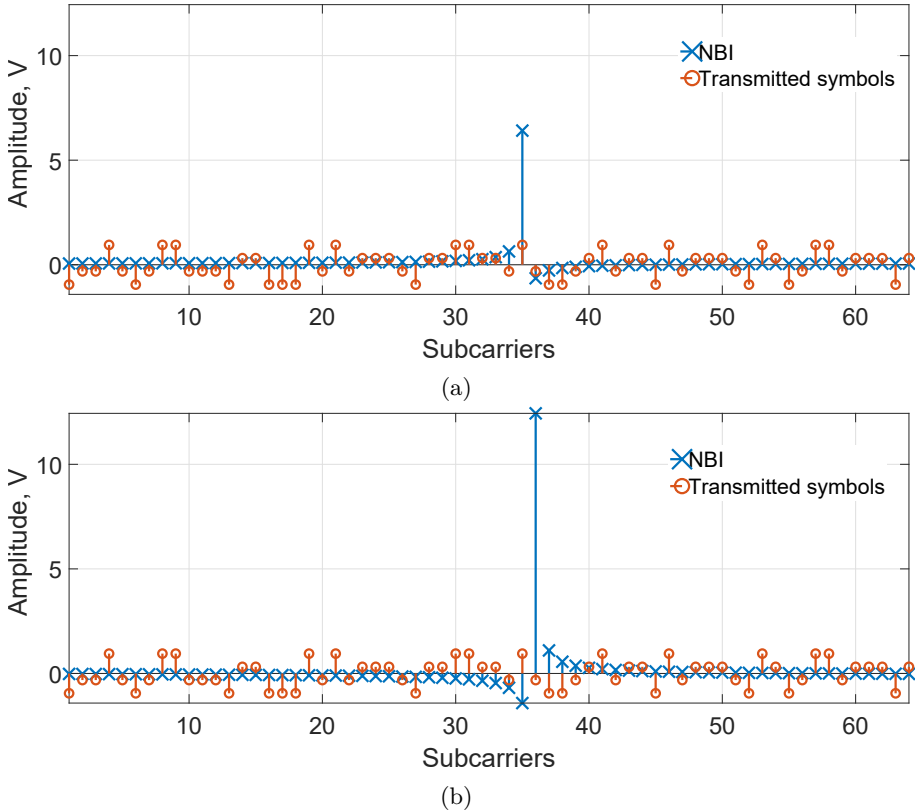
Figure 1.8: A non-coherent sampling of an OFDM signal when an NBI is injected into the transmission volume when the disturbance has the following relative subcarrier frequency: (a) 35.1, (b) 35.9.

The examples in Figs. 1.7a and 1.7b are very special cases of the spectral leakage phenomenon. Statistically, it is unlikely that an NBI will either coincide in frequency with any of the subcarriers or happen to be right in between two subcarriers. Consequently, the examples in Figs. 1.7a and 1.7b have only a slim chance of happening. In most cases the non-coherent sampling and, therefore, the spectral leakage case will prevail and, depending on the relative spectral distance between an NBI and the subcarriers that surround this disturbance, the energy of the spectral leakage can be greater for the subcarriers that lie to the left or right of the NBI. For example, if we assume that a disturbance happens between the 35th and 36th subcarriers, then when the disturbance has a 35.1 relative subcarrier frequency (as shown in Fig. 1.8a) the NBI's energy

will be more concentrated on subcarrier 35. The opposite case is shown in Fig. 1.8b, where the NBI has a relative subcarrier frequency of 35.9. In this case subcarrier 36 is the one most affected by the disturbance.

We know that both non-coherent and coherent sampling can occur in an OFDM system when an NBI is present in the transmission volume eventually leading to different disturbance energy distribution after the Fourier transform. However, the coherent case has a coding solution, whereas the non-coherent case resulting in spectral leakage requires further investigation.

1.4 Overview of the thesis

The thesis is titled "Making connectivity work reliably in harsh electromagnetic environments. Narrowband interference removal algorithms for OFDM-based communication". Harsh environments are those that can disrupt wireless communication in safety-critical ASs.

The research work focused on wireless-communication protocols to improve the robustness of the transmission and reception of information in harsh EM environments.

Future wireless-communication protocols in ASs will use OFDM technology, which is affected by NBIs or CW EMDs by introducing spectral leakage on the receiver side due to the Fourier transform of the non-coherently sampled signal. To address the vulnerability, techniques must be developed and added to the wireless-communication protocols to increase their resilience to harsh NBIs, after which their performance should be validated. Better dependability was achieved by creating a "harsher than real-life" EM environment so as to be sure that the ASs will remain as safe as possible, even in such EM conditions, to improve safety and prevent loss of life.

The thesis has six more chapters that are organised as follows:

1. Chapter 2: "Mod-remod" NBI removal algorithm. The chapter introduces an algorithm to remove the NBIs from OFDM-based systems. The algorithm is based on spectral leakage of the received signal and works with the pattern obtained by Fourier transform of the non-coherently sampled incoming OFDM signal. Once the pattern of the spectral leakage is identified, the NBI's parameters (phase, frequency and amplitude) are calculated, the disturbance is recreated and subtracted from the received signal. The coherent sampling (non-spectral leakage case) is addressed by implementing the Hamming coding technique and interleaving. The

algorithm is a mathematical model to be used in simulations. This model was simulated using a wide range of NBI phase values and its power, i.e., SIR. The performance of the algorithm was evaluated at relative positions of the NBI for the contiguous subcarriers. To make the simulations more realistic, the algorithm's performance in the presence of both NBI and white noise, modelled as Additive White Gaussian Noise (AWGN), was evaluated. Different modulation schemes and subcarrier numbers were also tested, based on which recommendations were made for optimal performance of the algorithm. The simulation results showed that the algorithm's gain (the difference between the simulation result without the algorithm and with it) was more than 80 dB for some simulation cases.

2. Chapter 3: "Differential" NBI removal algorithm. After working with the "Mod-remod" NBI removal algorithm, an additional mathematical model for removing the NBIs in OFDM-based wireless communication systems was derived. Instead of the total received data spectrum, as was the case in the "Mod-remod" algorithm, the "Differential" algorithm focuses on a few subcarriers that are most influenced by an NBI. Assuming that the NBI's power is greater than that of the white noise, the latter's component in the signal can be neglected. The "Differential" algorithm is also based on the spectral leakage pattern identified using a limited number of subcarriers. These subcarriers should have a sign change and asymptotically decrease in amplitude from a probable NBI's position. Since there can be multiple NBIs disturbing the signal at the same time, an iterative improvement technique is implemented, based on updating the NBI parameters during each step until the required accuracy or number of iteration steps is achieved. Once the NBIs' parameters are identified, the original noisy data symbols can be subtracted. As with Chapter 2, this chapter contains an extensive simulation showing the performance of the "Differential" NBI-removal algorithm versus different NBI configurations (power, phase, frequency, the relative disposition between the adjacent subcarriers), and AWGN powers (Signal-to-Noise Ratio (SNR)). The algorithm was also tested with multiple NBIs, different modulation schemes and subcarrier numbers. The simulation results showed that the "Differential" algorithm is able to improve the system's Bit Error Rate (BER) results by up to 49 % in some cases. The BER results for the SNR values higher than or equal to 20 dB do not exceed 1.3 %. Finally, the chapter provides a comparison between the "Differential", "Mod-remod" and the "Pande" [1] NBI removal solutions resulting in the "Differential" solution performing the best despite having built-in redundancy.

3. Chapter 4: Algorithm validation. Once the "Mod-remod" and "Differential" NBI-removal algorithms were tested in simulations, they were validated

in the laboratory. During the validation, the OFDM model was extended using [2]. To be able to distinguish the captured OFDM frame, synchronisation was investigated and an alternative timing-synchronisation method was proposed. Conventional synchronisation methods were not employed since the injection of an NBI would break the auto-correlation pattern of the preamble-based synchronisation algorithms. Other observations, e.g., hardware limitations due to the built-in Automatic Gain Control (AGC) are also covered. Finally, the simulated algorithms in the laboratory are validated. The algorithm's gains during the validation measurements reached 18.4 dB and 32.78 dB for the "Mod-remod" and "Differential" NBI removal algorithms, respectively.

4. Chapter 5: Wireless connectivity in the agricultural sector. This chapter investigates wireless-connectivity problems faced by the agricultural sector in terms of improvements to vehicles. For example, replacing wired sensors with wireless ones formed in a Wireless Sensor Network (WSN). Since an AgV has many metallic components, sensors could find it difficult to operate in this semi-reverberant environment. This chapter investigates the implementation of two different WSNs, testing their limits in a Reverberation Chamber (RC) and then comparing the results on a combine harvester. Recommendations are made for the use of WSNs in the agricultural sector as well as recreating an agricultural EM environment in the laboratory.

5. Chapter 6: Valorisation plan. This chapter presents valorisation of the solutions to improve wireless communications. Two NBI-removal algorithms were chosen for Software-As-A-Service (SAAS) in the automotive sector. This idea was assessed for competitors and customers. A strategy for entry into the market and capturing a share is proposed using a business model and an estimated cash flow.

6. Chapter 7: Conclusion. This chapter summarises the findings and observations. The main outcomes are presented. Finally, future research directions are outlined and final thoughts about the topic are given.

1.5   Conclusion

This introductory chapter provided an overview of ASs and the associated wireless-communication protocols. The technique used in these protocols is OFDM (an introduction to which is shown in the chapter), which is vulnerable to NBIs due to spectral leakage after the FFT block on the receiver side. This is the basis for the algorithms investigated in this thesis. The chapter then

outlined the goal and expected outcomes, followed by an introduction to each
of the subsequent chapters.

Chapter 2

"Mod-remod" NBI removal algorithm

The content and results of this Section have already been disseminated in [15] and [16]. In these publications, several counter-measures to mitigate the effects of a NarrowBand Interference (NBI) in Orthogonal Frequency Division Multiplexing (OFDM)-based systems were provided. In [15], the "Mod-remod" NBI removal algorithm was presented for the first time, while [16] extended the analysis of the performance of the "Mod-remod" algorithm to include the combined effect of an NBI and Additive White Gaussian Noise (AWGN).

2.1 Common ways of tackling NBIs in OFDM-based systems

The influence of NBIs on wireless communication systems is certainly not a new concern and has already been the focus of many researchers. These researchers have tried to solve this challenge. For example, in [17], the authors analysed a Long Term Evolution (LTE) system for future vehicle applications. They investigated its susceptibility to different types of ElectroMagnetic Disturbance (EMD), including NBI. They concluded that an NBI has the strongest influence on LTE systems when the disturbance occurs between two adjacent subcarriers. In [18], the authors investigated the influence of NBI on OFDM systems in general. The authors conducted a number of simulations corrupting an OFDM signal with an NBI at different frequencies between two adjacent subcarriers.

The results confirmed the findings achieved in [17] and showed that for an equal amount of power, an NBI degrades the performance of OFDM much more than, e.g., a broadband AWGN. In [19], the authors showed that 5G New Radio (5G NR) did not consider that an NBI's impact heavily depends on the disturbance's exact frequency position.

A conventional way of tackling not only NBIs but noise, in general, is with the help of coding techniques. For example, the authors in [20] and [21] conducted research on OFDM receivers that use Turbo codes. By assuming an NBI to have a power distribution similar to the one of Gaussian noise, the authors propose the weighted Log-Likelihood Ratio (LLR) [20] for turbo decoders at the receiver's side (but not limited to them) to reduce the NBI influence. [21] presents the modified version of the weighted LLR and also improves the performance of OFDM-based systems in the presence of NBIs. However, both aforementioned solutions presented in [20] and [21] assume an NBI to happen exactly on a subcarrier that is not always the case. Moreover, one may need to estimate the NBI Signal-to-Interference Ratio (SIR) in advance to make adjustments to the upper-bound limit of the proposed LLR calculation.

A different approach in which not only the receiver but also the transmitter underwent changes was proposed in [22]. The main contribution is to implement the Distance Preserving Mapping (DPM) coding technique in systems with convolutional codes to generate a codeword with certain spectrum specifications (spectral null codewords) and correction capabilities. The DPM technique contains spectral null code blocks that help to recognise and locate an NBI. After that, the look-up table technique based on the minimum Hamming distance between the corrupted codeword and any element of the mapper code is used to reduce the influence of the NBI. Due to the limited error correction capability of the look-up table technique the Viterbi decoder algorithm is used. However, the authors mentioned that the Viterbi algorithm is vulnerable to disturbances resulting in burst errors, and an NBI is one of these disturbances. Moreover, the NBI model is presented as a single OFDM subcarrier which after the Fast Fourier Transform (FFT) block results in one extra pulse, thus the spectral leakage phenomenon is not considered.

The already mentioned work [19] also showed that Low-Density Parity Check (LDPC) codes are vulnerable to NBIs. The authors showed the performance of LDPC for different relative spectral positions α of an NBI towards an adjacent subcarrier. Simulations showed that for a single Continuous Wave (CW) (a particular case of an NBI) bit errors start appearing at E_b/N_I ratio of 30 dB, whereas for AWGN LDPC shows no errors until the E_b/N_I ratio of 7 dB. With this, the authors showed the gravity of the NBI problem in OFDM-based systems and showed the lack of effectiveness of LDPC codes in the presence of NBIs. The other coding technique, Turbo coding, also showed its lack of

performance in the presence of impulsive noise [23]. The impulsive noise is the noise appearing in the channel in the form of short duration and, ideally, infinite amplitude pulse. Thus, an NBI having a large power can be assumed to act as an impulsive noise. In both [19] and [23], the decoder faces issues identifying the interference power during the decoding process. As a result, coding techniques are not further considered as a solution against NBIs.

At KU Leuven M-group, possible moving or standstill scenarios in rural and highway or urban environments were evaluated. Based on these scenarios and environments, the key parameters that should be considered in a simulation are formulated and two simulation methods for single and multiple NBIs were proposed [24]. For validation, in [24], a real-life test method in a Reverberation Chamber (RC) was proposed.

The authors of [19] rely on the impulsive behaviour (high amplitude spikes at certain frequencies) of an NBI and propose using limiters with adaptive thresholds. If only one NBI affects the signal, then impulsive behaviour is more pronounced in the frequency domain where two limiters are used. The first limiter is set for the largest envelope value of all constellation points of the chosen modulation scheme. Therefore, any NBI exceeding this threshold will be successfully filtered. The second filter is used for NBI values lower than the threshold of the first filter. This filter works on the soft information output from the demodulation block at the OFDM's receiver. When multiple NBIs affect the signal, their impulsive behaviour can be easily tracked in the time rather than in the frequency domain. Consequently, the limiter is set up for the maximum envelope of the OFDM's data signal. Though the idea with limiters and the consequent results in [19] improve the system's dependability against NBIs, the implementation is not optimal because it is not apparent how the system should distinguish a single NBI from multiple NBIs.

The aforementioned works ([17] — [19]) and others analysed during the literature review, showed that the NBI removal techniques can be formally split into three categories: frequency, time and mixed domain solutions.

2.1.1 Frequency domain-based NBI removal techniques

The frequency domain techniques are presented in this subsection. The patent [25] proposes an adapting spur cancellation block after the Discrete Fourier Transform (DFT) block at the receiver's side. This block can estimate the amplitude and phase of an NBI, recreate it and then subtract it from the DFT output vector. To expedite the estimation speed, the method only works with the largest absolute values to define a weighting pattern since an NBI affects, at the most, only a few subcarriers. The proposed method performs best when

an OFDM system contains pilot symbols. The invention [25] claims to cancel NBIs from an OFDM frame. Nevertheless, it has the disadvantage that it uses the assumption that the NBI's frequency is known. In [26], a single-tone NBI suppression technique is investigated. The proposed algorithm is based on the spectrum of the disturbance. Similar to the technique of [25], the single-tone NBI suppression technique [26] estimates the disturbance, reconstructs it and subtracts it from the signal. However, it is designed for a single NBI, whereas in reality, multiple simultaneous NBIs are possible. The authors in [27] propose an NBI cancellation algorithm. This algorithm identifies potential NBIs by exploiting a sliding moving average window. By this, the spectral leakage of different NBIs happening within the same frequency bandwidth as the signal is minimised. The authors assume that the disturbance frequency is known in advance. If it is not the case, they suggest using the interpolation method described in [28]. This interpolation in its turn is based on prior NBI Power Spectral Density (PSD). The authors of [29] propose interleaving and nulling the power exceeding a certain threshold in the frequencies disturbed by NBI. However, with nulling, the useful signal may also be nulled and, therefore, lost. The works [30], [31], use a cancellation algorithm in which the NBI frequency is either known in advance or is estimated using interpolation [28] that in its turn is based on a known power spectral density.

2.1.2   Time domain-based NBI removal techniques

The time domain solutions are the following. In [32], the author wants to circumvent the effect of the spectral leakage of an NBI and proposes to implement a notch filter in the time domain. However, the filter requires a so-called "signal-free training period" during which the phase-locked-loops can estimate the interferer carrier frequencies. Then, there is a series of works [33], [34], [35] dedicated to Nyquist windowing solutions. Nyquist windowing helps to reduce side lobes and preserve orthogonality. For that, it needs a repetitive pattern for every symbol. Therefore, a part of the guard interval or Cyclic Prefix (CP) is used. This part varies depending on the ElectroMagnetic (EM) environment. Therefore, the Nyquist windowing solution cannot guarantee stable performance.

2.1.3   A combination of time and frequency domain-based NBI removal techniques

A. Gomaa and N. Al-Dhahir [36] propose a combination in both the time and frequency domains. They worked on a compressive sensing technique that uses the sparsity of an NBI for vector reconstruction in the frequency

domain. The guard sequences were substituted for better performance by zero-padding. The compressive sensing technique was further implemented for multiple input multiple output OFDM systems containing multiple NBIs [37]. Then the work was furthermore extended to deal with independent and unknown frequency-selective fading channels [38]. Albeit the techniques based on compressive sensing do not require any prior information about an NBI, they are quite complex and require perfect knowledge of the desired channel for the projection matrices. The authors in [1] propose a method in which the InterCarrier Interference (ICI) is artificially introduced in the time domain for the NBI parameters' estimation. Then the NBI is erased, the signal is backshifted to negate the introduced ICI. For better performance, windowing is performed in the time domain. Nevertheless, the described method implies the NBI frequency to be accurately estimated which is the main bottleneck when dealing with this type of EMD. In [39], the peak-search method is proposed to cancel the influence of multiple NBIs in the frequency domain. The NBI estimation is done iteratively. First, the zero padding interpolation happens in the time domain to more accurately track the spectral position of an NBI. Then, a coarse frequency estimation that implements the peak-search scheme in the frequency domain is performed. Second, a fine frequency estimation is obtained by implementing the modified weighted phase average algorithm. Although the proposed NBI solution [39] performs better than [40] and [26], it is not optimised. Whenever the received spectrum is checked for remaining NBIs, an average power throughout subcarriers is taken. This might decrease the sensitivity of the solution to NBIs having high SIR values but still causing symbol flips. In addition, the solution [39] implements both zero-padding and iterative approaches that slow down processing.

The authors in [41] propose a multiple NBI estimation based on the chirp Z-transform in the frequency domain. An adaptive notch filter was implemented in the time domain. It allows distinguishing multiple NBIs from each other and removing them one by one during multiple iterations. The algorithm also has refinement steps that help to achieve the highest NBI accuracy. Although the proposed system filters out multiple NBIs having small frequency distances between each other, the computational complexity of using multiple order notch filters is not estimated. Moreover, as with every filter, the usage of notch filters not only filters an NBI but also filters a part of the useful signal.

The provided examples either require prior NBI information or entail high complexity and computational costs. Therefore, a new approach had to be worked out. Taking into account that the data rate (and so the symbol rate Bd) in modern OFDM systems is high, one may assume that the presence of an NBI within a single OFDM frame remains constant. This assumption is primarily motivated by the understanding that the harsh EM environment encountered

during an OFDM frame is likely to mainly consist of a few or a single CW EMD. However, it is important to note that this assumption is only applicable within a short time window of a single OFDM frame, otherwise, external factors such as time, space, particular events and scenarios influence the behaviour/origin of the CW EMD. The "Mod-remod" algorithm proposed in this chapter exploits this assumption and does not require any additional filters or prior information about the disturbance. The algorithm was tested in the presence of CW EMDs and white noise. However, as was mentioned before, a CW is a particular case of an NBI. Therefore, for less confusion the term NBI is used. Let us, first, start with a description of the "Mod-remod algorithm".

2.2 Description of the algorithm

2.2.1 OFDM frame transmission

For better comprehension of this section, a basic OFDM communication system is shown in Fig. 2.1. It represents the transmitter and the receiver of the communication system under consideration. Note that some blocks of this system are deliberately omitted to simplify the following explanation. Binary input data are modulated using a Quadrature Amplitude Modulation (QAM) or Phase-Shift Keying (PSK) modulator and represented as the complex number $S_m = I_m + jQ_m$, where m represents the subcarrier number. K symbols are used as an input to the Inverse Discrete Fourier Transform (IDFT) having a size of K samples in time as an output.

Each nth sample after the IDFT block can be written as:

$$x_n = \frac{1}{K} \sum_{m=0}^{K-1} (I_m + jQ_m)e^{j2\pi mn/K} = a_n + jb_n, \qquad (2.1)$$

where x_n is the current OFDM sample.

The system is assumed to be fully synchronised in both the time and frequency domain. CPs and pilot symbols are not implemented since we do not consider multipath fading effects. The OFDM samples x_n are then mixed to the passband carrier frequency f_c, as shown in (2.2), and transmitted.

$$s_n = a_n \cos(2\pi f_c \frac{n}{B_\mathrm{d}}) + b_n \sin(2\pi f_c \frac{n}{B_\mathrm{d}}), \qquad (2.2)$$

where the $\frac{n}{B_\mathrm{d}}$ expression represents time sample n with regard to the system's baud rate B_d.
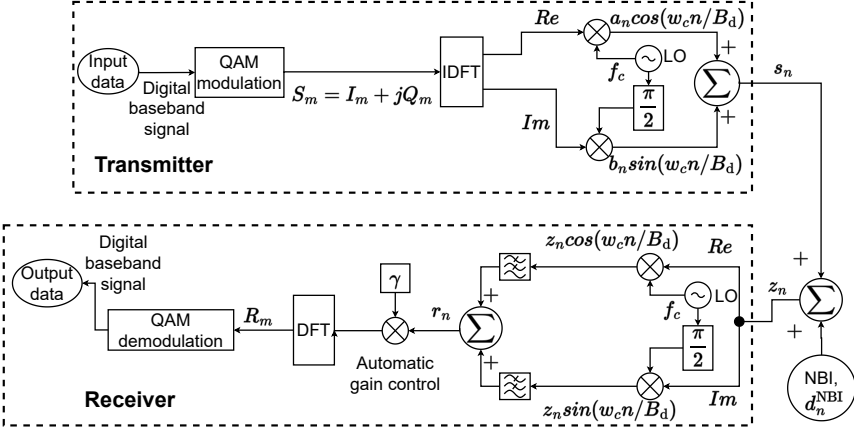
Figure 2.1: OFDM communication system.

During the transmission, the NBI, defined in (2.3) as d_n^{NBI}, is added to the time-domain OFDM signal s_n, resulting in the received time-domain signal z_n as defined in (2.4):

$$d_n^{\text{NBI}} = A_{\text{NBI}} \cos(2\pi f_{\text{NBI}} \frac{n}{B_{\text{d}}} + \theta_{\text{NBI}}). \tag{2.3}$$

$$z_n = s_n + d_n^{\text{NBI}}. \tag{2.4}$$

In (2.3), A_{NBI} denotes the NBI amplitude, θ_{NBI} and f_{NBI} represent the phase and NBI frequency, respectively. Let f_{diff} be the difference between f_c and f_{NBI}, so that $f_{\text{diff}} = f_{\text{NBI}} - f_c$. Then f_{diff} can be split into the sum of two parameters:

$$f_{\text{diff}} = (p + \alpha)H, \tag{2.5}$$

where H is the subcarrier spacing defined as $\frac{B_{\text{d}}}{K}$. The symbol p is an integer number, such that $p \in [-K/2; K/2 - 2]$. Note that K should be even. The parameter α defines the position of an NBI between the two subcarriers p and $p + 1$ (see Fig. 2.2a) and is within the range $[0 : 1[$. Note that when $\alpha = 0$, the NBI is located exactly on the subcarrier and only one subcarrier is affected by the NBI (coherent sampling happens, see Fig. 2.2b). All the other α values result in spectral leakage (non-coherent sampling which after passing through the Fourier transform results in NBI power leakage) and add an error value to all subcarriers (shown in Fig. 2.2a). The algorithm presented in this chapter exploits this phenomenon for OFDM communication. It also broadens the work
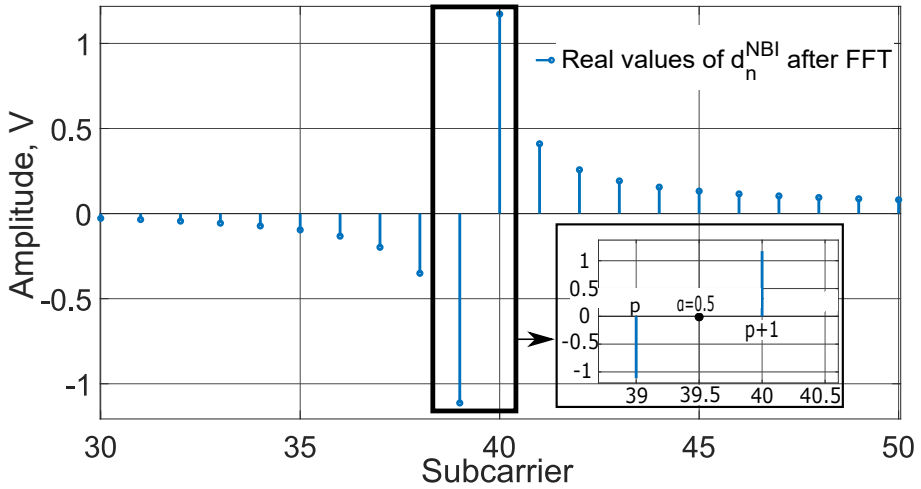
(a)
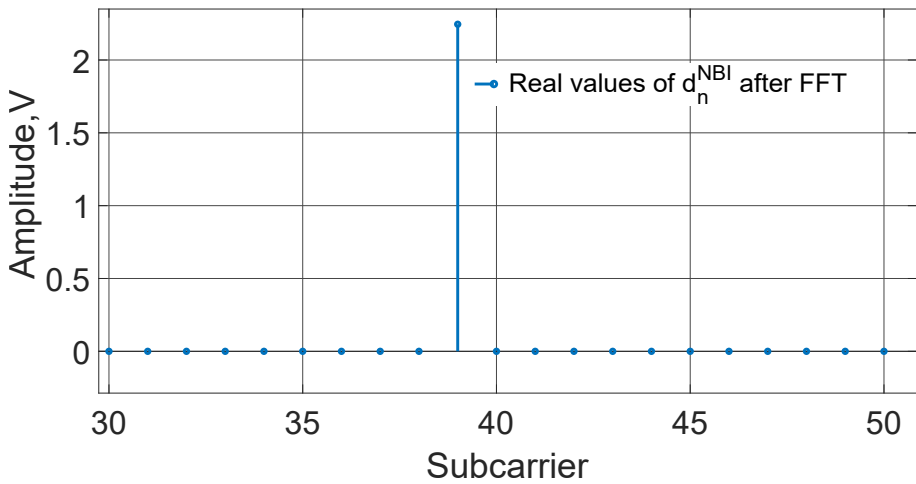
(b)

Figure 2.2: Real values of NBI after DFT at the 39th subcarrier. In both figures, the amplitude and phase of the interference stay the same. The position of the NBI with relation to the subcarriers p and $p+1$ surrounding it: (a) $\alpha = 0.5$ (b) $\alpha = 0$.

presented in [42] and [43], where the spectral leakage phenomenon was exploited to analyse the signal measured in time-domain near-field scanning.

At the receiver, samples are converted back to the baseband frequency as:

$$r_n = z_n \cos(2\pi f_c \frac{n}{B_\mathrm{d}}) + j z_n \sin(2\pi f_c \frac{n}{B_\mathrm{d}}). \tag{2.6}$$

After filtering out the high frequency components (higher than f_c), the received baseband signal becomes:

$$
\begin{aligned}
r_n = & \frac{a_n}{2} + j\frac{b_n}{2} \\
& + \frac{A_\mathrm{NBI}}{2} \left(\cos(\omega_c \frac{n}{B_\mathrm{d}} - \omega_\mathrm{NBI} \frac{n}{B_\mathrm{d}} - \theta_\mathrm{NBI}) + j\sin(\omega_c \frac{n}{B_\mathrm{d}} - \omega_\mathrm{NBI} \frac{n}{B_\mathrm{d}} - \theta_\mathrm{NBI}) \right) \\
= & \frac{a_n}{2} + j\frac{b_n}{2} + \frac{A_\mathrm{NBI}}{2} \left(\cos(2\pi f_\mathrm{diff} \frac{n}{B_\mathrm{d}} + \theta_\mathrm{NBI}) - jsin(2\pi f_\mathrm{diff} \frac{n}{B_\mathrm{d}} + \theta_\mathrm{NBI}) \right),
\end{aligned}
\tag{2.7}
$$

where ω_NBI and ω_c are angular frequencies of the NBI and carrier.

The received K samples are then transformed back to the frequency domain using a DFT with ideal automatic gain control to remove the division by two, as shown in (2.8):

$$R_m = \sum_{n=0}^{K-1} \gamma r_n e^{-j2\pi mn/K}, \tag{2.8}$$

where R_m is the received OFDM symbol, γ is an amplification coefficient due to a built-in Automatic Gain Control (AGC) and m is a subcarrier.

2.2.2 Extracting an NBI from an OFDM frame

The received samples after the DFT block derived with (2.8) can be represented as the sum of two components: the symbol component S_m and the NBI component E_m as shown in (2.9):

$$R_m = S_m + E_m. \tag{2.9}$$

Depending on the NBI power, the symbols after QAM demodulation can either be erroneous or correct. If they are correct, the QAM demodulation is not affected by the NBI component E_m and maps the received symbols back to the original symbols S_m. However, from a certain power level on, the NBI component introduces symbol flips, resulting in erroneous demodulation. In

that case, communication is impaired. Fig. 2.3 illustrates this, where the Quadrature Phase-Shift Keying (QPSK)-modulated symbols were disturbed with an NBI. The SIR was equal to 2 dB. The dashed black line subdivides Fig. 2.3 into four quadrants with four QPSK-modulated symbols (blue circles), shown for reference. The demodulation results in the correct symbols if a disturbed QPSK symbol (red circle) does not leave the reference signal's quadrant. If not, as it is in the bottom-right quadrant (there are two red symbols), the demodulated symbol is erroneous. The NBI component E_m is shown as the vector $\vec{E}$ with a solid line. All QPSK symbols are affected by the NBI (look at $\vec{E}_{1,2,3,4}$), yet only one symbol, namely the first, leads to a symbol flip. Let us look at the disturbed symbol. The actual distances of the first reference (sent) and disturbed (received) QPSK symbols are shown with vectors $\vec{S}_1$ and $\vec{R}_1$, respectively. The QPSK demodulator cannot identify the actual E_1 and S_1 values. Instead, it maps the received $1'$ symbol back to the QPSK symbol 4 in the bottom-right quadrant and will estimate the original vectors $\vec{S}_1$ and $\vec{E}_1$ as the new $\vec{S}_1^{\text{est}}$ and $\vec{E}_1^{\text{est}}$ vectors.
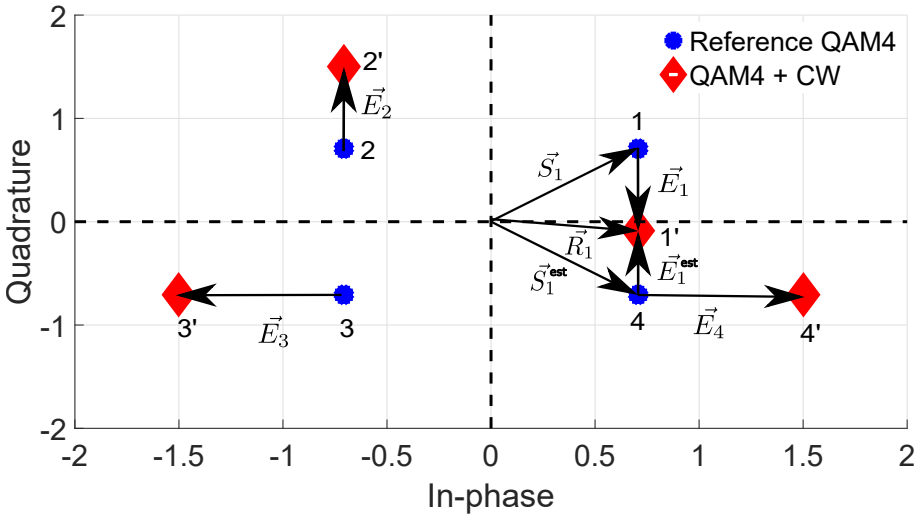
Figure 2.3: NBI influence on QPSK modulated symbols.

The NBI can be derived if one were to assume that the NBI component is small enough not to cause any symbol flip (i.e. the estimated $S_m^{\text{est}} = S_m$ and $E_m^{\text{est}} = E_m$), as shown in three out of four quadrants in Fig. 2.3. Next, applying the DFT on (2.7) and taking into account the amplification factor γ of an ideal AGC equal to two, as shown in (2.8), result in the equations (2.10) and (2.11)

for S_m and E_m, respectively.

$$S_m = 2 \sum_{n=0}^{K-1} \left((\frac{a_n}{2} + j\frac{b_n}{2}) e^{-j2\pi mn/K} \right)$$

$$= \sum_{n=0}^{K-1} \left(\frac{1}{K} \sum_{m=0}^{K-1} (I_m + jQ_m) e^{j2\pi mn/K} \right) e^{-j2\pi nm/K}$$

$$= \frac{1}{K} \sum_{n=0}^{K-1} \left(\sum_{m=0}^{K-1} (I_m + jQ_m) e^{j2\pi n(m-m)/K} \right)$$

$$= I_m + jQ_m. \tag{2.10}$$

$$E_m = A_{\text{NBI}} \sum_{n=0}^{K-1} \left(e^{-j(2\pi f_{\text{diff}} n/B_{\text{d}} + \theta_{\text{NBI}})} e^{-j2\pi mn/K} \right). \tag{2.11}$$

Note that at the receiver's side, the time domain signal was sampled. As a result, the time component t becomes $t = \frac{n}{B}$.

Taking into account (2.5), equation (2.11) becomes:

$$E_m = A_{\text{NBI}} \sum_{n=0}^{K-1} \left(e^{-j(2\pi((p+\alpha)H)n/B_{\text{d}} + \theta_{\text{NBI}})} e^{-j2\pi mn/K} \right)$$

$$= A_{\text{NBI}} e^{-j\theta_{\text{NBI}}} \sum_{n=0}^{K-1} \left(e^{-j2\pi n(p+\alpha+m)/K} \right). \tag{2.12}$$

E_m can be retrieved by subtracting the received symbol values R_m from the originally transmitted symbols S_m.

Combining (2.9) and (2.12) gives:

$$E_m = R_m - S_m = A_{\text{NBI}} e^{-j\theta_{\text{NBI}}} \sum_{n=0}^{K-1} \left(e^{-j2\pi n(p+\alpha+m)/K} \right). \tag{2.13}$$

Note that (2.13) becomes (2.14) in the special case when there is no spectral leakage ($\alpha = 0$):

$$E_m = \begin{cases} A_{\text{NBI}} e^{-j\theta_{\text{NBI}}} K & \text{if } m = -p \\ 0 & \text{if } m \neq p \end{cases}. \tag{2.14}$$
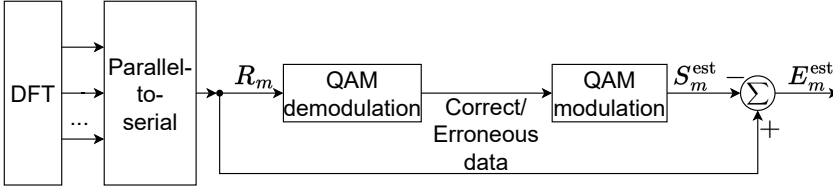
Figure 2.4: The NBI extraction procedure.

The mathematical procedures described above can be represented by Fig. 2.4. The received QAM symbols R_m after demodulation can either be correct or erroneous. By remodulating the demodulated R_m, an estimation S_m^{est} of the original S_m is obtained. This can lead to an estimation E_m^{est} of the original E_m by subtracting R_m from the remodulated symbols S_m^{est}.

If the symbols were erroneously demodulated, not all the S_m^{est} values will coincide with the initially transmitted symbol values S_m (see Fig. 2.1), and E_m^{est} will not be the actual E_m on certain subcarriers due to symbol flips.

An example of a situation for which the NBI component is large enough to cause symbol flips is shown in Fig. 2.5a and Fig. 2.5b for the real and imaginary parts, respectively. In both figures, the black line shows the error value E_m^{est}, the blue points show the received and remapped symbols S_m^{est}, while the red points show the originally transmitted symbols S_m. The black line, E_m^{est} clearly follows the spectral leakage pattern, known from [44] and also described in this work in Section 1.3, except for the subcarriers 32 to 35, where a difference and, hence, a symbol flip of S_m^{est} with regard to S_m are also visible.

2.2.3 Finding the NBI parameters

The previous subsection showed that when spectral leakage occurs ($\alpha \neq 0$), each subcarrier contains information about the NBI represented as E_m^{est} values. In this subsection, let us assume that E_m^{est} equals E_m, i.e. the power of the NBI is too low to cause any symbol flips. The parameters of the NBI can then be found by exploiting a specific relation between the first and second half of the subcarriers containing E_m. Let us show this mathematically, starting with the addition of E_m and $E_{m+\frac{K}{2}}$. Note that the integer operations on indices are ring-mapped back to the set, meaning that $m = K + 1$ maps to 1 and $m = 0$
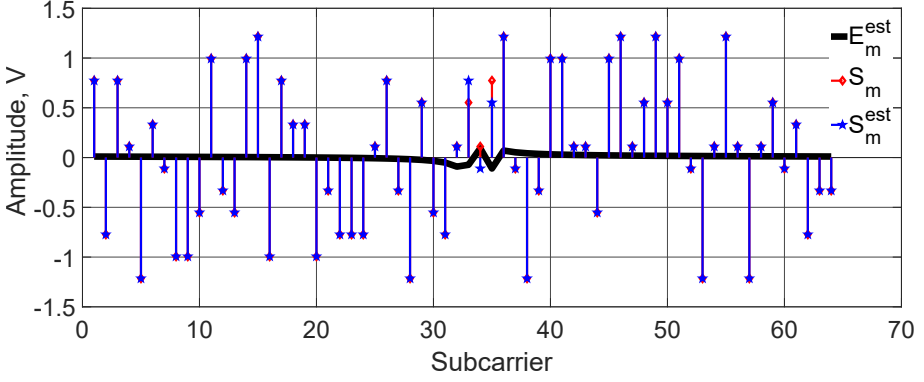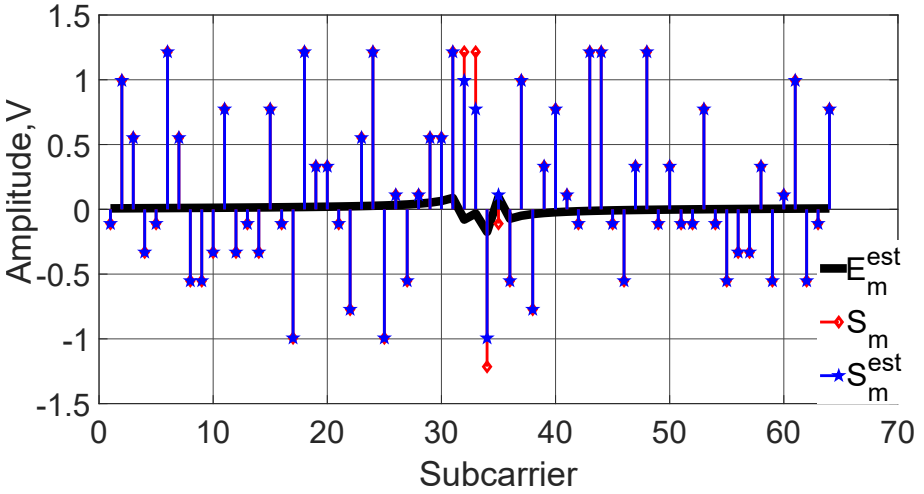
Figure 2.5: QAM128 with 64 subcarriers: (a) real part (b) imaginary part.

maps to K, i.e. modulo K calculus. First, $E_{m+\frac{K}{2}}$ will be:

$$E_{m+\frac{K}{2}} = A_{\text{NBI}} e^{-j\theta_{\text{NBI}}} \sum_{n=0}^{K-1} \left(e^{-j2\pi n(p+\alpha+m+K/2)/K} \right)$$

$$= A_{\text{NBI}} e^{-j\theta_{\text{NBI}}} \sum_{n=0}^{K-1} \left(e^{-j2\pi n(p+\alpha+m)/K} e^{-j\pi n} \right). \tag{2.15}$$

Combining (2.14) and (2.15) will result in:

$$E_m + E_{m+\frac{K}{2}} = A_{\mathrm{NBI}} e^{-j\theta_{\mathrm{NBI}}} \sum_{n=0}^{K-1} \left(e^{-j2\pi n(p+\alpha+m)/K} \right)$$

$$+ A_{\mathrm{NBI}} e^{-j\theta_{\mathrm{NBI}}} \sum_{n=0}^{K-1} \left(e^{-j2\pi n(p+\alpha+m)/K} e^{-j\pi n} \right)$$

$$= A_{\mathrm{NBI}} e^{-j\theta_{\mathrm{NBI}}} \sum_{n=0}^{K-1} \left(e^{-j2\pi n(p+\alpha+m)/K} (1 + e^{-j\pi n}) \right), \quad (2.16)$$

Keeping in mind that n is an integer, then

$$1 + e^{-j\pi n} = \begin{cases} 2 \text{ if n is even} \\ 0 \text{ if n is odd} \end{cases}.$$

By introducing $n = 2q$, the sum in (2.16) can be reduced (excluding all zeros) to a new sum:

$$E_m + E_{m+\frac{K}{2}} = 2A_{\mathrm{NBI}} e^{-j\theta_{\mathrm{NBI}}} \sum_{q=0}^{\frac{K}{2}-1} \left(e^{-j4\pi q(p+\alpha+m)/K} \right). \quad (2.17)$$

Similarly to (2.16) and (2.17), let us now take the difference between E_m and $E_{m+\frac{K}{2}}$ and conduct the same operations:

$$E_m - E_{m+\frac{K}{2}} = A_{\mathrm{NBI}} e^{-j\theta_{\mathrm{NBI}}} \sum_{n=0}^{K-1} \left(e^{-j2\pi n(p+\alpha+m)/K} (1 - e^{-j\pi n}) \right), \quad (2.18)$$

with,

$$1 - e^{-j\pi n} = \begin{cases} 2 \text{ if n is odd} \\ 0 \text{ if n is even} \end{cases}.$$

By introducing $n = 2q + 1$, the difference in (2.18) can be reduced (excluding all zeros) to:

$$E_m - E_{m+\frac{K}{2}} = 2A_{\mathrm{NBI}} e^{-j\theta_{\mathrm{NBI}}} \sum_{q=0}^{\frac{K}{2}-1} \left(e^{-j2\pi(2q+1)(p+\alpha+m)/K} \right)$$

$$= 2A_{\mathrm{NBI}} e^{-j\theta_{\mathrm{NBI}}} e^{-j2\pi(p+\alpha+m)/K} \cdot \sum_{q=0}^{\frac{K}{2}-1} \left(e^{-j4\pi q(p+\alpha+m)/K} \right).$$

$$(2.19)$$

Looking at equations (2.19) and (2.17), one may notice that they depend on each other. This dependency allows deriving the NBI frequency f_{diff}, which can be done by, first, combining expressions (2.19) and (2.17), resulting in:

$$E_m - E_{m+\frac{K}{2}} = (E_m + E_{m+\frac{K}{2}})\left(e^{-j2\pi(p+\alpha+m)/K}\right)$$

$$= (E_m + E_{m+\frac{K}{2}})\left(e^{-j2\pi f_{\text{diff}}/B_{\text{d}}}e^{-j2\pi m/K}\right). \qquad (2.20)$$

The NBI frequency f_{diff} is derived from (2.20) as:

$$f_{\text{diff}} = \frac{jB_{\text{d}}}{2\pi}ln\left(e^{-j2\pi f_{\text{diff}}/B_{\text{d}}}\right) = \frac{jB_{\text{d}}}{2\pi}ln\left(\frac{E_m - E_{m+\frac{K}{2}}}{E_m + E_{m+\frac{K}{2}}}e^{j2\pi m/K}\right). \qquad (2.21)$$

Once f_{diff} and E_m are known, the amplitude A_{NBI} and phase θ_{NBI} can also be calculated:

$$A_{\text{NBI}} = \left| \frac{E_m + E_{m+\frac{K}{2}}}{2\sum_{q=0}^{\frac{K}{2}-1} e^{-j4\pi q(f_{\text{diff}}/B_{\text{d}}+m/K)}} \right| \qquad (2.22)$$

$$\theta_{\text{NBI}} = j\ln\left(\frac{E_m + E_{m+\frac{K}{2}}}{2A_{\text{NBI}}\sum_{q=0}^{\frac{K}{2}-1} e^{-j4\pi q(f_{\text{diff}}/B_{\text{d}}+m/K)}}\right). \qquad (2.23)$$

As was shown in Figs. 2.3 and 2.5, if the NBI power is high enough, E_m^{est} is not always equal to E_m for one or more subcarriers (the subcarriers in Fig. 2.5, where S_m and S_m^{est} do not coincide). However, one may use the E_m^{est} values from the subcarriers where no symbol flip occured by the NBI (see Section 2.2.4). In this case, the estimation of f_{diff}, A_{NBI} and θ_{NBI} will be correct. It allows reconstructing NBI values, E_m, along subcarriers using (2.13). Figure 2.6 shows the real and imaginary parts of f_{diff} for the same example as in Fig. 2.5. Normally, the frequency value has to be real, however, due to symbol flips the demodulation and re-modulation procedures result in wrong symbols that were not originally transmitted. As a result, one may see negative frequencies in Fig. 2.6. Therefore, one should use the subcarriers with an imaginary part equal to zero ($m \in [5:32]$). This will result in the real f_{diff} values that can be used
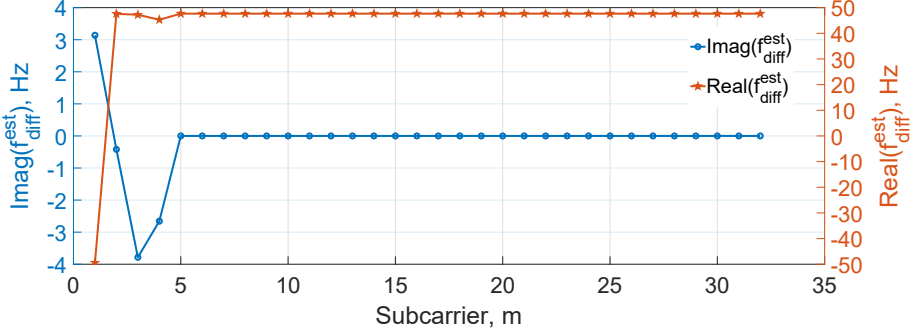
Figure 2.6: Real and imaginary estimation $f_{\text{diff}}^{\text{est}}$ values ($f_{\text{diff}} = 47.66$ Hz) for QAM128 with 64 subcarriers.

to make a correct estimation of the NBI. For $m \in [1:4]$, the imaginary part deviates from zero, thus these subcarriers cannot be used for NBI estimation, i.e. the correct f_{diff} can be found by looking for purely real-valued f_{diff}. Eventually, the subtraction of E_m^{est} from the received symbols R_m will result in the originally transmitted S_m symbols.

2.2.4 The algorithm

In this subsection, all previous subsections 2.2.1 — 2.2.3 of Section 2.2 are combined to create the complete algorithm, capable of removing the NBI influence on an OFDM frame. The work of the algorithm can be split into steps that are visualised in a flowchart in Fig. 2.7. In summary, the algorithm works as follows:

1. After QAM demodulation and re-modulation of the received symbols R_m, the error estimation E_m^{est} is calculated by taking the difference between the initially received symbols R_m and the re-modulation output S_m^{est} (eq. (2.13)).

2. The algorithm is designed so that it starts working only when the maximum NBI ($E_m^{\text{max\_est}}$) is greater than the threshold, which is half the minimum Euclidean distance ($\sqrt{(I_1 - I_2)^2 + (Q_2 - Q_1)^2}$, where I_1, I_2 and Q_1, Q_2 are the in-phase and quadrature coordinates of the two-dimensional $I - Q$ plane) between adjacent points in the $I - Q$ constellation plane of the modulation scheme (see Fig. 1.6). This threshold is chosen to be the "safe" zone within which the system is able to perform correct demodulation
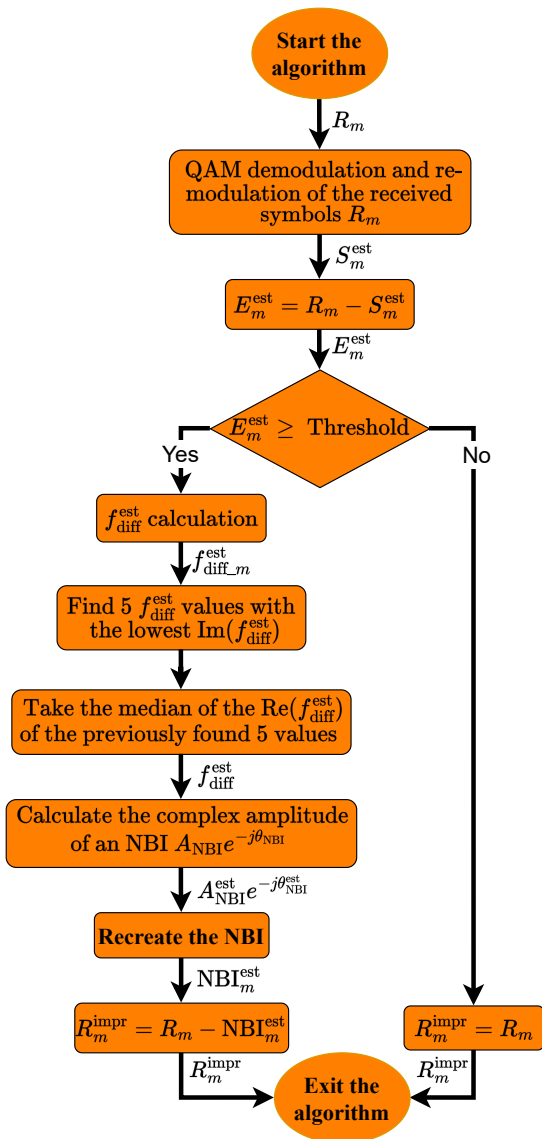
Figure 2.7: The "Mod-remod" algorithm's flowchart.

without symbol flipping. Therefore, if any of the obtained error estimation values E_m^{est} is lower than the threshold, the NBI cannot cause symbol flips

resulting in signal degradation. In this case, the improved spectrum R_m^{impr} will be equal to R_m.

On the contrary, if E_m^{est} is greater than or equal to the chosen threshold, $f_{\text{diff}}^{\text{est}}$ is calculated for $m \in [0 : K/2]$, leading to a set of possible $f_{\text{diff\_m}}^{\text{est}}$ estimations using (2.21). The complete set would be real and precisely the same if there are no symbol flips and numerical errors. However, if this is not the case, several additional steps have to be taken:

A. The frequencies $f_{\text{diff\_m}}^{\text{est}}$ with the five imaginary parts $\text{Im}(f_{\text{diff\_m}}^{\text{est}})$ closest to zero are identified since a high deviation of the $\text{Im}(f_{\text{diff\_m}}^{\text{est}})$ value from zero indicates an incorrect estimation of the f_{diff}. Five values are optimal for the subsequent median search operation since three values were not always accurate enough and seven, nine and more values were compromising the estimation at low SIR values, where more symbol flips were occurring.

B. Five $\text{Re}(f_{\text{diff\_m}}^{\text{est}})$ values are identified with the least deviant from zero $\text{Im}(f_{\text{diff\_m}}^{\text{est}})$ values. The most accurate results are achieved if a median is determined from these values, resulting in the estimation $f_{\text{diff}}^{\text{est}}$.

3. The estimation $f_{\text{diff}}^{\text{est}}$ found in the previous step is used to calculate the NBI phase and the amplitude using (2.22) and (2.23) giving $A_{\text{NBI}}^{\text{est}} e^{-j\theta_{\text{NBI}}^{\text{est}}}$.

4. The found NBI estimation $\text{NBI}_m^{\text{est}}$ is subtracted from the OFDM frame R_m after DFT resulting in the improved spectrum R_m^{impr}.

After the algorithm, R_m^{impr} is demodulated. The full workflow to estimate the NBI and remove it from the OFDM frame is shown in Fig. 2.8.
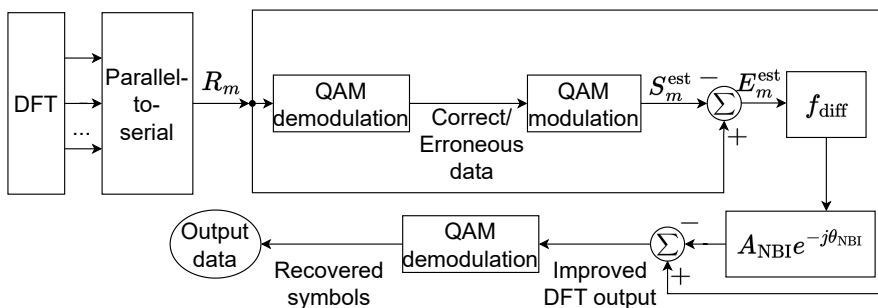
Figure 2.8: NBI cancellation block diagram.

Table 2.1: Simulation parameters for OFDM symbols

Parameter	Value
Modulation scheme	QAM(M), M= [16; 32; 64; 128; 256; 512; 1024; 2048]
Number of subcarriers, K, divided by subcarrier width	[60; 120; 240; 510; 1020; 2040]
Number of bits, Y	$log_2(M) \cdot K$
Baud rate, B_d	100
Coding technique	Hamming code(15,11)+interleaving
Subcarrier width, H	B_d/K

2.3   Evaluation of the algorithm

2.3.1   Simulation assumptions and main parameters

Before presenting the simulation parameters and results, it is necessary to state the main assumptions which were made in this work:

1. Perfect time and frequency synchronisations are assumed in the OFDM system.

2. No multipath fading during the tests resulting in no need for a CP and pilot signals.

3. Only one NBI disturbing the signal. This NBI was simulated as a CW EMD having constant amplitude and phase.

The OFDM symbols generation and the interference simulation were performed in MATLAB [45] at baseband frequencies. The OFDM symbols are constructed according to the simulation parameters shown in Table 2.2. The interference is added to the OFDM symbol according to the parameters shown in Table 2.2. For every possible EMD phase and every SIR, a new OFDM symbol is created with random input data. All results, shown in the following subsections, are averaged over all EMD phases per SIR. The simulations were performed for different cases of modulation schemes, a number of subcarriers and implementations (with and without the algorithm).

Note that no spectral leakage occurs when the NBI frequency is exactly on a subcarrier frequency ($\alpha = 0$). In this case, the algorithm cannot find the NBI.

Table 2.2: Simulation parameters for NBI

Parameter	Value
NBI phase[a](θ_{NBI}), degree (°)	[0:359]
Distance to the closest to NBI subcarrier[b] α	[0; 0.25; 0.5][c]
SIR[d] span, dB	[-70:50]
SIR step, dB	0.1
Noise amplitude[e] A_{NBI}, V	$A_{\mathrm{NBI}} = \frac{S_{\mathrm{RMS}}}{10^{\mathrm{SIR}/20}}$

[a] Per each phase θ_{NBI}, a new sequence of bits Y was generated;
[b] f_{NBI} and f_c are aligned in such a way that f_{diff} can take values between -50 Hz and 50 Hz;
[c] These values are chosen to be the most representative, other α parameters will have highly correlated results;
[d] $\mathrm{SIR} = 20\log_{10}(\frac{A_s}{A_{\mathrm{NBI}}})$, where A_s and A_{NBI} denote the amplitude of the signal and interference, respectively;
[e] S_{RMS} is the root-mean-squared value of the signal in the time domain; SIR is the current SIR value.

It can, however, introduce an error (bit flips) on the data of that subcarrier. The NBI can be treated as a burst error, against which a simple row-column interleaving is effective [14]. With the help of interleaving, one may remove the bit flips spread among subcarriers using an error-correcting technique capable of correcting at least one bit flip. The original bitstream is coded in this chapter using the Hamming(15,11) code. Coding and interleaving provide the needed result (elimination of NBI errors when $\alpha = 0$) with minimal overhead ($11/15 \approx 0.73$) and low computational cost.

2.3.2   Simulation results

With regard to the simulation parameters, the averaged (over 360 phases θ_{NBI}) Bit Error Rate (BER) was obtained for four different cases:

1. Without the algorithm and coding technique (uncoded, no algorithm);

2. Only with the Hamming coding & interleaving [46] (coded, no algorithm);

3. Only with the algorithm (uncoded, algorithm);

4. The algorithm along with the Hamming coding & interleaving (coded, algorithm).

Simulation results for QAM64 with 2040 subcarriers when $\alpha = [0; 0.25; 0.5]$ are presented in Figs. 2.9 and 2.10.
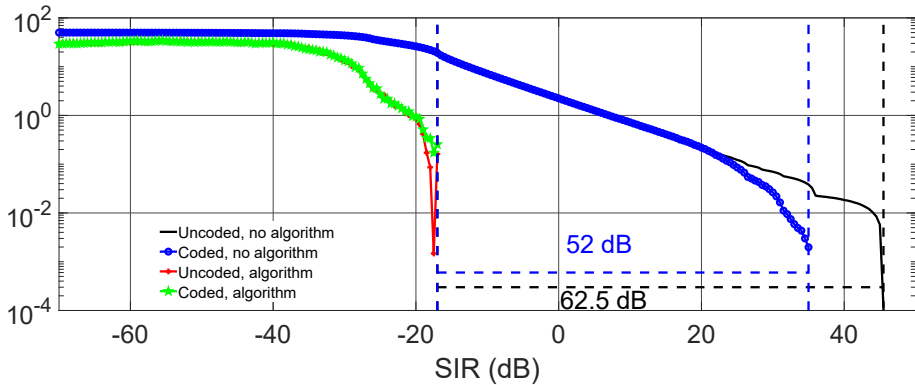
(a)
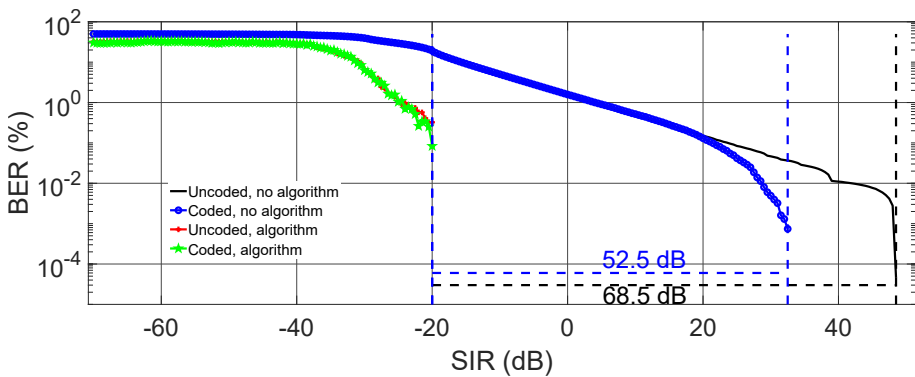
(b)

Figure 2.9: NBI removal with the Hamming coding & interleaving for an OFDM symbol with QAM64 modulation for different spectral leakage cases: (a) $\alpha = 0.5$, (b) $\alpha = 0.25$.

In Fig. 2.9a, the BER curves for $\alpha = 0.5$ are shown. The black curve shows the BER when neither the algorithm nor the error-correcting code is implemented. Note that the black curve has a sharp increase starting at an SIR level of approximately 45.5 dB. It is the point where CW EMD is just powerful enough to make one symbol error.
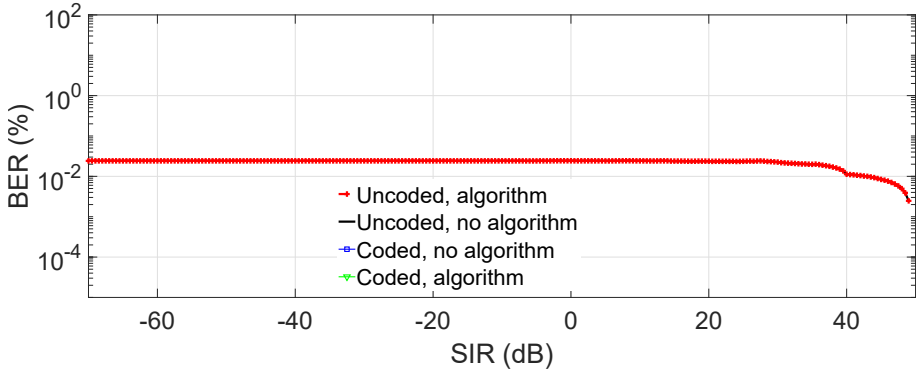
Figure 2.10: NBI removal with the Hamming coding & interleaving for an OFDM symbol with QAM64 modulation when there is no spectral leakage $\alpha = 0$.

The blue BER curve shows the case where only the error correction technique and interleaving were implemented. It shows a coding gain (the difference between the SIR levels between the message without the error correction technique along with the interleaving and the message with them) of approximately 10.5 dB. It already offers an immense benefit, mainly because the NBI disturbs symbols whose subcarriers lie close to the f_{diff} frequency. When using interleaving, the bit errors are spread over the complete OFDM frame and can, to some extent, be corrected by the Hamming coding.

Let us look at red and green curves. They represent the case when the algorithm is used on its own or combined with the Hamming coding & interleaving. One may notice that the BER curve moves considerably to the left for these curves. Figure 2.9 reflects the algorithm gain parameter. The algorithm gain is the difference between the SIR levels of the message without the error correction technique and the interleaving and the message with them and the algorithm. Figure 2.9a shows 62.5 dB or 52 dB from the blue curve, only implementing the error-correcting technique (the first points of the red and green curves coincide).

Fig. 2.9b shows the BER curves when the NBI happens at a quarter subcarrier spacing away from the nearest subcarrier ($\alpha = 0.25$). The results presented in Fig. 2.9b follow the same trend as in Fig. 2.9a with the following differences:

1. The gain of the Hamming coding & interleaving along with the NBI removal algorithm towards the Hamming coding & interleaving is 52.5 dB and towards the reference case (the black curve) is 68.5 dB;

2. The black, red, and green curves start at 48.5 dB and -20 dB (for the red and green curves), respectively.

Although the algorithm effectively works, it cannot detect and remove the error when the NBI frequency is precisely equal to the subcarrier frequency ($\alpha = 0$). However, as was mentioned in Section 2.3.1, the combination of interleaving over all subcarriers and Hamming(15,11) code solves this issue. This can be noticed in Fig. 2.10, where the red curve (only the algorithm is applied) and the black curve (nothing is implemented, reference) are exactly the same. The other two cases, when the Hamming coding & interleaving were used (green and blue curves), resulted in BER equal to zero throughout the SIR range and, hence, cannot be seen on the graph.

The algorithm's performance for different spectral leakage cases for QAM64 with 2040 subcarriers can be seen in Fig. 2.11. The black line corresponds to the algorithm gain calculated with regard to the minimal BER value for the reference case shown as the black line in Figs. 2.9 and 2.10. Similarly, the blue line is connected with the blue line in these figures. The following comparison of Fig. 2.11 with Figs. 2.9 and 2.10 shows that the obtained gains depicted in Fig. 2.9 are particular cases of Fig. 2.11. For α equal to zero the blue line of Fig. 2.11 reaches zero because the implementation of the Hamming coding & interleaving results in no errors. The gain reaches the maximum value for the black line because the reference case has no protection against burst CW EMD concentrated on one subcarrier. Without the algorithm and the Hamming coding & interleaving, the reference case has a large BER value.
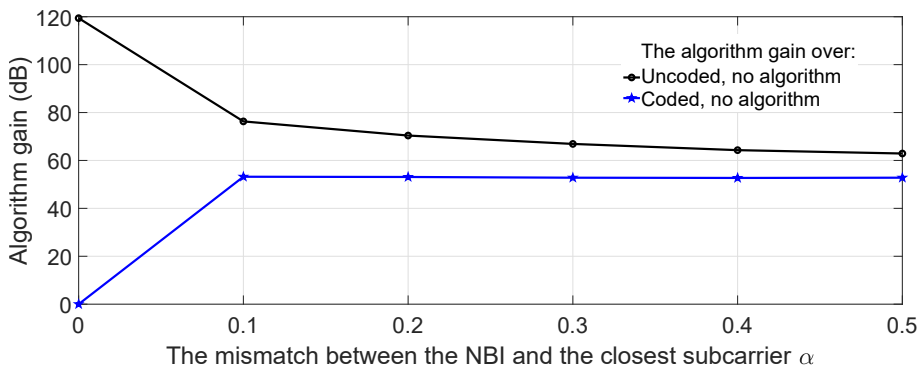
Figure 2.11: NBI removal algorithm gain against α for QAM64 with 2040 subcarriers.

The simulations were also performed for different modulation orders M and number of subcarriers K. For example, Fig. 2.12a shows the algorithm's gain
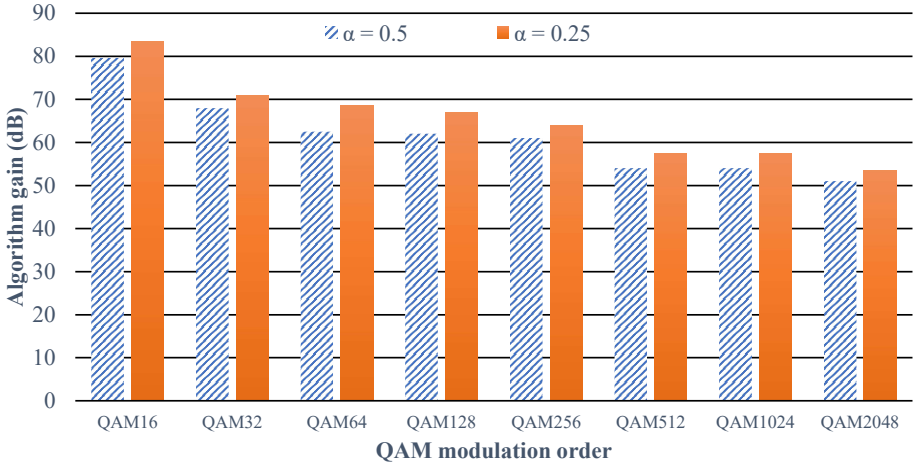
(a)
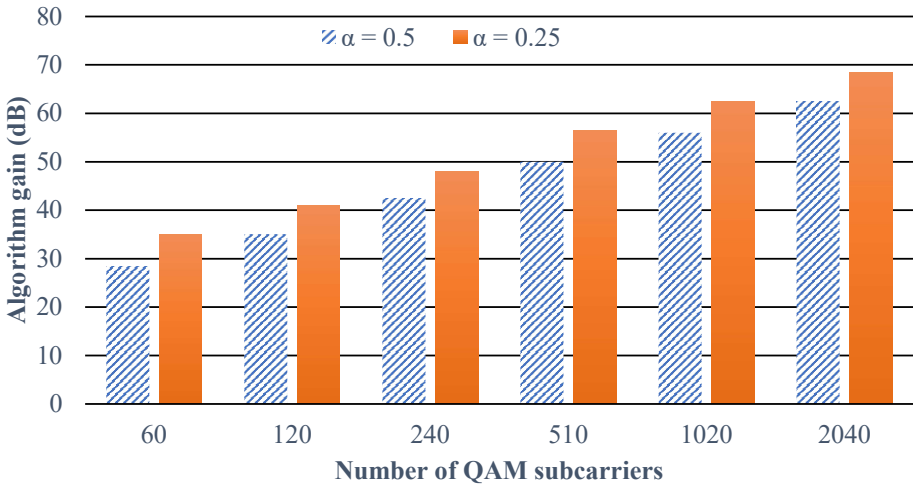
(b)

Figure 2.12: NBI removal algorithm gain results for: (a) variable QAM modulation order, (b) variable number of QAM subcarriers.

for a fixed number of subcarriers that was equal to 2040 with a variable QAM modulation order that was varied between QAM16 and QAM2048. Figure 2.12b reflects the case when the QAM modulation order was fixed to QAM64 while

the number of subcarriers varied between 60 and 2040. Figure 2.12 depicts the results for spectral leakage parameters α equal to 0.5 and 0.25.

As can be seen from Fig. 2.12a, the NBI removal algorithm's performance deteriorates somewhat (from 79.5 dB for QAM16 to 51 dB for QAM2048) with the increase of the QAM modulation order. This is due to the constant numerical noise. With the increase of the QAM modulation order M, the distance between symbols becomes smaller and the significance and influence of the numerical noise (calculation errors) become greater, thus reducing the algorithm's performance.

In Fig. 2.12b, the algorithm's gain increases when the number of subcarriers increases. It can be explained as follows: the NBI affects the same number of bits irrespective of the number of subcarriers. With the increase in the number of subcarriers, the number of subcarriers K that can be correctly demodulated with the presence of the NBI also increases. In this way, the possibility of finding the correct value of the disturbance frequency f_{diff} increases.

2.3.3 Performance evaluation under AWGN

The previous sections discussed the algorithm's performance when perfect channel conditions were assumed. A simulation using 60 subcarriers with QAM64 modulation and for $\alpha = 0.5$ was done with AWGN having a Signal-to-Noise Ratio (SNR) of 80 and 60 dB with regard to the original signal. The results for the SNR of 80 and 60 dB can be seen in Fig. 2.13a and Fig. 2.13b, respectively. When the SNR is 80 dB, the algorithm's performance, with or without the addition of Hamming error coding is as good as having no AWGN (shown in Fig. 2.13a). When the SNR is 60 dB, the algorithm appears to be heavily affected by the noise. Yet, with the addition of the Hamming coding & interleaving, the performance is still equal to the simulation case without AWGN.

To test the algorithm's limits against AWGN, extra simulations were performed for lower SNR values and different QAM schemes. Extra simulation parameters are presented in Table 2.3.

The performance of the "Mod-remod" removal algorithm for the QPSK modulation scheme with 240 subcarriers is presented in the heatmap in Fig. 2.14b. The performance is evaluated using the BER parameter. For reference, the QPSK performance without the algorithm but with the Hamming coding is shown in Fig. 2.14a. Figure 2.15 shows the performance of the algorithm for QAM16 and QAM64 modulation schemes with the number of subcarriers equal to 120 and 80, respectively. The number of transmitted bits for Figs. 2.14 and
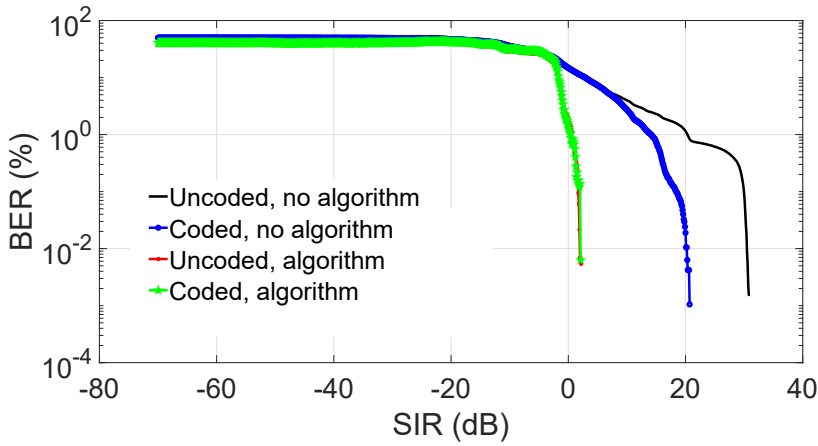
(a)
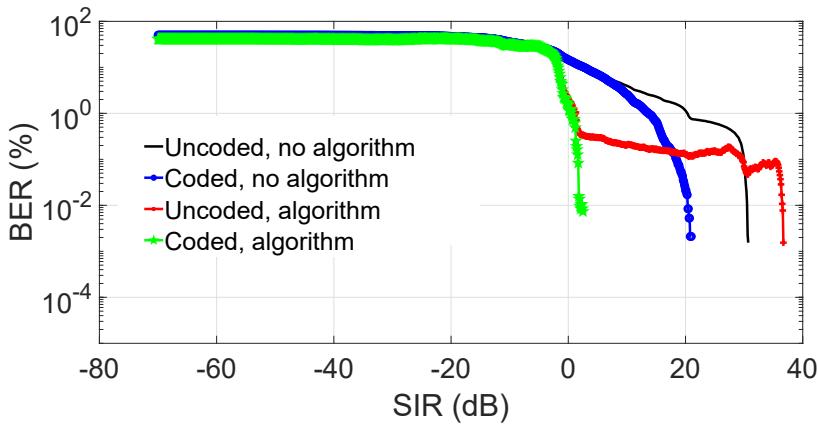
(b)

Figure 2.13: NBI removal algorithm gain against $\alpha = 0.5$ for QAM64 with 60 subcarriers and different AWGN SNR levels: (a) SNR = 80 dB, (b) SNR = 60 dB.

2.15 was the same. This allows for comparing the algorithm's performance for different modulation scheme orders to obtain the best performance. Both Figs. 2.14 and 2.15 have SIR and SNR spans that stretch from -30 dB to 50 dB and from -15 dB to 35 dB, respectively (see Table 2.3).

Using a colour palette in Figs. 2.14 and 2.15, the BER intensity is shown. The darker colours represent low BER values while brighter colours indicate larger BER values. Looking at Fig. 2.14b, one may notice that the SNR level of -15 dB makes the algorithm unable to distinguish the NBI and results in a BER of more than 48 % throughout the SIR span. For example, in [47] the noise levels for different frequency bands were much higher. In particular, for an interferer working in the Instrumental, Scientific and Medical (ISM) band of 2.4 GHz, the measured mean NBI power reached around -60 dBm. However, it was not the purpose of our simulations to test the algorithm's performance for a broad SIR span since it has already been shown above in Section 2.3.2. Going back to Fig. 2.14b and analysing the simulation results for higher, more probable SNR and SIR levels, one may notice that for the SNR value of 15 dB, the BER value does not exceed 6.95 %. For 25 and 35 dB SNR levels, the algorithm can achieve errorless performance starting from SIR higher than or equal to 30 dB, respectively.

If we compare the results in Fig. 2.14b with the ones in Fig. 2.14a, one may notice that the Hamming coding helps especially when the SNR and SIR levels are high. Therefore, the performance with the only Hamming coding (Fig. 2.14a) outperforms the algorithm's performance case (Fig. 2.14b). Nevertheless, this improvement is negligible and fades away when the SIR is lower than 0 dB. For example, throughout the whole SIR span at an SNR level of 25 dB, the algorithm has the highest BER at SIR equal to -30 dB which is around 1.4 %, while the BER varies from 0 % to around 43.9 % for the reference case.

The BER results differ for the higher modulation order schemes whose results are presented in Fig. 2.15. For example, in Fig. 2.15a the highest BER value for the highest SNR that is equal to 35 dB is 33.3 %. For QAM64, presented in Fig. 2.15b, this value is even higher and reaches 40.9 %. Both Figs. 2.15a and 2.15b contain errorless results, although they are limited to SIR levels happening at an SNR equal to 35 dB and starting from SIR higher than or equal to 30 dB

Table 2.3: Simulation parameters for extra algorithm's tests

Parameter	Value
Modulation scheme	QAM(M), M = [4; 16; 64]
Number of subcarriers	[240; 120; 80]
SIR span, dB	[-30:50]
SIR step, dB	10
SNR span, dB	[-15:35]
SNR step, dB	10
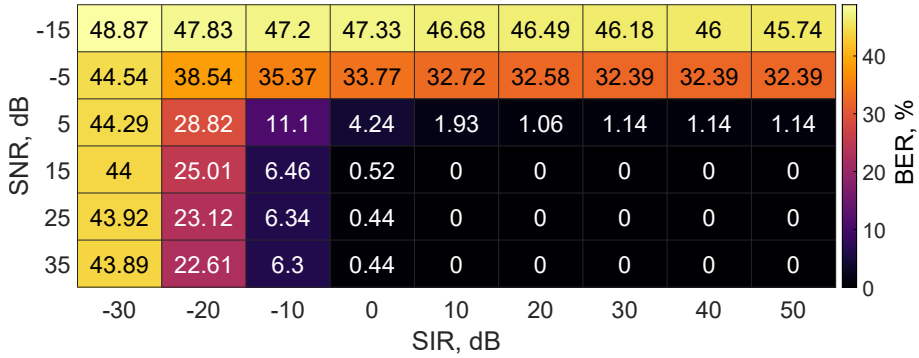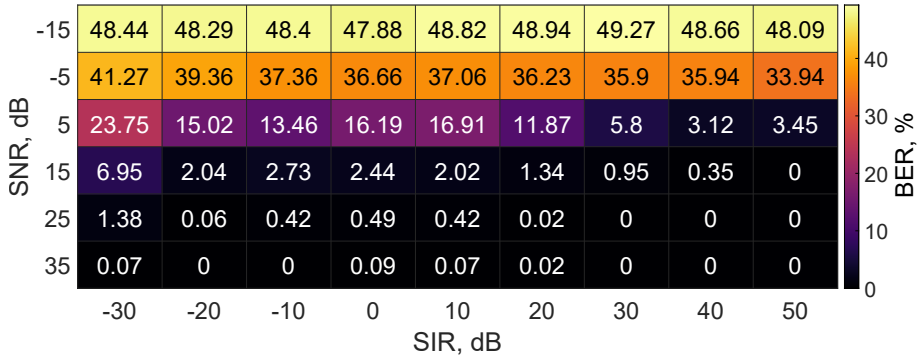
Figure 2.14: The BER performance of the "Mod-remod" algorithm under the influence of AWGN and NBI for the QPSK modulation scheme with 240 subcarriers: (a) without the algorithm, (b) with the algorithm.

and 40 dB, respectively.

The algorithm's performance can be estimated based on a certain BER threshold level. For example, for a given BER of 1 %, the OFDM system with the QPSK modulation scheme can potentially perform well, according to results, when $\text{SIR} \geq -30$ dB and $\text{SIR} \geq -20$ dB for an SNR equal to 35 and 25 dB, respectively. For QAM16 the working range decreases to $\text{SIR} \geq 20$ dB and $\text{SIR} \geq -10$ dB for an SNR equal to 35 and 25 dB, respectively. For QAM64, this range shrinks even more, the algorithm has a BER ≤ 1 % only for an SNR equal to 35 dB and 25 dB with an $\text{SIR} \geq 20$ and 30 dB, respectively. If one implements a

SNR, dB	-30	-20	-10	0	10	20	30	40	50
-15	47.53	48.17	48.76	49	46.94	46.27	45.58	44.89	44.89
-5	43.37	42.54	42.07	41.69	41.39	40.74	42.09	42.52	46.81
5	39.3	37.4	28.08	25.35	24.39	21.25	24.08	23.18	22.03
15	38.06	33.95	8.6	9.45	5.25	5.92	3.99	1.73	0.91
25	35.51	30.84	2.06	2.71	2.03	0.17	0.53	0.31	0
35	33.31	25.68	0.13	0.44	1.06	0.23	0	0	0

SIR, dB

(a)

SNR, dB	-30	-20	-10	0	10	20	30	40	50
-15	48.04	47.78	48.09	47.7	46.94	46.76	46.72	46.45	46.44
-5	45.87	45.6	44.15	43.41	42.65	44.17	44.27	43.54	43.34
5	43.15	42.99	35.6	32.23	28.61	26.5	28.62	28.03	30.51
15	41.62	41.61	30.28	21.1	15.28	12.31	10.86	10.95	15.07
25	40.93	41.45	28.81	4.68	5.29	2.95	0.77	0.48	0.42
35	40.85	40.94	27.07	2.65	1.48	0.98	0.17	0	0

SIR, dB

(b)

Figure 2.15: The BER performance of the "Mod-remod" algorithm under the influence of AWGN and NBI for different QAM modulation schemes and the number of subcarriers: (a) QAM16 with 120 subcarriers, (b) QAM64 with 80 subcarriers.

rule of thumb for telecommunications applications with an allowed BER equal to 10^{-9}, the working range of the algorithm will be even more limited. The reference cases for Fig. 2.15 are very similar and correlate with Fig. 2.14a and are, therefore, not shown.

Heatmaps presented in Fig. 2.15 clearly show better performance for lower orders modulation schemes. However, in order to explain this, a more detailed look at the frequency spectrum of the received signal has to be made.

2.3.4 The algorithm's QAM constellation and spectrum analysis

To better understand why the "Mod-remod" algorithm performs better with lower QAM schemes, let us look at the QAM constellation diagrams. Figure 2.16 depicts a QPSK constellation diagram. To not overload the figure with data, only four subcarriers are shown. The diagram presents the reference signal (blue stars) and disturbed received signals with both NBI & AWGN (red squares) and only with NBI (green triangles). The error between the reference symbol and the received one is outlined with a vector $\vec{E}$. It can be seen that the total error vector is composed of NBI and AWGN vectors, so $E^{\vec{\text{Total}}} = \vec{E}^{\text{NBI}} + \vec{E}^{\text{AWGN}}$. It can be noticed that $\vec{E_1}^{\text{AWGN}}$, $\vec{E_2}^{\text{AWGN}}$, $\vec{E_3}^{\text{AWGN}}$ do not influence the demodulation process of the received symbols. Symbol 2 is disturbed and causes a symbol flip. However, AWGN for this received symbol ($\vec{E_2}^{\text{AWGN}}$) does not affect the demodulation process. For the first and third symbols, there is no symbol flip and AWGNs $\vec{E_1}^{\text{AWGN}}$, $\vec{E_3}^{\text{AWGN}}$ do not affect the demodulation outcome. A completely different story happens with the fourth symbol where AWGN $\vec{E_4}^{\text{AWGN}}$ is high enough to displace the symbol to the other quadrant resulting in a symbol flip, wrong demodulation and potentially wrong NBI estimation by the algorithm.

Now let us look at a higher constellation order modulation. Fig. 2.17 shows a QAM64 constellation diagram. The simulation parameters for its generation are the same as for Fig. 2.16. Nevertheless, the number of subcarriers is different and set to 64. For the figure readability, received symbols disturbed by both NBI and AWGN (red squares) and by only NBI (green triangles) are presented for only 16 subcarriers. The reference QAM64 symbols are shown with blue circles for all 64 subcarriers. The black dashed circles outline the area in which a symbol can be correctly demodulated. It can be seen that, for example, for area 1 the received symbols both disturbed by NBI and AWGN are in area 1. The same cannot be noticed for area 2 where the received symbol disturbed by NBI is still inside the circle while the same symbol disturbed by NBI and AWGN is outside the circle. A similar explanation is applicable for the remaining symbols. For the higher modulation scheme order, the correct demodulation area is smaller resulting in more symbol flips due to the AWGN. This completely breaks the pattern of the NBI in the received signal making the NBI almost impossible to estimate correctly using the algorithm.

To further analyse the influence of the AWGN's error component $\vec{E}^{\text{AWGN}}$ in the total error $E^{\vec{\text{Total}}}$, let us look at the frequency spectra that can be seen on Fig. 2.18. This figure shows the absolute induced error of the received signal disturbed by NBI and AWGN per subcarrier in the frequency domain. From
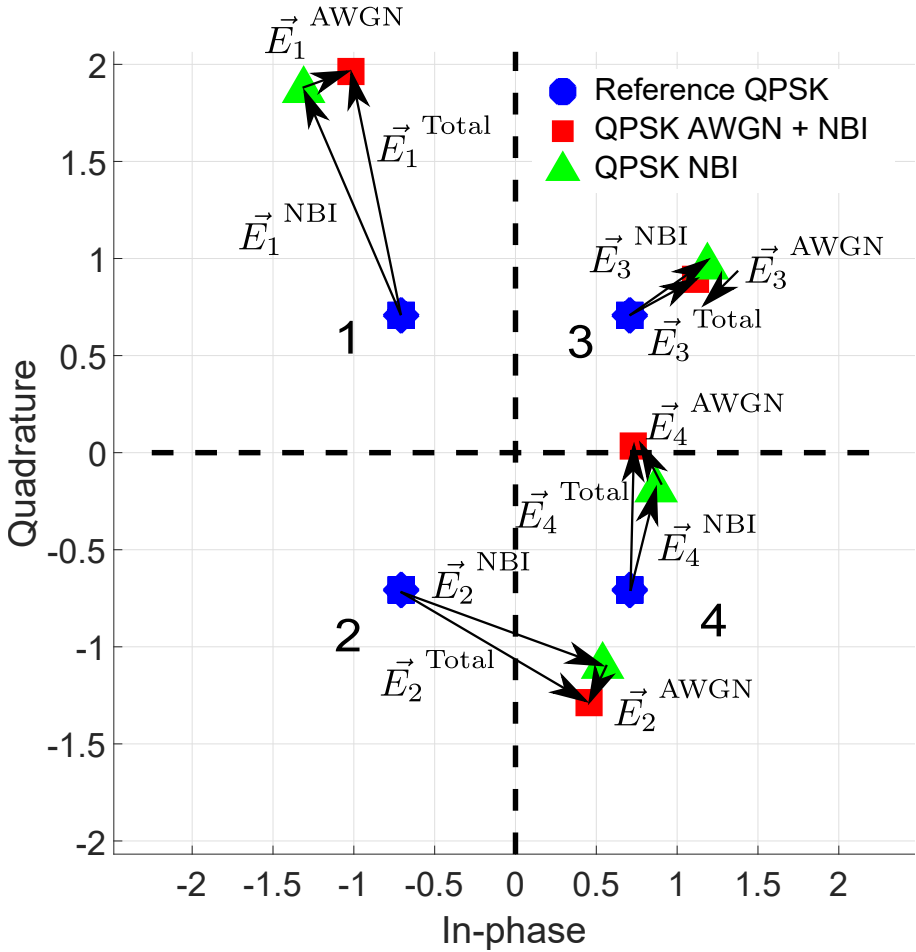
Figure 2.16: A QPSK constellation diagram with 4 subcarriers with SIR = 0 dB, SNR = 15 dB, $\Theta_{\mathrm{NBI}} = 50°$

Fig. 2.18, one may calculate the AWGN's relation towards the NBI and its influence on the total error. For this, a few mathematical equations have to be derived.

To get the AWGN's component, one may need, first, to get the total error E_m^{Total}. This can be calculated by subtracting the data in the frequency domain at the transmitter's side S_m before transmission from the received data right after the DFT block at the receiver's side R_m.
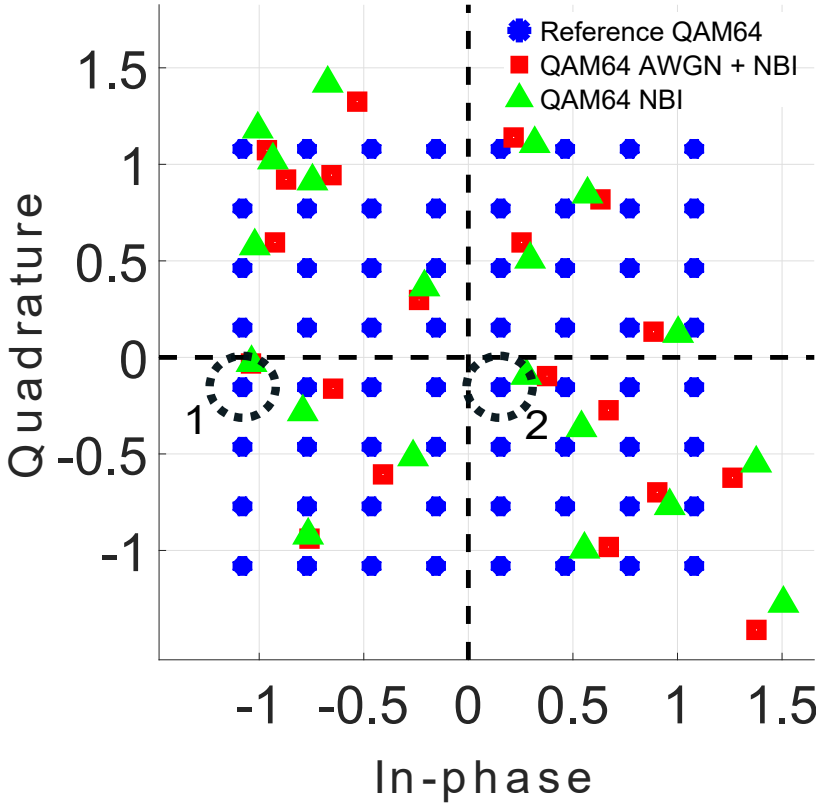
Figure 2.17: A magnified QAM64 constellation diagram with 64 subcarriers with SIR = 0 dB, SNR = 15 dB, $\Theta_{\mathrm{NBI}} = 50°$.

With the total error E_m^{Total} at hand, the AWGN component E_m^{AWGN} can be found by subtracting from the total error E_m^{Total} the generated NBI component E_m^{NBI}. Prior to that, let us transform the generated NBI component from the time domain d_n^{NBI} to the frequency domain by performing a DFT.

$$E_m^{\mathrm{NBI}} = \sum_{n=0}^{K-1} d_n^{\mathrm{NBI}} e^{-j2\pi mn/K}, \tag{2.24}$$

where n is the sample number and coincides with the subcarrier number defined earlier in (2.22) — (2.11).

Then the AWGN component E_m^{AWGN} can be obtained as:

$$E_m^{\mathrm{AWGN}} = E_m^{\mathrm{Total}} - E_m^{\mathrm{NBI}}. \tag{2.25}$$
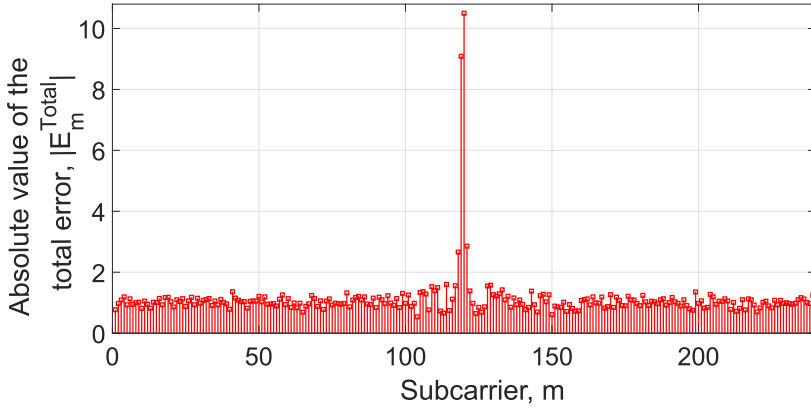
(a)
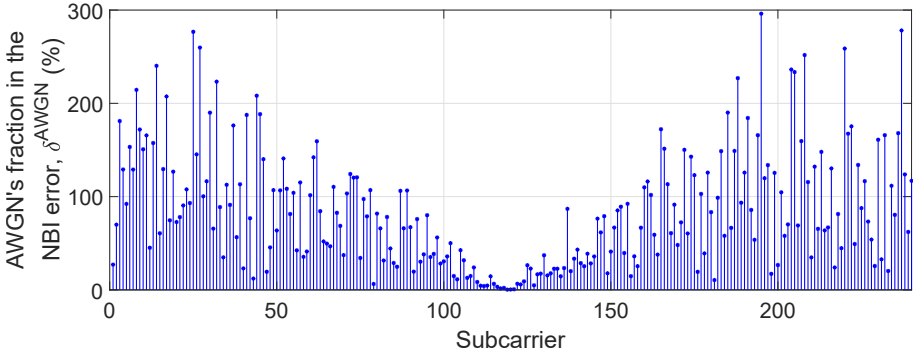
(b)

Figure 2.18: Frequency spectrum diagrams for the QPSK modulation scheme with 240 subcarriers: (a) the absolute received signal disturbed by both NBI and AWGN, (b) AWGN's error fraction $\vec{E}_m^{\text{AWGN}}$ towards the NBI error $\vec{E}_m^{\text{NBI}}$ in %.

The AWGN's error fraction in the NBI error is given by:

$$\delta_m^{\text{AWGN}} = \frac{|E_m^{\text{AWGN}}|}{|E_m^{\text{NBI}}|} \cdot 100\%. \tag{2.26}$$

$$E_m^{\text{Total}} = R_m - S_m. \tag{2.27}$$
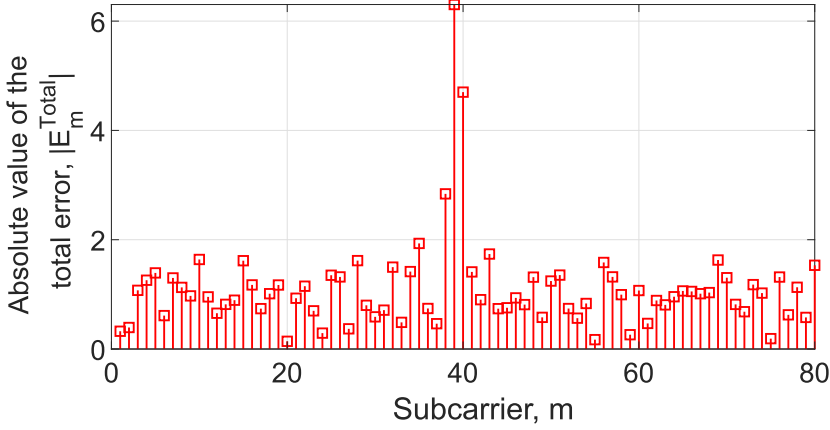
(a)
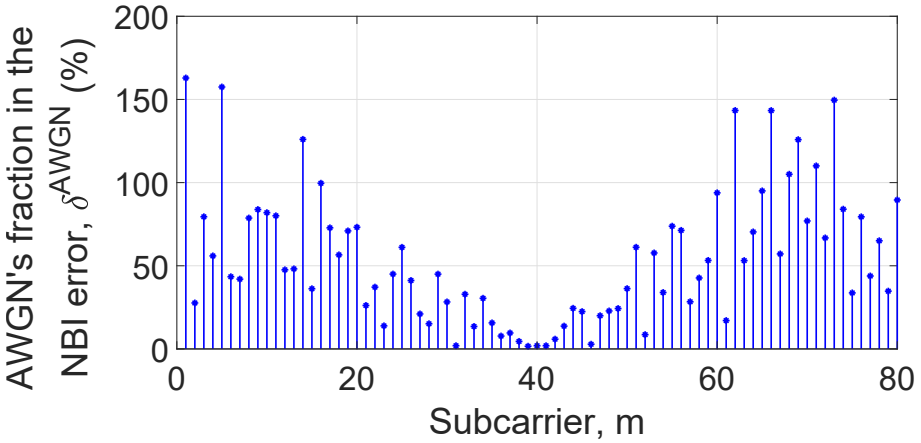
(b)

Figure 2.19: Frequency spectrum diagrams for the QAM64 modulation scheme with 80 subcarriers: (a) the absolute received signal disturbed by both NBI and AWGN, (b) AWGN's error fraction $\vec{E}_m^{\mathrm{AWGN}}$ towards the NBI error $\vec{E}_m^{\mathrm{NBI}}$ in %.

Equation (2.26) was used for making Figs. 2.18b and 2.19b. Comparing Figs. 2.18a and 2.19a with 2.18b and 2.19b one may notice a tendency: the higher the presence of the NBI in the received signal (subcarriers 119, 120 and 39, 40 for Figs. 2.18a and 2.19a), the lower the AWGN's influence on that frequency

of the signal. Hence, the AWGN's component in the total error is also lower. Due to spectral leakage, mainly the subcarriers close to the NBI's frequency are influenced the most resulting in higher NBI's error values. In contrast, the influence of AWGN on all subcarriers is equal on average. Therefore, δ_m^{AWGN} is higher on the sides and gradually decreases to minimal values in the region of subcarriers 118 — 123 and 39 — 41 in Figs. 2.18b and 2.19b. The "Mod-remod" algorithm relies on all the subcarriers and experiences higher error fluctuations due to AWGN in the regions where the NBI component is relatively low. Therefore, it is preferable to use the algorithm with lower order modulation schemes to have a bigger distance between symbols. This will decrease the probability of symbol flips and ease the error estimation and the subsequent demodulation process.

2.4   Conclusion

In this chapter, the "mod-remod" NBI removal algorithm was described. The NBI removal algorithm is compatible with PSK and QAM modulation schemes, exploits the spectral leakage phenomenon, and requires no prior information about the disturbance. The only condition required for the algorithm is that the NBI should not change within one OFDM symbol.

The algorithm was validated using a mathematical model recreated in simulations. The validation was performed for QPSK and QAM16—QAM2048 modulation schemes. The results demonstrate that by using the proposed "Mod-remod" NBI removal algorithm, one may achieve an algorithm gain that has the largest values for low modulation scheme orders with a large number of subcarriers. For example, for QAM16 with 2040 subcarriers, the algorithm's gain exceeded the value of 80 dB. Adding simple coding techniques such as the Hamming coding & interleaving improves the algorithm's performance for the non-spectral leakage case.

The proposed algorithm proved its efficiency, so the concept can be improved further. In reality, AWGN with low SNR levels along with multiple NBIs can impede proper communication. This is especially relevant for Autonomous Vehicles (AVs) and where safety is paramount. That is why a more detailed analysis of the "Mod-remod" algorithm's performance against AWGN has been conducted. It was shown that the algorithm performs much better for the lower QAM schemes since the NBI's and AWGN's influence on the demodulation process is greatly reduced. The simulations also revealed that the highest NBI's impact is presented on the subcarriers situated spectrally close to the frequency at which an NBI occured. This observation gave an idea for the next iteration

of the technique of removing an NBI in OFDM-based communication using the spectral leakage concept.

Chapter 3

"Differential" NBI removal algorithm

This chapter describes a differential cancellation algorithm for removing Narrow-Band Interferences (NBIs) from Orthogonal Frequency Division Multiplexing (OFDM) systems. The algorithm does not use any filtering and acts in the frequency domain relying on the spectral leakage phenomenon to not lose useful signal data. By using this property, the algorithm estimates, reconstructs and subtracts an NBI from the signal. The algorithm is able to work simultaneously with multiple NBIs and random noise modelled as Additive White Gaussian Noise (AWGN). The iterative approach helps to deal with each disturbance one after another, while the built-in refinement procedure improves the NBI frequency estimation. The solution does not require any prior information about the disturbance. The differential algorithm was validated through simulations covering different noise variations and spectral leakage cases. Albeit these simulations showed that the algorithm can work with very low Signal-to-Interference Ratios (SIRs) (lower than -100 dB), in reality, it is not the case due to hardware limitations. Nonetheless, the simulation results showed that the differential algorithm is able to remove multiple simultaneous NBIs along with the presence of AWGN in the Quadrature Amplitude Modulation (QAM) schemes significantly improving the Bit Error Rate (BER) performance.
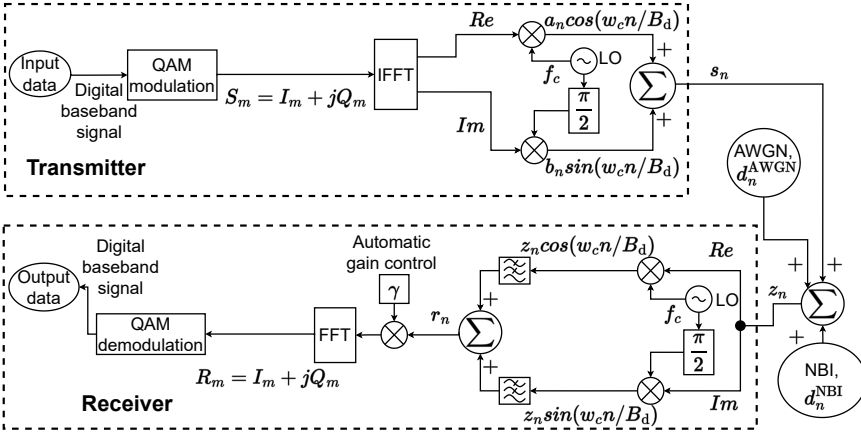
Figure 3.1: OFDM communication system.

3.1 Differential NBI removal algorithm

3.1.1 Extracting an NBI from an OFDM symbol

From Chapter 2, it is shown that when the described algorithm can correctly determine the induced NBI error, it can counteract its negative effect by subtracting the NBI spectral leakage pattern from the received signal (see Fig. 2.9). The "Mod-remod" algorithm described in Chapter 2 improves the robustness of OFDM symbols against NBIs. However, the spectral leakage pattern can be modified by white noise and the "Mod-remod" algorithm has to operate at lower modulation order schemes to yield the best performance. The work described in this chapter also relies on the spectral leakage pattern of an NBI. Nevertheless, the new technique approaches the NBI issue from a different perspective. The generated data at the transmitter's side are redundant in such a way that the digital baseband signal S_m is mirrored over two halves of the subcarriers, i.e. $S_{m+\frac{K}{2}} = -I_m - jQ_m$. This means that the sum of S_m and $S_{m+\frac{K}{2}}$ becomes equal to zero without any disturbance, so $S_m + S_{m+\frac{K}{2}} = 0$. Then the difference between the two correlated symbols results in a scalar multiplication with a factor of two: $S_m - S_{m+\frac{K}{2}} = 2S_m$. The reason to shift the modulated symbol with $K/2$ channels is to make use of periodicity within the Fourier transform.

The algorithm presented in this chapter is primarily made to tackle the

white noise that is always present in the system. Consequently, the OFDM communication system represented in Fig. 3.1 contains white noise modelled as AWGN. It is added as a cumulated noise from the receiver, transmitter and transmission channel. As a result, one may use the same mathematical expressions for OFDM signal conversions (e.g. Inverse Fourier Transform (IFFT), mixing with the carrier frequency f_c) used in Chapter 2.

Before the following explanation, let us look at the received spectrum R_m, shown in Fig. 3.2. In this figure, the signal is corrupted by an NBI with a chosen phase (45° in this case) with an SIR of -10 dB. The previously mentioned system's noise also affects the signal, the Signal-to-Noise Ratio (SNR) is equal to 30 dB. The α parameter ($\alpha \in [0:1[$) represents the spectral position of the NBI between two adjacent subcarriers p and $p + 1$ (see Fig. 3.2a), where $p \in [0; K - 2]$ and represents the current subcarrier. K is the total subcarrier number that should be even. The spectrum differs depending on where the NBI is situated (α parameter). As seen in Chapter 2, Fig. 2.2 shows that spectral leakage happens for all the α values but 0. The most severe influence from spectral leakage happens when α is equal to 0.5. The same applies to Fig. 3.2. However, looking at Fig. 3.2, one may notice high NBI values close to the frequency bins where the disturbance actually happened. Subcarriers at these frequency bins will be incorrectly demodulated irrespective of the extra random noise that can be added to the signal. This means that at these subcarriers AWGN will unlikely affect the NBI pattern and, therefore, the demodulation process. At the same time, the opposite happens at subcarriers that are distant from the NBI location (see Section 2.3.4). Considering that the receiver will be capable of tackling the random noise up to a certain limit using contemporary techniques [48] and with the aforementioned observations we may make an important assumption, i.e. we shall neglect the AWGN's presence. With this, the received signal R_m shown in Fig. 3.2 can be written as:

$$R_m = \frac{\gamma}{2}\left(S_m + \sum_{n=0}^{K-1}\left(e^{-j2\pi mn/K}A_{\mathrm{NBI}}e^{-j(2\pi(p+\alpha)n/K+\theta_{\mathrm{NBI}})}\right)\right), \qquad (3.1)$$

where S_m represents the data component in the received signal and γ is the Automatic Gain Control (AGC) amplification factor.

The received signal shifted by $K/2$ channels will give:

$$R_{m+\frac{K}{2}} = \frac{\gamma}{2}\left(S_{m+\frac{K}{2}} + \sum_{n=0}^{K-1}\left(e^{-j2\pi(m+\frac{K}{2})n/K}A_{\mathrm{NBI}}e^{-j(2\pi(p+\alpha)n/K+\theta_{\mathrm{NBI}})}\right)\right).$$
$$(3.2)$$
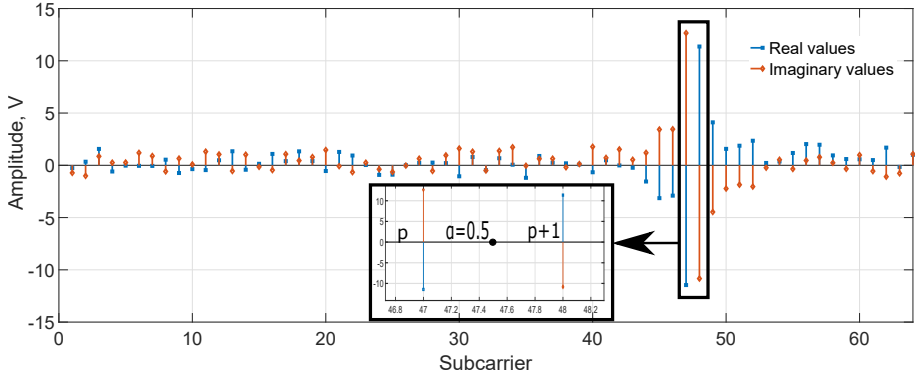
(a)
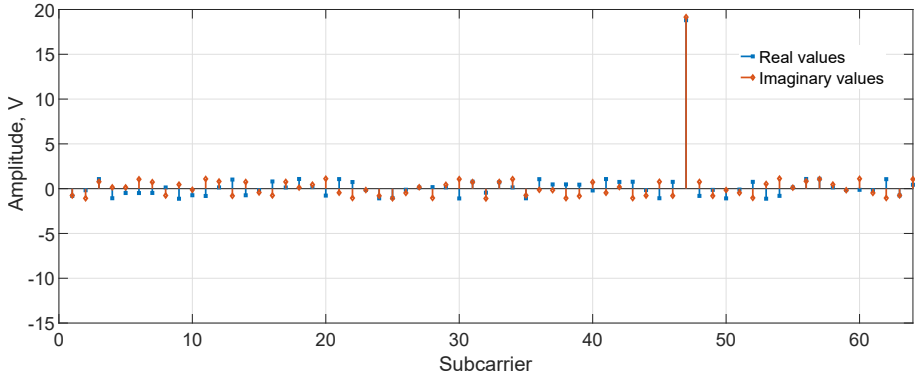
(b)

Figure 3.2: Real and imaginary values R_m value when SIR = -10 dB, SNR = 30 dB and the spectral leakage parameter α varies: (a) $\alpha = 0.5$, (b) $\alpha = 0$.

Taking into account that mirrored S_m and $S_{m+K/2}$ data symbols negate each other and the AGC factor is equal to two, the sum of (3.1) and (3.2) leads to:

$$
\begin{aligned}
R_m + R_{m+\frac{K}{2}} = \frac{\gamma}{2} \Bigg(& S_m + S_{m+\frac{K}{2}} \\
& + \sum_{n=0}^{K-1} \Big(A_{\text{NBI}} e^{-j(2\pi(p+\alpha)n/K+\theta_{\text{NBI}})} \big(e^{-j\pi mn/K} \\
& + e^{-j\pi(m+\frac{K}{2})n/K} \big) \Big) \Bigg) \\
= & \sum_{n=0}^{K-1} \Big(e^{-j2\pi mn/K} A_{\text{NBI}} e^{-j(2\pi(p+\alpha)n/K+\theta_{\text{NBI}})} \big(1 + e^{-j\pi n} \big) \Big).
\end{aligned}
$$

(3.3)

Taking into account that n is an integer value, expression (3.3) leads to the following:

$$1 + e^{-j\pi n} = \begin{cases} 2 \text{ if } n \text{ is even} \\ 0 \text{ if } n \text{ is odd} \end{cases}.$$

This can simplify (3.3) if the summation limits are changed by introducing $n = 2q$.

$$R_m + R_{m+\frac{K}{2}} = 2A_{\text{NBI}}e^{-j\theta_{\text{NBI}}} \sum_{q=0}^{\frac{K}{2}-1} \left(e^{-j4\pi q(p+\alpha+m)/K} \right). \tag{3.4}$$

Looking closer at the summation part of (3.4), one may modify this part using the finite geometric series:

$$\sum_{i=P_1}^{P_2} \alpha^i = \alpha^{P_1} \frac{1 - \alpha^{P_2-P_1+1}}{1-\alpha}. \tag{3.5}$$

Substituting $p + \alpha$ to $-a$ and implementing (3.5) will modify the summation part of (3.4) to:

$$\sum_{q=0}^{\frac{K}{2}-1} e^{-j4\pi q(p+\alpha+m)/K} = e^0 \frac{1 - e^{-j4\pi(\frac{K}{2}-1-0+1)(m-a)/K}}{1 - e^{-j4\pi(m-a)/K}}$$

$$= \frac{1 - e^{-j2\pi(m-a)}}{1 - e^{-j4\pi(m-a)/K}}. \tag{3.6}$$

Now let us note the numerator and denominator of (3.6) as E_m^{numer} and E_m^{denom}, respectively, and modify them even further by changing the exponential form to the trigonometric form:

$$E_m^{\text{numer}} = 1 - e^{-j2\pi(m-a)} = 1 - \cos(2\pi(a-m)) - j\sin(2\pi(a-m)). \tag{3.7}$$

$$E_m^{\text{denom}} = 1 - e^{-j4\pi(m-a)/K} = 1 - \cos(4\pi \frac{a-m}{K}) - j\sin(4\pi \frac{a-m}{K}). \tag{3.8}$$

Substituting $R_m + R_{m+\frac{K}{2}}$ by X_m for simplicity and taking the absolute value of a complex number in the polar coordinate system will give:

$$|X_m| = 2 \left| A_{\text{NBI}}e^{j\theta_{\text{NBI}}} \frac{E_m^{\text{numer}}}{E_m^{\text{denom}}} \right|. \tag{3.9}$$

Taking the absolute value of E_m^{numer} and E_m^{denom} in (3.7) will result in:

$$|E_m^{\text{numer}}| = \left((1 - \cos(2\pi(a-m)))^2 + (-\sin(2\pi(a-m)))^2 \right)^{0.5}$$

$$= \left(1 - 2\cos(2\pi(a-m)) + \cos^2(2\pi(a-m)) + \sin^2(2\pi(a-m)) \right)^{0.5}$$

$$= \left(2(1 - \cos(2\pi(a-m))) \right)^{0.5} = \left(2(1 + 2\sin^2(\pi(a-m)) - 1) \right)^{0.5}$$

$$= \left(4\sin^2(\pi(a-m)) \right)^{0.5} = 2\sin(\pi(a-m)). \tag{3.10}$$

$$|E_m^{\text{denom}}| = \left(\left(1 - \cos\left(4\pi\frac{a-m}{K} \right) \right)^2 + \left(-\sin\left(4\pi\frac{a-m}{K} \right) \right)^2 \right)^{0.5}$$

$$= \left(1 - 2\cos(4\pi(a-m)/K) + \cos^2(4\pi(a-m)/K) \right.$$

$$\left. + \sin^2(4\pi(a-m)/K) \right)^{0.5} = \left(2(1 - \cos(4\pi(a-m)/K)) \right)^{0.5}$$

$$= \left(4\sin^2\left(2\pi\frac{(a-m)}{K} \right) \right)^{0.5} = 2\sin\left(2\pi\frac{(a-m)}{K} \right). \tag{3.11}$$

Taking into account (3.10) and (3.11), (3.9) will become:

$$|X_m| = 2|A_{\text{NBI}}| \frac{\sin(\pi(a-m))}{\sin\left(2\pi\frac{(a-m)}{K} \right)} \tag{3.12}$$

If we assume that $|X_m|$ is the value with the largest spectral leakage impact from the NBI, then looking back at Fig. 3.2 one may notice the following. In case of no spectral leakage (Fig. 3.2b) only one subcarrier is disturbed which can be solved by using error correction techniques (e.g. tackling NBI as a burst error [14]). However, the case of coherent sampling is quite unlikely in practice because there is almost always a mismatch between the signal and ElectroMagnetic Disturbance (EMD) sampling. Thus the spectral leakage case will be dominant (Fig. 3.2a). This will lead to the second largest spectral

leakage neighbouring value that can be either before or after $|X_m|$, i.e. at $|X_{m-1}|$ or $|X_{m+1}|$. Depending on where the second peak happened the solution will slightly differ. Let us start from $|X_{m+1}|$.

$$|X_{m+1}| = 2|A_{\text{NBI}}| \frac{\sin(\pi(a - m - 1))}{\sin\left(2\pi \frac{(a-m-1)}{K}\right)}. \tag{3.13}$$

To get rid of the extra unknown parameter, namely A_{NBI}, let us find the ratio between (3.12) and (3.13):

$$\left| \frac{X_m}{X_{m+1}} \right| = \frac{\sin(\pi(a - m)) \sin(2\pi(a - m - 1)/K)}{\sin(2\pi(a - m)/K) \sin(\pi(a - m - 1))}. \tag{3.14}$$

Let us simplify eq. (3.14) using the following expressions:

$$\sin(2\pi(a - m - 1)/K) = \sin(\frac{2\pi(a - m)}{K} - \frac{2\pi}{K})$$

$$= \sin(\frac{2\pi(a - m)}{K}) \cos(\frac{2\pi}{K}) - \cos(\frac{2\pi(a - m)}{K}) \sin(\frac{2\pi}{K}). \tag{3.15}$$

$$\sin(\pi(a - m - 1)) = \sin((a - m)\pi - \pi)$$

$$= \sin(\pi(a - m)) \cos(\pi) - \cos((a - m)\pi) sin(\pi)$$

$$= -\sin(\pi(a - m)). \tag{3.16}$$

Using eqs. (3.15) and (3.16) in eq. (3.14) will result in the following:

$$\left| \frac{X_m}{X_{m+1}} \right| = \frac{\sin(\pi(a - m)) \left(\sin(\frac{2\pi(a-m)}{K}) \cos(\frac{2\pi}{K}) - \cos(\frac{2\pi(a-m)}{K}) \sin(\frac{2\pi}{K}) \right)}{-\sin(2\pi(a - m)/K) \sin(\pi(a - m))}$$

$$= \frac{\cos(\frac{2\pi(a-m)}{K}) \sin(\frac{2\pi}{K}))}{\sin(\frac{2\pi(a-m)}{K})} - \frac{\sin(\frac{2\pi(a-m)}{K}) \cos(\frac{2\pi}{K}))}{\sin(\frac{2\pi(a-m)}{K})}$$

$$= \frac{\sin(2\pi/K)}{\tan(2\pi(a - m)/K)} - \cos(\frac{2\pi}{K}). \tag{3.17}$$

From (3.14), it can be seen that only one parameter from the NBI is unknown. It is its spectral position represented as $a - m$ that can be derived as follows:

$$a - m = \frac{K}{2\pi} \arctan\left(\frac{\sin(2\pi/K)}{\left|\frac{X_m}{X_{m+1}}\right| + \cos(2\pi/K)}\right). \tag{3.18}$$

When the spectral position of the NBI is known, one may derive its complex amplitude:

$$A_{\text{NBI}}e^{-j\theta_{\text{NBI}}} = \frac{X_m E_m^{\text{denom}}}{2E_m^{\text{numer}}}. \tag{3.19}$$

If the second largest value happens before X_m similar expressions to (3.13)—(3.18) can be obtained:

$$|X_{m-1}| = 2|A_{\text{NBI}}|\frac{\sin(\pi(a - m + 1))}{\sin\left(2\pi\frac{(a-m+1)}{K}\right)}. \tag{3.20}$$

$$\left|\frac{X_m}{X_{m-1}}\right| = \frac{\sin(\pi(a - m))\sin(2\pi(a - m + 1)/K)}{\sin(2\pi(a - m)/K)\sin(\pi(a - m + 1))}$$

$$= -\frac{\sin(2\pi/K)}{\tan(2\pi(a - m)/K)} - \cos(2\pi/K). \tag{3.21}$$

$$a - m = \frac{K}{2\pi} \arctan\left(\frac{-\sin(2\pi/K)}{\left|\frac{X_m}{X_{m-1}}\right| + \cos(2\pi/K)}\right). \tag{3.22}$$

Therefore, the algorithm will identify the spectral position of the NBI and based on the value of X_{m+1} and X_{m-1} will choose the suitable expression, i.e. (3.18) or (3.22).

Once the NBI has been found and defined, the received data symbols can be recovered by taking a difference between R_m and $R_{m+\frac{K}{2}}$. This difference can be derived similarly to eq. (3.3).

$$R_m - R_{m+\frac{K}{2}} = S_m - S_{m+\frac{K}{2}}$$

$$+ A_{\text{NBI}}e^{-j\theta_{\text{NBI}}} \cdot \sum_{n=0}^{K-1}\left(e^{-j2\pi mn/K}\, e^{-j2\pi(-a)n/K}\left(1 - e^{-j\pi n}\right)\right). \tag{3.23}$$

Note that $S_m - S_{m+\frac{K}{2}} = 2S_m$.

The expression in (3.23) can be simplified resulting in the following:

$$1 - e^{-j\pi n} = \begin{cases} 2 \text{ if n is odd} \\ 0 \text{ if n is even} \end{cases}.$$

This will also change the summation limits since $n = 2q+1$. Taking into account eq. (3.5) and new summation limits, (3.23) can be simplified to the following expression:

$$R_m - R_{m+\frac{K}{2}} = 2S_m$$

$$+ A_{\text{NBI}}e^{-j\theta_{\text{NBI}}} \cdot \sum_{q=0}^{\frac{K}{2}-1} \left(e^{-j2\pi m(2q+1)/K} \; e^{-j2\pi(-a)(2q+1)/K} 2 \right)$$

$$= 2S_m + 2A_{\text{NBI}}e^{-j\theta_{\text{NBI}}}e^{j2\pi(a-m)/K} \frac{1 - e^{j2\pi(a-m)}}{1 - e^{j4\pi(a-m)/K}}. \qquad (3.24)$$

After the simplification, with the NBI parameters known, one may correct the disturbed data by removing the NBI following the spectral leakage pattern. Mathematically it is represented as the data component derivation from (3.24):

$$S_m = \frac{1}{2} \left(R_m - R_{m+\frac{K}{2}} \right.$$

$$\left. -2A_{\text{NBI}}e^{-j\theta_{\text{NBI}}}e^{j2\pi(a-m)/K} \cdot \frac{1 - e^{j2\pi(a-m)}}{1 - e^{j4\pi(a-m)/K}} \right). \qquad (3.25)$$

3.1.2   Non-spectral leakage case

This section will show mathematical proof for the case without spectral leakage.

Looking at Fig. 3.3, one may notice that only one subcarrier is disturbed by the NBI. Others do not exceed the threshold starting from which the algorithm is initialised. The threshold is calculated in percentage of the minimum absolute Euclidean distance between neighbouring points on the I—Q constellation of the chosen modulation scheme. Therefore, if the error value $|X_m|$ exceeds at least half of the threshold, there might be a symbol flip. As a result, the algorithm is initialised. The threshold for Fig. 3.3 is equal to 50 %. Depending on which value is bigger, $|X_{m-1}|$ or $|X_{m+1}|$, equations (3.18) or (3.22) will be used. They, in their turn, depend on the X_m values. When the difference is large,
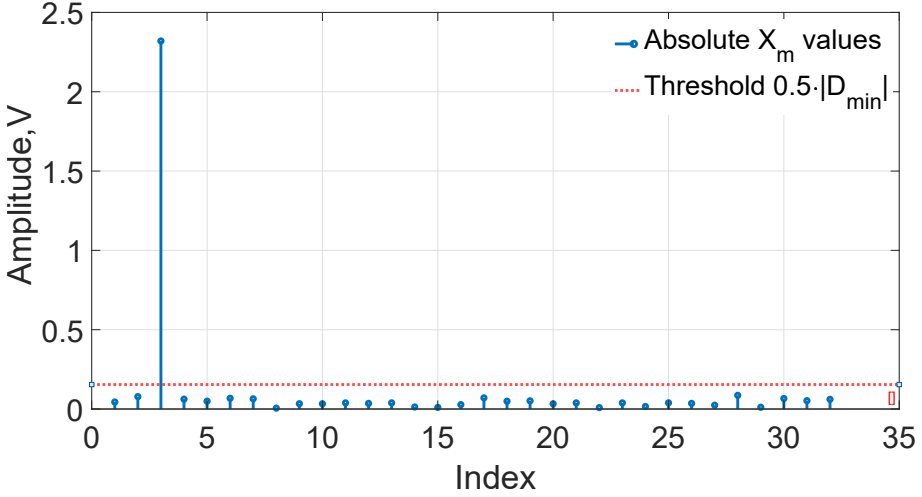
Figure 3.3: X_m values when $\alpha = 0$, i.e. non-spectral leakage case. SIR = 10 dB, SNR = 30 dB, $\theta_{\mathrm{NBI}} = 24°$.

$X_m \gg X_{m-1}$ and $X_m \gg X_{m+1}$. This means that the ratios between X_m and its adjacent ones will be substantial. Moreover, the higher the SIR level, the higher the ratios will be leading to $X_m/X_{m-1} \to \infty$ and $X_m/X_{m+1} \to \infty$. This means that the arguments of arctangents in (3.18) and (3.22) will go to zero. Therefore, the $a - m$ expressions will also go to zero. Thus, a and m will be infinitely close to each other, which only happens when $\alpha = 0$, i.e. non-spectral leakage case takes place.

The proposed algorithm is implemented for all spectral leakage cases. The chance that an NBI will perfectly coincide or will be spectrally very close to the signal (non-spectral leakage case condition) is very slim and, consequently, not covered in this chapter. In Chapter 2, it has already been shown that the non-spectral leakage case can be tackled using coding techniques.

3.1.3 The algorithm's NBI detection

While the algorithm's mathematical part was described in previous subsections, the actual algorithm's procedure still has to be shown. Let us provide it for the situation in which two NBIs are disturbing the signal at the same time. Two flowcharts are added as an extra aid for the algorithm's explanation (see Figs.

3.4 and 3.5). The flowcharts contain enumerated blocks for ease of navigation and reference.
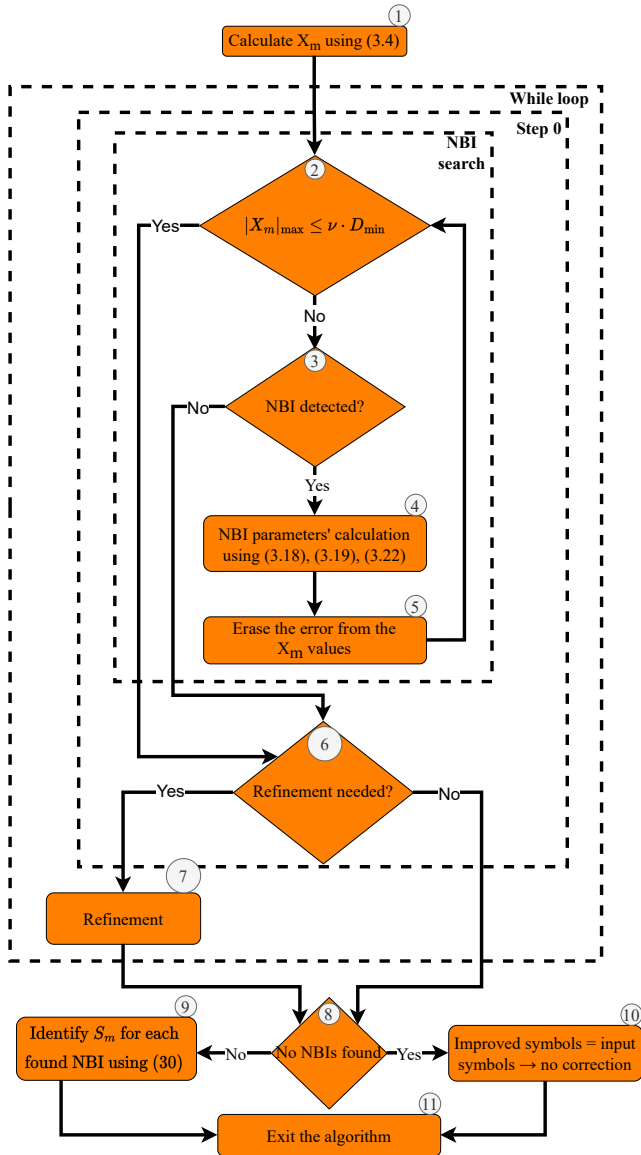
Figure 3.4: The algorithm's flowchart. General overview.
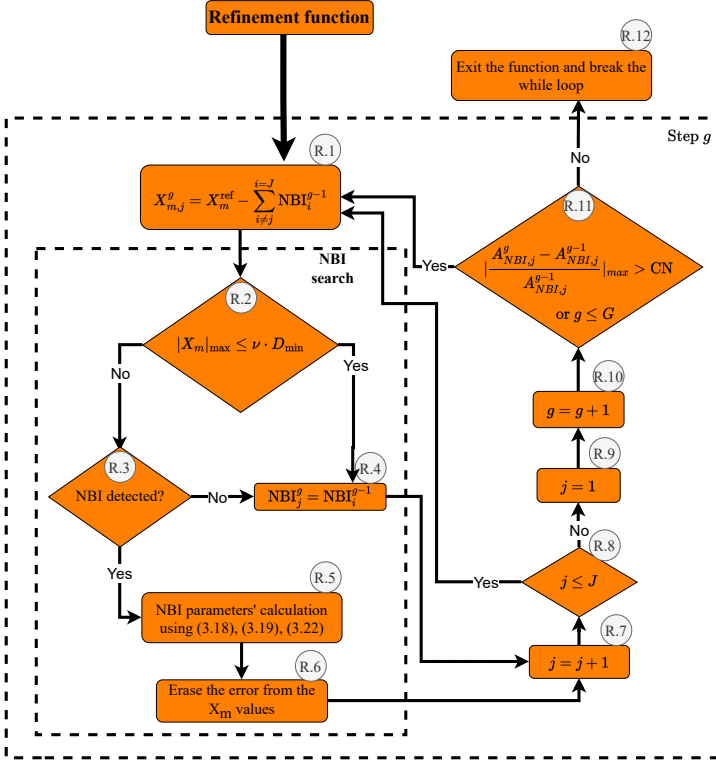
Figure 3.5: The algorithm's flowchart. The refinement procedure.

Let us first look at the general algorithm's flowchart (Fig. 3.4). It can be noticed that the flowchart contains the "while loop", the "Step 0" and "NBI search" parts that are outlined with dotted lines. In the beginning, X_m values (block 1 in Fig. 3.4) are obtained by summing $R_m + R_{m+\frac{K}{2}}$ as shown in (3.4). Then the NBI search starts. First, the algorithm checks if there are any X_m values exceeding the threshold (block 2) that is regulated by the percentage (ν) of the minimum absolute Euclidean distance ($D_{\min}$) between neighbouring points on the I—Q constellation of the chosen modulation scheme. If multiple values are found, the algorithm takes the largest of them and checks if it contains a spectral leakage pattern (block 3). This pattern should create a sign change in either real or/and imaginary parts. On top of that sign change, an asymptotic behaviour should be present, meaning that the X_m values should asymptotically decrease in values the further they are from the sign change. The asymptotic behaviour should be visible on at least two bins on each side of the sign change
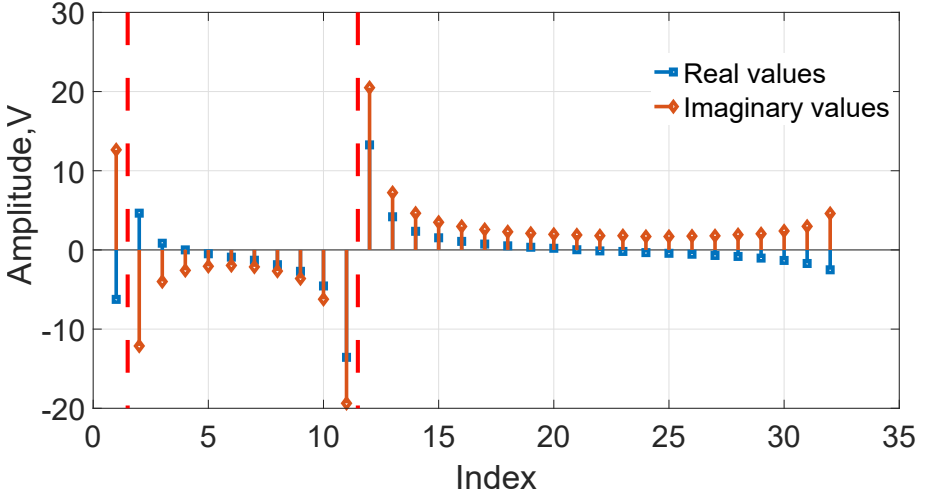
Figure 3.6: Real and imaginary X_m values when SIR1 = -10 dB, SIR2 = -15 dB, SNR = 30 dB, $\theta_{\text{NBI1}} = 24°$, $\theta_{\text{NBI2}} = 146°$.

place. For example, let us look at Fig. 3.6, which contains two NBIs at an SNR level of 30 dB with SIR levels of -10 and -15 dB. Asymptotes are shown with red dashed lines. Both NBIs have a sign change and asymptotic behaviour in this particular case. When the algorithm finds this spectral leakage pattern, it calculates the NBI's parameters using expressions (3.18), (3.19) and (3.22) (block 4). With the NBI's parameters, one may reconstruct the error values (E_m) and get the updated values (X_m^{upd}) by subtracting the reconstructed error values from the X_m values in accordance with the following equations (block 5):

$$E_m = A_{\text{NBI}} e^{j\theta_{\text{NBI}}} \frac{1 - e^{j2\pi(a-m)}}{1 - e^{j4\pi(a-m)/K}}. \tag{3.26}$$

$$X_m^{\text{upd}} = X_m - E_m. \tag{3.27}$$

After that, the algorithm goes back to block 2. To speed up the process and minimise the potential error caused by the rough estimation in case of multiple NBIs, the algorithm does not check the place where the previously found NBI happened. It means that the four subcarriers (two for a sign flip and two more for asymptotic behaviour) that were used to locate the previous NBI will not be used for further NBI searches. If we look at Fig. 3.6, then for the NBI happening between the 11$^{\text{th}}$ and 12$^{\text{th}}$ indices, the indices 10—13 will not be checked for a neighbouring NBI.

When the algorithm identified more than one NBI, refinement happens. However, it takes place when the number of NBIs is at least equal to two (block 6). The refinement flowchart is presented in Fig. 3.5 and its blocks are also enumerated. The refinement allows gradually decreasing the NBI's estimation error. For that, the NBI's parameters have to be found again. However, before that, the influence of the other found NBIs has to be subtracted from the reference value X_m^{ref} (block R.1 in Fig. 3.5) that is calculated as the sum of $R_m + R_{m+\frac{K}{2}}$. For example, if we take the example from Fig. 3.6, then for the case of two found NBIs at step "0", the values at step "1" during the refinement can be written as:

$$X_{m,1}^1 = X_m^{\text{ref}} - \text{NBI}_2^0. \tag{3.28}$$

$$X_{m,2}^1 = X_m^{\text{ref}} - \text{NBI}_1^0. \tag{3.29}$$

The NBI search (blocks R.2, R.3, R.5, R.6) is equal to the one described before. If no NBIs were found, the value at step g will be equal to the value of that NBI from step $g - 1$ (block R.4).

The refinement occurs until a Convergence Number (CN), block R.11, is reached. It means that the maximum relative difference of complex amplitudes of the found NBIs ($A_{\text{NBI},j}^g$) will become less or equal to CN. Again, in order to optimise the time needed for the refinement, the convergence is limited to a certain number of steps G. If the convergence is not reached within this number, the refinement ends with the values that have been found at step G.

After the refinement, the received data are either improved using eq. (3.25) or remain unchanged if no NBIs are found (blocks 9 or 10 in Fig. 3.4). The corrected data component calculated from eq. (3.25) will result in $K/2$ symbols. Yet, we know that the originally modulated symbols S_m were modulated to meet the condition $S_m + S_{m+\frac{K}{2}} = 0$. Therefore, the remaining $K/2$ symbols will be appended to the corrected S_m symbols as a copy of them but with a negative sign.

3.2 Optimisation of the algorithm

Before starting full-fledged simulations, a few small adaptations of the algorithm and one remark have to be made.

Let us start with a remark that is related to the AWGN's power. As was mentioned previously, coding techniques are incorporated into modern wireless communication protocols. We do not include them in our solution because this

is out of the current research. However, we make sure that the Low-Density Parity Check (LDPC) codes guarantee a BER level of at least 10^{-2} for QAM64 modulation schemes with an SNR level of 16 dB [49], [50]. With this, we shall be using this SNR level throughout our simulations.

3.2.1 Optimising the threshold parameter v

For the most optimal algorithm performance satisfying various electromagnetic environments, thus, simulation cases, let us identify a threshold parameter v that is a percentage value of the minimum absolute Euclidean distance between neighbouring points on the I—Q constellation of the chosen modulation scheme ($D_{\min}$). Figure 3.7 represents the BER performance of the algorithm with different values of v when an SNR is equal to 16 dB, one NBI is present and α is equal to 0.5. The solid black and dashed red lines outline reference cases when the algorithm was not used. The solid black line represents the case when both AWGN and an NBI were present in the system while the dashed red line shows the BER performance when only AWGN was in the system. Between these reference lines, one may notice the BER performance of the algorithm with different v threshold parameters starting from 0 to 1.5 with a step of 0.25 and one extra value for $v = 0.5$. In the situation when v is equal to 5 (shown with the pink line with solid circular markers in Fig. 3.7), it can be seen that
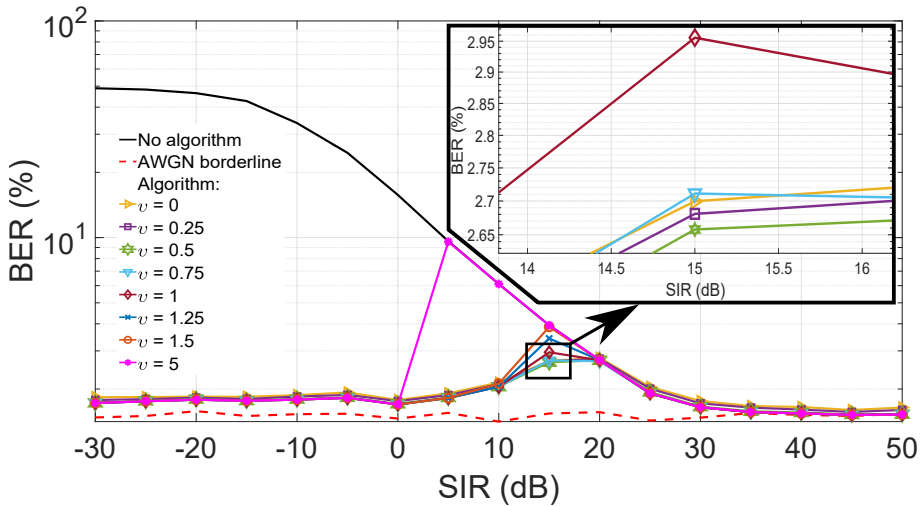
Figure 3.7: The algorithm's BER performance with different v thresholds.

the highest v value makes the threshold value $D_{\min}$ too high, increasing it by five times and turning the algorithm insensible to an NBI having an SIR greater or equal than 5 dB. Other values of v are similar. A magnified part of this graph shows a visible difference in the region of an SIR range between 14 and 16 dB. Though the BER performance in this region does not differ more than 0.05%, one may see that v equal to 0.5 results in the best performance. This can be explained as follows. When v is equal to 0.5, the threshold is right in between two adjacent values on the I—Q constellation. This is the borderline above which a symbol flip occurs resulting in the wrong demodulation.

3.2.2 Optimising the refinement procedure

As was seen from Figs. 3.4 and 3.5, the refinement is completed either when the complex amplitudes of the found NBIs converge or a certain number of refinement steps has been reached. First, let us identify the optimal number of refinement steps.

Figure 3.8a depicts the BER performance of the algorithm when $K/4$ subcarriers separate two NBIs from each other, so they do not cause any significant influence on the algorithm's performance. The NBIs are variable and simultaneously disturb the signal along with AWGN an SNR, which is equal to 16 dB. Again, one may notice two reference curves: the black solid line showing the BER performance when two NBIs and AWGN are present in the system and the red dashed line depicting the BER performance when only AWGN is present. The algorithm's BER performance between these reference lines is shown for a different number of Refinement Steps (RSts). The worst performance (the yellow line with triangular markers) is when the RSt number is equal to zero meaning that refinement does not occur. Below this line is the violet line with rectangular markers that shows the performance when one RSt was used. The performance in comparison to the non-refinement case has improved drastically. However, there is a group of curves that lie on top of each other which have a better performance when the refinement number is equal to one. Therefore, the algorithm should have at least two RSts before the most optimal results will be obtained. With this, we shall be using two RSts in the simulations further. More in-depth results for more than two simultaneous NBIs and their subsequent discussion will be given in Section 3.3.5.

After identifying the RSt number, it is important to know which CN or precision is needed during the convergence check. Again two variable NBIs along with AWGN having an SNR of 16 dB were disturbing the signal. Figure 3.8b represents a heatmap with a different BER performance for various CNs varying from $1E - 6$ to 0.1 when α equals 0.5. The simulations are extended to an
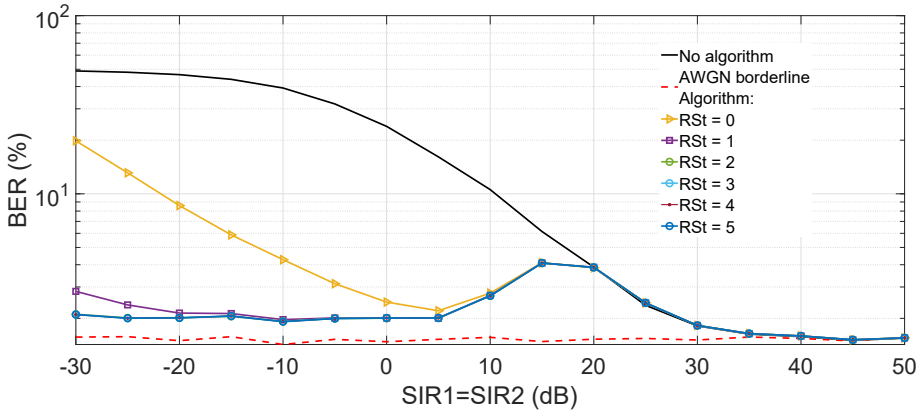
(a)
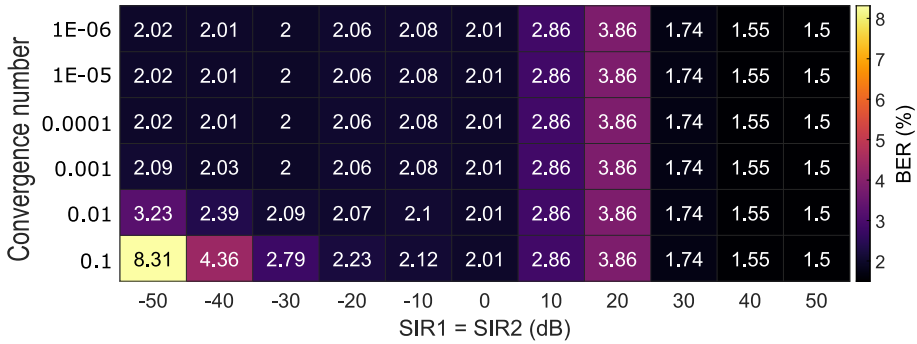
(b)

Figure 3.8: The refinement optimisation procedure: (a) The refinement steps optimisation (b) The convergence number optimisation.

SIR level equal to -50 dB to make a more accurate choice of the convergence number. As can be seen, starting from an SIR of 0 dB, results do not change because the interference level is comparable or even lower than the signal level. Hence, the two refinement steps are unlikely to cause any visible change to the results. Therefore, the main indicator that will affect our choice lies in the left part of the heatmap in the SIR region from -50 to 0 dB. It can be seen that CNs from $1E-6$ to $1E-4$ have identical values, whereas starting from 0.001 the BER performance of the algorithm gets worse. With this, we shall be using the CN of $1E-4$ throughout our remaining simulations.

Table 3.1: Simulation parameters for OFDM symbols

Parameter	Value
Modulation scheme	QAM(M), M= [16; 32; 64; 128; 256; 512; 1024; 2048]
Number of subcarriers, K	[64; 128; 256; 512; 1024; 2048]
Number of bits, Y	$log_2(M) \cdot K$
Baud rate, B_d	100
Subcarrier spacing, H	B_d/K

3.3 Evaluation of the algorithm

Before going into the simulation parameters and the subsequent results, the expression for the received signal R_m after the Discrete Fourier Transform (DFT) block (shown in Fig. 3.1) has to be reviewed. As mentioned in Section 3.1, R_m does not include any random noise component. Let us write down the same expression with the added random noise, $d_\mathrm{n}^{\mathrm{AWGN}}$, that is modelled as AWGN.

$$R_m = S_m + \sum_{n=0}^{K-1} \left(e^{-j2\pi mn/K} \left(A_{\mathrm{NBI}} e^{-j(2\pi(d+\alpha)n/K + \theta_{\mathrm{NBI}})} + d_\mathrm{n}^{\mathrm{AWGN}} \right) \right). \quad (3.30)$$

3.3.1 Simulation parameters

All the simulations were performed on MATLAB [45] assuming that there is no multipath fading and time, frequency synchronisations and compensations are perfect, resulting in no need for equalisation, pilot signals and Cyclic Prefix (CP)es in the OFDM system under consideration. For all the simulations the noise model is AWGN.

The simulation parameters for the OFDM symbols and the NBIs along with AWGN can be found in Tables 3.1 and 3.2, respectively. The algorithm was tested mainly against one NBI along with AWGN. Nevertheless, the algorithm's limits were also tested against multiple simultaneous NBIs with AWGN for QAM64 with 64 subcarriers. To make the simulation reflect a realistic environment, simulations were performed for 360 possible phases θ_{NBI}. After that, the results were averaged. Moreover, to avoid the correlation of the results, the transmitted bits were varied during each NBI phase. In addition, the NBI phases for simulations with multiple NBIs were pseudorandomly chosen, so each NBI phase was unlikely to coincide.

Table 3.2: Simulation parameters for NBIs and AWGN

Parameter	Value
NBI phase[a](θ_{NBI}), degree	[0:359]
Distance to the closest NBI subcarrier,[b] α	[0.25; 0.5]
SIR[c] span, dB	[-30:50]
SIR step, dB	5
SNR[d] span, dB	[-10:30]
SNR step, dB	10
Reference SNR[e] , dB	16
Noise amplitude,[f] A_{NBI}, V	$A_{\text{NBI}} = \frac{S_{RMS}}{10^{\text{SIR}/20}}$

[a] Per each phase θ_{NBI}, a new sequence of bits Y was generated;
[b] f_{NBI} and f_c are aligned in such a way that f_{diff} can take values between -50 Hz and 50 Hz;
[c] SIR $= 10 \log_{10}(\frac{P_s}{P_{\text{NBI}}})$, where P_s and P_{NBI} denote the power values of the signal and interference, respectively;
[d] SNR defines the AWGN's power with regard to the signal power;
[e] The reference SNR value is used during simulations against constant AWGN;
[f] S_{rms} — a root-mean-squared value of the signal in the time domain; SIR — NBI's current SIR value.

3.3.2 The algorithm's performance under a single NBI and constant AWGN

The influence of a single NBI together with AWGN is presented in Fig. 3.9. This figure represents two cases: when the spectral leakage is maximum ($\alpha = 0.5$, Fig. 3.9a) and when the spectral leakage's influence is asymmetrical, i.e. it is more distinct at one side of the place where an NBI happened than at the other ($\alpha = 0.25$, Fig. 3.9b). Figure 3.9 has two reference curves when the algorithm is not in action: the black one when the NBI and AWGN are present in the system and the dashed red one when only the white noise was in the system. The yellow line with round markers on this figure represents the algorithm's performance. For low SIR values, both of these yellow curves present an OFDM transmission improvement in terms of the BER performance. In addition, this improvement is very similar for both α cases. The results for α equal to 0.5 are slightly worse throughout the whole SIR span, except for the region between 0 and 15 dB. This can be explained as follows: α equal to 0.5 leads to the highest spectral leakage and, therefore, to a larger error that results in a higher BER for the reference case. In the region of an SIR between 0 and 15 dB, the results in terms of the BER performance change due to the algorithm's
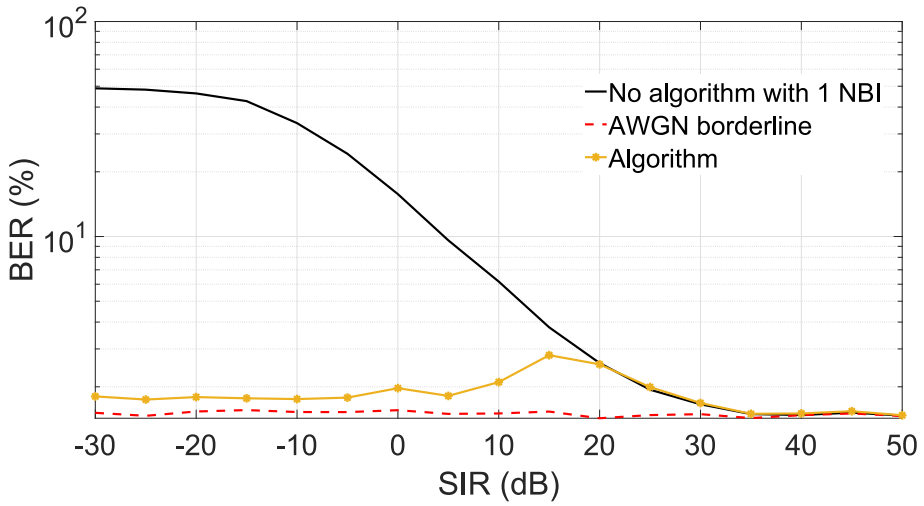
(a)
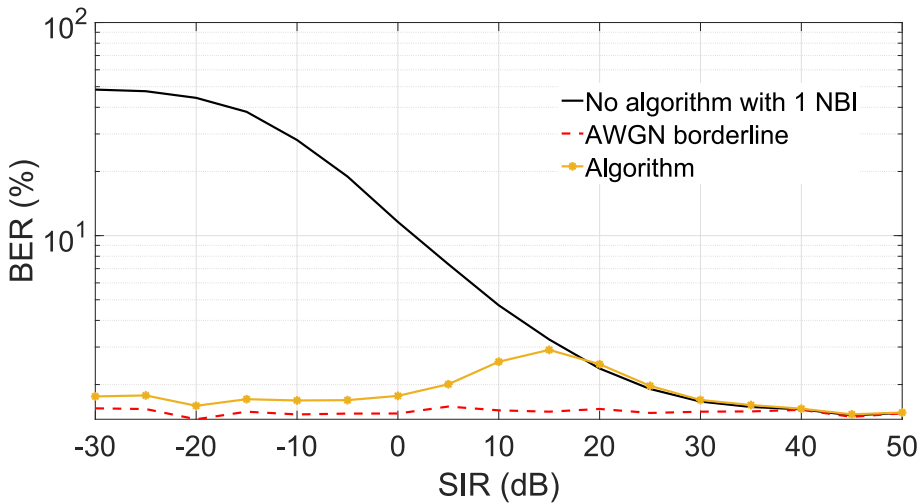
(b)

Figure 3.9: Differential NBI removal algorithm's performance when SIR = var, SNR = 16 dB and the spectral leakage parameter α varies: (a) $\alpha = 0.5$, (b) $\alpha = 0.25$.

error approximations. All the BER variations for the presented α cases do not vary more than 0.5 %. This leads to the observation that the spectral leakage parameter, α, does not affect the algorithm's performance at low SIR levels (lower than 0 dB).

One may also notice that starting from an SIR level higher than 5 dB, the BER performance of the algorithm worsens and already at an SIR level of 20 dB, the algorithm does not perform any better than the reference black curve corresponding to the case when the algorithm was not in action. This can be explained as follows. The algorithm's derivation assumes that the AWGN's share in the total error is negligible compared to that of the NBI. As the SIR level increases and becomes comparable to the SNR, which was equal to 16 dB in our case, the algorithm's estimation becomes less accurate. Therefore, the BER curves overlap.

3.3.3 The algorithm's performance under a single NBI and variable AWGN

The algorithm's performance against both varying NBI and AWGN can be shown using heatmaps that are presented in Fig. 3.10. Like in the previous subsection, two α cases are shown, 0.5 and 0.25, respectively. From the figures, it can be seen that the BER performance of the algorithm for both α cases is similar with slight differences. However, as was for Fig. 3.9, these BER differences do not exceed more than 0.5 %.

Figure 3.10 shows that starting from an SNR level higher than or equal to 20 dB, the BER does not exceed more than 1.16%.

In contrast to the algorithm's performance shown in Fig. 3.10, the system's performance without the algorithm is shown in Fig. 3.11. It presents heatmaps when one single NBI and AWGN were disturbing the signal. Comparing the heatmaps from Fig. 3.10 and 3.11, one may notice that the algorithm at SNR levels lower than 10 dB expands the system's capabilities of withstanding NBIs, especially at low SIR levels. The lower the SIR value, the bigger the benefit from the algorithm.

3.3.4 The algorithm's performance under two NBIs separated by a different number of subcarriers

In order to show the algorithm's capability of handling multiple NBIs, the algorithm was tested against two simultaneous NBIs separated by a varying

SNR (dB) \ SIR (dB)	-30	-25	-20	-15	-10	-5	0	5	10	15	20	25	30	35	40	45	50
-10	44.78	44.71	44.85	44.77	44.61	44.65	44.28	44.37	44.03	44.38	44.29	44.73	44.68	44.42	44.29	44.32	44.54
0	31.86	31.99	31.74	32.11	31.8	31.86	31.92	32.2	31.76	31.59	30.84	31.49	31.15	31.34	31.46	31.22	31.16
10	10.32	10.7	10.52	11.05	10.54	10.66	10.35	10.45	11.18	11.21	10.77	10.25	10.07	9.88	10.23	10.12	10.05
20	0.11	0.11	0.09	0.12	0.1	0.11	0.11	0.14	0.6	1.1	0.92	0.39	0.13	0.1	0.05	0.07	0.05
30	0	0	0	0	0	0	0	0	0.42	0.91	0.69	0.1	0	0	0	0	0

(a)

SNR (dB) \ SIR (dB)	-30	-25	-20	-15	-10	-5	0	5	10	15	20	25	30	35	40	45	50
-10	44.68	44.58	44.52	44.47	44.87	44.61	44.58	44.87	44.85	44.47	44.55	44.52	44.61	44.61	44.3	44.57	44.6
0	31.99	31.55	31.8	31.56	32.07	32.36	32.14	31.76	31.93	31.62	31.4	31.52	31.18	31.15	31.19	31.45	31.33
10	10.64	10.4	10.61	10.35	10.59	10.1	10.61	11.17	11.33	11.18	10.6	10.31	9.98	10.03	9.91	10.01	10.05
20	0.1	0.1	0.1	0.09	0.12	0.09	0.13	0.13	0.56	1.16	0.86	0.45	0.15	0.09	0.05	0.06	0.08
30	0	0	0	0	0	0	0	0	0.31	0.64	0.66	0.39	0	0	0	0	0

(b)

Figure 3.10: Differential NBI removal algorithm's performance when SIR = var, SNR = var and the spectral leakage parameter α varies: (a) $\alpha = 0.5$, (b) $\alpha = 0.25$.

number of subcarriers. Figure 3.12 shows this simulation setup for α equal to 0.5 and 0.25. Along with two NBIs, AWGN with an SNR of 16 dB is also present in the simulation. The first NBI happens right in between the 15th and 16th subcarriers. If the spacing is equal to zero, it means that both NBIs are on top of each other. If the spacing is equal to one, the second NBI happens between the 16th and 17th subcarriers and so on. The black solid lines with a textbox near them show the reference cases when two NBIs and AWGN (SNR is equal to 16 dB) were present in the system with a disabled algorithm. The red dashed line at the bottom of Fig. 3.12 shows the other reference case when only AWGN was in the system and without applying the algorithm. The other lines represent
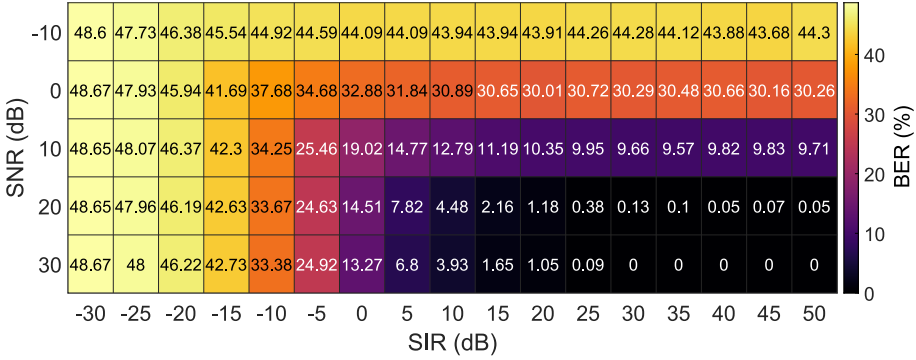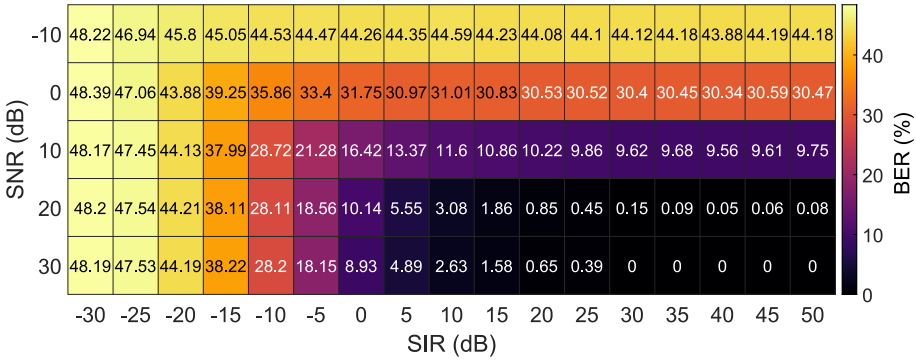
Figure 3.11: The BER performance of the system without the differential NBI removal algorithm when SIR = var, SNR = var and the spectral leakage parameter α varies: (a) $\alpha = 0.5$, (b) $\alpha = 0.25$.

the algorithm's performance with two NBIs having different SIR levels and constant AWGN. The SIR levels are between -30 dB and 45 dB with a step of 15 dB. It can be seen that the algorithm's performance gets worse for some subcarrier spacing (1—3 for both α cases). The NBIs are located so close to each other that the algorithm is unable to identify the correct parameters. Due to periodicity, there is a sudden increase in BER when the subcarrier spacing is close to half of the subcarriers (starts from a spacing equal to 30 subcarriers for Fig. 3.12).

Apart from the regions with no BER improvement, the remaining BER
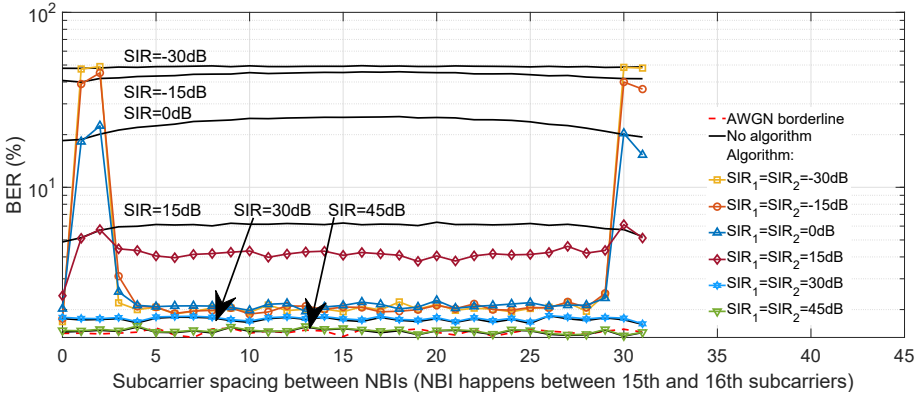
(a)
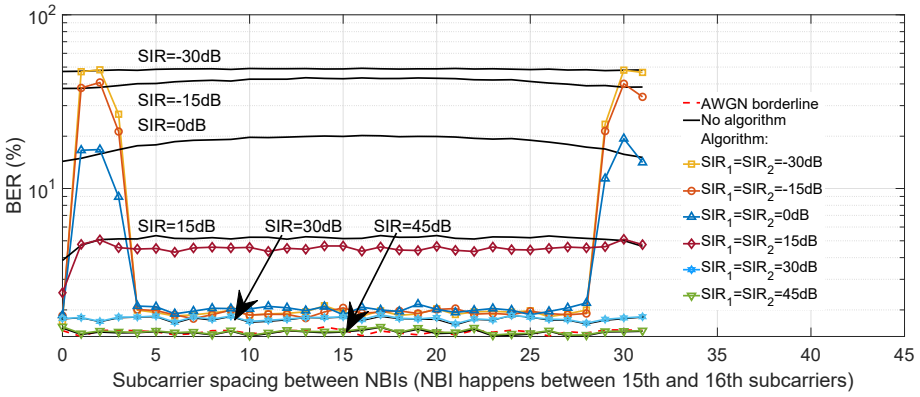
(b)

Figure 3.12: Differential NBI removal algorithm's performance against multiple NBIs when SIR = var and the spectral leakage parameter α varies: (a) $\alpha = 0.5$, (b) $\alpha = 0.25$.

performance is on average constant for a subcarrier spacing between neighbouring NBIs between 4 and 28. For this constant NBI performance region, the BER level does not exceed 4.6 % for the SIR level of 15 dB. The BER values of other SIR levels do not exceed a BER of 2.3 % for both α cases. The BER performance of the algorithm is slightly worse for α equal to 0.25 for the SIR level equal to 15 dB. The explanation for that is alike to the one for Fig. 3.9.

From Fig. 3.12, it can be concluded that there should be a distance of at least

four and no more than 28 subcarriers between two adjacent NBIs for the case with 64 subcarriers. For other subcarrier numbers, the distance between two neighbouring NBIs should be between 4 and $K/2 - 4$, where K is the total subcarrier number.

3.3.5 The algorithm's performance under multiple NBIs and constant AWGN

So far, the algorithm's performance has already been described for different SNR values and a single or two NBIs disturbing the signal simultaneously. This subsection will show the algorithm's capabilities against a different number of NBIs simultaneously disturbing the signal.

With the minimum absolute distance between two adjacent NBIs defined in the previous subsection, one may test the BER performance of the algorithm against multiple NBIs. Therefore, the algorithm will be tested against multiple NBIs separated by four subcarriers. QAM64 modulation scheme with 64 subcarriers can have a maximum of eight NBIs with this subcarrier separation.

Figure 3.13 reflects this. The figure contains the reference cases outlined with the black solid line. These lines present the reference cases for a different number of NBIs (from eight to one, top to down) simultaneously disturbing the signal along with AWGN when the algorithm was disabled. The red dashed line represents the reference case when only AWGN with an SNR equal to 16 dB was present in the system. Between the reference curves, there are multicoloured curves with different markers that represent the BER performance of the algorithm for a different number of NBIs. The curves are aligned in such a way that the lowest BER (the yellow line with square markers) is achieved for the case with one NBI. Then above there is the green line with triangular markers for the case with two NBIs and so on until eight NBIs.

Table 3.3: Simulation results for different subcarrier separations

Parameter		Value							
SIR, dB		-30							
Subcarrier number separation		4	5	6	7	4	5	6	7
Spectral leakage parameter		α=0.5				α=0.25			
BER, %	Two NBIs	2.16	2.15	1.96	2.04	2.11	2.10	1.87	1.91
	Three NBIs	2.56	2.32	2.42	2.31	6.64	2.22	2.51	2.04
	Four NBIs	3.75	2.79	2.75	2.69	11.07	3.19	2.56	2.41
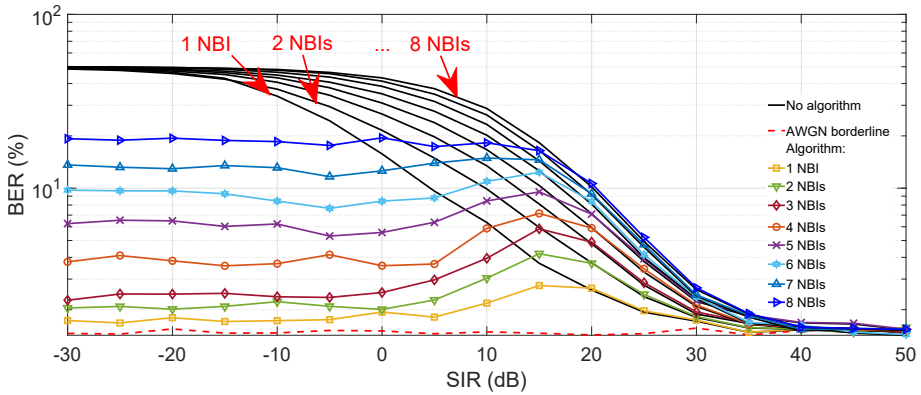
(a)
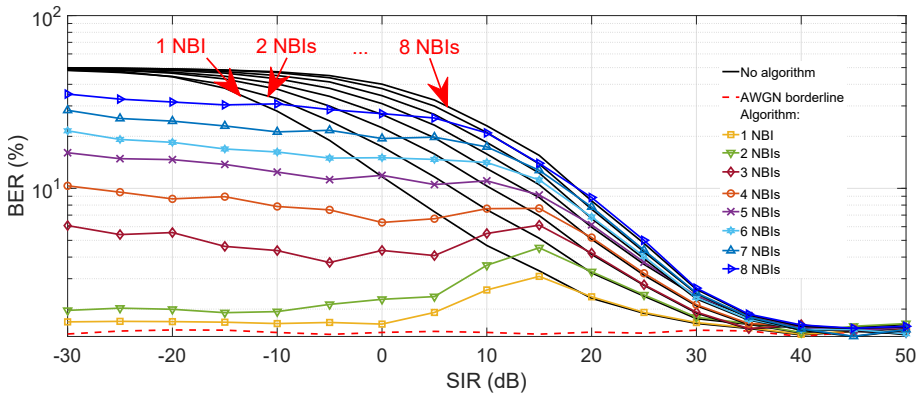
(b)

Figure 3.13: Differential NBI removal algorithm's performance against multiple NBIs when SNR = 16 dB with four subcarriers separation and the spectral leakage parameter α: (a) $\alpha = 0.5$, (b) $\alpha = 0.25$.

From Fig. 3.13, one may see that though the BER performance for both α cases is similar in terms of pattern, it still differs. If for α equal to 0.5, the maximum BER for eight simultaneous NBIs is 19.49 % at an SIR equal to 0 dB, then the same result for α equal to 0.25 is much higher and equal to 27.07 %. For both α cases each extra NBI increases the bit errors. This happens due to the overlap between the influence of NBIs on each other eventually leading to worse error estimations. The α case of 0.25 gives worse results because it becomes
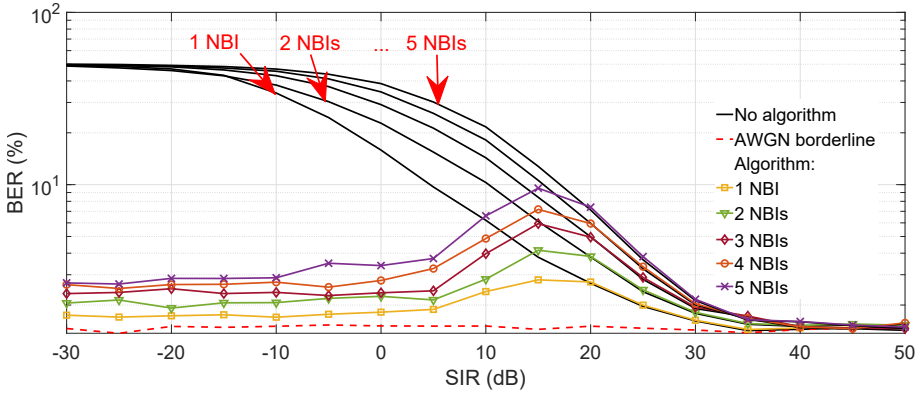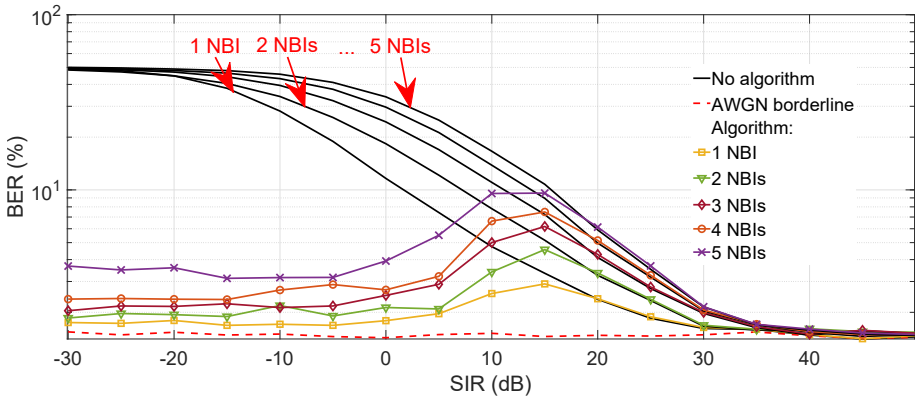
Figure 3.14: The performance of the differential NBI removal algorithm against multiple NBIs when SIR = var, SNR = 16 dB with six subcarriers separation and the spectral leakage parameter α varies: (a) $\alpha = 0.5$, (b) $\alpha = 0.25$.

more difficult for the algorithm to distinguish two NBIs, especially during various NBIs' phase combinations adversely affecting the detection procedure. Consequently, more simulations have to be performed to identify an optimal subcarrier separation between NBIs.

An excerpt of these simulations is shown in Table 3.3 showing the BER performance for both α cases with different subcarrier separations between NBIs. The results contain the BER performance of up to four simultaneous NBIs for

SIR and SNR equal to -30 and 16 dB, respectively. Looking at Table 3.3, one may notice that the algorithm performs better with each additional subcarrier between NBIs, so the dependency of NBIs on the performance of the algorithm is less. Starting from six subcarriers between adjacent NBIs, the correlation between results shrinks to ≈0.2%. A further increase in subcarrier separation does not bring a lot of improvement. Therefore, it is considered that at least six subcarrier separation has to be between adjacent NBIs for the algorithm to perform sufficiently. Figure 3.14 represents the full simulation for five simultaneous NBIs with six subcarriers separation.

One may also notice a degradation in the algorithm's performance for Fig. 3.14 in the SIR region from 0 to 20 dB that happens due to the decreasing NBI's share in the total error and, therefore, worse error estimation by the algorithm.

3.3.6 The algorithm's impact on different modulation schemes and a subcarrier number

Up until now, the results have been shown for the system with 64 subcarriers and QAM64. The algorithm's performance for different modulation schemes and a subcarrier number is shown in Fig. 3.15. For convenience, the QAM64 modulation scheme was chosen when the subcarrier number was varied (Fig. 3.15a), while for variable modulation schemes, a constant number of subcarriers equal to 64 was used (Fig. 3.15b). The simulations were performed for a single NBI (SIR is variable) and AWGN with an SNR of 16 dB. The results depict the algorithm's BER impact for two spectral leakage cases ($\alpha = 0.5$ and $\alpha = 0.25$ having subscripts in figures as 0.5 and 0.25, respectively). The algorithm's impact is the difference in BER between the reference case when the algorithm is not in action and the BER performance of the system when the algorithm is active. Figure 3.15 represents heatmaps having subscripts for different α cases on their horizontal axes.

Figure 3.15 presents a downward pattern in terms of the algorithm's BER impact either towards an increase in subcarriers or a modulation scheme order. In addition, the algorithm's BER impact for $\alpha = 0.25$ is lower than for $\alpha = 0.5$. The explanation for that is the following. The most extreme case for spectral leakage is when $\alpha = 0.5$. It means that more energy leaks to subcarriers. Therefore, more subcarriers can be affected negatively. As a result, the reference BER performance degrades as presented in the heatmaps. One may also notice that Fig. 3.15 has a negative BER impact meaning that the algorithm's BER performance is worse than the reference case without the algorithm. Nevertheless, this BER degradation does not exceed more than 0.03 % and 0.8 % for Figs. 3.15a and 3.15b, respectively. This degradation in the algorithm's BER impact

SIR (dB)	$64_{0.5}$	$64_{0.25}$	$128_{0.5}$	$128_{0.25}$	$256_{0.5}$	$256_{0.25}$	$512_{0.5}$	$512_{0.25}$	$1024_{0.5}$	$1024_{0.25}$	$2048_{0.5}$	$2048_{0.25}$
-30	46.94	46.51	46.95	46.41	46.51	45.54	45.66	43.67	43.63	41.37	41.27	36.54
-10	32.02	26.55	26.46	20.76	21.06	15.75	15.8	11.44	11.44	8.23	8.18	5.8
10	3.99	2.34	3.08	1.91	2.26	1.6	1.58	1.08	1.14	0.8	0.81	0.56
30	-0.03	-0.02	-0.02	-0.01	-0.02	-0.03	-0.01	-0.02	-0.01	-0.02	0.02	0
50	-0	-0.01	-0.01	-0.02	-0.02	-0.02	-0.01	-0.02	-0.01	-0.01	-0.01	-0.01

Subcarrier number with regards to alpha values

(a)

SIR (dB)	$16_{0.5}$	$16_{0.25}$	$64_{0.5}$	$64_{0.25}$	$128_{0.5}$	$128_{0.25}$	$256_{0.5}$	$256_{0.25}$	$512_{0.5}$	$512_{0.25}$	$1024_{0.5}$	$1024_{0.25}$	$2048_{0.5}$	$2048_{0.25}$
-30	48.92	47.75	46.94	46.51	43.85	43.96	40.53	40.14	36.93	36.64	32.92	33.1	29.88	29.12
-10	26.55	18.74	32.02	26.55	32.95	27.47	30.46	25.98	28.09	24.74	25.12	21.68	22.42	19.62
10	1.7	0.88	3.99	2.34	4.21	2.39	4.16	2.33	4.09	2.29	3.52	1.81	3.13	1.6
30	0	0	-0.03	-0.02	-0.13	-0.15	-0.28	-0.35	-0.5	-0.48	-0.62	-0.7	-0.66	-0.62
50	0	0	-0	-0.01	-0.07	-0.16	-0.26	-0.3	-0.5	-0.5	-0.68	-0.63	-0.58	-0.7

Modulation order with regards to alpha values

(b)

Figure 3.15: The algorithm's BER impact comparison for different modulation schemes and a subcarrier number when the system is disturbed by AWGN with SNR = 16 dB, SIR = var: (a) QAM64 with a different subcarrier number, (b) Different modulation schemes for 64 subcarriers.

only happens when the SNR value exceeds the SIR value or in other words, the main assumption about the SIR being lower than the SNR is infringed. Let us look closer at these heatmaps separately.

A reader can notice a decrease in the algorithm's impact with an increase in subcarriers (see Fig. 3.15a). The explanation for that is the following. By increasing the number of subcarriers, the root-mean-square value of the time-domain signal remains the same on average. This means that the same SIR value will negatively affect the same number of subcarriers, i.e. more likely to cause a symbol flip. Consequently, though the same number of symbols is affected, the reference BER will be lower and the algorithm's impact decreases

despite the algorithm performing as well as for a lower subcarrier number.

When the modulation scheme order is increased (see Fig. 3.15b), the algorithm's performance decreases due to high symbol congestion. It becomes much easier not only for an NBI to cause a symbol flip but also for AWGN. With this, the algorithm becomes more sensitive to random AWGN spikes, which can make the algorithm find disturbances at subcarriers where there are no actual NBIs. As a result, the algorithm's performance decreases with an increase in a modulation scheme order. For example, for a modulation scheme of 2048, the algorithm's BER gain does not exceed ≈ 30 %, while for QAM16 the maximum possible BER impact was registered at ≈ 49 %. The influence of AWGN on the signal has already been shown in [16] and recommendations were given to stick to a lower modulation scheme orders for a higher algorithm's output.

3.4 Algorithms' comparison

After conducting thorough simulations on the "Differential" NBI removal algorithm, it was decided to compare the two proposed algorithms. Moreover, the time and frequency domain technique proposed by T. Pande and others in [1] was also added to the comparison.

Let us call the solution [1] as the "Pande" algorithm. This solution identifies the spectral position of an NBI in two stages: the rough estimation happens by estimating the maximum value of the received signal, while the fine estimation happens by calculating the S-curve metric. The metric is presented in Fig. 3.16 and it is the analogy of the early-gate synchroniser.

The metric M is calculated using the following expression:

$$M = \frac{|R_{m-1}|^2 - |R_m|^2}{|R_{m-1}|^2 + |R_m|^2},$$ (3.31)

where R_m is the received signal at the subcarrier m that results in the maximum R_m value.

After locating the NBI, the "Pande" algorithm shifts the received signal in the time domain by the frequency offset α by the multiplication operation. This allows for shifting the spectrum in such a way that the NBI happens to be on a subcarrier, so no spectral leakage happens. Then, it is removed from the signal by nulling in the frequency domain the subcarrier to which the NBI was shifted. After that, the received spectrum is shifted back by the NBI frequency offset in the time domain. Finally, the improved signal is converted again to the frequency domain after which decoding happens. The authors, in [1], also
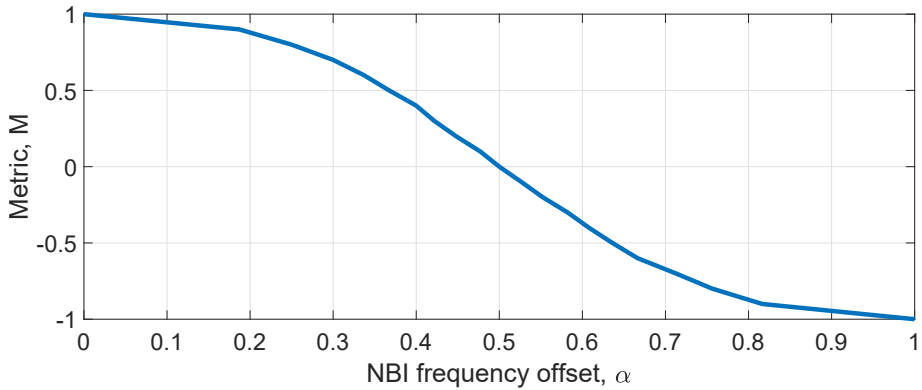
Figure 3.16: The S-curve metric for the T. Pande solution [1].

propose to use windowing for negating the NBI frequency estimation errors, however, it is omitted in the following comparison.

To perform a fair comparison between different solutions, the varying with a step of 1 dB SNR and SIR parameters were brought to the common basis E_b/N_0 and E_b/N_I, respectively. The simulation tests were performed for a single NBI with the frequency offset α equal to 0.5. The modulation scheme was QAM64. Due to the "Mod-remod" algorithm, which uses Hamming coding, the number of subcarriers was put to 60.
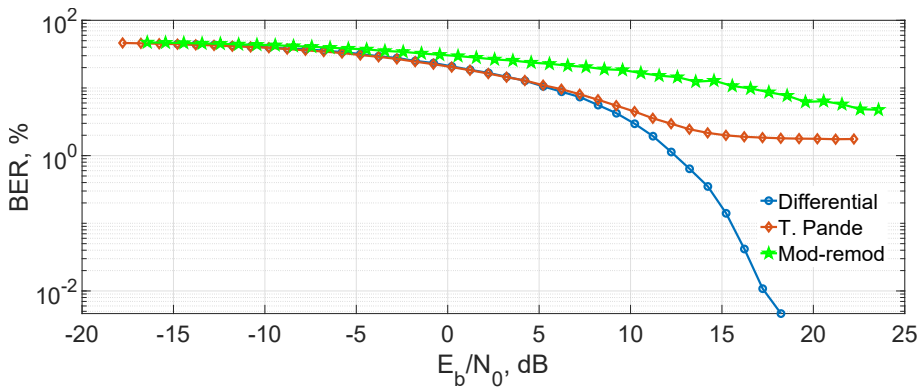
Figure 3.17: Simulation results comparison between different algorithms when SNR was variable from -10 to 30 dB and SIR was put to be equal to 0 dB.

Figure 3.17 presents the simulation results when the SNR was variable and SIR was put to be equal to 0 dB. The blue line represents the "Differential" algorithm, while the orange and green lines stand for "Pande" and "Mod-remod" algorithms. The first two solutions use maximum values of the received signal to locate the disturbance, while the latter depends on values less influenced by the disturbance. Since there is always AWGN present, it is extremely difficult for the "Mod-remod" algorithm to locate the NBI. Consequently, it shows worse results in comparison to other solutions. Unlike the "Pande" solution which has no redundant bits, the "Differential" algorithm introduces half of the sent bits as redundant. Nevertheless, even with this redundancy rate, it is capable of locating the NBI more accurately. Hence, the performance of the "Differential" algorithm is better than the one of the "Pande".

If one instead of SNR starts varying SIR values and keeps the SNR value equal to be equal to 16 dB as was done for solely "Differential" algorithm simulations, then one may notice a similar trend shown in Fig. 3.18a with the one presented in Fig. 3.17. The "Differential" algorithm excels while the "Mod-remod" algorithm has the highest BER. The explanation for this performance is the same as for Fig. 3.17 as the SNR of 16 dB affects the estimation of both the "Mod-remod" and "Pande" algorithms more than it does for the "Differential" one. However, if one conducts the same simulations for the larger SNR (i.e. smaller AWGN power), the resulting curves follow a different pattern. Figure 3.18b shows this when SNR was equal to 60 dB. Both the "Differential" and "Pande" solutions have bit errors at relatively large noise levels. However, if the "Pande" algorithm had minor estimation errors that led to eventually large BER values, the "Differential" algorithm could precisely recognise the frequency offset α value. Nevertheless, the "Differential" algorithm still had errors due to the folding spectrum operations. Normally, when an NBI is found, its α parameter and approximate subcarrier are obtained for the folded spectrum. Due to the periodicity in the spectrum, the subcarrier location is either in the first or second halves of the spectrum. The algorithm foresees that and identifies the subcarrier by calculating the residual energy in the received spectrum by subtracting the recreated NBI happening in the first half. Then it compares the residual energy for the recreated NBI happening in the second half. By comparing these energies, the algorithm decides the NBI subcarrier location in favour of the lower residual energy. When an NBI has powers lower than the signal, the implemented energy comparison method is not always accurate (see Fig. 3.18b). Nevertheless, starting from the E_b/N_I level lower than 2.2 dB, the "Differential" algorithm does not have any errors at all, whereas the "Pande" method stabilises at the BER level of 1.7 % at E_b/N_I values lower than -4 dB. The "Mod-remod" algorithm does not have any errors when it can still identify the subcarriers less affected by the spectral leakage effect. Consequently, there are no bit errors until the E_b/N_I ratio reaches -4.4 dB. Then, the "Mod-remod"
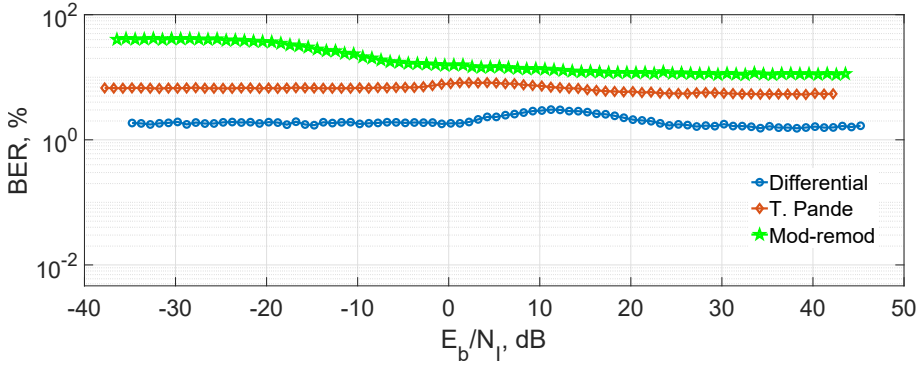
(a)
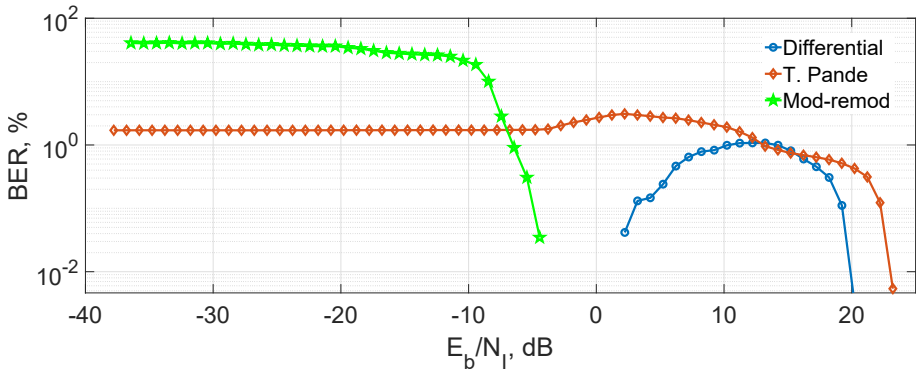
(b)

Figure 3.18: Simulation results comparison between different algorithms when SIR was variable from -30 to 50 dB and SNR was put to be equal to: (a) 16 dB, (b) 60 dB.

curve shoots up until BER equals 18.5 % at the E_b/N_I of -9.4 dB and then gradually rises up to the BER value of 40 %.

3.5 Conclusion

In this chapter, the differential NBI removal algorithm has been proposed. The differential NBI removal algorithm does not require any prior information about

the disturbance. It only demands the NBI to be constant during one OFDM symbol.

Extended tests against a single NBI with a variable SIR number have been performed. Along with an NBI, the system's noise was present and modelled as an AWGN. With simulations, it has been shown that the differential algorithm works on average the best when the threshold parameter (v) of the minimum Euclidean distance between the adjacent symbols on a constellation diagram is equal to 0.5. The algorithm's accuracy is improved by the iterative refinement block that is based on the convergence of the found NBI parameters. A tradeoff between accuracy and computational cost for refinement happens when the CN is equal to 0.0001 and this precision is within two refinement iterations.

The algorithm has been validated for multiple scenarios for QAM64 with 64 subcarriers. For a single NBI with a constant AWGN, the algorithm's performance is substantially better than for the reference case without the algorithm and at times can reach up to 49 % of BER improvement. The highest algorithm's output was noted for low modulation scheme orders and a small number of subcarriers.

The algorithm was then tested against a variable SNR parameter achieving the BER results not exceeding 1.3 % for the SNR values higher or equal to 20 dB.

Varying a number of simultaneous NBIs resulted in different algorithm's optimal BER responses (i.e. the low correlation between results for different α cases) when a subcarrier separation between two adjacent NBIs was at least six subcarriers.

The "Differential" algorithm was also compared with "Mod-remod" and "Pande" solutions showing the best performance for a broad range of E_b/N_0 and E_b/N_I values. The algorithm has sometimes difficulties in identifying the NBI subcarrier due to folding spectrum operations, albeit it happens at very low NBI and AWGN powers at the same time (SNR greater than or equal to 60 dB and E_b/N_I is higher than or equal to 2.2 dB).

The differential NBI removal algorithm proved its efficiency in simulations. Nevertheless, the purpose of this work is to make this solution beneficial for industrial purposes. Therefore, extra work has to be performed to the algorithm's validation in the lab setting to finally deploy the algorithms on communication board units in a real environment.

Chapter 4

Practical validation of the NBI removal algorithms

Chapters 2 and 3 detailed the "Mod-remod" and "Differential" NarrowBand Interference (NBI) removal algorithms, respectively. It was shown that these algorithms were derived assuming that the communication system was synchronised in both time and frequency and that there were no reflections and, hence, no multipath fading. While it is acceptable to initially develop, derive and simulate a theory, caution must be exercised when testing these algorithms, even in a laboratory setting.

During the algorithms' validation, a number of problems arose. First, both of the aforementioned algorithms ("Mod-remod" and "Differential") were made for subcarriers entirely composed of data. In contrast, real systems are more complicated and contain guard, Direct Current (DC) and pilot subcarriers. Second, the initial implementation of the "Mod-remod" algorithm completely made the used synchronisation and equalisation blocks unable to perform their task. Consequently, Orthogonal Frequency Division Multiplexing (OFDM) frames could not be detected and communication could not take place. As a result, there were attempts to validate the algorithm not using conventional synchronisation. For instance, the communication was frequency-synchronised by using the same reference local oscillator frequency at the transmitting and receiving devices. Timing synchronisation was not real-time and was performed by calculating the lowest Bit Error Rate (BER) and the largest Modulation Error Rate (MER) value of the captured sequence. Therefore, this chapter will show the main hurdles of the algorithms' deployment and solutions that were implemented to overcome these hurdles. *Some of the findings have been*

obtained during the supervision of Master's students Brian Leeman [51] and Jop Bouckaert. The parts of content and results of the chapter have already been disseminated in [52]. That publication provides the validation model and results for the "Mod-remod" NBI removal algorithm.

4.1 Synchronisation in wireless communication

The communication devices that were used to validate the algorithms pertain to the Software-Defined Radio (SDR) group. The Institute of Electrical and Electronics Engineers (IEEE) P1900.1 Working Group defines in [53] an SDR as any radio capable of realising its physical-layer functions using software. The physical layer is defined in [54] and is responsible for the connection between network nodes as well as raw data (series of zeroes and ones) transmission between them. SDRs are highly configurable and allow the implementation of different communication standards and, therefore, the creation of various networks. For example, a Software-Defined Network (SDN) is an emerging communication type allowing to realise self-healing mesh networks that form a backbone for some Wireless Sensor Networks (WSNs) about which more explanation will be given in the next chapter.

Due to the programmable SDR devices, one may create a time-discrete signal following a certain set of rules (usually prescribed by standards) and allowing it to be precisely recovered at the receiver's side. Irrespective of the chosen way, or in other words the chosen communication protocol, for creating a time-discrete signal, the system has to be synchronised in order to establish a communication session. Due to imperfections in the timing clocks and Local Oscillators (LOs) of the transmitter and receiver, there are timing and frequency offsets leading to data loss if not or wrongly synchronised.

For better visualisation of the consequences of synchronisation, let us look at Fig. 4.1. It represents a received OFDM signal captured by a signal analyser. The figure contains the signal's real and imaginary I-Q values along with its frequency spectrum. On top of the figure, the main capturing receiver's parameters are shown. From the I-Q values it can be seen that the captured OFDM signal consists of two identical OFDM frames separated by zero-padded samples. The first step of a synchronisation process is to identify the beginning of an OFDM frame. This will allow distinguishing the transmitted signal from any other existing signals (referred to as noise) in the captured data. This process of finding the OFDM frame's beginning is called Coarse Timing Offset (CTO) estimation or packet detection. Time and frequency synchronisation go hand-in-hand together. Consequently, as soon as the CTO estimation happened, Coarse
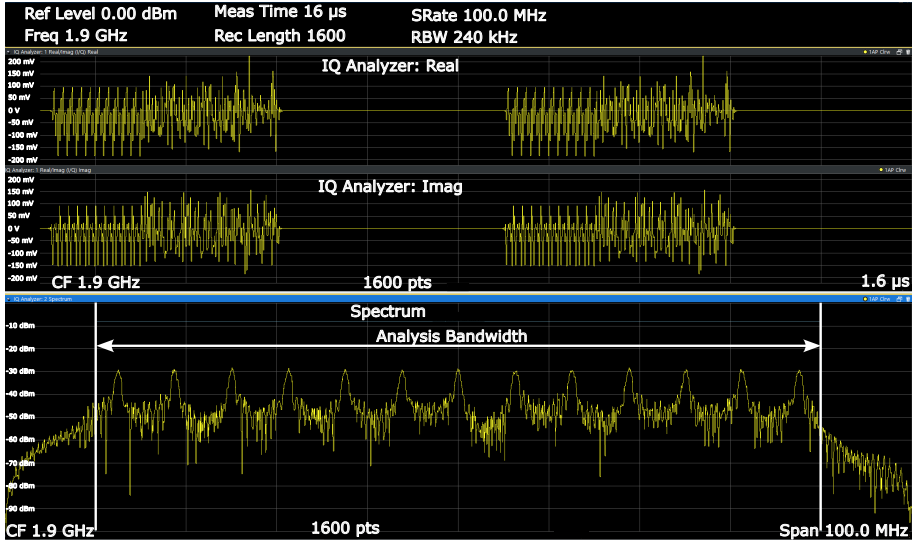
Figure 4.1: A typical example of a captured signal by a spectral analyzer.

Frequency Offset (CFO) estimation, takes place. Both the frequency and phase offsets can be represented as a circular rotation along the I-Q diagram of the received signal. A simple example of a Quadrature Phase-Shift Keying (QPSK) signal with and without carrier frequency offset is presented in Fig. 4.2. It can be seen that the frequency offset is not big enough to cause demodulation issues for the received QPSK signal. However, for higher modulation scheme orders it might cause demodulation errors. In addition, it gives a clear image of what is happening to the signal if the frequency offset correction is not happening.

After the initial CTO and CFO synchronisation procedures, a refinement happens. This refinement is often called fine synchronisation. Fine Timing Offset (FTO) synchronisation or sample timing detection tracks the OFDM frame beginning to the correct sample. Knowing the exact symbol allows for performing Fine Frequency Offset (FFO) correction. Subsequently, channel estimation and equalisation have to take place to properly address the effects of multipath fading. As a result, after channel estimation and equalisation, the signal is adjusted for the present amplitude and frequency imperfections that were introduced due to synchronisation estimation errors. Finally, the received signal is additionally updated using pilots, so the remaining phase and amplitude imperfections are put to a bare minimum. Schematically, this can be shown as a block scheme presented in Fig. 4.3. Before looking closer at each of
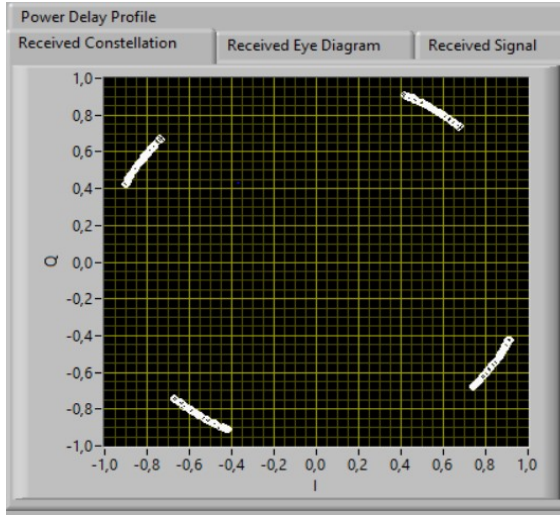
(a)
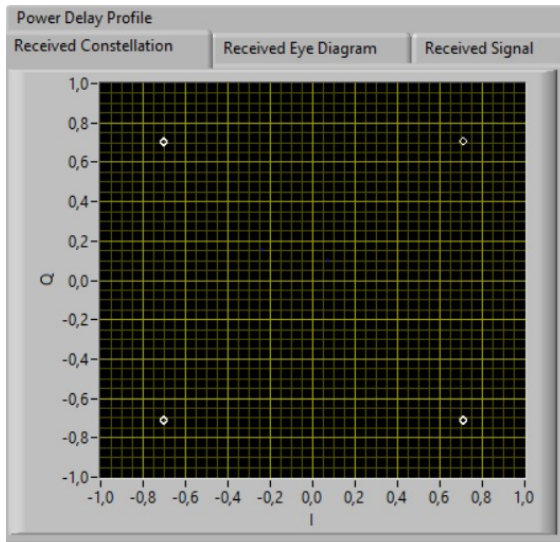
(b)

Figure 4.2: Not corrected (a) and corrected (b) carrier frequency offset.

these blocks, let us, first, determine the frame composition.
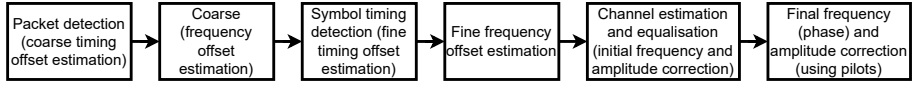
Figure 4.3: OFDM synchronisation system.

The used OFDM communication system that is recreated in this manuscript with the help of SDRs is based on the Wireless Local Area Network (WLAN) 802.11a standard [2]. The OFDM frame consists of a preamble, header and payload, each of which differs in generation and duration. Figure 4.4 represents a block scheme of an OFDM frame the basis of which was taken from IEEE802.11a. Let us look closer at each of the aforementioned OFDM frame's parts.
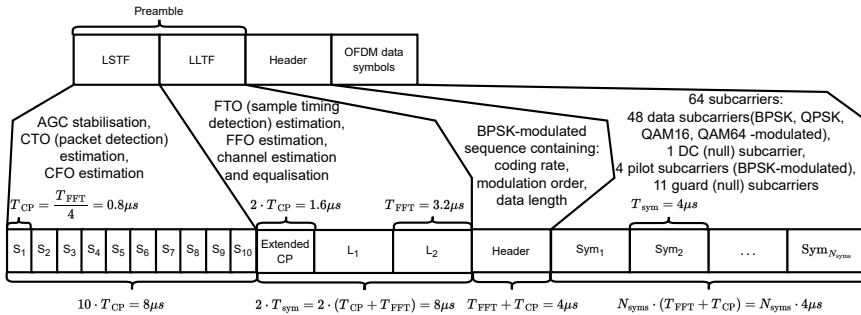
Figure 4.4: OFDM frame based on the WLAN 802.11a standard [2].

The preamble consists of training sequences that are called Legacy Short Training Field (LSTF) and Legacy Long Training Field (LLTF). These training sequences are prepended to an OFDM frame in the time domain. LSTF is generated with a length of a Cyclic Prefix (CP) that is equal to $T_{\text{FFT}}/4$, where T_{FFT} is the Fast Fourier Transform (FFT) duration. The LSTF consists of ten FFT duration quarters. Each short LSTF training symbol is marked as $S_1 \ldots S_{10}$ in Fig. 4.4. This is equal to two complete OFDM symbols that last for 8 μs. Ten copies of the short sequence allow Automatic Gain Control (AGC) to stabilise. It also allows performing the CTO (packet detection) and CFO estimations.

LLTF comprises two long training symbols L_1 and L_2. These two symbols are identical and their duration is equal to two FFT durations (T_{FFT}). LLTF also

contains an extended CP, which is double the size of a normal CP and precedes two long training symbols. Consequently, LLTF is equal to 8 μs. Based on LLTF, FTO (sample timing detection) and LLTF estimations become possible. It is also for channel estimation and equalisation procedures.

A visualisation of the preamble containing the aforementioned LSTF and LLTF in the time domain is presented in Fig. 4.5. Each copy of the total LSTF sequence parts is separated using a black dashed line. In contrast, the red dashed line is used for LLTF sequence parts.
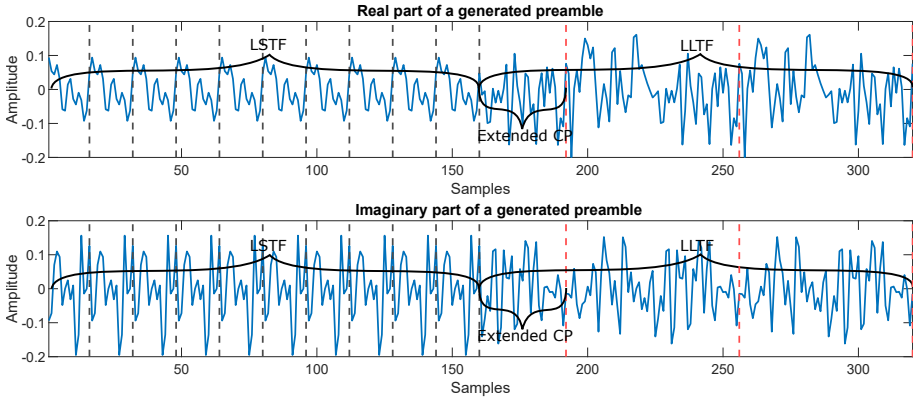
Figure 4.5: OFDM preamble composition.

Once an OFDM frame is recognised and the needed synchronisation steps are performed, the receiver should know the data length or the number of OFDM symbols along with the used coding rate and modulation order scheme. The header serves this purpose. To be robust at wide Signal-to-Noise Ratio (SNR) ranges, the training sequence, from which the header is composed, is Binary Phase-Shift Keying (BPSK)-modulated (see Fig. 4.4).

With the needed information from the header, the receiver is able to recognise a number of OFDM symbols N_{syms} that were sent in the OFDM data symbol part. Each symbol consists of a CP and data symbol, which lasts a complete FFT period T_{FFT}. Therefore, one symbol has a duration of $4\mu s$. As was mentioned in Chapter 1, CP is a repetition of the tail of the data symbol. The latter consists of 64 subcarriers. The frequency spectrum of the created OFDM data symbol is presented in Fig. 4.6. It can be seen that orthogonality is preserved among subcarriers. To protect the OFDM system and other systems working on adjacent frequencies from each other, guard subcarriers are introduced on the sides of an OFDM symbol. They carry no energy, thus the name "null"
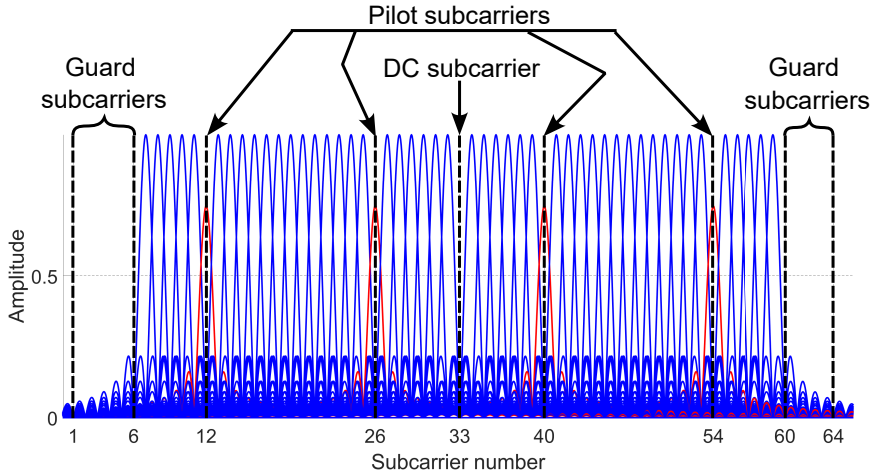
Figure 4.6: OFDM data symbol structure.

can be found in literature and they do not carry data symbols. Next to guard subcarriers carrying null energy, there is one more subcarrier with zero energy, the DC subcarrier. It is located in the middle of the created data symbol. The remaining subcarriers are pilot and data subcarriers, which are marked with red and blue colour. As was shown in Fig. 4.4, pilot subcarriers are bound to BPSK modulation, whereas data subcarriers have a wider option of modulation schemes. Therefore, for visualisation purposes, the amplitude difference between pilot and data subcarriers can be noticed.

Since the OFDM frame composition has been covered, it is appropriate to give a bit more explanation about the synchronisation process in the realised system to understand the main hurdles and bottlenecks that occurred during the algorithms' deployment and validation.

4.1.1 OFDM packet detection

To start a synchronisation procedure, the system must know when to initialise. OFDM packet detection or CTO estimation serves this purpose. As was mentioned in the previous section, this is done with the help of a known training sequence from which an OFDM is composed. This is when LSTF is used. The packet method can be described using the example of the double sliding window packet detection [55].

The double sliding window packet detection algorithm calculates the energy of two sliding windows A and B represented in Fig. 4.7. These windows are deemed to be stationary with regard to the upcoming packet. The figure shows the response of the double sliding window packet detection algorithm at different sampling instances n. The vertical axis in Fig. 4.7 stands for the packet detection metric m_n. The metric is calculated as the ratio between the energy g_n and y_n within the sliding windows A and B.

$$g_n = \sum_{u=0}^{M-1} r_{n-u} r_{n-u}^* = \sum_{u=0}^{M-1} |r_{n-u}|^2, \tag{4.1}$$

where r_n is the received signal, n is a sample number, u is a sample number within the sliding window A, M is the sliding window size, and * is a complex conjugate sign used further in equations as well.

$$y_n = \sum_{l=0}^{M-1} r_{n-l} r_{n-l}^* = \sum_{l=0}^{M-1} |r_{n-l}|^2, \tag{4.2}$$

where l is a sample number within the sliding window B.

$$m_n = \frac{g_n}{y_n}. \tag{4.3}$$

Let us look once more at Fig. 4.7. When the packet has not reached yet the sliding windows, the latter correlate the noise resulting in a flat metric (zone I in Fig. 4.7). As soon as the packet comes within the window A, the metric starts rising (zone II). The rise goes on until the packet completely covers window A resulting in the metric maximum value. After this moment, the further propagation of the packet decreases the metric as the packet starts covering window B (zone III). When the packet is completely within two sliding windows, the metric becomes again flat and the following packet propagation does not result in the metric change (zone IV). The OFDM packet is deemed to be detected when the metric value reaches the threshold (see Fig. 4.7).

The detection method presented in this manuscript is based on the one described in [56]. This method is similar to the double sliding window packet detection algorithm. However, the method [56] is adapted by benefiting from the repetitiveness (periodicity) of the LSTF short training symbols. Let us introduce two sliding windows C and P. The former is calculated as the crosscorrelation between the received signal r_n and its delayed version. The delay D is equal to the length of an LSTF's short training symbol. For IEEE802.11a, the delay is equal to 16. Window P normalises the crosscorrelation value of window C. Consequently, window P is calculated as the autocorrelation value.
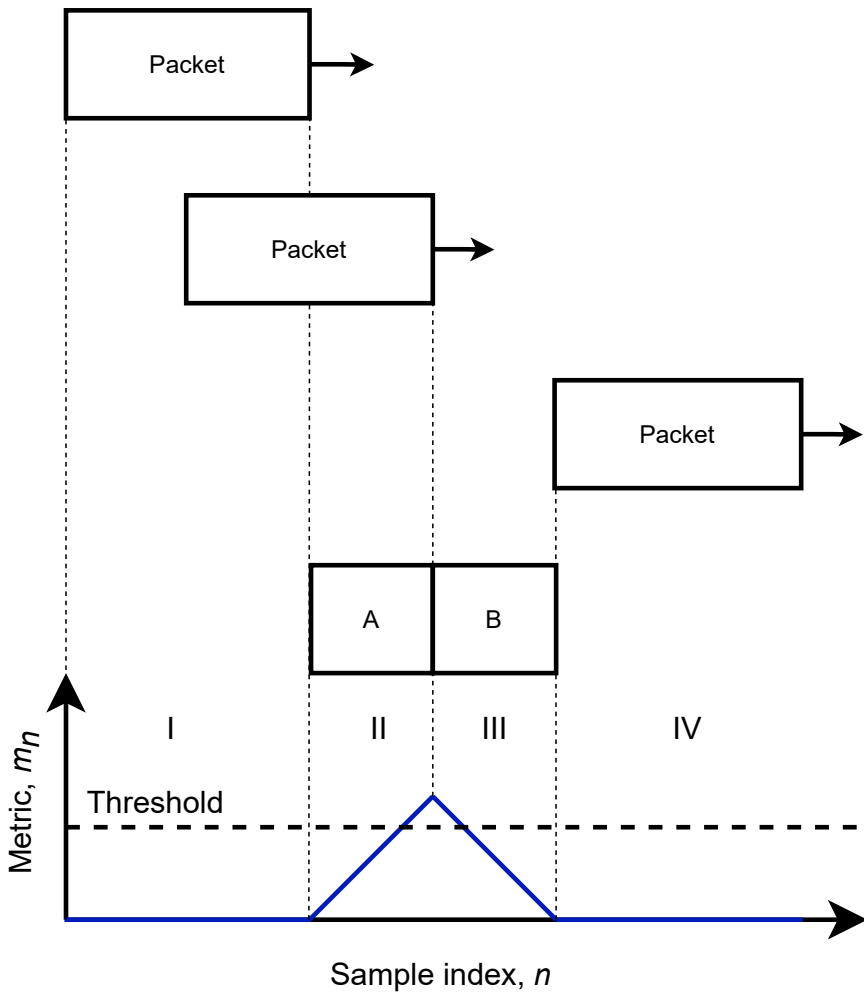
Figure 4.7: Representation of the working principle of the double sliding window detection algorithm.

Mathematically, the energy values of windows C and P can be written using the following equations:

$$c_n = \sum_{u=0}^{M-1} r_{n+u} r_{n+u+D}^*. \tag{4.4}$$

$$p_n = \sum_{u=0}^{M-1} r_{n+u+D} r_{n+u+D}^* = \sum_{u=0}^{M-1} |r_{n+u+D}|^2. \tag{4.5}$$

The detection metric m_n:

$$m_n = \frac{|c_n|^2}{(p_n)^2}. \tag{4.6}$$

Due to a normalisation procedure, the packet detector's metric m_n should have a value close to 1 when the packet is detected. Since an OFDM frame consists of 10 identical LSTF short training symbols (except for a carrier frequency offset), the metric values will reach a plateau with the values oscillating around 1. This plateau will indicate the beginning of an OFDM's frame. To not miss the beginning of the frame, one should correctly select this metric.

Figure 4.8a shows a captured sequence of an OFDM signal, while Fig. 4.8b depicts the CTO estimation based on metric m_n. It can be seen that the receiver captured two full OFDM frames. Consequently, there are two plateaus in Fig. 4.8b, of which only one is scaled up. The metric starts rising from approximately the 480$^{\text{th}}$ sample and reaches the plateau at approximately the 530$^{\text{th}}$ sample. Due to a non-multipath environment, the height of the plateau is continuously around 1 and has a duration of LSTF. The two distinct peaks reaching the amplitude of approximately 570 happen due to a sharp power decrease as soon as an OFDM frame ends.

4.1.2 Carrier frequency offset estimation

As was mentioned before, oscillators at the transmitter's and receiver's sides will always have slightly different sampling periods resulting in a carrier frequency offset. As was shown in Fig. 4.2a, the carrier offset rotates subcarriers and may introduce InterCarrier Interference (ICI). The latter causes a loss of orthogonality, eventually leading to communication degradation.

Exploiting the derivation of [55], the received signal $R_{l,m}$ (l and m are the current OFDM symbol and subcarrier, respectively) depends on the following term which is introduced due to the carrier frequency offset:

$$e^{j2\pi m t_\Delta l \frac{T_s}{T_u}}, \tag{4.7}$$

where T_s and T_u are the durations of the total OFDM symbol and the useful data portion. t_Δ is the sampling period offset.

$$t_\Delta = \frac{T_{\text{Tx}} - T_{\text{Rx}}}{T_{\text{Tx}}}, \tag{4.8}$$
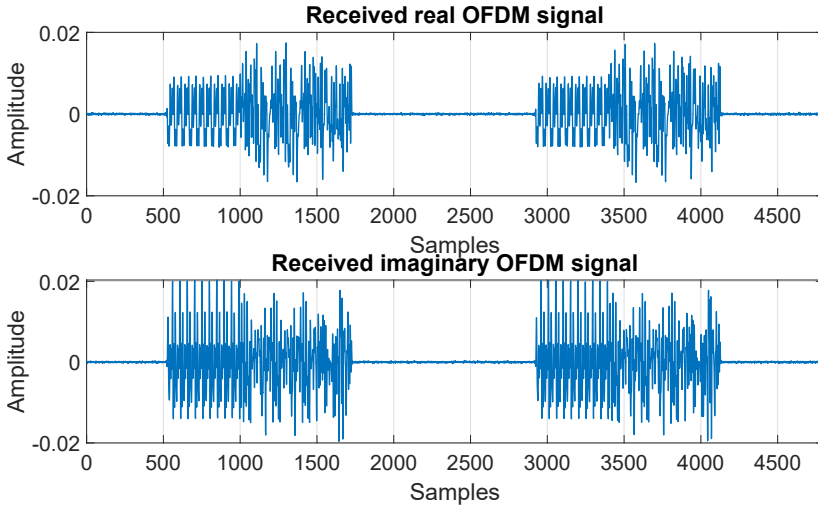
(a)
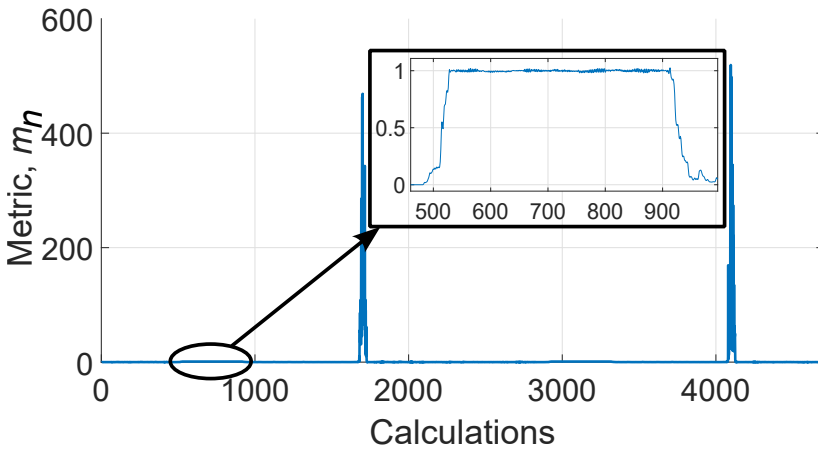
(b)

Figure 4.8: (a) Real & imaginary received noisy (SIR $= 25$ dB) values of the transmitted OFDM signal, (b) Coarse timing synchronisation.

where T_{Tx} and T_{Rx} are the sampling periods of the transmitter and receiver, respectively.

Expression (4.7) represents the rotation angle the received signal will experience.

It can be noticed that the rotation is proportional to the subcarrier and OFDM symbol numbers m and l. This means that the larger these values, the more the received signal will be rotated.

There are multiple ways of estimating the carrier frequency offset. Some are mostly used in broadcast or continuous transmission type OFDM systems (e.g. non-data-aided algorithms and CP-based algorithms), whereas, for WLAN applications, data-aided algorithms are used. Since for validation purposes, the IEEE802.11a standard was used as a basis for frame composition, the data-aided carrier frequency offset estimation algorithm is described below.

The data-aided carrier frequency offset estimation algorithm uses a maximum-likelihood estimator which works with the training information embedded into the preamble of a transmitted OFDM preamble. The required training information is bound to have at least two consecutive repeated symbols. Both LSTF and LLTF meet this condition.

To derive the carrier frequency offset, one may, first, need to perform some preliminary operations. Below, only the final expressions are shown, while [55] provides a more detailed derivation.

If one assumes that the noise component is so small that it can be neglected, the received complex baseband signal r_n can be written as:

$$r_n = s_n e^{j2\pi f_\Delta n T_s}, \tag{4.9}$$

where $f_\Delta = f_{\text{Tx}} - f_{\text{Rx}}$ is the carrier frequency offset that is equal to the difference between the transmitter and receiver carrier frequencies, s_n is the transmitted signal, n is the current sample number.

The maximum-likelihood frequency offset estimator uses an intermediate value z to define the carrier frequency offset. The intermediate value is calculated as a crosscorrelation between two sequential identical training symbols. During the CFO estimation, LSTF training symbols are used, whereas for the FFO estimation, LLTF training symbols are implemented.

$$z = \sum_{n=0}^{L-1} r_n r_{n+D}^* = e^{-j2\pi f_\Delta n T_s} \sum_{n=0}^{L-1} |s_n|^2, \tag{4.10}$$

where D is the delay between two consecutive identical training symbols, L is the length in samples of the training symbol.

It can be noticed that the last expression (4.10) has the rotation angle (phase offset) proportional to the carrier frequency offset. This will allow writing down an expression for the carrier frequency offset estimation:

$$\hat{f}_\Delta = -\frac{1}{2\pi D T_s} \phi_z, \tag{4.11}$$
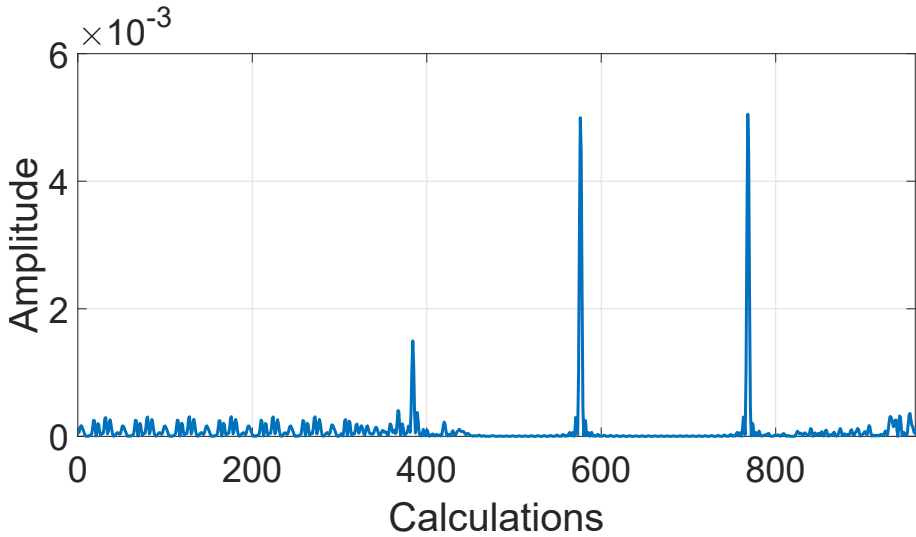
Figure 4.9: FTO estimation of the captured OFDM signal.

where ϕ_z is the phase offset taken as the angle of the argument of z.

4.1.3 OFDM symbol timing detection (FTO estimation)

Once a rough estimate of the beginning of the OFDM frame is found, a more precise (up to a sample) timing estimation can be performed. This timing refinement is done by calculating the crosscorrelation of the received signal r_n and a known reference t_m training symbol. This symbol is a known LLTF long training symbol. As a result, the OFDM symbol timing detection estimate $\hat{t}_s$ is the maximum absolute value of the aforementioned crosscorrelation:

$$\hat{t}_s = \arg\max_n \left| \sum_{m=0}^{L-1} r_{n+m} t_k^* \right|^2 , \qquad (4.12)$$

where n represents the current sample number of the received signal, m is the current index number within the sliding window.

The crosscorrelation result of (4.12) will give two distinct peaks (see Fig. 4.9) representing starting positions of the LLTF halves.

4.1.4   Equalisation

To properly address the communication channel effects in the received signal, one may need to perform equalisation. Since LLTF has a duration of two complete OFDM symbols, it contains all the subcarriers that are in the signal. If we assume that the LLTF sequence experiences the same channel effects as the signal, then after the removal of CPs from half of the received OFDM LLTF sequence, the resulted values can be represented as:

$$R_m = H_m \cdot S_m, \tag{4.13}$$

where m is a subcarrier number, R_m is half of the received LLTF sequence, H_m is the influence of the transmission channel resulting in the signal's attenuation or amplification and S_m is the originally transmitted half of the received LLTF sequence.

To reverse the effects of the channel on the signal, one may need to take the inverse of the channel frequency response:

$$W_m = \frac{1}{H_m} = \frac{S_m}{R_m}, \tag{4.14}$$

where W_m is the equalisation factor for a subcarrier m.

To perform equalisation one may need to perform the aforementioned actions (equations 4.13, 4.14) for the second half of the LLTF sequence and average the obtained W_m values. After that, the adverse effects of the transmission channel are negated by multiplying the averaged W_m values by the received data values.

4.1.5   Final frequency and amplitude adjustments using pilots

When the signal is adjusted in time and frequency and even equalised, there can still remain phase and frequency offsets that are corrected using pilots. Pilots are like the preamble predefined and known by the receiver. They are embedded within payload or data symbols. Pilots correct the remaining phase rotations that are present in OFDM data symbols. These rotations can be visualised as complex gains. Therefore, they can be estimated in a similar fashion as it was done in Section 4.1.4 for equalisation. It results in autocorrelating the received and original pilots:

$$e(y) = \frac{1}{N_p} \sum_{\text{num}=0}^{N_p-1} p_{\text{num}}(y)\hat{p}^*_{\text{num}}(y), \tag{4.15}$$

where y is the current OFDM symbol, N_p is the total number of pilots, num is the current pilot, p_{num} is the original pilot, $\hat{p}_{\text{num}}(y)$ is the received estimation of a pilot num.

Now, when the basic principles of synchronisation of the used OFDM communication system have been shown, it is time to mention the main hurdles linked with the synchronisation chain during the algorithms' deployment.

4.2   Main hurdles in the synchronisation chain during the algorithms' deployment

4.2.1   Preamble issues

The spectral leakage phenomenon pertained to an NBI (Continuous Wave (CW) ElectroMagnetic Disturbance (EMD)) as was discussed in Section 2.2.1 spreads the disturbance energy throughout the OFDM signal, thereby disturbing not only the payload but also the OFDM's preamble. Figure 4.10 shows this. It represents the OFDM's preamble in time domain without (Fig. 4.10a) and under the influence of an NBI (Fig. 4.10b). It can be noticed that the repeatability of LSTF and LLTF sequence parts is not met in Fig. 4.10b as seen in Fig. 4.10a. This means that synchronisation cannot be done properly since it is based on autocorrelating repeatable preamble's LSTF and LLTF sequences. This means that the beginning of an OFDM frame either will not be detected or will be detected but erroneously. That is what happened during the initial tests using SDRs.

4.2.2   Pilots and guardsubcarriers issues

The "Mod-remod" and "Differential" algorithms described in Chapters 2 and 3, respectively, were simulated for an OFDM frame only containing a payload. This was a valid assumption since the transmission channel was free from multipath fading and both the transmitter and receiver were perfectly synchronised in time and frequency. Therefore, the synchronisation block and OFDM's overhead could be omitted. However, this is not the case in a real OFDM system. For example, pilots have to be incorporated into an OFDM frame. In addition, these pilots might solely use the BPSK modulation technique, as for example in [2]. At the same time, data subcarriers can be modulated using not only BPSK but also QPSK and some Quadrature Amplitude Modulation (QAM) schemes (QAM16, QAM64 in IEEE802.11a, see [2]).
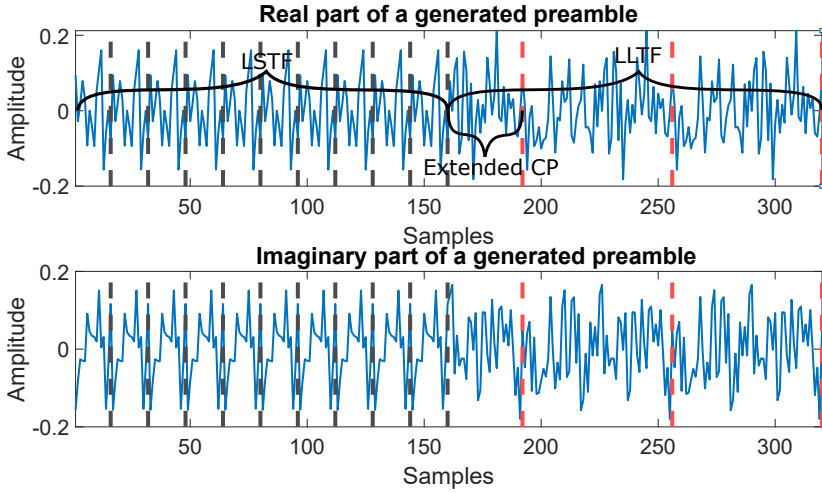
(a)
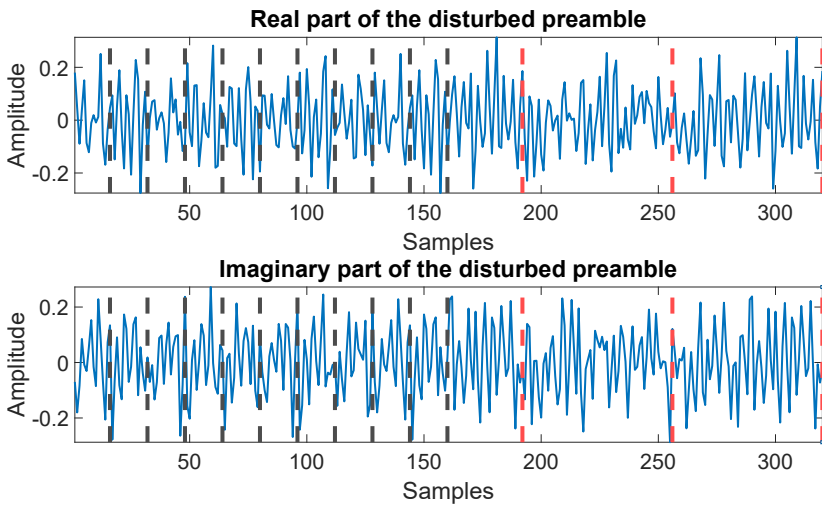
(b)

Figure 4.10: Real & imaginary values of an OFDM preamble when : (a) an NBI is not present on the preamble, (b) an NBI disturbs the preamble.

The other hurdle that appeared lies in the OFDM frame composition as well. This time it is connected with the use of guardband subcarriers that are located

on the sides of an OFDM signal (left- and rightmost subcarriers on the frequency spectrum in Fig. 4.1) and additionally protect the signal both from leaking to additional operating systems working in a similar frequency range and getting leaks from these neighbouring systems. These guardbands carry no energy, so no modulation is used on these subcarriers. This means that the effects of the transmission channel (an NBI is one of them, for example) have to be visible and this potentially will facilitate the work of the algorithms. However, in our case, the real issue with these guardbands comes when equalisation happens. Because of that, guardband subcarriers are nulled and, as a consequence, a valuable piece of the transmission channel information is lost. To circumvent that, one may either need to not perform equalisation at all or use it only for data subcarriers.

4.2.3 System noise

Last but not least is the white noise or the system noise modelled as Additive White Gaussian Noise (AWGN) in previous chapters (Chapters 2 and 3) during simulations. While the "Differential" algorithm was specifically made to be able to tackle the ambient noise to some extent (at least higher or equal to an SNR level of 20 dB), the "Mod-remod" algorithm is not that robust against it and simulations could work correctly with an SNR level higher or equal than 60 dB. However, during measurements the noise levels reached approximately 35.3 dB making the "Mod-remod" algorithm challenging to implement.

4.3 The "Mod-remod" algorithm deployment using ADALM-PLUTO SDRs

The first attempt at deploying the "Mod-remod" algorithm was during the supervision of Master's student, Brian Leeman [51]. The deployment was done with the help of ADALM-PLUTO SDRs [57]. Programming the ADALM PLUTO SDR can be done via different programming languages, including Matlab on which the NBI removal algorithms were written. Therefore, SDR programming was performed using this tool as well. Due to the aforementioned hurdles, the used OFDM communication system could not correctly perform synchronisation. Therefore, it was impossible to test the algorithm since the disturbance disrupts the repetitiveness between LSTF and LLTF sequences in the OFDM's preamble. Consequently, equalisation cannot be done properly since it is based on autocorrelating repeatable preamble's LLTF sequences. As a result, an NBI has to be injected into the system while not affecting the

Table 4.1: OFDM system parameters

Parameter	Value
Modulation scheme	QAM16
Number of subcarriers	64
Bandwidth, kHz	500
Carrier frequency, GHz	2.38
Guardband subcarriers	6 left, 5 right
Pilot subcarriers position	[12, 26, 40, 54]
DC subcarrier (yes/no)	Yes
Payload	100 text messages (UTF-8 converted)
Closest subcarrier to an NBI	10
Spectral leakage parameter, α	0.5

preamble. Therefore, it was decided to add the NBI in code on a received OFDM frame after synchronisation and equalisation. This will allow the preamble part of the OFDM signal to be NBI-free. Figure 4.11 represents this new update to the NBI cancellation block that was initially shown in Chapter 2, Fig. 2.8. Injecting an NBI in code will not make the performed tests reflect the reality. However, at least the algorithm would be able to work with real data obtained using the Wi-Fi OFDM-based protocol stack. For the created system, this stack was modified to allow the algorithm to perform its job. First, the modulation scheme for pilot and data subcarriers was forced to be the same. Second, equalisation for guardband subcarriers was done using the average equalisation coefficients of data and pilot subcarriers. Third, the guardband subcarriers were not fed into the algorithm. Instead, they were combined afterwards with the received estimated error values after the "demodulation-modulation" procedure. The OFDM system parameters are outlined in Table 4.1.
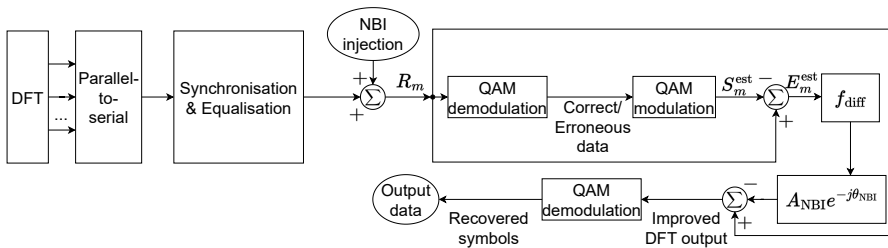
Figure 4.11: Updated NBI cancellation block diagram.

First, the described system was tested without SDRs, in other words, simulations were performed to check the system. Figure 4.12 [51] shows an NBI estimation obtained in the "Mod-remod" algorithm's block for real and imaginary values. Different colours on the figure represent different OFDM symbols. The two horizontal dashed lines having amplitudes of approximately 0.24 represent a half minimum Euclidean distance between adjacent symbols on the I-Q diagram and are thresholds indicating an NBI in a received symbol. Looking once more at Fig. 4.12, one may notice two distinct peaks at subcarriers 10 and 11 indicating the presence of an NBI. From these peaks, the disturbance fades within 10 subcarriers. The amplitude values for the subcarriers where the NBI has already faded, do not fluctuate very much and they are aligned in smooth lines close to zero. This means that there was no white noise in the system. In such a system the algorithm could perfectly identify an NBI and subtract it from the received OFDM signal. This resulted in zero bit errors (BER = 0 %). Therefore, the obtained results will be deemed as ground truth results with which will be compared the following test measurements obtained when using ADALM-PLUTO SDRs.
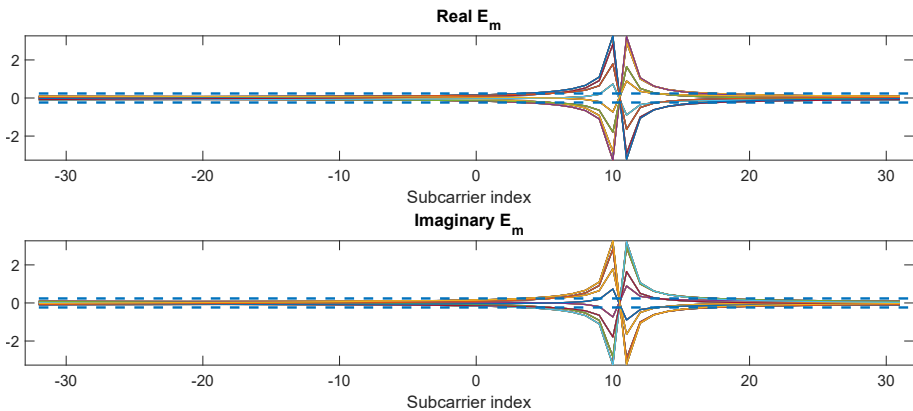
Figure 4.12: Estimated NBI spectrum using the algorithm during simulations.

A completely different story happened when SDRs were in use. Figure 4.13 [51] depicts that not only the NBI estimation values are entirely different (compare $|E_m| \approx 3.3$ versus $|E_m| \approx 78.1$ corresponding to Figs. 4.12 and 4.13, respectively) but also white noise manifestation is huge enough to cause a symbol flip (both real and imaginary values exceed the threshold values). This will lead to the wrong NBI removal procedure and inevitably result in bit errors. The I-Q constellation diagram for this measurement is presented in Fig. 4.14 [51]. For that specific test the BER was equal to 14.6 %.
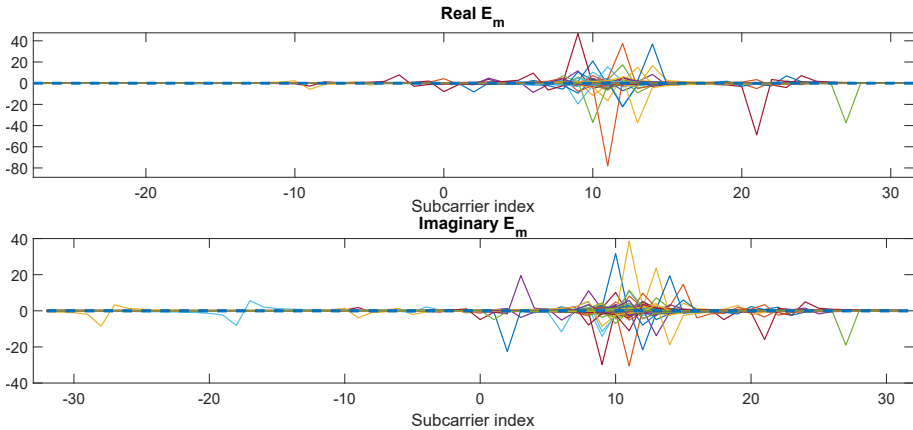
Figure 4.13: Estimated NBI spectrum using the algorithm during tests with SDRs.

The results show that even though the NBI's injection happened right after the synchronisation and equalisation blocks, it was still insufficient to counter the channel's imperfections, which led the algorithm not to perform as intended. The measurements indicated that the test approach and some algorithm's adjustments had to be tackled.

4.4 Circumventing the synchronisation and equalisation issues

Since an NBI causes the implemented synchronisation and equalisation methods to fail, an alternative has to be found. Investigating new synchronisation methods or improving them is not a trivial problem and not the primary goal of this manuscript (however, it has to be tackled as future work). Both synchronisation and equalisation procedures rely on the known training sequences contained in the preamble. Therefore, an NBI has to be injected into the system while not affecting the preamble. Consequently, it was decided to add the NBI in code on a transmitted OFDM frame and let the preamble part of the OFDM signal be NBI-free.
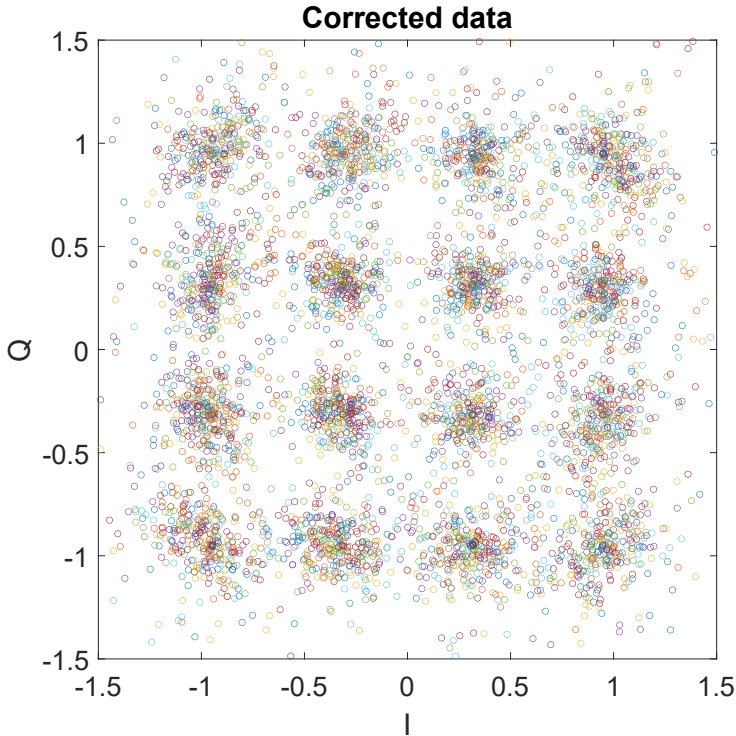
Figure 4.14: I-Q constellation diagram after the NBI removal using the "Mod-remod" algorithm.

4.4.1   Synchronising the validation system

The used transmitter and receiver can be frequency synchronised by using the same local reference frequency of 10 MHz. As for timing synchronisation, a set of actions called the "Bruteforce" timing synchronisation method was used.

Once the receiver captures an incoming signal, the "Bruteforce" timing synchronisation method starts working to locate the beginning of an OFDM frame. This search calculates the BER and SNR for every sample. The sample with the lowest BER and largest SNR is deemed to be the beginning of the OFDM frame. The "Bruteforce" method is easy to realise. However, it makes the validation not real-time, i.e. it cannot immediately start a new communication session before the synchronisation ends. Nevertheless, this method allows for identifying the beginning of an OFDM frame and subsequently performing the

algorithm, which is the main goal that had to be achieved.

Let us describe the "Bruteforce" method using the real example of the two used devices. The Rohde & Schwarz (R&S) SMM100A [58] is a vector signal generator that was used as the transmitter, while the R&S FSVA3000 [59] is a signal and spectrum analyser that was used as the receiver. The devices were frequency synchronised (10 MHz reference frequency) and the system noise was decreased by using a cabled connection between the devices. The test setup is visualised in Fig. 4.15. The OFDM frame's composition was based upon [2], except for the header that was not used in our system. An OFDM signal was created in Matlab [45]. The generated signal contained a full OFDM frame plus an "idle" period in which zeroes were transmitted. The transmitter was constantly sending the same generated sequence, so the "idle" period was done intentionally for better visualisation at the receiver's side.
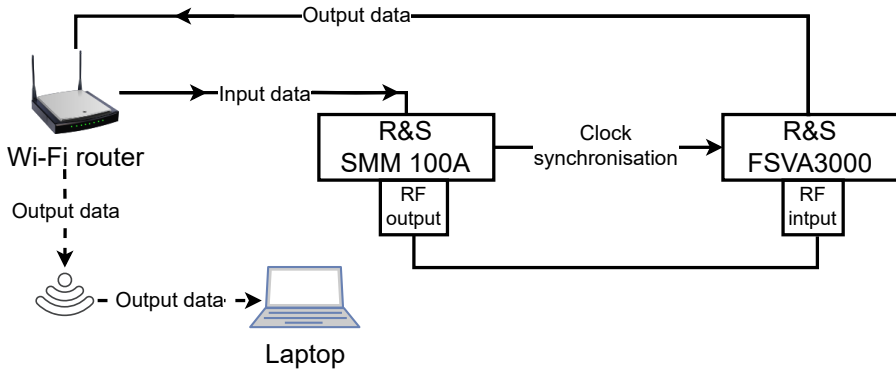
Figure 4.15: The algorithms' validation test setup.

The receiver was set up to obtain at least two OFDM signals. For a better signal resolution and SNR, an oversampling took place. For QAM16 with 64 subcarriers an OFDM frame has a length of 400 samples. With an "idle" period it becomes 800. Considering the receiver's capturing time and an oversampling of three, one can witness in Fig. 4.8a 4800 received samples.

The created OFDM system can be found in Fig. 4.16 in which an NBI is added into the system after the Inverse Fourier Transform (IFFT) and the addition of a CP.

The calculated parameters needed for the "Bruteforce" synchronisation method are shown in Fig. 4.17. For defining the SNR, the "Bruteforce" method exploits the built-in Matlab function that calculates the MER. It can be deemed as a
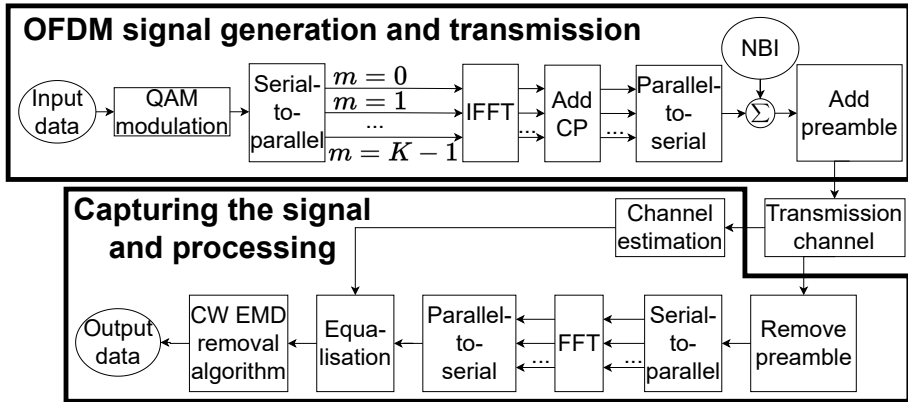
Figure 4.16: The created OFDM system for validation.

form of an SNR measurement since it calculates the average deviation of the received I-Q symbols from the reference constellation points.
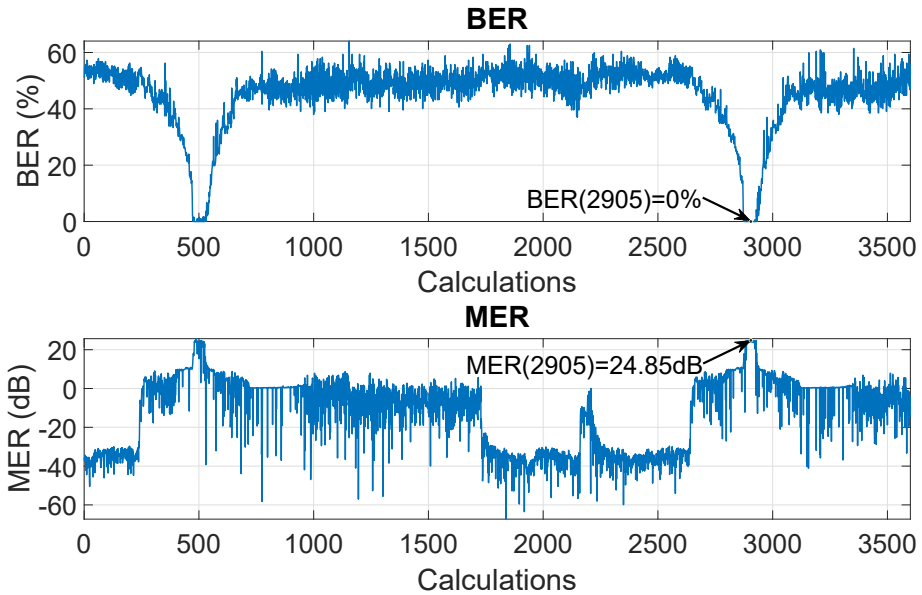
Figure 4.17: BER & MER of the received noisy (SIR = 25 dB) OFDM signal.

Looking back at Fig. 4.17, one may notice that the number of calculations differs from the number of samples shown in Fig. 4.8a. Given that the number of samples is 400 and the oversampling factor is 3, the number of calculations will become 3600 (see Fig. 4.17). Despite the difference, a noticeable correlation is visible between these figures. Analysing Fig. 4.17 further, one may notice that the smallest BER (0 %) and the maximum SNR value (approximately 24.9 dB) happen at the 2905th sample. Let us analyse more the region around that sample. The BER drop starts from approximately the 2773rd sample. Then BER reaches its minimum value (in this case it is 0 %) already at the 2875th sample. It can be noticed that more zero-BER samples create a plateau in Fig. 4.17. This can be explained as follows. An OFDM frame contains a preamble that is not considered during the OFDM demodulation when performing the FFT, so the remaining samples consist of a CP and data and pilot subcarriers. The former is a mere repetition of the end of the payload meaning that during an FFT operation, the resulting frequency content of the OFDM symbol remains the same except for a phase shift that is negated by the following equalisation operation. If one looks now at the graph with MER, it can be noticed that there is also a plateau at the same sample range as was for BER. The recovered symbols plotted on the I-Q diagram can be seen in Fig. 4.18. The figure represents all the possible QAM16 constellation points and the received OFDM I-Q constellation points obtained with the help of the "Bruteforce" method. It can be seen that all the points almost ideally coincide with the reference ones.

The "Bruteforce" method was tested on wireless communication using ADALM PLUTO SDRs. The results of the latter were also validated through a Blade Radio Frequency (RF), a fully programmable SDR that allows transmitting and receiving on the same device [60]. The tests were performed for various modulation schemes. The results are outlined in Table 4.2.

From Table 4.2 it can be seen that two different SDR systems perform in a similar fashion having an SNR level of almost 20 dB and BER close to 0 %. Introducing the "Bruteforce" method does not affect the BER performance of the systems under consideration. However, it affects the SNR level boosting it up to 30 dB. Considering the previous experience with the "Mod-remod" algorithm and its susceptibility to white noise, this "Bruteforce" method timing synchronisation is a good option for this algorithm.

4.5   Validation measurements

The validation measurements were performed at the KU Leuven, Bruges Campus test facility. First, an OFDM packet and an NBI are created on a computer.
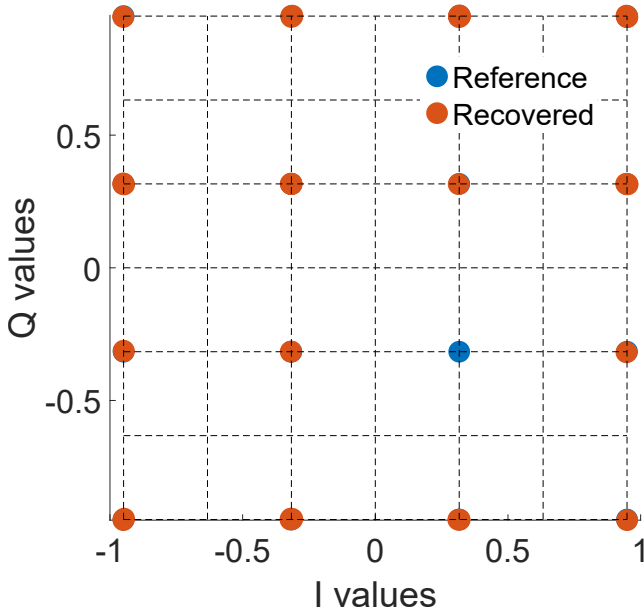
Figure 4.18: I-Q diagram of the received OFDM signal synchronised in time using the "Bruteforce method".

Table 4.2: Checking the performance of the "Bruteforce" timing synchronisation method

Used SDRs	Modulation scheme							
	BPSK		QPSK		QAM16		QAM64	
	Timing synchronisation method results (BER, %/SNR, dB)							
	Original	BF[a]	Original	BF	Original	BF	Original	BF
ADALM PLUTO	0/22.29	0/ 31.43	0/19.38	0/ 30.05	0.14/ 20.39	0/ 31.57	0.12/ 18.76	0/ 29.64
Blade RF	0/24.87	0/ 30.97	0/24.13	0/ 30.94	0/22.43	0/ 30.15	0.76/ 23.14	0/ 30.74

[a] BF stands for Bruteforce.

After that, the noisy packet is sent via the Ethernet cable to the transmitter which is connected via an RF cable to the receiver. Via this cable, the noisy packet reaches the transmitter. Finally, the captured signal is sent via the

Ethernet cable back to the computer. The latter performs the needed processing which consists of the OFDM packet search and the NBI removal algorithm implementation.

4.5.1 Defining the validation parameters

The main system and NBI parameters are outlined in Table 4.3. The modulation scheme was chosen to be QAM16 because, as was shown in [16], the algorithm performs the best with the lowest possible modulation scheme order. For a better analysis, the receiver performed oversampling, meaning that the receiver's sampling frequency was larger than the one of the transmitter. An NBI was constructed and injected into the OFDM system so that it will be always exactly between two contiguous subcarriers. In this way, the resulting (after the FFT block) spectral leakage will have a detrimental effect. Therefore, no extra coding techniques such as Hamming or interleaving were used, in contrast to [15].

Let us characterise the spectral leakage by the spectral leakage parameter α that will be equal to a relative distance of an NBI between two subcarriers. In our case, α is equal to 0.5.

The Signal-to-Interference Ratio (SIR) for an NBI was calculated as:

$$\text{SIR} = 20 \log_{10}(\frac{S_{\text{RMS}}}{A_{\text{NBI}}}), \tag{4.16}$$

where S_{RMS} is the root mean square value of the signal, while A_{NBI} denotes the amplitude of the interference.

4.5.2 Hardware limitations

One aspect of real communication often excluded in simulations is the receiver's ability to regulate the power of the incoming signal. This regulation is called AGC. AGC makes the output power stay constant and large enough in order to ensure the maximum resolution of the analog-to-digital converter. This means that low-power signals are amplified and vice-versa.

Let us look at Fig. 4.19, which shows the system's BER response to a varying NBI that does not create spectral leakage ($\alpha = 0$). The BER response is measured when the algorithm is deactivated. The results are shown for both simulations and physical measurements. The simulation results are shown with a blue dashed line. It can be noticed that starting from an SIR level of 10 dB, the BER performance of the system does not change anymore with a decrease

Table 4.3: OFDM and NBI parameters

Parameter	Value
Modulation scheme	QPSK, QAM16, QAM64
Number of subcarriers, K	64
DC subcarrier	Yes
Pilot subcarriers	[12, 26, 40, 54]
Guardband subcarriers	6 on the left and 5 on the right
Baud rate, B_{d}	100
Clock rate, MHz	100
Signal power, dBm	-30
Oversampling factor at the receiver's side	3
Subcarrier width, H	B_{d}/K
NBI phase (θ_{NBI}), degree	45
Distance to the closest NBI subcarrier, α	0.5
SIR span,[a] dB	[-50:25]
SIR step, dB	5 dB
NBI amplitude, A_{NBI}	$A_{\mathrm{NBI}} = \dfrac{S_{\mathrm{RMS}}}{10^{\mathrm{SIR}/20}}$

[a] During the measurements, per every SIR value, five bit sequences were used to result in a smoother result after averaging.

in the SIR level. However, this is not the case for measurements (look at the solid black line). While perfectly coinciding with the simulations curve until the SIR value of -25 dB, the measurements' BER results start degrading at SIR values lower than -25 dB. This happens due to the aforementioned AGC. After the AGC, the OFDM signal becomes so small that it reaches the noise level of the AGC. This means that the quantisation noise on the OFDM signal is largely increased. It leads to data loss resulting in BER degradation.

Since the scope of this thesis is to validate the algorithm under a broad SIR span, the data loss at low SIR levels due to AGC puts hardware limitations on the algorithm. This means that the algorithm can be validated up to a specific SIR.
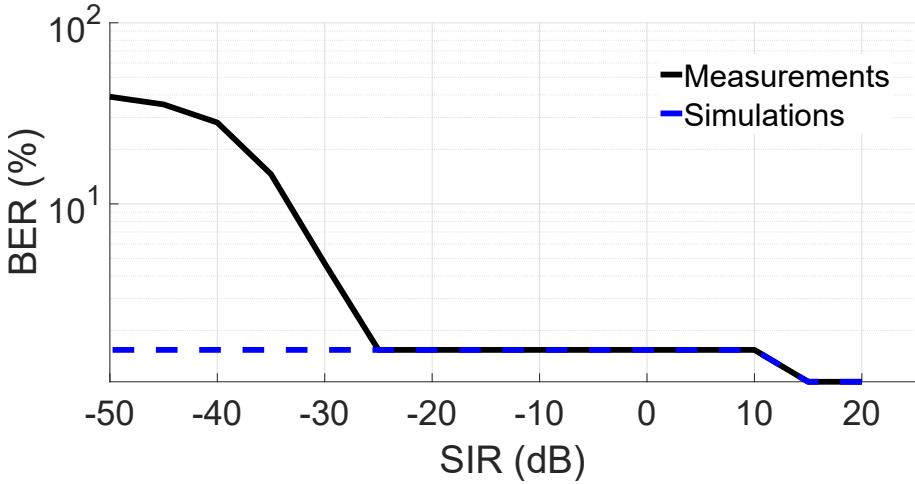
Figure 4.19: The BER performance of the system when there is no spectral leakage ($\alpha = 0$).

4.5.3   Measurement results

Before measurements with an NBI, the system was evaluated under the influence of white noise. It was equal to 35.3 dB. The BER of the OFDM system under validation with an NBI inserted in the OFDM symbol is shown in Fig. 4.20. The dashed blue line presents the algorithm's performance, while the solid black line is the reference performance of the system without the algorithm. It can be seen that both curves have the BER values lower than 0.3 % at SIR levels higher than 20 dB. Both the reference and algorithm curves gradually increase their BER value with the decrease in SIR values, with the reference curve increasing its BER values earlier. Therefore, a visible difference between the two curves can be seen. For better visualisation, a magnified part can also be seen in Fig. 4.20. With this magnified part, estimating the algorithm's gain (a difference in dB between the reference and algorithm curves for a given BER level) for BER levels between 1 and 10 % is more manageable. For example, for a BER level of 1 %, the algorithm's gain is 5.9 dB, while for other BER levels, it increases and reaches its maximum value of $\approx$ 15.1 dB for a BER level of 3 %.

The "Mod-remod" and "Differential" algorithms' gains for other BER levels up to 5 % are calculated and presented in Fig. 4.21a and Fig. 4.21b, respectively. These heatmaps also show the gain for QPSK and QAM64 modulation schemes that are used in OFDM that comply with [2].
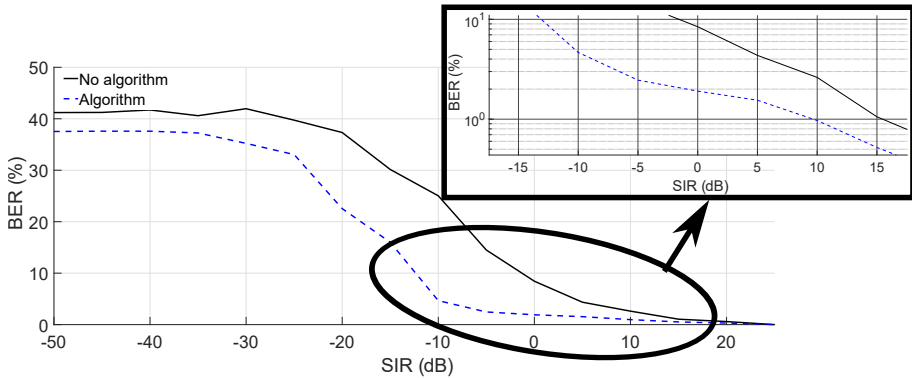
Figure 4.20: The BER performance of the QAM16 OFDM system with the "Mod-remod" algorithm when the spectral leakage parameter $\alpha = 0.5$.

The "Mod-remod" algorithm's gain for QPSK reaches its maximum gain at 18.36 dB for a BER level of 3 %, while for QAM64 it is equal to 11.05 dB for a BER level of 4 % (see Fig. 4.21a). This shift in the maximum algorithm's gain (the highest and lowest are for QPSK and QAM64, respectively) can be explained by a change in the OFDM itself. The lower the modulation order scheme is used the more robust the system is. As has already been investigated in [16], the system benefits from the algorithm the most at low modulation order schemes. Also, once the maximum gain for a particular modulation scheme at a certain BER level has been reached, the algorithm's gain decreases. As shown in Fig. 4.19, this happens due to a rising disturbance power and AGC, after which a digitisation error occurs and the algorithm makes wrong estimations.

The "Differential" algorithm gain's pattern can be visible on the heatmap in Fig. 4.21b. Due to a lower vulnerability to white noise, the "Differential" algorithm is able to withstand the noise present in the system with no impact on its performance. As a result, higher gains are obtained at the lowest BER levels. One may also notice that the largest gains are achieved for the QAM64 modulation scheme with a peak value of 32.78 dB for a BER level of 1 %. This happens due to the more considerable amount of bits affected by an NBI that results in the worse performance of the system without the algorithm. Comparing the performance of the two algorithms, one may notice that the "Differential" algorithm performs better than the "Mod-remod" algorithm and can perform up to more than 31 dB better.

The presented measurement results in Figs. 4.20 and 4.21 cannot be compared with previous simulations presented in [15] and Chapters 2 and 3 as "A-to-B"
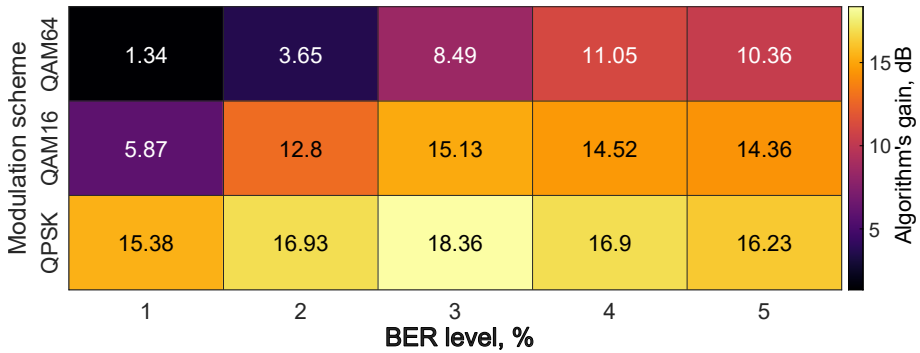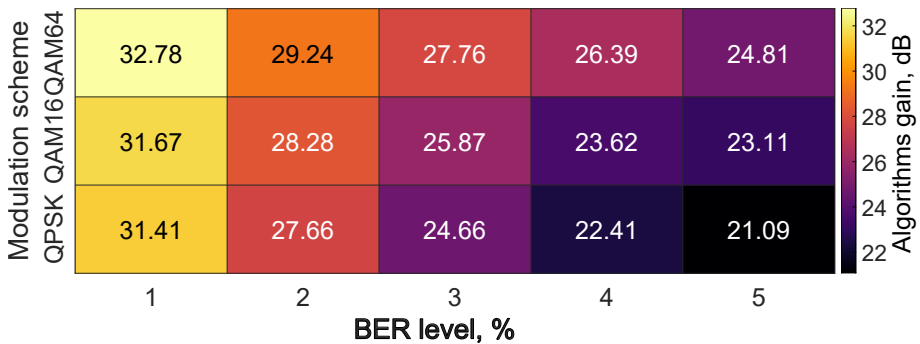
Figure 4.21: The algorithm's gain for different modulation schemes when the spectral leakage parameter $\alpha = 0.5$: (a) the "Mod-remod" algorithm, (b) the "Differential" algorithm.

for a few reasons. First, simulations do not account for the work of AGC. Second, the simulations did not use guardband and DC subcarriers for the the "Mod-remod" algorithm. During the validation procedure, these subcarriers carried no information and as a result, were unmodulated. This means that these subcarriers could be directly used for defining the spectral leakage pattern of an NBI. Because of no re-modulation procedure on these subcarriers, the chance of the wrong NBI estimation is minimal. The same can be applied to pilot subcarriers that also do not undergo the re-modulation procedure since the pilot values are known. Nevertheless, the presented measurements show that both algorithms succeed in removing an NBI since the BER performance

of the OFDM system improves.

4.6   Conclusion

The NBI removal algorithms for OFDM-based systems described in [15] and Chapters 2 and 3, were practically validated in this chapter. The algorithms were tested for QPSK, QAM16 and QAM64 based upon [2]. As a result, the chapter provided OFDM frame composition and the needed synchronisation steps correctly set up the measurement devices.

The initial measurement tests on ADALM-PLUTO and BladeRF SDRs showed that neither synchronisation nor equalisation work properly if an NBI is injected into the transmitted OFDM signal. An NBI makes the preamble parts too different to perform a proper autocorrelation. Therefore, the NBI was injected in code in such a way that only OFDM symbols were disturbed, meaning the preamble was unaffected by the generated NBI. This allowed performing correct equalisation. The ADALM-PLUTO SDRs devices were frequency synchronised using a method based on [2], while the R&S devices were frequency synchronised by using the same local reference frequency. The timing synchronisation was done by capturing an OFDM sequence and performing BER and SNR measurements on the obtained signal. The sample with the lowest BER and maximum SNR value was used as the frame's beginning.

During the validation measurements, it was shown that irrespective of the algorithm's performance the BER performance of the system will decrease as the SIR level becomes lower. This happens due to hardware limitations caused by the receiver's built-in AGC that could not be considered in simulations. In addition, the algorithms' realisation and the environments in which they were tested differed in the original algorithms and the system under validation. This means an "A-to-B" comparison between the simulation and validation results cannot occur. Nevertheless, the algorithms' gains during the validation measurements reached almost 18.4 dB at the BER level of 3 % for the QPSK modulation scheme when the "Mod-remod" algorithm was in use. The gain for the "Differential" algorithm was higher and reached 32.78 dB for a BER level of 1 %.

The validation results showed that the algorithm is deployable on real equipment in laboratory settings with certain hardware and software adjustments. The algorithm works and the system benefits from it. However, further research has to be performed regarding synchronisation and algorithm compatibility to be able to deploy the algorithm on a real-time OFDM system.

Chapter 5

Wireless connectivity in the agricultural sector

The content and results of this Chapter have already been disseminated in [61]. This publication presents a study on the ElectroMagnetic (EM) robustness of IO-link Wireless (IOLW) and SmartMesh IP for their use on an agricultural vehicle. The publication also provides measurements of the key Quality of Service (QoS) parameters and their further analysis.

The previous chapters gave an overview of one of the most prevalent wireless communication technologies, Orthogonal Frequency Division Multiplexing (OFDM). It has been investigated for its vulnerabilities. It was shown that NarrowBand Interferences (NBIs) compromise its performance. As a result, two NBI cancellation algorithms were proposed and were attempted to be deployed in the lab settings. However, OFDM is not the sole protocol actively used in the daily life of casual customers and industry. Due to a variety of wireless communication technologies, it is impossible to investigate all of them and this is not the purpose of this manuscript. Therefore, this chapter will focus more on industrial wireless communication technologies that can find their implementation in the agricultural sector. As a result, this chapter will provide plausible use case scenarios for wireless communication in the agricultural sector regarding the reverberant EM environment inherent in this sector. For that, two wireless communication protocols (IOLW [62] and SmartMesh IP [63]) representing different Wireless Sensor Networks (WSNs) (star and mesh) were, tested in a double Reverberation Chamber (RC) and then compared with the measurements made on an actual combine harvester. The results showed that a fully reverberant environment is harsher than the actual combine harvester.

Thus, the initial steps were made to dampen the RC with absorbers to comply with the environment created in a harvester.

5.1 The use of wireless sensor networks in the agricultural sector

While wireless communication has become inherent to our daily life, this is not yet the case for industrial applications where wired communication like Industrial Ethernet is still prevalent. However, wired communication has several drawbacks as we increasingly equip machinery with sensors. First, modifying a wired communication network after installation can be quite strenuous and time-consuming. Second, all necessary cabling is often hard to reach for maintenance or repair. Third, especially in application areas like automotive, avionic or agricultural, cables add significant extra weight to the product-at-hand [64].

In this chapter, we focus on the application of wireless communication in the agricultural sector that moves towards the concept of Smart Farming (SF) [65]. SF refers to the extensive use of technologies (e.g. Internet-of-Things (IoT), robotics and artificial intelligence) to increase the quantity and quality of agricultural products while optimising the required human labour. SF might result in numerous sensors on board an Agricultural Vehicle (AgV). The sensors could collect various types of data pertaining to both the AgV and its surroundings. This data may include the AgV's speed, position, component temperature, vibration levels, as well as information about the environment, such as soil conditions, humidity and temperature [66]. Also, there is a clear need to lower the ecological footprint of the farming industry, which involves making an AgV more energy-efficient. As a result, the AgV's weight should be minimised. Thus the use of wireless communication and, hence, WSNs is to be preferred over their wired equivalents.

As the concept of SF moves forward, it evolves to fully autonomous AgVs [67]. To guarantee the safety and trustworthiness of an autonomous AgV, stringent reliability and robustness requirements are being put onto WSNs. The QoS, with parameters like latency or Packet Error Rate (PER), should be nearly perfect despite all the harsh conditions the AgV encounters during its operation: various weather conditions, mud, etc. Moreover, AgVs will be more electrified. Hence, the increased use of power electronics will make the EM environment on the AgV more challenging and a proper choice of the wireless protocol to be used needs to be made. Here, robustness does not only imply that the wireless protocol can withstand EM disturbances, but also implies that it can handle multipath fading that occurs because of the metallic nature of the AgV.

A lot of different WSN protocols, proprietary solutions and technologies are available on the market: ZigBee, ISA100.11a, WIA-PA and others [68]. One should understand the needs of the wireless system and choose a solution accordingly. For example, some solutions provide high data rates but consume a lot of energy [69], whereas others have a larger coverage and lower data rates [70]. There are also solutions that can extend the existing WSN by introducing the mesh topology [71]. Finally, some technologies allow the network to "heal" by finding new routing ways [72]. Let us aggregate, some of the existing WSN technologies suitable for industrial applications in Table 5.1.

Despite the variability of WSN technologies presented in Table 5.1, each solution differs in terms of its overall organisation, architecture and, hence, their robustness. For example, ZigBee does not support channel hopping whereas WirelessHART does. A very relevant parameter of a WSN protocol is its network topology. There are three main such WSN topologies (see Fig. 5.1): a star, a mesh or a hybrid mesh. In a star topology, all sensors S are directly connected to the gateway unit G. In a mesh network, this is not the case and one or multiple hops through other sensors (acting as routers) are needed to be done to deliver information from a sensor to the gateway unit and vice versa. While this might increase latency compared to the star topology, it allows for extending the range of the WSN. Consequently, the usage of a hybrid mesh network combining both star and mesh topologies can be a good compromise if arranged well.

Considering a plethora of WSN protocols, one may need to choose a few of them co-existent with each other and suitable for an AgV for further reliability tests. It was decided to focus the attention on the solutions based on IEEE 802.15.4 standard because it offers the lower network layers of wireless personal area networks. These networks focus on low-cost and low-power communication between devices. From IEEE 802.15.4, SmartMesh IP was chosen. A counterpart to it will be IO-link Wireless, a non-IEEE 802.15.4 solution.

As was mentioned earlier, an AgV has a lot of metallic parts. This will lead to a multipath fading environment during wireless communication of the deployed sensors. To design a proper WSN and to thoroughly test it, one may need to have a reliable and controllable facility. An RC can be used as this facility since an RC is able to recreate a lot of wireless communication environments. This can be done by matching the delay spread of the real environment to the one recreated in an RC. The matching can be performed by changing the delay spread of the chamber adding absorbers inside the chamber (loading) or changing the stirred and unstirred components (Line-of-Sight (LoS) and Non-Line-of-Sight (Non-LoS) tests) [83]. As a result, it was decided to test IO-link Wireless and SmartMesh IP protocols for their robustness in a harsh EM environment of an RC.

Table 5.1: Industrial WSN technologies

WSN technology		$f_{\mathbf{oper}}$[a]	Coverage	Data rate	Topology
BLE[73]		2.4 GHz	35 m	9.6 Gbit/s	Star, Mesh
Wi-Fi[69]		2.4, 5 GHz	100 m	2 Mbit/s	Mesh, broad-cast, piconet
Z-wave[71]		868 MHz	30 m	40 kbit/s	Mesh
LoRa[70]		868 MHz	several km	50 kbit/s	Star
Cellular	GPRS,EDGE, 3G-HSDPA,3G-HSDPA+[74]	[0.38; 1.9], [0.7;3] GHz	several km	[128.4 kbit/s; 337 Mbit/s]	Star
	5G	[0.6; 6], [24;86] GHz	several km	20 Gbit/s	Star
	NB-IoT[75]	[0.6; 6] Ghz	several km	250 kbit/s	Star
	LTE-CatM1, LTE-Cat1[75]	[0.6; 6] Ghz	several km	[1; 10] Mbit/s	Star
Sigfox[76]		868 MHz	800 m	600 bit/s	Star
IEEE 802.15.4 [77]	ZigBee[78], ISA100.11a[79]	2.4 GHz	[90;500] m	250 kbit/s	Star, Mesh, Cluster
	WirelessHART [80], Thread[81]		[30; 90] m		Mesh
	6LoWPAN[82]		100 m		Star
	SmartMesh IP[72]		at least 200 m		Mesh
IOLW[62]		2.4 GHz	20 m	1 Mbit/s	Star

[a] f_{oper} - operating frequency in Europe.

5.2 Basic introduction to IO-link wireless and SmartMesh IP

This section will give some basic but essential information about the working principle of IO-link Wireless and SmartMesh IP protocols and their key features
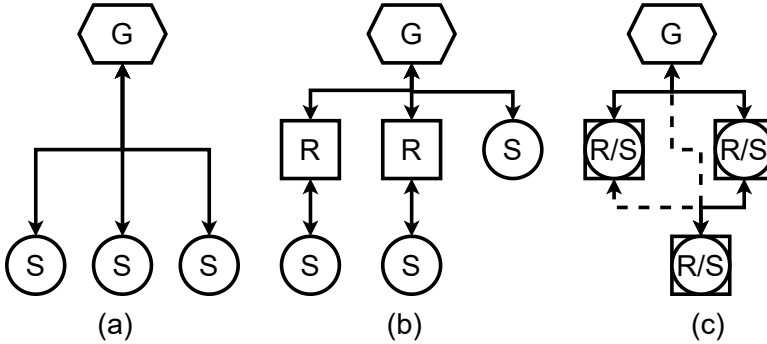
Figure 5.1: WSN topologies: (a) Star topology, (b) Hybrid topology, (c) Mesh topology. G - gateway, S - sensor, R - router, R/S - a sensor having router capabilities.

suitable for the agricultural sector.

5.2.1 IO-link Wireless

IOLW [62] is a wireless extension to the IO-link protocol [84]. IO-link is standardised in IEC 61131-9 [85] and is compatible with the popular fieldbus technologies (PROFIBUS, PROFINET, EtherCAT and others).

IOLW is a star WSN topology in which the gateway and sensors are called the Master and Devices, respectively. IOLW supports both Frequency Division Multiple Access (FDMA) and Time Division Multiple Access (TDMA). It implements frequency hopping with blacklisting to further strengthen its reliability.

Due to TDMA, the communication phase is split between time slots. Let us show it in Fig. 5.2 which is an adaptation of the uplink assignments shown in [62]. From the figure, one may notice that a Device is assigned to one of the five available tracks of the Master. Each track can allocate up to eight time slots. This means that the Master supports up to 40 Devices.

A Master is able to communicate using all the available tracks at the same time. This is possible due to a different frequency allocation per track. By using the incorporated frequency hopping tables, optimal bandwidth usage happens. Each communication session is split into cycles. Each of these cycles utilises FDMA/TDMA with a retransmission option. The cycle by default is set up to 5 ms and consists of three duration equally sub-cycles. IOLW frames contain
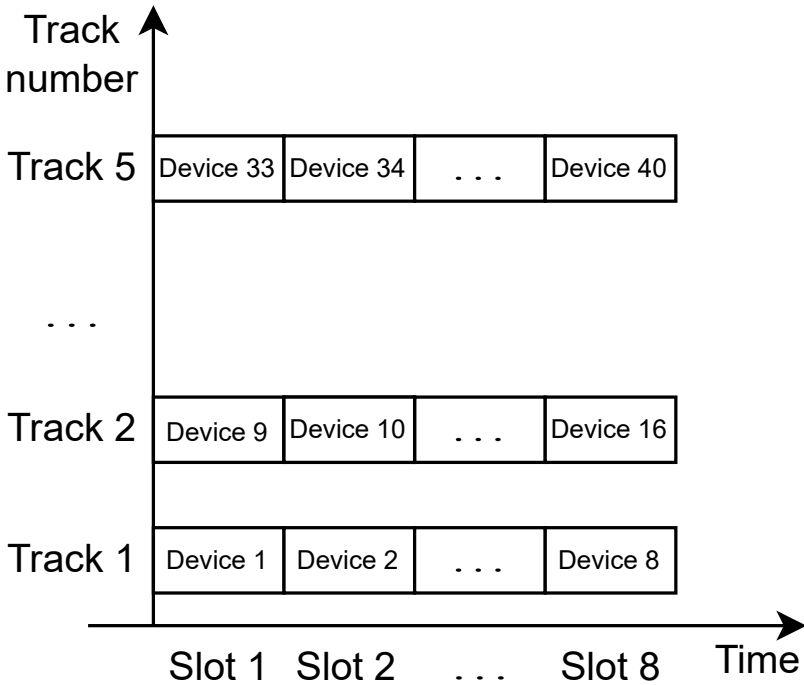
Figure 5.2: Time slot allocation in IOLW.

information that is sent regularly (process data) or occasionally (acyclic data and events in case of the emergent state of a sensor).

IOLW's link quality is based on the Residual Failure Probability (RFP). RFP depends on the maximum number of retransmissions and PER: $\text{RFP} = \text{PER}^{1+\text{MaxRetry}}$. A link quality of 100 % corresponds to the $\text{RFP} = 10^{-9}$. Other corresponding values are shown in Table 5.2.

RFP is only one of many tools responsible for the protocol's reliability. Therefore, it contains a complete overhead stack in the architecture leading to relatively small payloads. Within one default frame of 5 ms, IOLW supports payloads of 37 and 15 bytes for downlink and uplink, respectively.

Table 5.2: Relation between RFP and link quality

RFP	Link quality, %
10^{-9}	100
$5 \cdot 10^{-9}$	80
10^{-8}	60
$5 \cdot 10^{-8}$	40
$8 \cdot 10^{-8}$	20

5.2.2   SmartMesh IP

Unlike IOLW, SmartMesh IP uses a mesh topology. SmartMesh IP is a proprietary solution from Analog Devices [72]. It is based on IEEE 802.15.4 and enables the network participants to be access points towards the gateway. The gateway and sensors are called the Manager and Motes, respectively.

SmartMesh IP exploits channel blacklisting and the Time-Slotted Channel Hopping (TSCH) technique in which the communication time is split into time slots helping to overcome intersymbol interference by minimising packet collision. In addition to multiple mesh connections between Motes, the communication is toughened by retransmissions despite SmartMesh IP packets being User Datagram Protocol (UDP) packets each of which is 90 bytes long [63].

To maintain the meshed network, the Manager is responsible for collecting "health" reports. These reports are sent from every Mote in the network and contain information about Motes' parameters like path stability, reliability, latency or the Received Signal Strength Indication (RSSI). Using these reports, the Manager determines the Mote's neighbours and path stability for the subsequent network optimisation. For example, if, according to the "health" report, some of Mote's "parents" (the sensors on the way to the gateway unit) do not have the needed reliability (can be adjusted but the default value is 99.99 %), then it seeks for the other "parents" which will eventually improve the network's reliability. These "health" reports are sent hourly, however, depending on the network requirements, the reports can even run continuously to make the WSN more robust and adapt to any changes in the environment.

SmartMesh IP opens a huge variety of options ([63], [86]) suitable for the agricultural sector. Moreover, the meshed WSN can add more freedom to the sensors' positioning. This is why SmartMesh IP was chosen as a counterpart to IOLW.

5.3   Robustness of IOLW and SmartMesh IP inside an RC

Since an AgV contains a lot of metallic parts, it represents a multipath environment which can be recreated in an RC. To test the harshest EM environment, the performance of the IOLW and SmartMesh IP protocols was tested inside the double RC available at KU Leuven Bruges Campus. The AgV's rotating parts were recreated with the help of rotating stirrers inside RCs. Fig. 5.3 shows a schematic overview of the overall test setup for both protocols. The actual double RC is shown in Fig. 5.4. It comprises larger and smaller rooms that are next to each other and are both stirred. In their common wall, an opening can be made. The double RC allows studying LoS and Non-LoS conditions.

5.3.1   Performance of IOLW inside an RC

The IOLW test setup comprised only one Master and one Device. However, across the different experiments, both were placed at different locations.

The aim of these tests was to investigate under which conditions or parameters, the wireless communication will remain errorless or almost errorless (a few sporadical errors are tolerated). Therefore, the following test procedure was used (Fig. 5.3):

1. Test series 1: in one LoS test, both the Manager and Device were placed on the wooden table inside the larger RC.

2. Several Non-LoS tests:

    (a) Test series 2: both the Master and Device were still in the larger RC but while the Master was still on the wooden table, the Device was placed behind the stirrer.

    (b) Test series 3: the Master was put in the smaller RC, while the Device was on the wooden table in the larger RC.

    (c) Test series 4: the Master was put in the smaller RC, while the Device was put behind the stirrer in the larger RC.

During the tests on IOLW, all the parameters can be conventionally split into modifiable and monitoring groups.

The modifiable, meaning that we can control their values, parameters are:

Conventional signs:

or ✖ Overlapping units from IOLW and SmartMesh IP

● Mote's position ✖ Manager's position

○ Device's position ✖ Master's position —— Cable connection
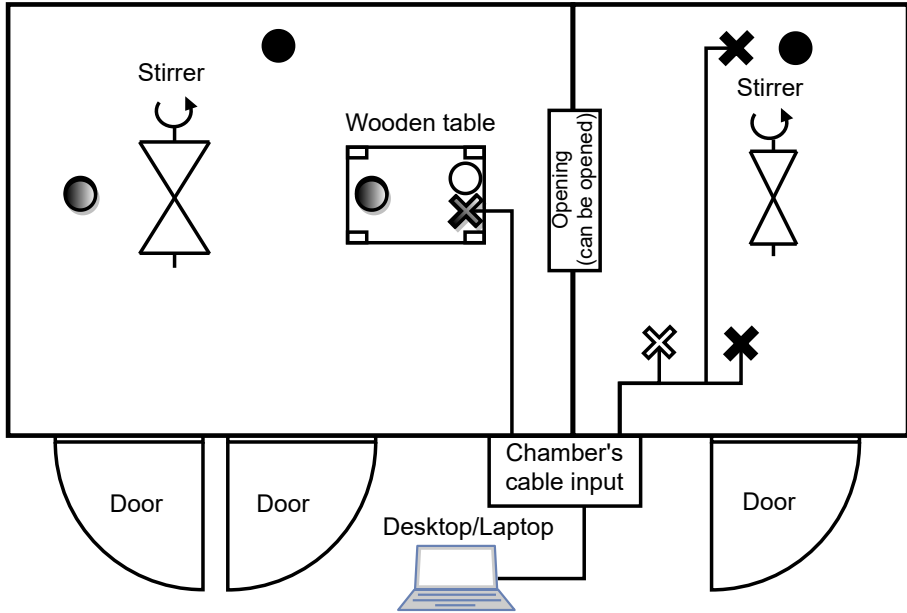
Figure 5.3: IOLW and SmartMesh IP test setups inside an RC.

1. Simulation cycle time, i.e. the maximum delay between two subsequent packets in ms;

2. The Number of ReTransmissions (NRTx);

3. The Transmission Power (TxP) level in dBm;

4. The stirrer's speed (was put to 30 rotations/min for all the tests).

The monitoring parameters, used for determining the performance, are:

1. Link quality indicators for the Master and Device in %. The larger this value is, the better the link quality is;
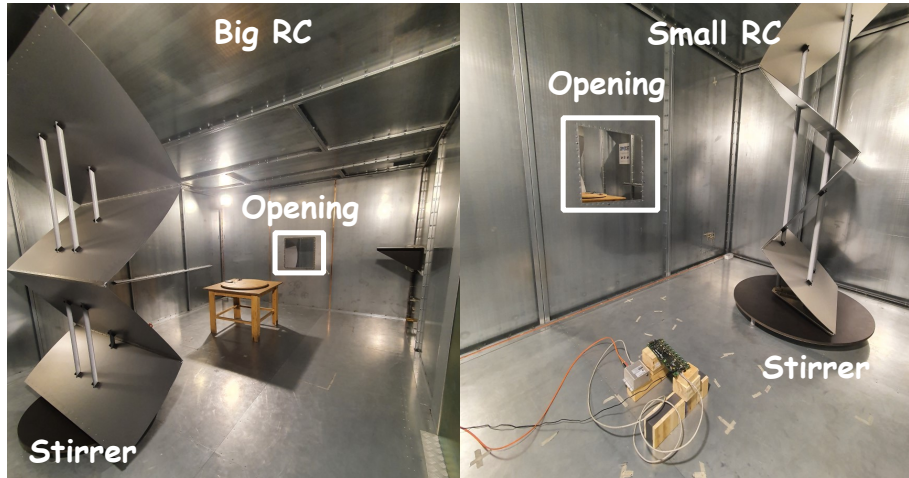
Figure 5.4: Double RC at KU Leuven, Bruges Campus.

2. RSSI for the Master and Device in dBm. Again, the higher, the better;

3. Two types of communication errors:

   (a) Due to the not received acknowledgement from the Device;

   (b) Due to exceeding the NRTx (accompanied by an event in IOLW).

The total number of sent packets during the tests with IOLW was the same and equal to 4096. Based on errors, two types of PERs can be calculated: the "technical" and "specification" PER that depend on the received acknowledgements and the exceeded NRTx, respectively. For example, if an acknowledgement is not received, the technical error counter will be incremented. Similarly, if the NRTx is surpassed, the specification error counter is increased. To not confuse the reader, the technical PER will be indicated PER_t, while the specification PER will be indicated as PER.

5.3.2   Performance of IOLW during LoS tests

For the used devices with their default parameters, the RCs were too reverberant for proper communication. This means that the delay spread (the derivative of Power Delay Profile (PDP)) of the established communication within the chamber was too large. Large delay spreads lead to a higher Bit Error Rate

(BER) [87]. Therefore, the Master's radio module was overflown with the arriving superimposed copies of the signal. Consequently, even during the LoS test, the communication was almost permanently lost, making it impossible to track the monitoring parameters. Therefore, the IOLW parameters had to be adapted.

The default TxP of 5 dBm was too high for the used test setup, resulting in a larger PDP and, therefore, having high amplitude reflected copies. Therefore, the TxP was decreased to 3 dBm resulting in an errorless LoS communication.

When the stirrer rotation was added to the experiment, it added extra resonant modes resulting in a wide variety of EM inside the chamber. This led to an increased number of EM field distributions making the IOLW's communication indiscernible. Therefore, the IOLW's WSN was hindered. Consequently, as during the case with the immobilised stirrer, the communication parameters were adapted to maintain errorless communication. The TxP and NRTx had to be changed and were put to -6 and 6 dBm, respectively.

As was shown in Fig. 5.2, IOLW uses time slots between communication cycles. These cycles could be regulated during the tests. The change in simulation cycle time did not affect communication in any way. For example, Table 5.3 shows the performance of IOLW in the office environment for 10 and 60 ms simulation cycle time. One may notice, that the error rate and other QoS parameters are very similar for these cases. Hence, the simulation cycle time was held at the same value (10 ms) during all the tests.

Table 5.3: IOLW test QoS parameters for different simulation cycle times

Simulation cycle time, ms	Errors[a]	PER_t, %	LQI_M[b], %	$RSSI_M$[c], dB	$RSSI_D$[d], dB	LQI_D[e], %
10	15	0.37	56.8	-51	-65	57
60	14	0.34	57.5	-55	-55	53

[a] Error values are based on packets that were not received from the first go;
[b] LQI_M - link quality indicator at the Master's side;
[c] $RSSI_M$ - received signal strength indicator at the Master's side;
[d] $RSSI_M$ - received signal strength indicator at the Device's side;
[e] LQI_M - link quality indicator at the Device's side.

5.3.3 Performance of IOLW during Non-LoS tests

Non-LoS tests decreased the unstirred component in the chamber, so the prevalent coupling between devices was happening due to the stirred component through reflections. From the LoS tests, it was already shown that increasing the stirred component was hindering communication. The same happened for the Non-LoS tests when both the Master and Device were located in the larger RC. The test results are presented in Table 5.4. One may notice that for errorless communication (PER = 0) the TxP had to be decreased from -2 to -6 dBm, while the moving stirrer added more reflections leading to increased errors (compare the PER value for the third and fourth runs). Consequently, a combination of the TxP of -6 dBm and NRTx of 6 could lead to errorless communication (PER = 0), albeit the data had to be retransmitted as there was no improvement in the PER_t for the fourth run.

The opening between the two RCs allowed for putting the Master in the smaller RC (see Fig. 5.3) while remaining in active communication. The Device was put on the wooden table in the larger RC. To maintain stable communication, the TxP and NRTx had to be put to at least 6 and 6 dBm, respectively. Table 5.5 illustrates the results of the measurements. The chosen values for TxP and NRTx allowed performing errorless tests with immobilised stirrers (see test run № 1 in the table). The stirrer rotation in the larger RC increased PER_t, however, due to sufficient retransmissions no packets were lost. Rotation of the stirrer in the smaller RC led to lost packets due to the vicinity of the stirrer to the Master. Finally, the rotation of both stirrers worsened the communication even further (see test run № 4).

The last test was performed to push the limits of IOLW, when the Master

Table 5.4: IOLW test QoS parameters for Non-LoS tests: test series 2

Test run №	Test layout description	NRTx	TxP, dBm	PER_t, %	PER, %
1	Test series 2 with a still stirrer	3	-2	6.32	0.049
2	Test series 2 with a still stirrer	3	-6	5.2	0
3	Test series 2 with a moving stirrer	3	-6	8.47	0.42
4	Test series 2 with a moving stirrer	6	-6	9.01	0

remained in the smaller RC, while the Device was put further away from the Master behind the stirrer in the larger RC. In this way, the signal had to bounce multiple times to reach the Master. The results presented in Table 5.6 slightly worsened in comparison to the test series 3 (e.g. compare PER_t for test run № for Tables 5.5 and 5.6). The stirrer rotation in the larger RC exceeded the NRTx, so some packets became lost resulting in the PER of 0.073. Rotating both stirrers at the same time worsened the communication even further. Nevertheless, even the worst PER value that was equal to 0.098 % is a relatively low number meaning that the IOLW-based communication can be robust in a reverberant environment by increasing the NRTx and decreasing the TxP.

Table 5.5: IOLW test QoS parameters for Non-LoS tests: test series 3

Test run №	Test layout description	NRTx	TxP, dBm	PER_t, %	PER, %
1	Test series 3 with still stirrers	6	-6	9.01	0
2	Test series 3 with the moving stirrer in the larger RC	6	-6	18.19	0
3	Test series 3 with the moving stirrer in the smaller RC	6	-6	12.33	0.049
4	Test series 3 with moving stirrers in both RCs	6	-6	12.7	0.073

Table 5.6: IOLW test QoS parameters for Non-LoS tests: test series 4

Test run №	Test layout description	NRTx	TxP, dBm	PER_t, %	PER, %
1	Test series 4 with still stirrers	6	-6	10.47	0
2	Test series 4 with the moving stirrer in the larger RC	6	-6	13.06	0.073
3	Test series 3 with moving stirrers in both RCs	6	-6	12.67	0.098

5.3.4   Performance of SmartMesh IP inside an RC

Apart from achieving the best possible communication, the experiments on SmartMesh IP were also targeted to find the minimum possible latency giving the lowest possible PER (PER $\approx$ 0) in an unloaded RC. Thus, customised programs were written for both the Manager and Motes.

The Mote's programming can be split into three stages: program writing in C, C to binary conversion and flashing the binary file onto the Mote to be initialised at every startup.

The Mote's program is made to listen to the WSN and echo any message upon receiving it.

Fig. 5.5 depicts the main stages of the Manager's program. First, the test parameters are set up, such as PUBLISH_RATE (time delay between two subsequent packets), STIRRER_SPEED (stirrer's speed) and other parameters. Then the Manager is initialised and creates a WSN by finding operational Motes. These Motes immediately deliver their connection parameters (e.g. RSSI). After that, the Manager subscribes to all the data notifications from Motes and starts transmitting data to the selected Mote. If a packet is sent from a Mote, the program processes it and saves it in the list. Upon sending all the packets, the program compares the sent list of packets with the received packets' list. This comparison allows the program to calculate the number of correctly received packets, lost packets, disturbed packets, the total time needed to send and receive packets and the PER.

The tests performed at RCs were similar to those for IOLW (see Fig. 5.3). In the beginning, a series of tests with 1000 packets was performed. The next series was performed with 100 packets. The test results are shown in Table 5.7. The difference between the results of the two series was approximately equal to the factor of 10. Consequently, to optimise the testing time, a decision was made to proceed with 100 packets. The main parameter affecting the QoS parameters was the Publish Rate (PR).

For the tests in the larger RC, both LoS and Non-LoS (test series 1 and 2) tests gave a PER equal to zero with PR equal to 4. The Elapsed Time (ET) between the first sent and the last received packet was 408 s.

When the Manager was moved to the smaller RC and the Mote was put on the table in the larger RC (test series 3), the PER raised to 9 % with the PR of 4 s. That resulted in the ET of 411 s.

For test series 4 when the Mote was moved behind the stirrer in the larger RC with the Manager remaining in the smaller RC, the connection was dropped
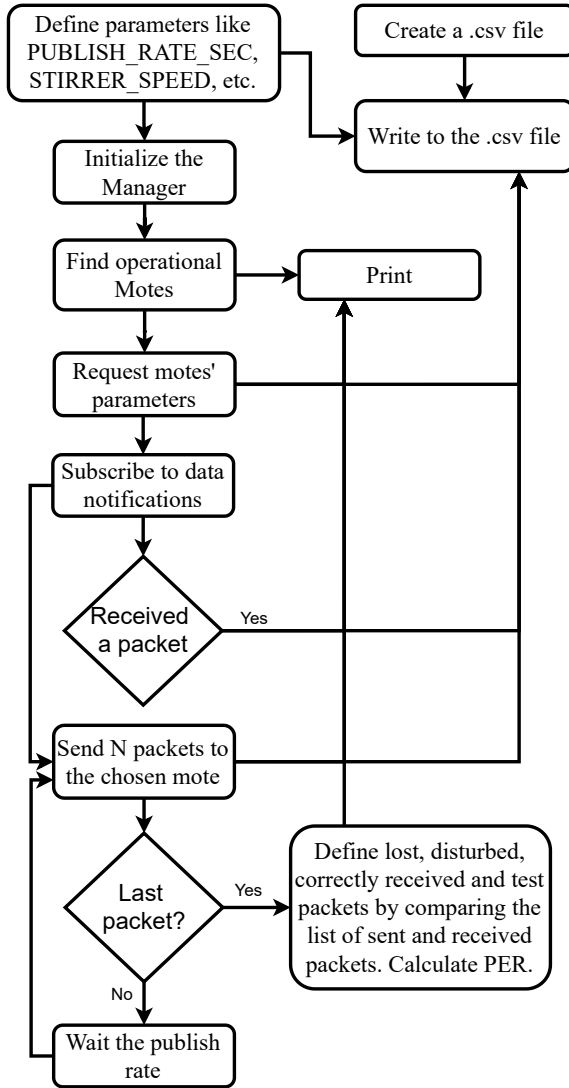
Figure 5.5: Manager's echo program flowchart.

due to the increased reflections. Therefore, the PR was raised to 6 s, allowing to establish the connection, though the PER became 12 % and the ET increased to 613 s.

For the same test series 4, the stirrer rotation in the smaller RC influenced the connection, sometimes facilitating it and giving an errorless performance, sometimes worsening it (the maximum achieved PER was 14 %).

5.3.5 Concluding the robustness tests inside an RC

Let us summarise IOLW and SmartMesh IP results in Tables 5.8 and 5.9. Test series were classified into four series and corresponded to the test procedure described in 5.3.1.

IOLW and SmartMesh IP have different architectures. Hence, their latency per packet L_p and per byte L_B in ms is calculated differently. IOLW controls the latency by the cycle time equal to 10 ms during all the tests. Hence the Device will be regularly sending data within this time. SmartMesh IP assigns time slots to Motes using a particular pattern. Therefore, the latency was measured using timestamps of sent & arrived packets and then averaged.

Tables 5.8 and 5.9 show that, albeit the PER of IOLW is slightly worse during LoS tests, it remains stable and does not exceed more than 0.44 %. This was achieved by varying NRTx and TxP parameters. Alternatively, SmartMesh IP loses more packets during Non-LoS tests and has both higher latency per packet and byte. Nevertheless, the packet's payloads differ for these two WSN technologies. When IOLW was transmitting two bytes of raw data, SmartMesh IP had a higher payload of 90 bytes. IOLW forces to send data from Devices within each cycle time. It means that sensors have to be more active compared to SmartMesh IP in which Motes go to sleep mode right after the packet is sent. Since the agricultural sector performs comprehensive monitoring, the transmitting data can reach kilobytes and machines can work in the field the entire day. Therefore, it was assumed that SmartMesh IP consumes less energy. Hence the energy consumption question and the payload per packet

Table 5.7: SmartMesh IP test comparison for different numbers of transmitted packets

Number of transmitted packets	Received packets		PR, s	ET, s	PER, %
	Correctly echoed packets	Lost packets			
100	100	0	4	408.19	0
1000	100	0	4	4025.32	0

had higher priority over latency. Thus it was decided to further proceed only with SmartMesh IP and test it on the actual combine AgV.

5.4 Robustness of SmartMesh IP tests on an AgV

An additional test for SmartMesh IP was conducted on a tracked combine harvester CR9.90 [88] at Case New Holland industrial (CNHi), Zedelgem, Belgium.

The test setup is presented in Fig. 5.6. During the test, several Motes at very different positions were considered. One of them was deliberately put behind the metal lid (the sensor marked with dashed edge lines) to test the reverberant/shadowing nature of the AgV. Also, the Manager's position was

Table 5.8: IOLW test results inside an RC

Test series	PER, %	NRTx	TxP, dBm	L_p,[a] ms/-packet	L_B, ms/B
1	[0:0.22]	[2:6]	[-6:5]		
2	[0:0.56]	[3:6]	[-6:-2]	10	5 or 1.33[b]
3	[0:0.094]	6	-6		
4	[0:0.13]				

[a] The packet length (raw data) in the tested single-slot communication between one Master and Device was two bytes;   [b] In the case of double-slot communication, the packet length is increased to 15 bytes.

Table 5.9: SmartMesh IP test results inside an RC

Test series	PER, %	NRTx	TxP, dBm	L_p,[a] ms/-packet	L_B, ms/B
1	0			1890.0	21
2	0	3	8	2675.0	29.72
3	[4:9]			3203.3	35.59
4	[0:12]			6965.9	77.4

[a] The packet length in the tested communication between one Manager and Mote was 90 bytes.
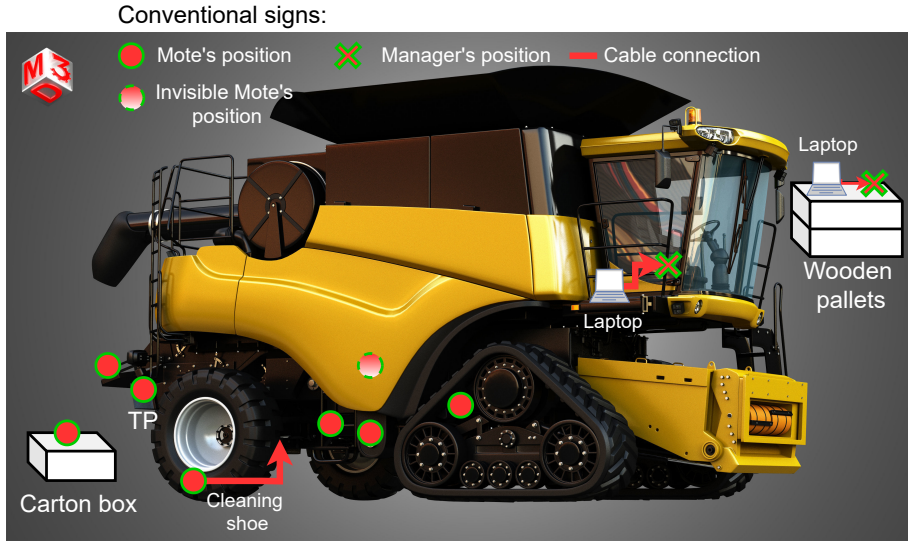
Figure 5.6: SmartMesh IP test setup at CNHi.

varied between outside the AgV on some wooden pallets or inside the cockpit. The communication program on SmartMesh IP devices had not been changed since the tests performed in RCs. However, one parameter of the WSN — a Hop Depth (HD) was included in the scope since the mesh consisted of more than one sensor. HD represents data circulation among the mesh participants. For example, if the HD is 10, there are no intermediary Motes between the data path from the Manager to the Mote and vice-versa. If the HD is 11, 10 % of the data will be sent through the intermediary Mote, while the remaining 90 % will flow directly to the Manager.

The test aimed to determine the minimum PR for a PER that reaches 0.

The initial test was performed with the Manager on wooden pallets. The PR was set to 4 s and the number of packets to send was 100. Table 5.10 shows the test results. All the Motes were directly connected with the Manager, except for sensor S3 which has an HD of 11. Fig. 5.6 depicts one Troublesome Place (TP) on the harvester. The TP Mote S4 had an HD of 10 and was the only one whose PER was higher than zero (namely 5 %). The average ET was 407 s.

For the second test, the setup remained the same except for the Manager that was put inside the cockpit. With the same PR equal to 4 (except for sensor S5) and 100 packets, all the Motes showed errorless results. Table 5.11 shows

results. The average ET was 404.8 s for the sensors with the PR equal to 4 s. Two Motes had an HD of 20, including the TP Mote S4. This means that the data flowed 100 % through an intermediary Mote and only then to the Manager.

The results for sensor S5 depicted in Table 5.11 showed that PR could be reduced and the total test time could be optimised by sending more packets with less waiting time between them. Consequently, the PR was decreased to 1 s and the number of packets increased to 1000. This resulted in the ET equal to 1029 s. Conducting the same tests as the ones shown in Table 5.11 with 1000 packets and 1 s PR resulted in the errorless performance for all the sensors except for S4 for which only two packets were lost (PER = 0.2 %). HD for these tests was equal to 10 for all the sensors.

Table 5.10: The SmartMesh IP test on an AgV when the Manager was put on wooden pallets

Acting sensor	HD	Number of trans- mitted packets	Received packets		PR, s	ET, s	PER, %
			Correctly echoed packets	Lost packets			
S1	10	100	100	0	4	416.17	0
S2	10	100	100	0	4	404.74	0
S3	11	100	100	0	4	418.73	0
S4	10	100	95	5	4	399.43	5
S5	10	100	100	0	4	399.36	0

Table 5.11: The SmartMesh IP test on an AgV when the Manager was put in the cockpit and sensor S5 was on a carton box

Acting sensor	HD	Number of trans- mitted packets	Received packets		PR, s	ET, s	PER, %
			Correctly echoed packets	Lost packets			
S1	10	100	100	0	4	399.46	0
S2	20	100	100	0	4	399.7	0
S3	10	100	100	0	4	409.07	0
S4	20	100	100	0	4	399.8	0
S5	10	100	100	0	3	299.99	0

As mentioned earlier, the lid was used to test the behaviour of a Mote in a more reverberant/shadowing environment. One Mote was placed under the lid. It did not lead to errors, supposedly due to a thin opening between the lid and the body of the harvester. Though the opening was small, its total area was sufficient to allow the signal to be transmitted to the Manager error-free.

The same test setup was repeated with the Manager outside on wooden pallets. The PR was decreased two times and became 0.5 s. This did not affect any Mote (not even the one under the lid) except for the TP Mote S4, which had an HD of 10 and a PER of 2.4 %. The ET reached 525 s. This results in an L_p of 25.24 ms or an L_B of 0.28 ms. The increase of the PER in the last test is predictable because the distance between devices was increased. Nevertheless, the changing HD is not straightforward since SmartMesh IP is a proprietary protocol with a hidden stack.

Testing SmartMesh IP on the AgV not only revealed its capability to work in such a harsh setup with many reflections but also gathered one of the possible scenarios of the EM environment in the agricultural sector. With this, we proceeded further and decided to maximise the correlation between the lab environment (the RCs) and the actual one (the AgV).

5.5 Recreating the agricultural EM environment in the lab setting

Since the EM environment inside RCs is too reverberant compared to an AgV (the difference in L_p is almost five times), a typical way of making it less reverberant is to make the RCs' delay times smaller. This can be achieved by using absorbers (see Fig. 5.7).

The test was aimed to define the EM environment starting from which the PR parameter inside the RC will coincide with the one achieved during tests on the harvester. Therefore, the PR of 0.5 s with 1000 sent packets were preserved. The positioning was the hardest in terms of wireless communication: the Manager was in the smaller RC, while the Mote was in the bigger RC behind the stirrer.

After a number of tests with different configurations, the optimal positioning was found (see Fig. 5.7). This configuration not only preserved the PR parameter but also resulted in the PER of 4.1 % which is within the PER range of the harvester's tests (the maximum PER there was 5 %, see Table 5.10).

The situation can be further improved by adding more absorbers and positioning them at specific places in the chamber. However, this is out of the scope of this

Conventional signs:

Absorber's position

Optimal absorber's position

◯ Mote's position ✖ Manager's position — Cable connection

Stirrer

Wooden table

Opening (can be closed)

Stirrer

Chamber's cable input

Door Door Desktop/Laptop Door
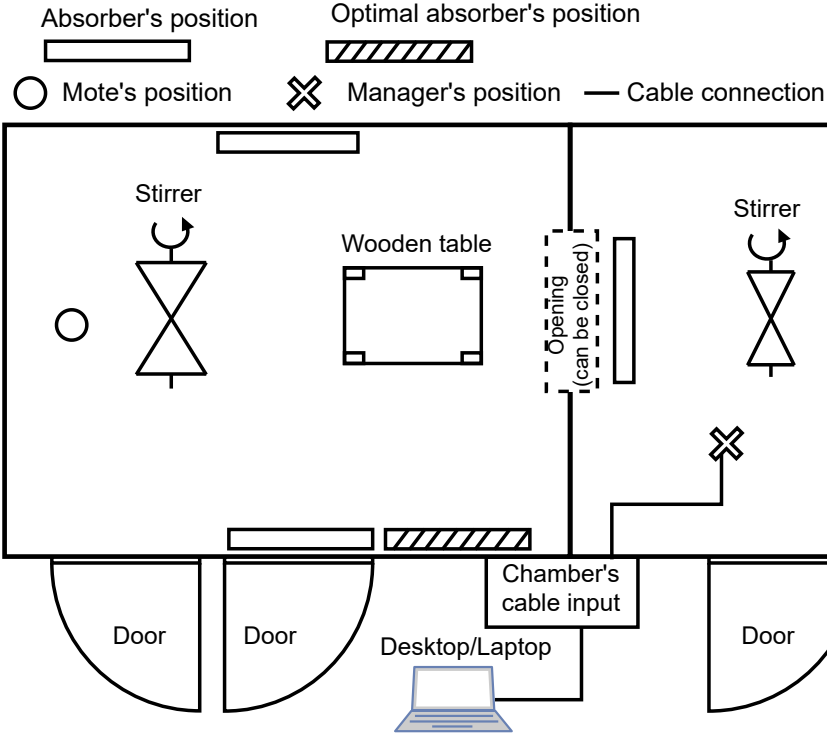
Figure 5.7: Simulating the harvester's EM environment in the lab setting.

manuscript and it is kept for research work.

5.6 Conclusion

This chapter investigated the problem of robust wireless communication on an AgV considered as a semi-reverberant EM environment. This study helps to select the most optimal protocol for the WSN on an AgV.

The chapter considered two WSN protocols: IOLW and SmartMesh IP. Each of them is robust with regard to the multipath fading environment inherent to the agricultural field and capable of tackling the tasks needed on the AgV. For this purpose, one may need to tailor different modifiable protocol parameters for

specific needs. Thus, NRTx and TxP are key parameters of IOLW, whereas, for SmartMesh IP, PR plays a vital role in optimizing the QoS.

The tests conducted on the tracked harvester gave valuable insights into a probable EM environment on an AgV. The obtained results will be further extended to achieve a uniform procedure of replicating the EM environment of an AgV in the lab environment.

Chapter 6

Valorisation plan

The content and results of this Chapter have already partly been disseminated in [52]. This publication presents a validation of the NarrowBand Interference (NBI) "Mod-remod" removal algorithm.

This chapter provides a valorisation plan for the conducted PhD research. The chapter proposes the NBI removal algorithms as a main product, which could be realised as Software-As-A-Service (SAAS). The valorisation plan gives a short description with some technical details of the proposed software product. After that the societal benefits are outlined. This chapter also shows the market overview along with how to penetrate it taking into account potential customers and competitors. Then the business model is also proposed stressing the needed investments and an estimated cash flow. The chapter ends with concluding remarks.

6.1   What is involved in the valorisation?

The current technological advancements are pushing humanity to automate, digitise and render more and more aspects and processes of human life "smart" or even autonomous. This means that data transmission and communication play an essential role in society. For example, Industry 4.0 and the upcoming complementing Industry 5.0 will extensively use communication and data transfer. For example, [89] summarises the Industry 4.0 requirements originally made by 3rd Generation Partnership Project (3GPP) and 5G Alliance for Connected Industries and Automation (5G-ACIA) in [90] and [91] identified

the Industry 4.0 use cases and applications. [89] also divides these use cases into three traffic classes: deterministic periodic, deterministic aperiodic and non-deterministic. The first two traffic classes depend on the end-to-end latency meaning that data must be received within a certain deadline. For example, depending on the application, the end-to-end latency of deterministic periodic traffic varies between 1 and 6 ms, whereas for deterministic aperiodic traffic this range is almost the same and is between 1 and 5 ms [89]. The data communication requirements on Quality of Service (QoS) parameters are very stringent; for some use cases, latency should not exceed more than 1 ms, and reliability has to be higher than or equal to 0.99999 [89]. This means that during a communication session, data must be transmitted in one go, obtained by the receiving side, and also understood and deciphered. In other words, the intended message has to be split from the noise that comes along. Taking into account the booming rise of wireless technologies, this only escalates the interference issue. For example, the number of mobile subscriptions at the beginning of 2022 was already more than 8.65 billion [92]. In addition, the number of new Bluetooth (BT) devices was 7.0 billion [93], while the number of Wireless Local Area Network (WLAN)-connected devices worldwide in 2021 reached 22.2 billion [94].

Though each industry sticks to a specific standard group that stipulates a number of admissible protocols, the basis for them can be the same. This also concerns wireless communication, the foundation technique of which, especially for Autonomous Systems (ASs), is Orthogonal Frequency Division Multiplexing (OFDM) [5]. Despite its indisputable advantages (for more detail, see Chapter 2), OFDM is vulnerable to ElectroMagnetic Disturbances (EMDs), one of which is Continuous Wave (CW) EMD or NBI.

An NBI by itself can be negated in a wireless communication system providing that it coincides in frequency with any of the subcarriers of an OFDM system by implementing coding techniques and interleaving, for example, [15]. However, when there is a frequency mismatch between a disturbance and subcarriers that is not a multiple of a subcarrier width, then the spectral leakage phenomenon happens. This means that due to the Fourier transform of a non-coherent sampled signal the NBI's energy leaks throughout an OFDM symbol. As a result, the communication session is disturbed since the receiver cannot correctly demodulate the received symbol. In addition to that, as was shown in Chapter 4, the receiver may even face difficulties in recognising an OFDM frame. This requires one or more retransmissions, which is unacceptable in some applications.

After a thorough literature investigation, it was decided to create a solution that will be (i) effective against an NBI, (ii) be able to be deployed on actual communication units and (iii) be economically beneficial. This literature investigation is described in Chapter 2, Section 2.1. The solution comprises the

NBI removal algorithms presented in Chapters 2 and 3. Both these algorithms provide overall OFDM communication improvement. Since the solutions are constantly being improved for better performance, the QoS parameters of OFDM systems in which the algorithms were deployed are also changing. Nevertheless, the "Mod-remod" algorithm already provides an algorithm's gain of more than 10 dB (depending on the chosen modulation scheme). The "Differential" algorithm shrinks the throughput but, in return, it provides a more significant resistance against white noise and improves the Bit Error Rate (BER) performance by up to 42 % in simulations and the algorithm's gain to more than 27 dB (depending on the chosen modulation scheme). Moreover, from the economic point of view, the algorithms are not based on assumptions limiting their deployment. The only requirement is that the NBI has to be constant within the period of one OFDM frame which is of the order of a few ms (e.g. 4 ms for IEEE802.11a [2]). The algorithms have already been deployed in a lab setting as proof of concept. For a more detailed in-depth explanation, please, refer to the corresponding Chapters 2, 3 and 4.

6.2   Market analysis

As was shown in Chapter 1, many safety-critical systems operating wirelessly, are vulnerable to NBIs. However, with the help of the proposed algorithms, the reliability of safety-critical systems can be boosted whenever there is an NBI environment. For example, drones can deliver critical cargo (e.g. blood samples) between different parts of a city [95]. The lifting capacity of a drone is about 10 kg. There are use cases when a fleet of drones needs to be used. The drones within the fleet should maintain Machine-to-Machine (M2M) communication, which is based on cellular communication [96]. As was shown in Chapter 1, cellular communication is prone to NBIs. Considering an urban environment, the latter can disrupt M2M communication. As a result, NBI removal algorithms can be implemented in different areas:

- Industrial (factories and plants with installed Wireless Sensor Networks (WSNs) that capture and gather vital data);

- Aerial;

- Agricultural;

- Medical;

- Automotive;

- And others.

Entering all of these sectors or a few of them at once not only puts different requirements on the proposed product (e.g. regulatory bodies) but also complicates the initial product's sales since every sector has its own supply hierarchy and "market rules". This makes such an endeavour too daunting. Consequently, it was decided to focus on one market, automotive, for the following reasons. First, there is a shortage of drivers [97]. Second, statistics show that 85 % of all road accidents are caused by human error [98]. As a result, there is a big demand for Autonomous Vehicles (AVs) and a lot of companies are actively testing them [99]. By 2030, some experts assume that the self-driving cars market size will be 62.4 million units [100]. For this booming market, regulatory bodies (e.g. 3GPP or Institute of Electrical and Electronics Engineers (IEEE)) have been working on standards and prescribed procedures that are also related to wireless communication [101], [102]. In addition, both 3GPP and IEEE will be using OFDM as a basis for their Vehicle-to-Everything (V2X) technology.

6.2.1   The product's benefits in the automotive sector

Since the automotive sector is the targeted market, the algorithms' or the product's benefits have to be adjusted. The product makes V2X communication to be dependable in the presence of NBIs. With this improvement, one may loose the safe distance constraints between vehicles allowing more units to be connected in the vicinity. As a result, the product can benefit city mobility. This is exceptionally viable in the capitals and big cities where traffic is already heavy.

The proposed product will require minimal extra hardware. The only hardware that could be needed is a computational chip to speed up the calculation processing. Let us estimate its processing speed. The processing time of a Long Term Evolution (LTE) decoder is equal to 70 μs [103], while the processing time of the proposed "Differential" and "Mod-remod" NBI removal algorithms is equal to 70568 and 55597 μs, respectively. This results in a ratio of 1008 and 794 for the "Differential" and "Mod-remod" NBI removal algorithms, respectively. The processing speed was not the main aim of the current research, as a result, the algorithms can still be improved in terms of their speed.

6.2.2   Market penetration strategy

Since the proposed solution tackles the ElectroMagnetic Interference (EMI) (NBI is a part of it) issue in wireless communication, it was decided to brand the potential product as "NoEMI".

Entering the automotive market with already established organisations will take time for the product to be sold. As a result, there are two possible products: the main one, which is an NBI removal algorithm and consultancy services. The algorithm would be positioned as SAAS, while consultancy services would be given in the area of ElectroMagnetic Compatibility (EMC) in wireless communication.

Though the product is partially validated (synchronisation issues still have to be resolved) during the tests in simulations and lab settings, it has to be deployed on V2X communication units. The V2X technology is realised on On-Board Unit (OBU) and Road-Side Unit (RSU), where the former is incorporated in a vehicle, while the latter is fixed on road infrastructural units like traffic lights or light poles. To be able to sell the product, first, it has to be tested both on OBUs and RSUs. This will require physical vehicle trials. The KU Leuven does not have the needed facilities for these tests. However, such facilities are available at KU Leuven's partners inside the European Union (Flanders Make [104]) and outside the European Union (Horiba Mira [105]). Due to the close collaboration between KU Leuven and Horiba Mira within the SAS project [106], Horiba Mira is deemed to be a potential partner. It is an automotive engineering consulting company that is actively working with the implementation of self-driving technologies. The company provides different services from research inquiries and thorough simulations to cybersecurity and physical testing of self-driving technologies. The latter is the main interest of the collaboration with Horiba Mira. The company's testing facility extends over approximately a 3.44 m^2 site. It allocates a diverse mix of testbeds that allow all-weather testing which can be realised as a fully-controlled, semi-controlled or public environment. This wide range of scenarios will enable us to test various use cases: cooperative merging, platooning and assured connected AV city which includes configurable junctions, parking in constricted and bad-lit areas and sensor-challenging environments [107]. Such a diverse test facility will make it possible to adjust the final product and improve it by testing in various weather conditions and use-case scenarios.

Since Horiba Mira provides a vast range of legal consultancy services covering regulatory and standardisation bodies (e.g. European Telecommunications Standards Institute (ETSI), IEEE or 3GPP). Hence, it is a viable option to start collaborating with them for a potential stipulation of NBI tests in V2X (Cellular-V2X (C-V2X)) systems. Next, to better advertise the product and to be aware of the latest trends, demands and market requirements, membership in automotive unions is required.

The 5G Automotive Association (5GAA) is a global organisation aiming to connect automotive and telecommunication industries to work together on state-of-the-art solutions for the upcoming transportation and mobility services

[108]. The organisation already accounts for 115 members that aim to achieve one objective, connected mobility. The members are split into seven working groups:

1. WG1 - Use cases and technical requirements. This group defines use cases and technical requirements along with performance indicators to certify connected mobility solutions.

2. WG2 - System architecture and solution development. This group reviews currently available solutions in wireless network deployment models, Radio Access Technology (RAT) and other technical areas to define, develop and recommend system architectures and interoperable solutions.

3. WG3 - Evaluation, testbeds and pilots. This group ensures that new C-V2X products conform to existing standards and are interoperable with each other.

4. WG4 - Standards and spectrum. This group provides recommendations to standards development organisations (e.g. ETSI and 3GPP) and agrees on spectrum requirements for V2X technologies.

5. WG5 - Business models and go-to-market strategies. This group chooses the most suitable approach to certification of the connected mobility solutions and agrees on criteria for business models.

6. Regulatory and public affairs. This group deals with policy and regulatory matters from a regional to global level to excel and support technology innovation and investment.

7. WG7 - Security & privacy. This group identifies security and privacy gaps in the studied solutions and their specifications.

Regarding the competence obtained at KU Leuven, the NoEMI can be an excellent asset to the WG1 and WG4 5GAA working groups.

Along with the standardisation bodies and automotive union companies, the other way to advertise and be in the loop with the latest trends in connectivity is through mobile network provider organisations. These organisations also drive the automotive market, since the OBUs and RSUs of AVs and road infrastructure, respectively, will be equipped with mobile network units. Similarly to the automotive union, the interests of mobile network providers are represented by the Global System for Mobile Communications Association (GSMA) [109]. Because mobile network technologies are incorporated in different domains, GSMA allocates certain groups for its associate members. As a result,

it is considered to aim for the operator and sector membership in which telecommunication regulatory bodies and automotive companies are represented.

Once the sector of operation and means of penetration are identified, it is important to know the direct customers and main competitors.

6.2.3 Potential customers and competitors

The potential customers can be represented by OBU and RSU companies. The choice of these companies mainly depends on the target geographical market.

For example, the Lacroix group which is based in France and operating throughout Europe and Northern America works towards the connected world. Having four production plants, Lacroix supplies electronic equipment and industrial Internet-of-Things (IoT) solutions for industrial, automotive, home & building automation, civil avionics & defence and healthcare market sectors [110]. The company provides connected technologies for smarter mobility for the automotive sector. This includes a range of activities, among which are V2X solutions. Lacroix produces its own OBUs and RSUs. They also work with V2X applications not only for AVs but also for the earlier stage, connected vehicles. Ultimately, the company collaborates with European research projects that deal with V2X and Intelligent Transportation Systems (ITS) solutions (e.g. the SCOOP project [111]). This is a very probable customer since it both produces OBUs and RSUs and performs research activities, which can be improved by the expertise and product of the NoEMI team.

Since the automotive market is a very challenging market to enter, it was decided to potentially distribute the NoEMI solution through the companies that are in the product value chain or deal with other companies from the product value chain. A very simplified version of the product value chain is presented in Fig. 6.1. It is shown as a pyramid with different tier suppliers from tier three to Original Equipment Manufacturers (OEMs). The higher the tier, the more complex and sophisticated the product is. For example, tier three provides raw materials, intermediate goods and components, while OEMs distribute the end-user product. As was mentioned earlier, one of the most probable NoEMI product solutions is SAAS which belongs to tier 2 and 1 products. Figure 6.1 also provides some typical companies per each layer of the product value chain. The companies marked in red are of special interest because they are deemed to be potential users of the NoEMI solution. For example, Qualcomm is actively working on C-V2X solutions [112]. However, they have not yet openly disclosed (as far as the author knows) that their solutions are as good as NoEMI against NBIs. In the same manner Harman Savari, Cohda Wireless and Bosch could

be potential clients to whom the NoEMI solution will be sold as a software addition to their existing products.
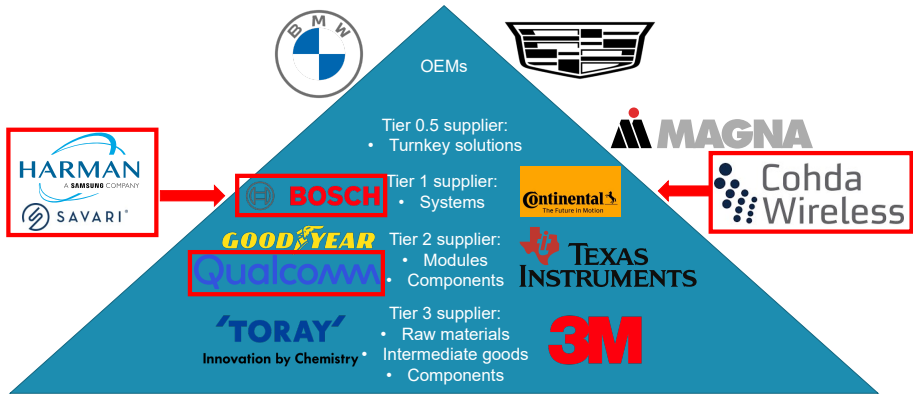
Figure 6.1: The automotive product value chain

The companies deemed to be potential customers can also turn out to be competitors as they may also come up with similar solutions in the near future or they are already working on the NBI issue in C-V2X systems.

6.3   Business model

The business model of the NoEMI establishment would be realised with the help of the KU Leuven research & development - tech transfer office. Through the university and venture organisations, NoEMI would aim to get 2.05 million euros as investments. This starting capital would mostly be used for recruiting suitable personnel, employee wages, office infrastructure, test and marketing costs and, finally, membership fees in standardisation organisations and automotive/telecommunication unions. Revenue streams would primarily consist of a SAAS licence sold for 2 euros per unit. The sold SAAS would be sold as a "black-box" solution with the algorithms' parts protected from pirating with the use of Microsoft Public Licenses (Ms-PL) [113]. The solution would be made to be easily installable and free service, updates and maintenance would be provided for customers. To tackle possible low sales numbers during the first years, NoEMI would also provide consultancy services in the area of wireless communication, EMC and research activities. The price per services would be hourly-based with 150 euros per hour price. The NoEMI financial

performance, presented in Fig. 6.2, reflects the company's potential cash flow
in euros (dashed line) and cumulatively sold licences in million units (solid
line) to time. It can be noticed that in the beginning there is no profit and
no sold licences. The main cost completely consumes the little turnover that
is obtained through consultancy services. However, starting from September
2024 the first partnership is planned to be established and licences would start
selling. Nevertheless, it will not be enough to cover all the expenses, thus cash
outflow happens (the cash flow line is going down). Starting from May 2027
the company's performance prediction shows steady income due to established
connections and partnerships. As a result, cash inflow takes place.
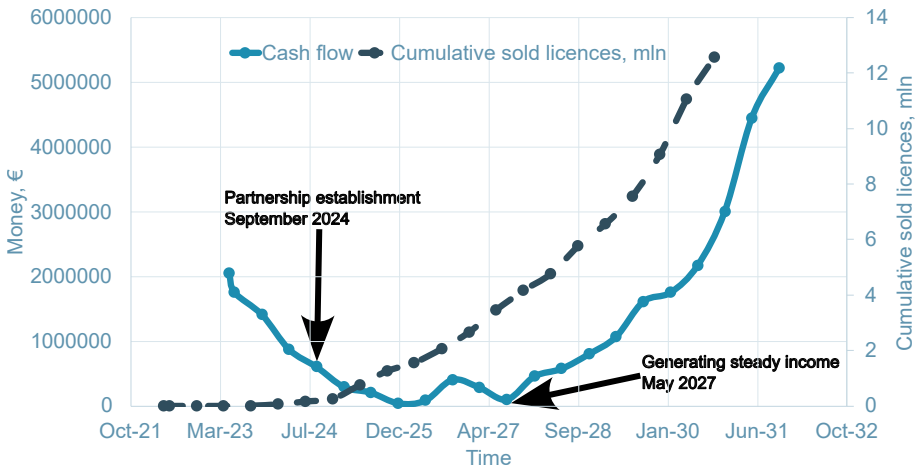
Figure 6.2: The NoEMI financial performance prediction

The NoEMI's ultimate market goal would be to gain at least 20 % of the market
in 10 years or by January 2033. At the same time, it is assumed that constant
product updates would follow due to a constant search for improvements within
the NoEMI team and collaborations with academia. The NoEMI product is not
bound to only NBIs in the automotive sector. The technology is planned to
be expanded to other types of NBI and other application fields (e.g. medical
systems or Agricultural Vehicles (AgVs)).

6.4   Conclusion

This chapter presents an NBI solution for future wireless communication systems of ASs as an SAAS product. The solution is based on the spectral leakage pattern of a disturbance in OFDM-based systems. The product is marketed under the brand name "NoEMI". It allows to benefit various ASs. However, the main target is the automotive sector within which the NoEMI product can improve city mobility by having more connected vehicles in the vicinity and reduced safe distance between them. This is possible due to increased NBI withstand levels of OFDM-based communication. Currently, two modifications of the NBI removal algorithm differ in their application level. For example, the "Mod-remod" algorithm is effective with low modulation scheme orders and relatively low ambient noise, while the "Differential" solution limits the throughput but is more robust against ambient noise. Nevertheless, the algorithm's gain for the "Mod-remod" and "Differential" algorithms can exceed 10 and 27 dB (depending on the modulation scheme and the BER level), respectively.

NoEMI could be further tested on the test facilities of KU Leuven's partner, Horiba Mira. This would allow the solution to be tuned and finalised. Marketing would happen through membership in automotive and telecommunication unions (e.g. 5GAA and GSMA). To even more strengthen the NoEMI's position in the market, close collaboration with standardisation bodies like ETSI or 3GPP is planned.

While the main NoEMI's customers are OBU and RSU companies, they are also competitors. Depending on which establishment can be achieved, it is decided to sell the NoEMI solutions through the already established "players" of the automotive product value chain as an option to their already existing products. Sales will be counted per sold OBU or RSU unit. At the same time, consultancy services could be offered in the field of research activities and EMC or wireless communication inquiries.

Finally, with a starting capital of 2.05 million euros acquired with the help of KU Leuven's research and development department and partner venture organisations, it is predicted that NoEMI would generate steady income within three years. The goal is to capture 20 % of the automotive market share by January 2030 through collaboration with academia and entering other markets by expanding a series of services that NoEMI can offer.

Chapter 7

Conclusion

7.1 Summary of the realised work

The research presented in this manuscript is a piece of the puzzle addressed by the Safer Autonomous Systems (SAS) European Training Network (ETN) project. The project aimed to make people trust Autonomous Systems (ASs) by increasing their overall safety. For that purpose, the work was split between different Work Packages (WPs), one of which was focusing on the design of inherently safe ASs. The ultimate goal of this WP was to integrate safety directly into the architecture of an AS. The upcoming ASs will highly depend on wireless connectivity to maintain the required dependability, which can reach the required level of 0.99999 for some applications. Therefore, the topic of this PhD thesis was formulated as "Making connectivity work reliably in harsh electromagnetic environments. Narrowband interference removal algorithms for OFDM-based communication".

7.1.1 Summary of the introductory chapter

With harsh ElectroMagnetic (EM) environments, the stress falls on Electro-Magnetic Disturbance (EMD), which can impair or completely disrupt wireless communication of a wireless system in such a way that it cannot perform its intended actions. After a thorough comparison of the potential wireless communication architecture of the upcoming ASs from different fields, it was found that Orthogonal Frequency Division Multiplexing (OFDM) is the main applied technology. OFDM is a very effective technique helping to optimally

use the frequency bandwidth by using the orthogonality property. This allows it to have larger throughput without InterCarrier Interference (ICI) compared to other transmission techniques. The inherent to wireless communication multipath fading is tackled by introducing a Cyclic Prefix (CP), which repeats the tail of its OFDM symbol. Nevertheless, OFDM is not flawless and has some drawbacks, among which is susceptibility to NarrowBand Interferences (NBIs).

An NBI is a type of EMD that introduces an unwanted signal over a narrow frequency range. A particular case of an NBI is a Continuous Wave (CW) EMD. As a result, a valid question was formulated: "How to tackle NBIs in OFDM-based systems?" Before proposing any solution, the influence of an NBI on an OFDM-based system was investigated. It was found that if the NBI's period is not aligned (the probability of the opposite resulting in coherent sampling is extremely small) with the one of an OFDM signal, then non-coherent sampling at the receiver's side occurs. This is the main problem as during the Fourier transform, it results in the NBI's energy leaking throughout the OFDM frame. This is a side-effect of the Fast Fourier Transform (FFT) operation.

7.1.2 Summary of the "Mod-remod" NBI removal algorithm chapter

After showing the research motivation in the introductory chapter (Chapter 1), this thesis described the software-based "Mod-remod" NBI removal algorithm (Chapter 2). Prior to describing the algorithm, the works of other research groups were thoroughly investigated. It formally allowed subdividing all the existing solutions into three groups depending on the domain in which NBI removal manipulations are happening. The groups are frequency, time and mixed domain solutions. The proposed "Mod-remod" algorithm falls into the frequency domain solution group.

The proposed "Mod-remod" NBI algorithm assumes that due to the high data rates in modern OFDM systems, an NBI remains constant within one OFDM frame. This allows the NBI to be represented as a CW EMD. The main advantage of the proposed algorithm is that it does not require any additional hardware filters or prior information about a disturbance.

Section 2.2 described the mathematical model of the algorithm and the OFDM system. During the mathematical derivation, it was shown that by demodulating and re-modulating the received OFDM signal after the FFT block at the receiver's side, one may obtain a number of NBI's frequency estimations, from which one is selected. This frequency estimation is further used to obtain the NBI parameters, such as amplitude and phase. With these parameters, one

may reconstruct the disturbance and subtract it from the received noisy OFDM symbol. In Section 2.3, the derived mathematical solution was evaluated using simulations. The simulations were conducted assuming that perfect time and frequency synchronisations take place between the transmitter and receiver; no multipath fading effects and only one NBI modelled as CW EMD was disturbing the OFDM signal. The simulations were performed in Matlab at baseband frequencies. During the simulations, various Signal-to-Interference Ratio (SIR) levels, disturbance phases and relative frequency positions of the NBI towards OFDM subcarriers were covered. The OFDM system also had different Quadrature Amplitude Modulation (QAM) schemes and a different number of subcarriers. To decrease the dependency between the results, multiple sets of data bits were generated.

Since the "Mod-remod" algorithm is based on the cases when an NBI introduces spectral leakage, the non-spectral leakage case was also addressed. In this case, an NBI can be addressed in a similar way as a burst disturbance from which the OFDM system can be protected by using coding techniques. For simplicity, the Hamming(15,11) code and interleaving were used.

The simulation results showed that the algorithm is capable of removing a single NBI from an OFDM system. In some cases, the algorithm's gain (the difference between the simulation result without the algorithm and with it) was more than 80 dB. Since an NBI affects the same number of subcarriers, it was also noticed that increasing the number of subcarriers in the OFDM system positively influences the Bit Error Rate (BER) performance of the algorithm. This happens because more NBI estimations become available. Changing the modulation scheme order does not affect the performance of the algorithm. The algorithm performs the same for different QAM schemes. Nevertheless, with the increase of the modulation order, the results can degrade due to the hardware/software precision as numerical noise can more likely introduce a symbol flip during the demodulation procedure.

When introducing white noise, modelled as Additive White Gaussian Noise (AWGN), in simulations with a Signal-to-Noise Ratio (SNR) higher than or equal to 80 dB, the performance of the algorithm is unaffected. However, decreasing the SNR up to 60 dB decreases the "Mod-remod" performance. The used Hamming and interleaving techniques can negate this BER degradation to a bare minimum. These large SNR levels are unlikely to be in wireless systems. Consequently, the "Mod-remod" NBI removal algorithm was tested against a broader span of SNR values. The results showed that the algorithm performs the best at low QAM modulation scheme orders (compare the BER of 1 % vs 8.6 % for Quadrature Phase-Shift Keying (QPSK) and QAM64, respectively, when SIR and SNR levels are equal to 0 and 25 dB, respectively). Nevertheless, even at low QAM scheme orders (e.g. QPSK), AWGN is able to affect the estimation

process of the algorithm making it perform worse. This happens due to the fact that the algorithm's final estimation is based on calculations conducted for all the subcarriers. Normally, without AWGN, the estimation is more accurate for subcarriers that are spectrally further away from NBI. This means that the energy spillage from the NBI is minimal at these subcarriers. On the other hand, the AWGN's influence on these subcarriers becomes comparable. As a result, the "Mod-remod" estimation is very sensitive to small fluctuations caused by AWGN or any other type of noise on subcarriers. Lower QAM modulation order schemes are inherently more robust to white noise and can withstand lower SNR levels. Therefore, a practical guideline was formulated for the use of the "Mod-remod" NBI removal algorithm. It states that to increase the efficacy of the latter in the presence of NBIs, one may need to use the lowest possible modulation scheme order.

7.1.3 Summary of the "Differential" NBI removal algorithm chapter

The initial research on NBI removal in OFDM systems resulting in the "Mod-remod" algorithm gave the needed insights for a new NBI removal algorithm's iteration. Chapter 3 described the "Differential" NBI removal algorithm. Instead of generating NBI estimations for all the subcarriers as was done in the "Mod-remod" algorithm, the "Differential" one uses the subcarriers at which the NBI energy is the largest. By limiting the used bandwidth in half and transmitting the mirrored signal along with the useful one, one may obtain the noise energy present in the transmission volume. This energy is obtained by summing the two halves of the obtained OFDM signal. Taking into account the same assumption as for the "Mod-remod" algorithm and assuming that the SIR level is larger than the SNR, one may neglect the influence of white noise. This was used during the mathematical derivation of the NBI parameters in Section 3.1. During the estimation process, an NBI is deemed to be found if two conditions on the summed spectrum are met: the two maxima values have to be of the opposite sign and the adjacent to these maxima values have to asymptotically decrease in value. As soon as the NBI parameters are defined, the NBI is recreated and subtracted from the difference between two halves of the received OFDM signal. If there are multiple NBIs, the "Differential" algorithm can iteratively find them and eliminate them. To increase the accuracy of the estimations, the refinement procedure is introduced. This is an iterative process during each iteration of which the NBIs decrease influencing each other's estimation calculations. The refinement happens until the convergence number is achieved or the number of refinement iterations is reached. The "Differential" algorithm NBI search along with refinement was described in Section 3.1.3.

To increase the algorithm's efficiency even more, a few optimisations have been performed and described in Section 3.2. In Section 3.2.1, the choice of the threshold parameter v was investigated. The parameter v is a percentage value of the minimum Euclidean distance $D_{\min}$ between neighbouring points on the I-Q constellation of the chosen modulation scheme. From the product of v and $D_{\min}$, the algorithm identifies the energy threshold exceeding which can lead to a symbol flip. During simulations for different threshold parameters v, it was identified that v equal to 0.5 leads to the best BER performance.

The next optimisation of the algorithm was in finding the optimal convergence number and the refinement iteration step number. This was addressed in Section 3.2.2. During simulations, two identical NBIs but spectrally spread from each other to not influence the estimation result, were disturbing the signal along with AWGN having the SNR equal to 16 dB. The simulations for various SIR levels showed that the optimal refinement step number is two, while the convergence number is $1E - 4$.

The "Differential" algorithm is also able to accurately estimate the NBI's parameters when no spectral leakage happens. The reasoning is presented in Section 3.1.2. Nevertheless, the accurate estimation happens when white noise is extremely low or it is not present in the system. Consequently, the non-spectral leakage case is not tested in simulations and it is recommended to use coding techniques (as was shown for the "Mod-remod" algorithm) to be able to increase the OFDM system's robustness.

Like the "Mod-remod" NBI removal algorithm, the "Differential" one is evaluated through simulations in Matlab. Numerous simulations for different NBI (SIR, phases and spectral leakage case scenarios) and system parameters (the number of subcarriers and modulation order schemes) were performed. White noise (modelled as AWGN) was introduced with different SNR values. For some simulation cases, the reference SNR level equal to 16 dB was used.

The simulation results when a single NBI and constant AWGN (the reference SNR value was used) were disturbing the OFDM signal (see Section 3.3.2) showed the following. For QAM64 with 64 subcarriers, the algorithm's performance significantly improved the system's BER performance which did not exceed 3 % throughout a vast range of SIR values (SIR = [-30;50] dB), while for the case without the algorithm, the BER value was close to 50 %. Nevertheless, this BER difference was at the lowest SIR level. The results also proved the initial assumption regarding the difference between SIR and SNR values. As soon as the SIR value was smaller than the SNR value for at least 10 dB, the algorithm's BER performance was on average constant, whereas when the difference between these values became less, the algorithm's performance started decreasing. At some point (for the simulation case the SIR was equal to 20 dB)

the algorithm stops looking for NBIs as its precision is no longer guaranteed due to large AWGN values and the system with the algorithm performs as the reference case system without the algorithm. Different spectral leakage cases did not noticeably affect the algorithm's performance.

When the algorithm was disturbed again by a single NBI and AWGN but with variable power, different spectral leakage cases did not significantly affect the algorithm's performance as well. The simulation results also showed that the algorithm significantly expands the OFDM system's capabilities of working under harsh conditions in terms of AWGN and NBI conditions. The results were presented in Section 3.3.3.

To optimise the spectral distance between two NBIs disturbing the signal and not affecting the algorithm's estimation capabilities, a series of simulations were performed. Section 3.3.4 described this and showed the performance of the algorithm when AWGN with a constant power was disturbing the signal as well as two simultaneous NBIs. The latter were separated by a different number of subcarriers. The simulations showed that the separation between two subsequent NBIs should be at least four subcarriers. Due to the folding operations on the spectrum (summation of the halves of the signal), the NBI separation should not exceed more than $K/2 - 4$.

With the insights obtained regarding subcarrier separation between NBIs, the "Differential" algorithm was tested under the influence of multiple NBIs and constant AWGN. These results were represented in Section 3.3.5 which showed the BER performance of the algorithm for a single NBI and compared it with the results when a number of NBIs is incremented by one up to eight simultaneous disturbances for QAM64 with 64 subcarriers. The simulations were performed for two spectral leakage cases where the spectral leakage parameter α, representing a relative spectral distance of an NBI towards two adjacent subcarriers, was equal to 0.5 and 0.25. The simulation results showed a degradation in the BER performance with each additional NBI. In addition, the difference in performance with different α parameters was more significant than for simulations with a single NBI. This indicated that the previously identified "safe" spectral distance between subsequent NBIs was not enough resulting in the BER performance degradation. Consequently, an extra series of simulations was performed to update the previously found spectral leakage distance between NBIs. Ultimately, the spectral distance of the minimum and maximum separation between disturbances is six and $K/2 - 6$ subcarriers, respectively. With this number, QAM64 with 64 subcarriers can withstand up to four simultaneous NBIs without any significant difference in performance for different α parameters. For example, the BER for $\alpha = 0.5$ and 0.25 for an SIR level of all NBIs equal to -30 dB and the SNR of 16 dB resulted in 2.75 and 2.56 %, respectively.

Section 3.3.6 showed the simulation results for a single NBI (variable SNR and α) along with AWGN when the OFDM system had different subcarrier numbers and modulation scheme orders. The results' tendency is similar to the one for the "Mod-remod" algorithm. However, the results are represented as the algorithm's impact which is the difference in the BER performance between the reference case when the "Differential" algorithm is inactive and the BER of the system when the algorithm is active. As a result, the algorithm's impact decreases with the increase in the number of subcarriers. With the increase of the latter, the BER performance of the reference case increases. Hence, with a constant BER performance of the algorithm, the overall algorithm's impact decreases. The modulation scheme order increases the BER performance degradation of both the NBI algorithm and the reference case. Consequently, the algorithm's impact decreases.

Finally, the "Differential" algorithm was compared with the "Mod-remod" algorithm and the "Pande" solution in Section 3.4. The comparison was done both for variable disturbance and white noise (E_b/N_I and $E_b/N0$, respectively). The simulation results showed that despite redundancy the "Differential" algorithm outperforms the other two solutions, however, when the SNR value is larger than or equal to 60 dB, then the "Differential" algorithm has occasional errors at large SIR values. This happens because the algorithm has difficulties accurately estimating at which half of the spectrum the NBI happened. The "Mod-remod" algorithm showed inferior results to the other two solutions except for very large SNR values. The "Pande" solution was mostly better than the "Mod-remod" algorithm but always worse than the "Differential" one.

7.1.4 Summary of the algorithms' validation chapter

After evaluation both of the algorithms in simulations, a practical validation was performed. Chapter 4 addressed this evaluation. The algorithms were validated using Software-Defined Radios (SDRs). However, while, in simulations, perfect timing and frequency synchronisation was assumed, the practical validation with SDRs had to tackle the synchronisation. The OFDM system recreated in Chapter 4 was based on the IEEE802.11a standard. This standard exploits identical training sequences (Legacy Short Training Field (LSTF) and Legacy Long Training Field (LLTF)) in the preamble part of an OFDM frame. This means that certain synchronisation methods based on cross- and autocorrelation operations could be used for (i) Coarse Timing Offset (CTO) and Coarse Frequency Offset (CFO) estimations and (ii) for Fine Timing Offset (FTO) and Fine Frequency Offset (FFO) estimations. A thorough analysis of these synchronisation methods was addressed in Section 4.1. In particular, Sections 4.1.1 and 4.1.2 showed the CTO and CFO estimation methods, while the rest of

Section 4.1 described the ways to further improve time, frequency and amplitude estimations. Nevertheless, these synchronisation methods are derived not taking into account a harsh EM environment introduced by NBIs. Consequently, the common synchronisation methods do not work when an NBI is injected. The synchronisation hurdles during the algorithm's deployment were mostly due to the significant degradation of the used training sequences in the preamble part of an OFDM frame. An injected NBI broke the synchronisation and equalisation of the OFDM system. This was reflected in Section 4.2 as well as in Section 4.3 which depicted the first attempts of the "Mod-remod" algorithm's deployment on ADALM-PLUTO SDRs. The main outcome of the first validation attempts was to either improve/change the synchronisation block or find a way of preserving the preamble. The latter was chosen to proceed with synchronisation challenges and this resulted in the need of injecting an NBI in code into an OFDM symbol, so the preamble is NBI-free. This made the OFDM system not real-time but it allowed performing synchronisation. The performed synchronisation procedures on the validation system are described in Section 4.4.1. Frequency synchronisation was performed by using the same local reference frequency of 10 MHz. The timing synchronisation was done by exploiting the "Bruteforce" method approach. According to this approach, in the captured OFDM signal, BER and Modulation Error Rate (MER) (can be assumed as an analogy to SNR) values were calculated. Among these calculations, the lowest BER calculation with the largest MER value would result in precise timing synchronisation. After covering the synchronisation procedures, Chapter 4 described validation measurements in Section 4.5. During the measurements, it was noticed that after a certain SIR level, the system's BER performance degrades irrespective of the algorithm's usage. This happens due to the receiver's built-in Automatic Gain Control (AGC) which makes the output power stay constant to ensure the maximum resolution of the analog-to-digital converter. Consequently, AGC puts hardware limitations on the algorithm meaning that the latter can be validated up to a certain SIR level. Measurement results were shown in Section 4.5.3. The measurements were performed for different modulation schemes and all of them showed that both the "Mod-remod" and the "Differential" algorithms improve the OFDM's BER performance. The largest algorithm's gain for the "Mod-remod" algorithm happened at the QPSK scheme for the BER threshold level (the reference BER value based on which the algorithm's gain was calculated) of 3 % and was equal to 18.36 dB. The "Differential" algorithm's largest algorithm's gain value was registered for QAM64 with the BER threshold level of 1 % and was equal to 32.78 dB. Though it was impossible to compare the simulation results with the ones from validation due to AGC and different OFDM frame compositions, the algorihtms are deemed to be validated.

7.1.5 Summary of the wireless sensor network technologies in the agricultural sector

Chapter 5 provided preliminary research on the possible hurdles the agricultural sector may face in its path to wireless connectivity. Future Agricultural Vehicles (AgVs) will benefit a lot from installing multiple sensors gathering valuable information and capable of significantly reducing maintenance costs. However, one may need to properly investigate not only the sensors but the wireless technologies they shall be exploiting. There are multiple available solutions to deploy a Wireless Sensor Network (WSN), which will connect numerous sensors. From such a variety the IO-link Wireless (IOLW) and SmartMesh IP technologies were selected to be further investigated. These two technologies work in the same frequency range of 2.4 GHz and provide high reliability. However, their WSN topology differs: SmartMesh IP has a "self-healing" mesh topology, while IOLW provides a star topology. The technologies were described in Section 5.2. To be potentially used on an AgV, the technologies were initially tested inside a Reverberation Chamber (RC). The RC provides a harsh EM environment in which the metallic walls of the chamber simulate metallic parts of an AgV and the stirrer simulates rotating parts inside the AgV. After thorough testing of IOLW and SmartMesh IP at different test configurations inside the RC (see Section 5.3), the SmartMesh IP technology was selected to be further tested on an AgV because SmartMesh IP consumes less energy compared to IOLW. The robustness measurements with SmartMesh IP on an AgV were described in Section 5.4. During the tests, the Publish Rate (PR) of 4 s which was maintained in the RC could be reduced to 0.5 s due to the less reverberant nature of the AgV compared to the one of the RC. Placing sensors beneath metal parts of the vehicle (e.g. a lid) did not affect the results. However, increasing the distance between the governing Manager device and its dependent Mote sensors affected the Packet Error Rate (PER) performance of the created WSN system. The larger the distance between the Manager and Motes, the higher the chance of lost packets. If the initial tests inside an RC gave the basic experience of working with the SmartMesh IP technology, the measurements on an AgV deepened the understanding of the potential of the technology and its behaviour on a real vehicle. This allowed the creation of an experimental setup (see Section 5.5) in which the EM environment of an AgV was aspired to be recreated by dampening the RC's EM environment by using absorbers.

7.1.6 Summary of the valorisation chapter

Chapter 6 provided a valorisation strategy for the conducted research. The main intellectual property that should generate income is the NBI removal

algorithms. The market analysis was shown in Section 6.2. The automotive field was selected as the target sector. The NBI removal algorithms could be used in Vehicle-to-Everything (V2X) communication to make it more dependable. This will contribute not only to overall safety but also to city mobility as with the increased safety one may keep a lower distance between cars, in other words, traffic optimisation happens. The algorithms will be branded as "NoEMI" and will be distributed as a Software-As-A-Service (SAAS) licence sold for two euros per unit. At the initial phase of the "NoEMI" activity, consultancy services in the area of ElectroMagnetic Compatibility (EMC) in wireless communication will also be provided. The algorithm's code will be under Microsoft Public Licenses (Ms-PL). As the algorithms are not yet finalised to be delivered to the market, KU Leuven's partners (e.g. Flanders Make or Horiba Mira) could assist "NoEMI" in validating the solutions outside the laboratory facility of KU Leuven. The main adopters and competitors of the "NoEMI" products are companies dealing with V2X solutions on On-Board Units (OBUs) and Road-Side Units (RSUs). The main advertising channels are technical conferences, associations, social media and standartisation bodies. The business model was described in Section 6.3. It is assumed that the initial investment of 2.05 million euros will suffice for the company to perform its activities. It is planned to establish the first partnership by September 2024. By May 2027, "NoEMI" aspires to generate steady income and recoup the initial costs of starting up a business. The ultimate goal is to get 20 % of the automotive market share in V2X, collaborate with academia and enter other markets by expanding the services "NoEMI" can offer.

7.2   Future work

The conducted research provided some solutions to the NBI problem in OFDM-based systems. However, already during the work, some questions arose that were either out of the scope of this manuscript or could not be tackled within the given time frame. For example, an NBI was represented as a CW EMD which is a particular case of an NBI. In general, an NBI can be assumed as any signal having a narrow bandwidth compared to the victim OFDM. Consequently, one needs to change the NBI model used in this manuscript. One of the ways, which is already under development within the M-group of the WaveCoRe team, is to change the parameters of a CW EMD (e.g. phase and amplitude) within one OFDM frame. In addition to that, the proposed algorithms have been evaluated with the presence of either AWGN or NBI noise. It is a fair comparison at the initial research stages but the influence of other EMD on the algorithms' performance has to be investigated as well. For example, modern OFDM communication systems are able to switch between different channel widths

depending on the environment, transmission needs and the user equipment capabilities. If for one OFDM frame, the disturbance was narrowband, then for the other frame with a different channel bandwidth it may not be the case.

Next to the NBI model update, one may also need to deal with synchronisation and channel estimation issues which were revealed during the validation process (see Section 4.2). These issues made the current validation use the "Bruteforce" timing synchronisation approach and the cable frequency synchronisation. Both of these synchronisation methods could validate the algorithms. Nevertheless, they cannot be used in real systems. Moreover, they prevent the algorithm from working in real time. As a result, one may need to carefully investigate the existing synchronisation methods and the extensions of the one described in Section 4.1 method based on the Schmidl-Cox principle [56]. After that, the examination of their performance upon the CW EMD injection is required for both potential synchronisation and NBI removal algorithm adjustments. The work in this direction has already been started and one PhD student from the M-group closely works on this matter.

The potential valorisation plan of the conducted research is also based on the synchronisation and transmission assumptions. However, to deliver a "NoEMI" product to the market, one may need to extensively test the algorithms not only in static but also in moving scenarios, in other words, multipath fading tests have to be performed. OFDM systems are inherently safe in multipath fading conditions, so the algorithm's work should not be affected. Nevertheless, the tests have to be performed. Before collaborating with the external partners, one may KU Leuven facilities - both semi-anechoic and RC chambers where the rotating table and stirrer will simulate the multipath environments. Finally, with the onset of V2X communication, a lot of OBUs and RSUs became available on the market. To minimise the initial test costs, one may purchase one of these V2X communication units and deploy the algorithm on them for the following tests at KU Leuven facilities.

The commonly used Direct Current (DC)-DC converters can also contribute as an NBI source as their switching frequency generates a pulse which can be assumed as a CW EMD. Bluetooth (BT) connections can also be considered as an NBI. The simulations showed that the "Differential" NBI removal algorithm is able to work with multiple NBIs happening at the same time. It may potentially improve the co-existence and robustness of OFDM systems. Nevertheless, no tests have been performed regarding this topic. One may need to test the influence of BT devices and DC-DC converters on OFDM systems and define if the NBI removal algorithms can guard the system in the presence of these NBI sources.

To improve the bandwidth usage of the "Differential" NBI removal algorithm,

one may consider using pilots for NBI tracking. Moreover, the NBI search can be further improved by using longer FFT at the receiver's side. This will potentially decrease the NBI's influence on the system and, thus, improve the NBI search capabilities of both the "Differential" and "Mod-remod" algorithms.

Wireless communication in the agricultural sector briefly touched on in Chapter 5 also opens directions for future topic continuation. For example, one may collaborate closely with industry and be up-to-date with the actual industrial needs of the WSNs. It was decided to use the SmartMesh IP technology based on energy consumption. This was mainly backed up by the large packet size of SmartMesh IP compared to IOLW. However, for control signals requiring a few bits and low latency, IOLW can be more beneficial as it showed lower latencies compared to SmartMesh IP. Moreover, energy usage tests could also be conducted to prove the previously mentioned assumptions.

The influence of NBIs on SmartMesh IP and IOLW should also be tested as the insights obtained during the NBI "hunting" in OFDM systems could also be helpful for WSN protocols.

Finally, the touched research topic of recreating the agricultural EM environment in the laboratory setting described in Section 5.5 is also a potential research direction. It can facilitate the general approach of performing conducted and radiated emission measurements and can potentially be used as a pre-compliance simulation tool.

Bibliography

[1] Tarkesh Pande, Il Han Kim, and Anuj Batra. A method for narrowband interference mitigation in OFDM by minimizing spectral leakage. *2015 IEEE International Symposium on Power Line Communications and Its Applications, ISPLC 2015*, pages 19–23. doi:10.1109/ISPLC.2015.7147583.

[2] IEEE802.11-2020. IEEE Standard for Information Technology–Telecommunications and Information Exchange between Systems - Local and Metropolitan Area Networks–Specific Requirements - Part 11: Wireless LAN Medium Access Control (MAC) and Physical Layer (PHY) Specifications. *IEEE Std 802.11-2020 (Revision of IEEE Std 802.11-2016)*, pages 1–4379. doi:10.1109/IEEESTD.2021.9363693.

[3] Taylor Petroc. Number of mobile (cellular) subscriptions worldwide from 1993 to 2021.
Available at: `https://www.statista.com/statistics/262950/global-mobile-subscriptions-since-1993/`, accessed: April 10, 2023.

[4] GSMA. The Mobile Economy.
Available at: `https://www.gsma.com/mobileeconomy/#trends/`, accessed: April 10, 2023.

[5] Aleksandr Ovechkin. Future Wireless Communication Protocols in Autonomous Systems.
Available at: `https://etn-sas.eu/2020/03/23/future-wireless-communication-protocols-in-autonomous-systems/`, accessed: April 10, 2023.

[6] Tom Krisher et al. Tesla cars involved in 10 of the 11 new crash deaths linked to automated-tech vehicles.

Available at: `https://fortune.com/2022/10/19/tesla-cars-involved-in-10-of-the-11-new-crash-deaths-linked-to-automated-tech-vehicles/`, accessed: April 10, 2023.

[7] ETSI TR 102 638. ETSI TR 102 638 V1.1.1. Intelligent Transport Systems (ITS); Vehicular Communications; Basic Set of Applications; Definitions. Standard, The European Telecommunications Standards Institute.
Available at: `https://www.etsi.org/deliver/etsi_tr/102600_102699/102638/01.01.01_60/tr_102638v010101p.pdf/`, accessed: October 2, 2023.

[8] Marko Höyhtyä, Jyrki Huusko, Markku Kiviranta, Kenneth Solberg, and Juha Rokka. Connectivity for autonomous ships: Architecture, use cases, and research challenges. In *2017 International Conference on Information and Communication Technology Convergence (ICTC)*, pages 345–350. doi:10.1109/ICTC.2017.8191000.

[9] Christian Bettstetter. Communications and Path Planning of Drones. Available at: `https://bettstetter.com/research/uav/`, accessed: October 2, 2023.

[10] Xi Zhang, Marcus Geimer, Patrick O. Noack, and Ludwig Grandl. Development of an intelligent master-slave system between agricultural vehicles. In *2010 IEEE Intelligent Vehicles Symposium*, pages 250–255. doi:10.1109/IVS.2010.5548056.

[11] Intuitive Surgical. OnSite for the da Vinci Surgical System Overview. Available at: `https://www.davincisurgerycommunity.com/intuitive/docs/813331-33_OnSite_Whitepaper.pdf/`, accessed: October 2, 2023.

[12] Andrea Goldsmith. *Wireless communications*. Cambridge University Press. doi:10.1017/CBO9780511841224.

[13] Jammer from China. WiFi/Bluetooth Jammers.
Available at: `https://http://www.jammerfromchina.com/categories/WiFi%7B47%7DBluetooth_Jammers/`, accessed: October 3, 2023.

[14] Y.Q. Shi, Xi Min Zhang, Zhi-Cheng Ni, and N. Ansari. Interleaving for combating bursts of errors. *IEEE Circuits and Systems Magazine*, 4(1): 29–42. ISSN 1558-0830. doi:10.1109/MCAS.2004.1286985.

[15] Aleksandr Ovechkin, Tim Claeys, Dries Vanoost, Guy A. E. Vandenbosch, and Davy Pissoort. A Novel Method of Removing the Influence of

Continuous Electromagnetic Wave Disturbances in OFDM Systems. *IEEE Transactions on Electromagnetic Compatibility*, pages 1–10. doi:10.1109/TEMC.2021.3121167.

[16] Aleksandr Ovechkin, Brian Leeman, Dries Vanoost, Tim Claeys, Guy A. E. Vandenbosch, and Davy Pissoort. Influence of AWGN on the Possibility to Remove a Continuous Wave EM Disturbance in OFDM systems. In *2022 International Symposium on Electromagnetic Compatibility – EMC Europe*, pages 667–672. doi:10.1109/EMCEurope51680.2022.9900995.

[17] Peter Ankarson, Jan Carlsson, Bjorn Bergqvist, Stefan Larsson, and Markel Bertilsson. Impact of different interference types on an LTE communication link using conducted measurements. *IEEE International Symposium on Electromagnetic Compatibility*, 2015-Septm:177–182. ISSN 21581118. doi:10.1109/ISEMC.2015.7256154.

[18] Karina Mariana Fors, Kia Cecilia Wiklundh, and Peter F. Stenumgaard. On the Mismatch of Emission Requirements for CW Interference Against OFDM Systems. *IEEE Transactions on Electromagnetic Compatibility*, 60(5):1555–1561. doi:10.1109/TEMC.2017.2775649.

[19] Karina Fors, Erik Axell, Sara Linder, and Peter Stenumgaard. On the Impact of CW interference on 5G NR. *EMC Europe 2019 - 2019 International Symposium on Electromagnetic Compatibility*, pages 1049–1054. doi:10.1109/EMCEurope.2019.8871665.

[20] Sheetal Kalyani and K. Giridhar. Interference mitigation in turbo-coded ofdm systems using robust statistics. In *VTC Spring 2008 - IEEE Vehicular Technology Conference*, pages 1191–1195. doi:10.1109/VETECS.2008.252.

[21] S. Kalyani and K. Giridhar. Interference mitigation in turbo-coded ofdm systems using robust llrs. In *2008 IEEE International Conference on Communications*, pages 646–651. doi:10.1109/ICC.2008.127.

[22] K. Ouahada, H. C. Ferreira, A. J. Han. Vinck, A. J. Snyders, and T. G. Swart. Cancellation and error correction for narrowband interference with spectral nulls codes and ofdm modulation. In *AFRICON 2007*, pages 1–7. doi:10.1109/AFRCON.2007.4401559.

[23] PC Hsian and PC Chin. Evaluation of variance mismatch for serial turbo codes with Talwar penalty function under interference of impulsive noise. *J. Eng. Sci. Technol*, 5(3):350–360.

[24] Claeys, Tim and Ovechkin, Aleksandr and Pissoort, Davy. The Need For and How To Evaluate Continuous Wave Immunity of Wireless Systems used in V2X Applications. doi:10.1109/emceurope48519.2020.9245766.

[25] Andreas Bury. Method And Apparatus To Cancel Additive Sinusoidal Disturbances In OFDM Receivers. Patent US Patent 8,611,443 B2, United States Patent and Trademark Office.
Available at: `https://patents.google.com/patent/US8611443B2/zh`, accessed April 10, 2023.

[26] Tingting Zhao, Hui Zhao, Yuping Zhao, Xiang Cheng, and Bo Ai. A Frequency-Domain Estimation Scheme for Single-Tone Interference in OFDM Systems. In *2011 Third International Conference on Communications and Mobile Computing*, pages 409–412. doi:10.1109/CMC.2011.82.

[27] Mohamed Marey and Heidi Steendam. Cancellation of digital narrowband interference formulti-carrier systems. *Lecture Notes in Electrical Engineering*, 1 LNEE:127–136. ISSN 18761100. doi:10.1007/978-1-4020-6129-5_13.

[28] R. Nilsson, F. Sjoberg, and J.P. LeBlanc. A rank-reduced LMMSE canceller for narrowband interference suppression in OFDM-based systems. *IEEE Transactions on Communications*, 51(12):2126–2140. ISSN 1558-0857. doi:10.1109/TCOMM.2003.820761.

[29] Thokozani Shongwe and A. J. Han Vinck. Interleaving and nulling to combat narrow-band interference in PLC standard technologies PLC G3 and PRIME. In *2013 IEEE 17th International Symposium on Power Line Communications and Its Applications*, pages 258–262. doi:10.1109/ISPLC.2013.6525860.

[30] Donatella Darsena. Successive narrowband interference cancellation for OFDM systems. *IEEE Communications Letters*, 11(1):73–75. ISSN 1558-2558. doi:10.1109/LCOMM.2007.061075.

[31] Donatella Darsena and Francesco Verde. Successive NBI Cancellation Using Soft Decisions for OFDM Systems. *IEEE Signal Processing Letters*, 15:873–876. ISSN 1558-2361. doi:10.1109/LSP.2008.2001808.

[32] Alan J. Coulson. Bit error rate performance of ofdm in narrowband interference with excision filtering. *IEEE Transactions on Wireless Communications*, 5(9):2484–2492. doi:10.1109/TWC.2006.1687772.

[33] C. Muschallik. Improving an OFDM reception using an adaptive Nyquist windowing. *IEEE Transactions on Consumer Electronics*, 42(3):259–269. doi:10.1109/30.536046.

[34] S.H. Muller-Weinfurtner. Optimum Nyquist windowing in OFDM receivers. *IEEE Transactions on Communications*, 49(3):417–420. doi:10.1109/26.911448.

[35] A.J. Redfern. Receiver window design for multicarrier communication systems. *IEEE Journal on Selected Areas in Communications*, 20(5): 1029–1036. doi:10.1109/JSAC.2002.1007383.

[36] Ahmad Gomaa and Naofal Al-Dhahir. A Compressive Sensing Approach to NBI Cancellation in Mobile OFDM Systems. In *2010 IEEE Global Telecommunications Conference GLOBECOM 2010*, pages 1–5. doi:10.1109/GLOCOM.2010.5683790.

[37] Ahmad Gomaa and Naofal Al-Dhahir. A Sparsity-Aware Approach for NBI Estimation in MIMO-OFDM. *IEEE Transactions on Wireless Communications*, 10(6):1854–1862. doi:10.1109/TWC.2011.040411.101118.

[38] Ahmad Gomaa and Naofal Al-Dhahir. Compressive-Sensing-Based Approach for NBI Cancellation in MIMO-OFDM. In *2011 IEEE Global Telecommunications Conference - GLOBECOM 2011*, pages 1–5. doi:10.1109/GLOCOM.2011.6133545.

[39] Hengyao Wang, Xiaoying Zhang, and Shan Wang. Narrowband interference suppression in OFDM systems. In *2016 8th International Conference on Wireless Communications Signal Processing (WCSP)*, pages 1–6. doi:10.1109/WCSP.2016.7752511.

[40] Arun Batra and James R. Zeidler. Narrowband interference mitigation in OFDM systems. In *MILCOM 2008 - 2008 IEEE Military Communications Conference*, pages 1–7. doi:10.1109/MILCOM.2008.4753296.

[41] Chengwen Zhang, Xudong Hu, Yutao Liu, and Shipeng Wang. Multiple Interacting Narrowband Interferences Suppression Algorithm for OFDM Systems. *IEEE Access*, 8:62310–62321. doi:10.1109/ACCESS.2020.2984816.

[42] Tim Claeys, Dries Vanoost, Joan Peuteman, Guy A. E. Vandenbosch, and Davy Pissoort. Removing the Spectral Leakage in Time-Domain Based Near-Field Scanning Measurements. *IEEE Transactions on Electromagnetic Compatibility*, 57(6):1329–1337. ISSN 1558-187X. doi:10.1109/TEMC.2015.2447051.

[43] Tim Claeys, Dries Vanoost, Joan Peuteman, Guy A. E. Vandenbosch, and Davy Pissoort. An Iterative Interpolated DFT to Remove Spectral Leakage in Time-Domain Near-Field Scanning. *IEEE Transactions on Electromagnetic Compatibility*, 60(1):202–210. ISSN 1558-187X. doi:10.1109/TEMC.2017.2699738.

[44] Tim Claeys. *Increasing the Accuracy and Speed of EMI Near-Field Scanning.* PhD thesis, KU Leuven, Leuven, Belgium.
Available at: https://kuleuven.limo.libis.be/discovery/

fulldisplay?docid=lirias1981941&context=SearchWebhook&
vid=32KUL_KUL:Lirias&search_scope=lirias_profile&adaptor=
SearchWebhook&tab=LIRIAS&query=any,contains,LIRIAS1981941&
offset=0, accessed April 10, 2023.

[45] The MathWorks Inc. MATLAB 9.13.0.2049777 (R2022b).
Available at: `https://nl.mathworks.com/products/matlab.html`, ac-
cessed: April 9, 2023.

[46] Jonas Van Waes, Jonas Lannoo, Jens Vankeirsbilck, Andy Degraeve,
Joan Peuteman, Dries Vanoost, Davy Pissoort, and Jeroen Boydens.
Effectiveness of hamming single error correction codes under harsh
electromagnetic disturbances. In *2018 International Symposium
on Electromagnetic Compatibility (EMC EUROPE)*, pages 271–276.
doi:10.1109/EMCEurope.2018.8485176.

[47] Alexandros Palaios, Vanya M. Miteva, and Petri Mähönen. Contemporary
Study of Radio Noise Characteristics in Diverse Environments. *IEEE
Access*, 6:25621–25631. doi:10.1109/ACCESS.2017.2654064.

[48] Mahdi Bersali, Hocine Ait-Saadi, and Messaoud Bensebti. Performance
analysis of polar codes vs turbo codes over AWGN channel. In *2017 5th
International Conference on Electrical Engineering - Boumerdes (ICEE-
B)*, pages 1–6. doi:10.1109/ICEE-B.2017.8192032.

[49] Orzechowski Robert. Performance Analysis of LDPC Coded OFDM
System. In *XIV Poznań Conference in the field of Telecommunications
and Electronics. Telecommunications Workshop - PWT 2010*, pages 1–4.

[50] M. Shokair, A. Ebian, and K. H. Awadalla. Performance Evaluation
of WiMAX System Using Different Coding Techniques. In Roberto C.
Hincapie and Javier E. Sierra, editors, *Advanced Transmission Techniques
in WiMAX*, chapter 13. IntechOpen, Rijeka. doi:10.5772/29843.

[51] Brian Leeman. SDR implementation of OFDM CW EMI removal
algorithm. Master's thesis, KU Leuven, Leuven, Belgium.
Available at: `https://kuleuven.limo.libis.be/discovery/`
`fulldisplay?docid=alma9992668358401488&context=L&vid=32KUL_`
`KUL:KULeuven&lang=en&search_scope=All_Content&adaptor=Local%`
`20Search%20Engine&tab=all_content_tab&query=any,contains,`
`Leeman%20Brian&offset=0`, accessed: April 10, 2023.

[52] Aleksandr Ovechkin, Brian Leeman, Dries Vanoost, Tim Claeys, Guy
A. E. Vandenbosch, and Davy Pissoort. Deploying a continuous wave
electromagnetic disturbance removal algorithm on an ofdm system. In

2023 International Symposium on Electromagnetic Compatibility – EMC Europe, pages 1–6. doi:10.1109/EMCEurope57790.2023.10274365.

[53] IEEE1900.1-2019. IEEE Standard for Definitions and Concepts for Dynamic Spectrum Access: Terminology Relating to Emerging Wireless Networks, System Functionality, and Spectrum Management. *IEEE Std 1900.1-2019 (Revision of IEEE Std 1900.1-2008)*, pages 1–78. doi:10.1109/IEEESTD.2019.8694195.

[54] ISO/IEC 7498-1:1994. ISO/IEC 7498-1:1994 Information technology — Open Systems Interconnection — Basic Reference Model: The Basic Model. Standard, International Organization for Standardization. Available at: `https://www.iso.org/standard/20269.html`, accessed: April 10, 2023.

[55] John Terry and Juha Heiskala. *OFDM Wireless LANs: A Theoretical and Practical Guide.* Sams publishing. ISBN 0672321572.

[56] T.M. Schmidl and D.C. Cox. Robust frequency and timing synchronization for OFDM. *IEEE Transactions on Communications*, 45(12):1613–1621. doi:10.1109/26.650240.

[57] ANALOG DEVICES. ADALM PLUTO. Overview. Available at: `https://www.analog.com/en/design-center/evaluation-hardware-and-software/evaluation-boards-kits/adalm-pluto.html#eb-overview`, accessed: April 10, 2023.

[58] Rohde & Schwarz. R&S©SMM100A vector signal generator. Available at: `https://www.rohde-schwarz.com/us/products/test-and-measurement/vector-signal-generators/rs-smm100a-vector-signal-generators_63493-834088.html`, accessed: April 10, 2023.

[59] Rohde & Schwarz. R&S©FSVA3000 Signal and spectrum analyzer. Available at: `https://www.rohde-schwarz.com/us/products/test-and-measurement/benchtop-analyzers/rs-fsva3000-signal-and-spectrum-analyzer_63493-601504.html`, accessed: April 10, 2023.

[60] Nuand. BladeRF 2.0 micro. Available at: `https://www.nuand.com/bladerf-2-0-micro/`, accessed: April 10, 2023.

[61] Aleksandr Ovechkin, Brian Leeman, Dries Vanoost, Tim Claeys, Marcel Verhoeven, and Davy Pissoort. A Study of Electromagnetic Robustness of IO-Link Wireless and SmartMesh IP for Applications on an Agricultural Vehicle. In *2022 International Symposium on Electromagnetic Compatibility – EMC Europe*, pages 7–12. doi:10.1109/EMCEurope51680.2022.9901221.

[62] IO-Link Specification. IO-Link Wireless - System Extensions. Standard, IO-Link Community, Karlsruhe, Ger.
Available at: `https://io-link.com/share/Downloads/System-Extensions/IO-Link_Wireless_System_10112_V11_Mar18.pdf`, accessed: April 10, 2023.

[63] SmartMesh IP User's Guide SmartMesh. SmartMesh IP User's Guide SmartMesh. Standard, Linear Technology Corporation, US.
Available at: `https://www.analog.com/media/en/technical-documentation/user-guides/smartmesh_ip_user_s_guide.pdf`, accessed: April 10, 2023.

[64] Raja Akram et al. Security and performance comparison of different secure channel protocols for Avionics Wireless Networks. In *2016 IEEE/AIAA 35th Digital Avionics Systems Conference (DASC)*, pages 1–8. doi:10.1109/DASC.2016.7777966.

[65] Lucio Colizzi et al. Chapter 1 - Introduction to agricultural IoT. In *Agricultural Internet of Things and Decision Support for Precision Smart Farming*, pages 1–33. Academic Press. ISBN 978-0-12-818373-1. doi:10.1016/B978-0-12-818373-1.00001-9.

[66] Radomir Prodanović et al. Wireless Sensor Network in Agriculture: Model of Cyber Security. *Sensors*, 20(23). ISSN 1424-8220. doi:10.3390/s20236747.

[67] Case IH. Autonomous tractor technology shows way forward for farming: enhancing efficiency and working conditions in agriculture.
Available at: `https://media.cnhindustrial.com/EMEA/CASE-IH/autonomous-tractor-technology-shows-way-forward-for-farming--enhancing-efficiency-and-working-condit/s/d9d11785-2881-4577-afc2-23e6dadbfc91`, accessed: April 10, 2023.

[68] Richard Zurawski. *Industrial Communication Technology Handbook*. Industrial Information Technology. CRC Press, Boca Raton, FL, 2nd edition. ISBN 9781482207323. doi:10.1201/b17365.

[69] The Working Group for WLAN Standards. IEEE 802.11[TM] WIRELESS LOCAL AREA NETWORKS.
Available at: `https://www.ieee802.org/11/#`, accessed: May 18, 2023.

[70] LoRa Alliance. LoRa Technology.
Available at: `https://lora-alliance.org/`, accessed: May 18, 2023.

[71] Z-Wave Alliance. Z-Wave Technology.
Available at: `https://z-wavealliance.org/`, accessed: May 18, 2023.

[72] ANALOG DEVICES. SmartMesh IP Solutions.
Available at: `https://www.analog.com/en/applications/`
`technology/smartmesh-pavilion-home/smartmesh-ip.html`,
accessed: April 10, 2023.

[73] Bluetooth©. Bluetooth Technology Overview.
Available at: `https://www.bluetooth.com/learn-about-bluetooth/`
`tech-overview/`, accessed: May 18, 2023.

[74] 3GPP Consortium. Specifications & Technologies.
Available at: `https://www.3gpp.org/specifications-technologies`,
accessed: May 18, 2023.

[75] 3GPP Consortium. Release 13.
Available at: `https://www.3gpp.org/specifications-technologies/`
`releases/release-13`, accessed: May 18, 2023.

[76] Sigfox©. What is Sigfox 0G Technology.
Available at: `https://www.sigfox.com/what-is-sigfox/`, accessed:
May 18, 2023.

[77] IEEE. IEEE Standard for Low-Rate Wireless Networks. *IEEE Std
802.15.4-2020 (Revision of IEEE Std 802.15.4-2015)*, pages 1–800.
doi:10.1109/IEEESTD.2020.9144691.

[78] The Connectivity Standards Alliance. Zigbee. The Full-Stack Solution for
All Smart Devices.
Available at: `https://csa-iot.org/all-solutions/zigbee/`, accessed:
May 18, 2023.

[79] International Society of Automation. ISA100, Wireless Systems for
Automation.
Available at: `https://www.isa.org/standards-and-publications/`
`isa-standards/isa-standards-committees/isa100`, accessed: May
18, 2023.

[80] FieldComm Group. WirelessHART. HART WITHOUT THE WIRES.
Available at: `https://www.fieldcommgroup.org/technologies/`
`wirelesshart#:~:text=WirelessHART%20is%20a%20wireless%`
`20communications,WirelessHART%20using%20mesh%20networking%`
`20technology.`, accessed: May 18, 2023.

[81] ThreadGroup. What is Thread.
Available at: `https://www.threadgroup.org/What-is-Thread/`
`Thread-Benefits`, accessed: May 18, 2023.

[82] Internet Engineering Task Force. IPv6 over Low power WPAN (6lowpan).
Available at: `https://datatracker.ietf.org/group/6lowpan/about/`,
accessed: May 18, 2023.

[83] E. Genender, C.L. Holloway, K.A. Remley, J. Ladbury, G. Koepke,
and H. Garbe. Use of reverberation chamber to simulate the
power delay profile of a wireless environment. In *2008 International
Symposium on Electromagnetic Compatibility - EMC Europe*, pages 1–6.
doi:10.1109/EMCEUROPE.2008.4786832.

[84] IO-Link Specification. IO-Link Interface and System Specification.
Standard, IO-Link Community, Karlsruhe, Ger.
Available at: `https://io-link.com/share/Downloads/Package-2020/`
`IOL-Interface-Spec_10002_V113_Jun19.pdf`, accessed: April 10, 2023.

[85] IEC 61131-9:2022. Programmable controllers - Part 9: Single-drop digital
communication interface for small sensors and actuators (SDCI). Standard,
International Organization for Standardization, Geneva, CH.
Available at: `https://webstore.iec.ch/publication/68534`, accessed:
April 10, 2023.

[86] SmartMesh IP Application Notes. SmartMesh IP Application Notes.
Standard, Linear Technology Corporation, US.
Available at: `https://www.analog.com/media/en/technical-`
`documentation/application-notes/smartmesh_ip_application_`
`notes.pdf`, accessed: April 10, 2023.

[87] Yue Chen and J.C.-I. Chuang. The effects of time delay spread on TCM
in portable radio environments. In *Proceedings of ICUPC '95 - 4th IEEE
International Conference on Universal Personal Communications*, pages
133–137. doi:10.1109/ICUPC.1995.496874.

[88] New Holland. Combine Harvesters CR Revelation range brochure.
Available at: `https://assets.cnhindustrial.com/nhag/eu/en-`
`uk/assets/pdf/combine-harvesters/cr-revelation-stage-v-`
`brochure-uk-en.pdf`, accessed: April 10, 2023.

[89] Jan García-Morales, M. Carmen Lucas-Estañ, and Javier Gozalvez.
Latency-sensitive 5g ran slicing for industry 4.0. *IEEE Access*, 7:143139–
143159. doi:10.1109/ACCESS.2019.2944719.

[90] 3GPP TR 22.804. Study on Communication for Automation in Vertical
Domains (v16.3.0, Release 16). Technical Report 3GPP TR 22.804,
3GPP.
Available at: `https://portal.3gpp.org/desktopmodules/`

Specifications/SpecificationDetails.aspx?specificationId= 3187, accessed: April 10, 2023.

[91] 5G-ACIA. 5G for Connected Industries and Automation (Second Edition). White paper, 5G-ACIA, Lyoner Strasse 9 60528 Frankfurt am Main, Germany.
Available at: https://5g-acia.org/wp-content/uploads/5G-ACIA_WP_5G-for-Connected-Industries-and-Automation-Second-Edition_SinglePages.pdf, accessed: April 10, 2023.

[92] Petroc Taylor. Mobile Communications - Statistics & Facts.
Available at: https://www.statista.com/topics/1147/mobile-communications//#topicOverview, accessed: April 10, 2023.

[93] Bluetooth©. 2022 Bluetooth® Market Update.
Available at: https://www.bluetooth.com/2022-market-update/#:~:text=Annual%20Device%20Shipments&text=In%20fact,%20in%202022,%20analysts,),%20from%202021%20to%202026./, accessed: April 10, 2023.

[94] Thomas Alsop. WLAN connected devices worldwide 2016-2021.
Available at: https://www.statista.com/statistics/802706/world-wlan-connected-device/, accessed: April 10, 2023.

[95] Nordic Unmanned. Cargo drone delivers blood samples between hospitals in the Greater Oslo area.
Available at: https://nordicunmanned.com/news/cargo-drone-delivers-blood-samples-between-hospitals/, accessed: May 19, 2023.

[96] Mitch Campion, Prakash Ranganathan, and Saleh Faruque. UAV swarm communication and control architectures: a review. *Journal of Unmanned Vehicle Systems*, 7(2):93–106. doi:10.1139/juvs-2018-0009.

[97] IRU. Europe driver shortage to triple by 2026 if no action: new IRU report.
Available at: https://www.iru.org/news-resources/newsroom/europe-driver-shortage-triple-2026-if-no-action-new-iru-report, accessed: May 19, 2023.

[98] IRU. Safety first: IRU marks UN Global Road Safety Week.
Available at: https://www.iru.org/news-resources/newsroom/safety-first-iru-marks-un-global-road-safety-week?utm_source=twitter&utm_medium=Social&utm_campaign=Falcon, accessed: May 19, 2023.

[99] Colruyt Group. Collect&Go tests unmanned vehicle in Londerzeel.
Available at: `https://press.colruytgroup.com/collectgo-tests-`
`unmanned-vehicle-in-londerzeel#:~:text=Londerzeel%2C%2023%`
`20November%202022%20%2D%20Collect%26Go,teleoperation%20with%`
`20advanced%20autopilot%20functionality.`, accessed: May 19, 2023.

[100] Business Wire. Self-Driving Cars Market Global Forecast to 2030:
Increasing Demand for Level 1 and Level 2 Cars and Rising Investment
in Development of Level 4 and Level 5 Cars Will Propel Market.
Available at: `https://www.businesswire.com/news/home/`
`20220215005655/en/Self-Driving-Cars-Market-Global-Forecast-`
`to-2030-Increasing-Demand-for-Level-1-and-Level-2-Cars-`
`and-Rising-Investment-in-Development-of-Level-4-and-Level-`
`5-Cars-Will-Propel-Market---ResearchAndMarkets.com#:~:`
`text=The%20global%20self%2Ddriving%20cars,at%20a%20CAGR%`
`20of%2013.3%25./`, accessed: April 10, 2023.

[101] Alain Sultan. 5G System Overview.
Available at: `https://www.3gpp.org/technologies/5g-system-`
`overview/`, accessed: April 10, 2023.

[102] IEEE802.11bd-2022. IEEE Standard for Information Technology–
Telecommunications and Information Exchange between Systems Local
and Metropolitan Area Networks–Specific Requirements Part 11: Wireless
LAN Medium Access Control (MAC) and Physical Layer (PHY)
Specifications Amendment 5: Enhancements for Next Generation V2X.
*IEEE Std 802.11bd-2022 (Amendment to IEEE Std 802.11-2020 as
amended by IEEE Std 802.11ax-2021, IEEE Std 802.11ay-2021, IEEE
Std 802.11ba-2021, IEEE Std 802.11-2020/Cor 1-2022, and IEEE Std
802.11az-2022)*, pages 1–144. doi:10.1109/IEEESTD.2023.10063942.

[103] Luping Xiang, Robert G. Maunder, and Lajos Hanzo. Concurrent OFDM
Demodulation and Turbo Decoding for Ultra Reliable Low Latency
Communication. *IEEE Transactions on Vehicular Technology*, 69(2):
1281–1290. doi:10.1109/TVT.2019.2961746.

[104] Flanders Make. DESIGN AND PROTOTYPING OF AUTONOMOUS
WORKING VEHICLES.
Available at: `https://www.flandersmake.be/en/research/services/`
`design-prototyping-autonomous-working-vehicles`, accessed: May
19, 2023.

[105] Horiba Mira. Connected and Autonomous Vehicles.
Available at: `https://www.horiba-mira.com/Connected-and-`
`Autonomous-Vehicles/`, accessed: May 19, 2023.

[106] The SAS project. European Training Network for Safer Autonomous Systems.
Available at: `https://etn-sas.eu/`, accessed: May 19, 2023.

[107] Horiba Mira. Assured CAV.
Available at: `https://www.horiba-mira.com/brochures/assuredcav/#p=1`, accessed: April 10, 2023.

[108] 5GAA Automotive Association. Connected Mobility for people, vehicles, and transport infrastructure.
Available at: `https://5gaa.org/`, accessed: April 10, 2023.

[109] GSMA. Representing the worldwide mobile communications industry.
Available at: `https://www.gsma.com/`, accessed: April 10, 2023.

[110] Lacroix. Our electronic expertise for Smart World markets.
Available at: `https://www.lacroix-electronics.com/market-sectors/`, accessed: April 10, 2023.

[111] Project SCOOP. Project's website.
Available at: `https://www.scoop.developpement-durable.gouv.fr/en/`, accessed: April 10, 2023.

[112] Qualcomm. Improved V2X capabilities for safety and autonomous driving.
Available at: `https://www.qualcomm.com/products/automotive/snapdragon-digital-chassis/c-v2x`, accessed: April 10, 2023.

[113] Joinup. Microsoft Public License.
Available at: `https://joinup.ec.europa.eu/licence/microsoft-public-license/`, accessed: October 2, 2023.

Curriculum

Personal Information

- **Name:** Aleksandr Ovechkin

- **Address:** Frank Van Ackerpromenade, 8, bus S602, 8000, Bruges, West Flanders, Belgium

- **Mobile:** +32 456 11 35 13

- **Email:** aleksandr.ovechkin@kuleuven.be | aleksandr.v.ovechkin@gmail.com

- **Date of birth:** July 9th 1995

Education

- 06/2019 - current: PhD in Engineering Technology, Electrical Engineering, KU Leuven, Bruges Campus, Belgium

- 09/2016 - 07/2018: Master of Science with honours in Electric Power Engineering and Electrical Engineering, National Research University "Moscow Power Engineering Institute", Moscow, Russia

- 09/2015 - 05/2018: Bachelor of Science with honours in Economics, National Research University "Moscow Power Engineering Institute", Moscow, Russia

- 09/2013 - 06/2017: Diploma of professional retraining in Informatics, Computer Engineering and Electrical Engineering in English language, National Research University "Moscow Power Engineering Institute", Moscow, Russia

- 09/2012 - 07/2016: Bachelor of Science in Electric Power Engineering and Electrical Engineering, National Research University "Moscow Power Engineering Institute", Moscow, Russia

Experience

- 06/2019 - current: Research on Electromagnetic Compatibility and reliable wireless communication. PhD researcher at KU Leuven Bruges Campus, Bruges, Belgium

- 2021: Investigation and testing of wireless communication protocols suitable for agricultural needs. Internship at CNHi, Zedelgem, Belgium

- 2020: Conducting tests on Wi-Fi 3 to reveal the weak spots of OFDM communication. Visiting researcher at the University of York, York, the United Kingdom

- 02/2018 - 06/2019: Designing cable systems and electrical equipment and cableways layout for nuclear power plants. Electrical design engineer at Joint-Strock Company Atomstroyexport, Moscow, Russia

- 05/2017 - 01/2018: Designing low-voltage electrical supply schemes. Electrical design engineer at Bastion, Tula, Russia

- 2015: Mounting and maintenance of cable lines. Internship at Teplo Centr Stroy, Moscow, Russia

- 2015: Maintenance of substation 750 kV "Belyj Rast". Internship at FGC UES, Moscow region, Russia

- 2014: Assembling and maintaining electric power transmission lines. Electrical lineman of the second grade (Internship) at Rosenergostroj, Rostov region, Russia

Training

- Central Lecture Research Integrity

- Managing your PhD

- Academic Writing for Junior Researchers

- Software Defined Radio and Networking

- EMC-based design

- Exploitation of Research - Technology & Knowledge Transfer

- The Six Biases of Decision-Making

- The Three Secrets to Effective Time Investment (Blinkist Summary)

- Writing Email

- Creative problem-solving LIVE

- EMI Test Receiver Basics: Is it time to upgrade from your spectrum analyzer?

- Emission Measurements for Electrical and Electronic Equipment

- Fundamentals Of EMI

- Toward Reliable and Scalable Vehicle-to-Everything (V2X)

- Structured Working

- Giving a high-impact presentation

- Short Pulse Technologies with Illustrative Applications

- Introduction to Risk Analysis

- Introduction to leadership

- Networking for researchers: the basics

List of publications

Publications as Main Author

- **Ovechkin, A.**, Leeman, B., Vanoost, D., Claeys, T., Vandenbosch, G. A. E., Pissoort, D. (2023). Deploying a Continuous Wave Electromagnetic Disturbance Removal Algorithm on an OFDM System. In: Proceedings of 2023 International Symposium on Electromagnetic Compatibility – EMC Europe, (1-6). Presented at the 2023 International Symposium on Electromagnetic Compatibility – EMC Europe, Krakow, Poland. ISBN: 979-8-3503-2400-6. doi: 10.1109/EMCEurope57790.2023.10274365

- **Ovechkin, A.**, Leeman, B., Vanoost, D., Claeys, T., Verhoeven, M., Pissoort, D. (2022). A Study of Electromagnetic Robustness of IO-Link Wireless and SmartMesh IP for Applications on an Agricultural Vehicle. In: Proceedings of 2022 International Symposium on Electromagnetic Compatibility – EMC Europe, (7-12). Presented at the 2022 International Symposium on Electromagnetic Compatibility – EMC Europe, Gothenburg, Sweden. ISBN: 978-1-6654-0788-5. doi: 10.1109/EMCEurope51680.2022.9901221

- **Ovechkin, A.**, Leeman, B., Vanoost, D., Claeys, T., Vandenbosch, G. A. E., Pissoort, D. (2022). Influence of AWGN on the Possibility to Remove a Continuous Wave EM Disturbance in OFDM systems. In: Proceedings of 2022 International Symposium on Electromagnetic Compatibility – EMC Europe, (667-672). Presented at the 2022 International Symposium on Electromagnetic Compatibility – EMC Europe, Gothenburg, Sweden. ISBN: 978-1-6654-0788-5. doi: 10.1109/EMCEurope51680.2022.9900995

- **Ovechkin, A.**, Claeys, T., Vanoost, D., Vandenbosch, G. A. E., Pissoort, D. with Ovechkin, A. (corresp. author) (2021). A Novel Method of Removing the Influence of Continuous Electromagnetic Wave Disturbances in OFDM Systems. IEEE Transactions on Electromagnetic Compatibility, 64 (2), 338-347. doi:

- **Ovechkin, A.**, Claeys, T., Vanoost, D., Dawson, J., Vandenbosch, G. A. E., Pissoort, D. (2021). Characterizing the Robustness of Wi-Fi and Bluetooth against Continuous Wave EM Disturbances inside a Reverberation Chamber. In: The 2021 IEEE International Joint EMC/SI/PI and EMC Europe Symposium proceedings, (1031-1038). Presented at the 2021 JOINT IEEE INTERNATIONAL SYMPOSIUM ON ELECTROMAGNETIC COMPATIBILITY, SIGNAL & POWER INTEGRITY, EMC EUROPE, Glasgow, the UK, 26 Jul 2021-20 Aug 2021. ISBN: 978-1-6654-4888-8. doi: 10.1109/EMC/SI/PI/EMCEurope52599.2021.9559299

Publications as Co-author

- Claeys, T., **Ovechkin, A.**, Vanoost, D., Vandenbosch, G. A. E., Pissoort, D. (2020). The Need For and How To Evaluate Continuous Wave Immunity of Wireless Systems used in V2X Applications. In: 2020 International Symposium on Electromagnetic Compatibility - EMC EUROPE, (1-6). Presented at the 2020 International Symposium on Electromagnetic Compatibility - EMC EUROPE, Rome, Italy. ISBN: 978-1-7281-5580-7. doi: 10.1109/EMCEUROPE48519.2020.9245766

FACULTY OF ENGINEERING TECHNOLOGY
DEPARTMENT OF ELECTRICAL ENGINEERING
ESAT-WAVE-CORE
Spoorwegstraat 12 8200 Bruges - Sint-Michiels
B-3001 Leuven
M-group@kuleuven.be
https://iiw.kuleuven.be/onderzoek/m-group